The STAR Beam Use Request for Run-22 and data taking in 2023-25

The STAR Collaboration

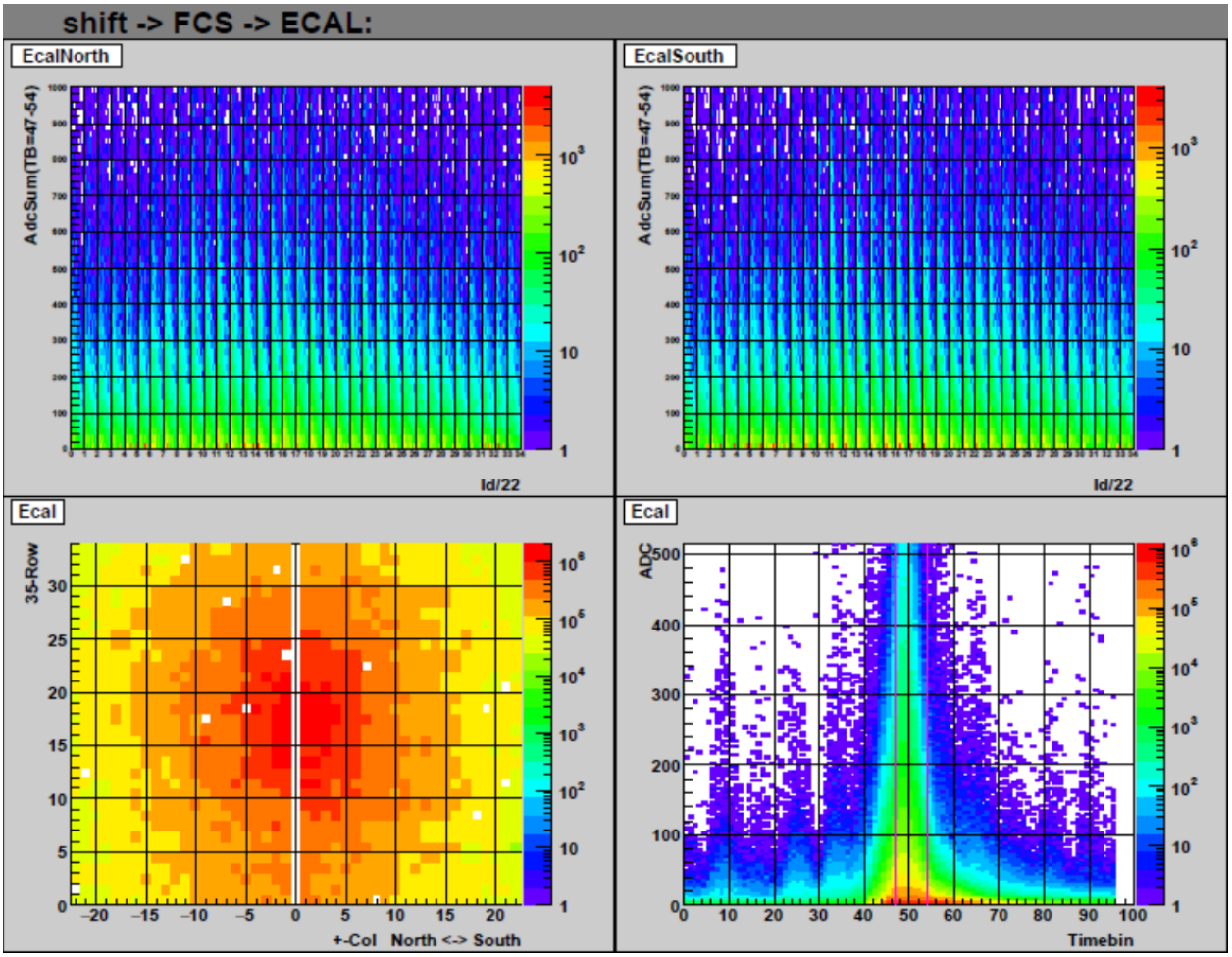

FCS EMCAL plots from online monitoring during Run-21.
Bottom left: distribution of hits across all the EMCAL modules.
Bottom right: energy deposition as a function of time bin in the electronics readout.
Top: Energy deposition vs module ID.

Executive Summary

This Beam Use Request outlines the strong physics programs proposed by STAR collaboration for data taking during Run-22 and 2023-2025.

STAR's **highest scientific priority** is to initiate the "must-do" Cold QCD forward physics program enabled by the newly completed suite of forward detectors via the collection of transversely polarized *pp* data at 510 GeV in Run-22. A combination of soft and hard probes collected during 2023-25 will be used to probe the QGP's microstructure and continue our unique forward physics program via the collection of high statistics Au+Au, *p*+Au, and *pp* data at $\sqrt{s_{\rm NN}} = 200$ GeV.

Run-22 takes full advantage of STAR's new forward detection capabilities, consisting of a Forward Calorimeter System (FCS) and a Forward Tracking System (FTS) located between $2.5 < \eta < 4$, while also capitalizing on the recent BES-II detector upgrades. As shown in Table 1, we propose **a dedicated 20 cryo-week transversely polarized *pp* run at $\sqrt{s} = 510$ GeV**. We note that an 18 cryo-week run would very detrimental to STAR achieving all our physics goals. Due to the need to commission the new detectors in the first weeks of running, a reduction of two weeks will result in more than a ∼15% reduction in our sampled luminosity estimates; the loss will occur once the detectors and RHIC will be operating at their most efficient.

Table 1: Proposed Run-22 assuming 20 cryo-weeks, including an initial one week of cool-down and a two weeks set-up time.

$\sqrt{s}$ (GeV)	Species	Polarization	Run Time	Sampled Luminosity	Priority
510	*pp*	Transverse	16 weeks	400 pb^{-1}	1

These data will enable STAR to explore, with unprecedented precision, forward jet physics that probe both the high-x (largely valence quark) and low-x (primarily gluon) partonic regimes.

The STAR collaboration has also identified a number of topics that together make a compelling case to take data during Runs 23-25 alongside sPHENIX, and successfully complete RHIC's scientific mission. This scientific program is enabled by the first opportunity to capitalize on the combination of the BES-II and Forward Upgrades that generate STAR's unique capabilities of PID over an extended rapidity acceptance and down to very low transverse momentum, while maintaining a low material budget. We propose to collect data from Au+Au, *p*+Au, and *pp* collisions at $\sqrt{s_{\rm NN}} = 200$ GeV as outlined in Table 2.

Significantly increased luminosities, the extended acceptance at mid-rapidity due to the iTPC, improved event plane and triggering capabilities of the EPD, and the ability to probe the previously inaccessible forward region are all exploited in our Hot QCD program, that informs on the microstructure of the QGP, and our Cold QCD program that will utilize transverse polarization setting the stage for related future measurements at the EIC.

By combining the data collected via Au+Au collisions at 200 GeV in Run-23 and Run-25 we will be able to address important questions about the inner workings of the QGP, including the temperature dependence of the shear and bulk viscosities, the 3-D nature of the initial state, how global vorticity is transferred to the spin angular momentum of particles on such short time scales and the chiral properties of the medium.

In Run-24 STAR considers it critical that we collect approximately equal nucleon-nucleon luminosities for pp and p+Au at 200 GeV. In this way we can optimize the statistical precision of several critical observables that require comparisons between results in both pp and p+Au. We request transversely polarized protons for both datasets. Assuming 28 cryo-weeks in Run-24 we expect to record samples that represent a factor 4.5 times the luminosity that STAR sampled during transversely polarized pp collisions in Run-15 and 3 times the luminosity sampled during transversely polarized p+Au collisions in Run-15.

Table 2: Proposed Run-23 - Run-25 assuming 28 cryo-weeks of running every year, and 6 weeks set-up time to switch species in 2024. Sampled luminosities assume a "take all" triggers.

$\sqrt{s_{\rm NN}}$ (GeV)	Species	Number Events/ Sampled Luminosity	Year
200	Au+Au	10B / 31 nb^{-1}	2023
200	pp	235 pb^{-1}	2024
200	p+Au	1.3 pb^{-1}	2024
200	Au+Au	10B / 31 nb^{-1}	2025

As requested, we also considered the scenario that each run is reduced to only 20 cryo-weeks in 2023-25. The dramatic decrease in sampled luminosity resulting from this scenario will have a serious negative impact on us achieving all of our physics goals outlined in this BUR.

If such a negative scenario unfolds, the STAR collaboration would continue to request Au+Au, p+Au, and pp running as outlined in Table 3 to take the best possible advantage of our recent upgrades. The ordering of this running could be optimized to minimize time lost to moving the magnets for p+Au running. This scenario would result in a significant increase in both the statistical and systematic uncertainties of all the data. The hard probe, thermal di-lepton, and photon-induced di-lepton and J/ψ Au+Au programs would be very detrimentally hit. The impact of the nuclear PDFs, fragmentation functions, and gluon saturation measurements would also be affected; these require comparisons of the same observables measured in both pp and p+Au collisions.

Finally in Section 5 we propose the collection of two datasets if the opportunity arises after collection of our higher priority datasets outlined above. One proposal enables the determination of nuclear deformation parameters of heavy-ion nuclei which are important to improve our modeling and subsequent understanding of the hydrodynamical response of the medium. Information on these deformation parameters are of significant interest to the nuclear structure physics community, and heavy ion collisions have very different sensitivity

Table 3: Proposed Run-23 - Run-25 assuming 20 cryo-weeks of running every year, and 6 weeks set-up time to switch species in 2024. Sampled luminosities assume a "take all" triggers.

$\sqrt{s_{\rm NN}}$ (GeV)	Species	Number Events/ Sampled Luminosity
200	Au+Au	12B / 37 nb^{-1}
200	pp	214 pb^{-1}
200	p+Au	1.2 pb^{-1}

on and might probe different aspects of these parameters.

The other proposal expands our fixed-target program to include other light beam and target combinations. These data will help clarify the role and mechanisms of nucleon stopping. In addition, light nucleus cross sections in the target/projectile regions using beams of 3-50 GeV/n are of great interest to the NASA Space Radiation community.

Contents

1 Highlights from the STAR Program

1.1 Highlights from the Heavy Ion Program

1.1.1 Bulk Correlations

Over the past years, the STAR collaboration has performed a series of correlation measurements directed towards a comprehensive understanding of the QCD phase diagram and the bulk properties of the QGP phase. Here we highlight the most recent STAR results on bulk correlations, which are expected to shed light on the QCD phase diagram as well as on the transport properties of the QGP.

Net-proton Number Fluctuations and a Crossover Search

One of the main goals in heavy-ion collision experiments is to understand a phase diagram of QCD matter with respect to temperature (T) and baryon chemical potential ($\mu_{\rm B}$). In the Beam Energy Scan program (BES-I), heavy-ion collision experiments were carried out by varying the collision energy in order to scan a wide region of the baryon chemical potential, $30 < \mu_{\rm B}$ (MeV) < 400. The STAR experiment has measured higher-order fluctuations up to the fourth-order of net-proton multiplicity distributions from the BES-I. The fourth-order fluctuations were found to have a non-monotonic beam energy dependence within 3.1σ significance [1]. More precise measurements with enhanced statistics at low collision energies of $3.0 < \sqrt{s_{\rm NN}}$ (GeV) < 19.6 will be performed with data from the Beam Energy Scan program phase II (BES-II) and the Fixed-Target program (FXT).

On the other hand, it is also important to establish the nature of the phase transition experimentally at small $\mu_{\rm B}$ region. A smooth crossover is predicted at $\mu_{\rm B} = 0$ by first principle lattice-QCD calculations [2], however, there is currently no direct experimental evidence. Theoretically, the sixth-order fluctuations of baryon numbers are expected to be negative near the phase transition temperature [3–5]. The STAR experiment has measured the sixth-order fluctuations, C_6/C_2, of net-proton distributions using high statistics datasets at $\sqrt{s_{\rm NN}}$=27, 54.4, and 200 GeV. Figure 1 shows net-proton C_6/C_2 as a function of collision centrality. Most of the data points for 27 and 54.4 GeV are consistent within uncertainties with a statistical baseline ($C_6/C_2 = 1$). On the other hand, the C_6/C_2 values at 200 GeV are negative systematically from peripheral to central collisions. The experimental results are compared with lattice-QCD and UrQMD calculations. Results for 27 and 54.4 GeV are consistent with UrQMD calculations, while for 200 GeV results are below the UrQMD calculations. The negative values observed in central collisions are qualitatively consistent with QCD-based model and lattice QCD calculations within large uncertainties. The current results are dominated by large statistical uncertainties, which makes it difficult to extract definitive physics messages. The statistical accuracy for 200 GeV will be significantly improved by Au+Au collisions in Run-23 and Run-25.

Global Polarization of Ξ and Ω Hyperons in Au+Au collisions at 200 GeV:

The phenomenon of global polarization in heavy-ion collisions results from the partial

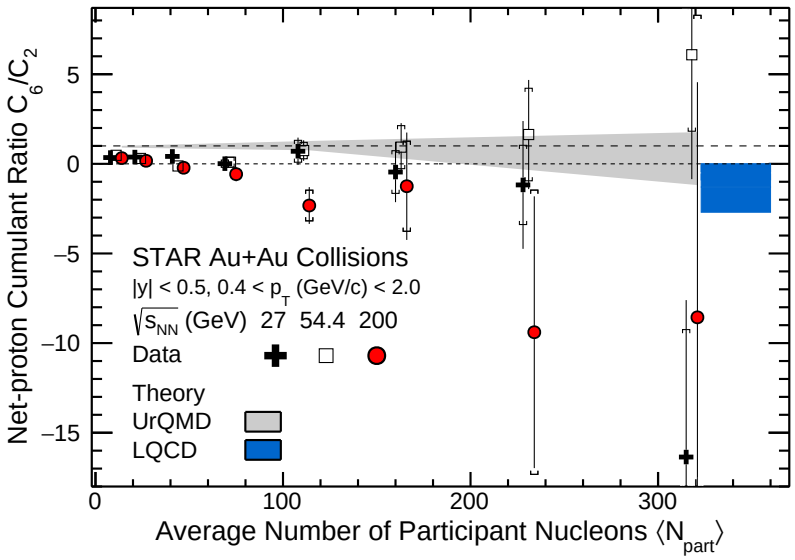

Figure 1: Centrality dependence of net-proton C_6/C_2 in Au+Au collisions for $\sqrt{s_{\rm NN}}$ = 27, 54.4, and 200 GeV within $|y| < 0.5$ and $0.4 < p_T$ (GeV) < 2.0. Points for different beam energies are staggered to improve clarity. A shaded band show the results from UrQMD model calculations. Lattice QCD calculations for $T = 160$ MeV and $\mu_{\rm B} < 110$ MeV are shown as a blue band at $\langle N_{\rm part} \rangle \approx 340$.

transformation of the orbital angular momentum of colliding nuclei into the spin angular momentum of the particles produced in the collision [6, 7]. Consequently, these particles display global polarization along the direction of the initial orbital momentum of the nuclei. Global polarization was first measured by the STAR Collaboration in the beam energy scan Au+Au collisions [8].

Although the energy dependence of the Λ polarization can be reasonable described by theoretical models [9–12], several questions remain open, and a detailed modeling of global polarization and a dynamical approach of spin is under development. Therefore, further experimental inputs are crucial for understanding vorticity and polarization phenomena in heavy-ion collisions. Recently STAR reported the first measurements of the global polarization of spin $s = 1/2$ Ξ^- and $\bar{\Xi}^+$ hyperons, as well as spin $s = 3/2$ Ω hyperons in Au+Au collisions at 200 GeV.

Figure 2 shows the collision energy dependence of the Λ hyperon global polarization previously measured [8, 14] along with the new Ξ and Ω global polarizations measurements at $\sqrt{s_{\rm NN}} = 200$ GeV. For Ξ and Ω, to reduce the statistical uncertainty, we averaged over particle and antiparticle, 20%-80% centrality range, transverse momentum $p_T > 0.5$ GeV/c, and rapidity $|y| < 1$. Global polarization of Ξ^- and $\bar{\Xi}^+$ measurements determined via the daughter Λ polarization show positive values, with no significant difference between Ξ^- and $\bar{\Xi}^+$ (P_Ξ (%) = 0.77±0.16 (stat.)±0.49 (syst.) and $P_{\bar{\Xi}}$ (%) = 0.49±0.16 (stat.)±0.20 (syst.)). The average polarization value obtained by this method is $\langle P_\Xi \rangle$ (%) = 0.63 ± 0.11 (stat.) ± 0.26 (syst.). The Ξ+$\bar{\Xi}$ polarization was also measured via analysis of the angular distribution

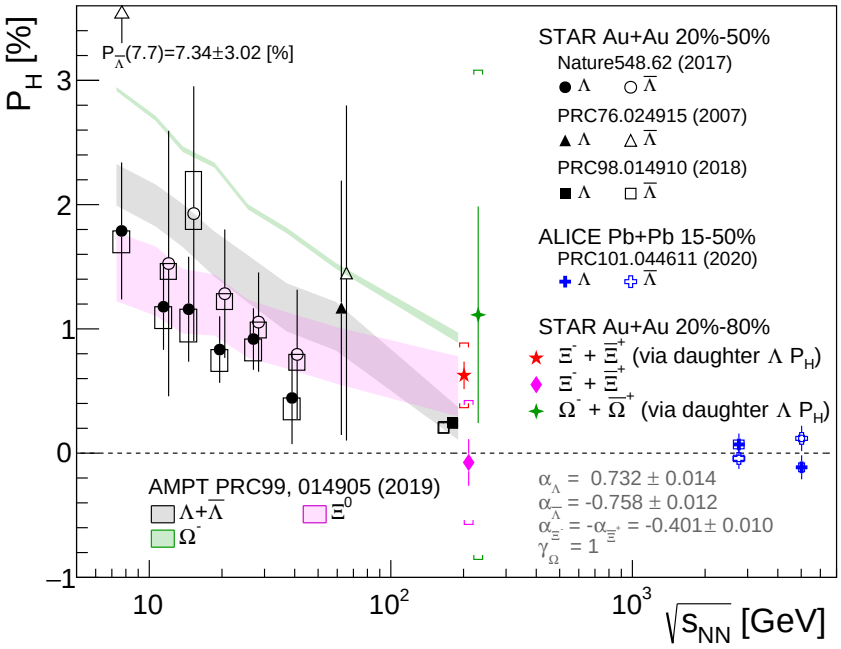

Figure 2: The energy dependence of the hyperon global polarization measurements. The points corresponding to Λ and $\bar{\Lambda}$ polarizations, as well as Ξ and Ω points in Au+Au collisions at $\sqrt{s_{\rm NN}}$ = 200 GeV are slightly shifted for clarity. Previous results from the STAR [8, 13] and ALICE [14] experiments compared here are rescaled by new decay parameter indicated inside the figure. The data point for $\bar{\Lambda}$ at 7.7 GeV is out of the axis range and indicated by an arrow with the value. The results of the AMPT model calculations [15] for 20-50% centrality are shown by shaded bands where the band width corresponds to the uncertainty of the calculations.

.

of daughter Λ in Ξ rest frame. This result, $\langle P_\Xi \rangle$ (%) $= -0.07 \pm 0.19$ (stat.) ± 0.50 (syst.), has larger uncertainty in part due to a smaller value of α_Ξ compared to α_Λ, which leads to smaller sensitivity of the measurement. The weighted average of the two measurements is $\langle P_\Xi \rangle$ (%) $= 0.47 \pm 0.10$ (stat.) ± 0.23 (syst.), which is larger than the polarization of inclusive $\Lambda + \bar{\Lambda}$ measured at the same energy for 20%-80% centrality, $\langle P_\Lambda \rangle$ (%) $= 0.24 \pm 0.03 \pm 0.03$ [8], although the difference is still not significant considering the statistical and systematic uncertainties of both measurements. The Ω^- global polarization, presented in Fig. 2, is $\langle P_\Omega \rangle$ (%) $= 1.11 \pm 0.87$ (stat.) ± 1.97 (syst.) for 20%-80% centrality events, more precise measurements will be needed to make a definitive statement. Future measurements with higher precision will shed light on the uncertainty of the decay parameter γ_Ω, as well as experimental results on the global polarization of spin-3/2 particles, providing critical information about spin dynamics in heavy-ion collisions.

Nuclear Deformation Measurements

Deformation is a fundamental property of atomic nuclei that reflects the correlated nature of the dynamics of nucleons within a quantum many-body system. The majority of atomic nuclei possess an intrinsic deformation, most of which are an axial quadrupole, or ellipsoidal,

deformation.

Prior relativistic heavy-ion collision measurements from STAR reported strong signatures of nuclear deformation using detailed comparisons between Au+Au collisions and U+U collisions [16]. These measurements suggest that U+U collisions are much more deformed in their ground state. Consequently, we can say that detailed comparisons between different nuclei enabled us to examine the geometry of the colliding ions.

Recently it has been suggested to examine the geometry of the colliding nuclei using the correlation coefficient, $\rho(v_n^2, [p_T])$ [17–22];

$$\rho(v_n^2, [p_T]) = \frac{\mathrm{cov}(v_n^2, [p_T])}{\sqrt{\mathrm{Var}(v_n^2)}\sqrt{\mathrm{Var}([p_T])}}, \tag{1}$$

which might be more sensitive to the initial-state geometry, because it leverages the correlation between the eccentricity-driven flow harmonics v_n and the average transverse momentum of particles in an event $[p_T]$. The latter is related to the transverse size of the overlap region, so events that have similar energy-density but smaller initial-state transverse size should have a larger radial expansion and consequently larger mean transverse momentum [23]. It has also been proposed that the $\rho(v_n^2, [p_T])$ correlator is sensitive to the correlations between the initial size and the initial-state deformation of colliding nuclei [24, 25].

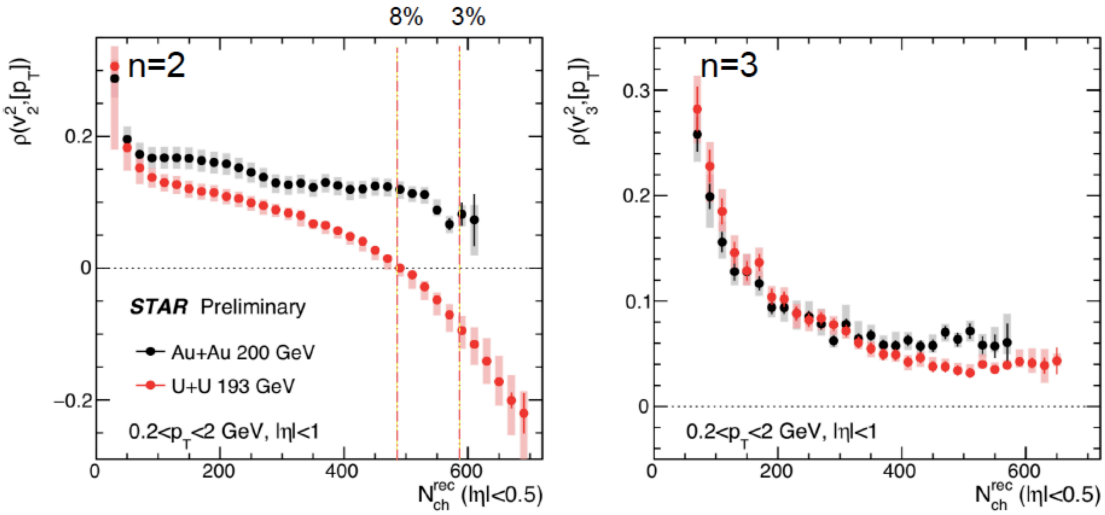

Figure 3: The N_{ch} dependence of the $\rho(v_2^2, [p_T])$ correlator panel (a) and $\rho(v_3^2, [p_T])$ correlator panel (b) for U+U at 193 GeV and Au+Au at 200 GeV.

.

Figure 3 presents the N_{ch} dependence of the $\rho(v_2^2, [p_T])$ correlator, left panel, and $\rho(v_3^2, [p_T])$ correlator, right panel, for U+U at 193 GeV and Au+Au at 200 GeV. Data are shown for $0.2 < p_T < 2.0$ GeV/c and $|\eta| < 1.0$. The presented $\rho(v_2^2, [p_T])$ measurement is shown to be negative in central U+U collisions, while it is positive in central Au+Au collisions. Such an effect is compatible with the theoretical expectations [25], and is caused by the prolate deformation of ^{238}U nuclei. Also the $\rho(v_2^2, [p_T])$ in U+U collisions is lower than in Au+Au

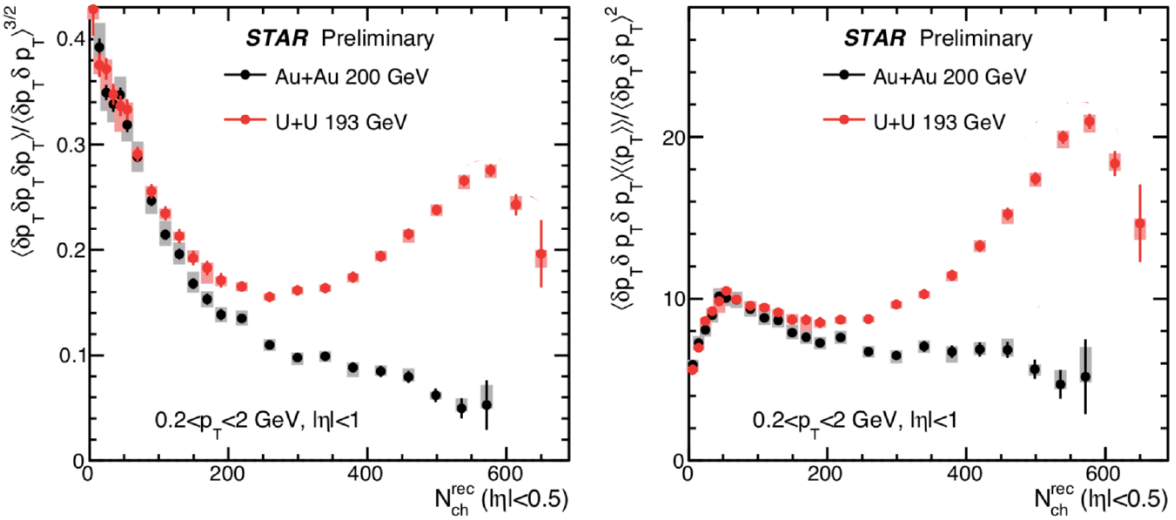

Figure 4: The N_{ch} dependence of the standard skewness left panel and intensive skewness right panel for U+U at 193 GeV and Au+Au at 200 GeV.

.

collisions across essentially the full N_{ch} range. In the right panel we present $\rho(v_3^2, [p_T])$ that shows minor difference between Au+Au and U+U collisions.

Also, it had been argued that the $p_{\rm T}$ dimensionless skewness depends on the system size and shape [26]. The standardized and *intensive* skewness are shown in Fig. 4 for U+U at 193 GeV and Au+Au at 200 GeV. The presented dimensionless skewness measurement shows a nonmonotonic trend for U+U at central collisions. This large difference between U+U and Au+Au could be attributed to the deformation of ^{238}U nuclei.

Azimuthal Anisotropy Measurements of Strange and Multi-strange Hadrons in U+U collisions at 193 GeV

Stronger constraints on transport and hydrodynamic model simulations can be achieved via investigating the azimuthal anisotropy of identified particles as a function of transverse momentum and collision centrality. Also, one can understand the initial conditions in heavy-ion collisions via varying the collision system size. This could be achieved by performing collisions of Uranium nuclei which have a deformed shape. Uranium nuclei possess a prolate shape [27], consequently, there are collision configurations (body-body collisions) in which the initial overlap region is not spherical even in central collisions. Moreover, depending on the angles of the two colliding Uranium nuclei relative to the reaction plane, several other collision configurations of U+U collisions are possible [28–30]. Studying these various collision shapes will provide an additional constraint for the initial conditions in models [31–33].

Recently we reported the results on flow coefficients v_n (n = 2, 3, and 4) for tge strange hadrons, K^0_s, ϕ, Λ, Ξ, and Ω at mid-rapidity ($|y| < 1.0$) in U+U collisions at $\sqrt{s_{NN}}$ = 193 GeV. Figure 5 presents the measurements of v_n coefficients scaled by $n_q^{n/2}$ as a function of $\mathrm{KE_T}/n_q$, for strange and multi-strange hadrons in U+U collisions at $\sqrt{s_{NN}}$ = 193 GeV.

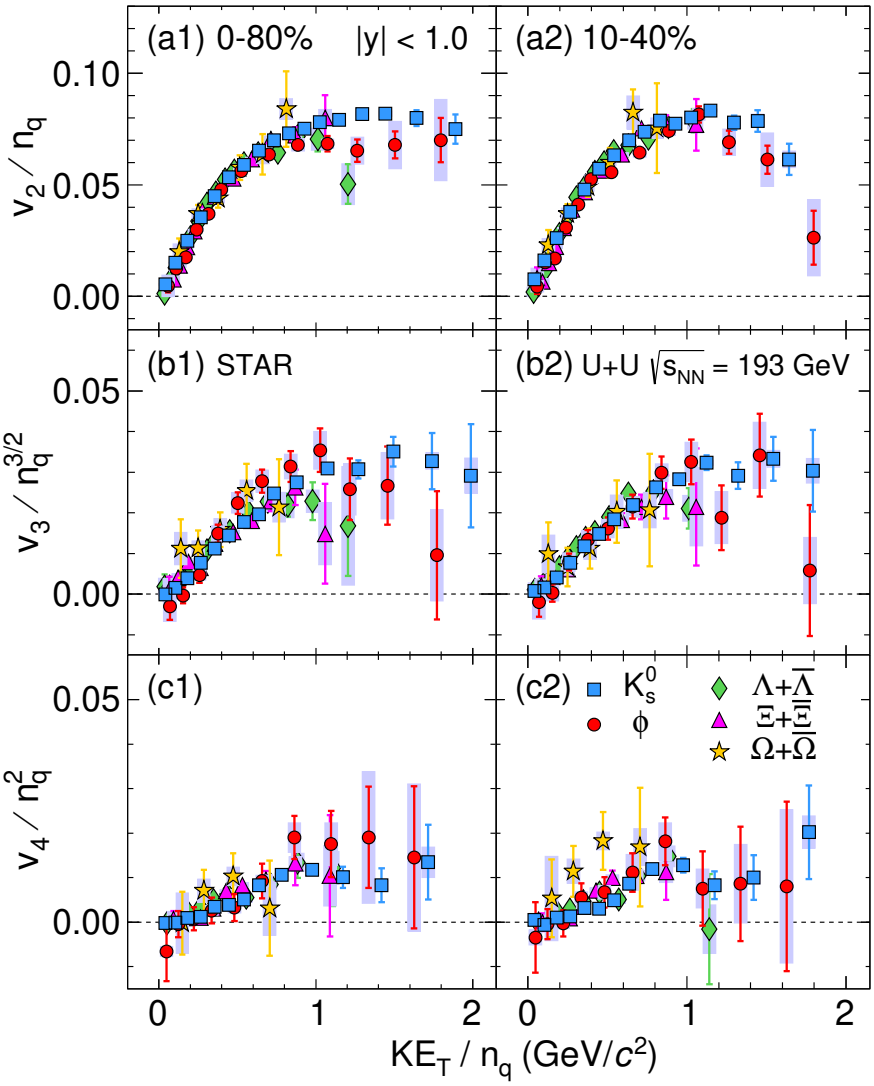

Figure 5: Flow coefficients v_2, v_3, and v_4 as a function of transverse kinetic energy $\mathrm{KE_T}/n_q$ for various particles at mid-rapidity ($|y| < 1$) in U+U collisions at $\sqrt{s_{\mathrm{NN}}}$= 193 GeV, scaled by the number of constituent quarks (n_q) to the power $n/2$. Left panels represent results for minimum bias (0-80%) and right panels for centrality class (10-40%). The error bars represent statistical uncertainties. The bands represent point-by-point systematic uncertainties.

.

Our measurements show that the NCQ scaling holds within experimental uncertainties for each harmonic order n =2,3 and 4. The $v_n/n_q^{n/2}$ vs. $\mathrm{KE_T}/n_q$ values lie on a single curve for all the particle species within ±15%. The measured NCQ scaling of v_n coefficients indicates the evolution of partonic collectivity during the QGP phase in heavy-ion collisions. This observed scaling also suggests the formation of hadrons through quark coalescence in the intermediate p_{T} range (2.0< $p_{\mathrm{T}}(GeV/\mathrm{c})$ < 4.0) [34, 35]. Although there are considerable differences between U+U and Au+Au in the collision geometry, the hydrodynamical evolution and the coalescence mechanism for hadron formation persist-key features of QGP drops formed in

nucleus-nucleus collisions.

Studies of Strong Interactions

The study of nucleon-nucleon (NN), nucleon-hyperon (NY), and hyperon-hyperon (YY) interactions are fundamental to understanding the physics of relativistic heavy-ion collisions, neutron stars, and the existence of various exotic hadrons. A significant amount of NN scattering data allows us to construct precise NN potential models. However, the limited availability of NY scattering data and no scattering data for the YY systems creates understanding the NY and YY potentials complicated and challenging. It has become possible to study with Lattice QCD constraints of the strong interactions [36]. Commonly, the experimental information on the bound states of strange baryons and nucleons (hypernuclei) are used to provide information on YY interactions [37]. However, the extraction of strong interactions' parameters becomes difficult due to, e.g., contamination by many-body effects.

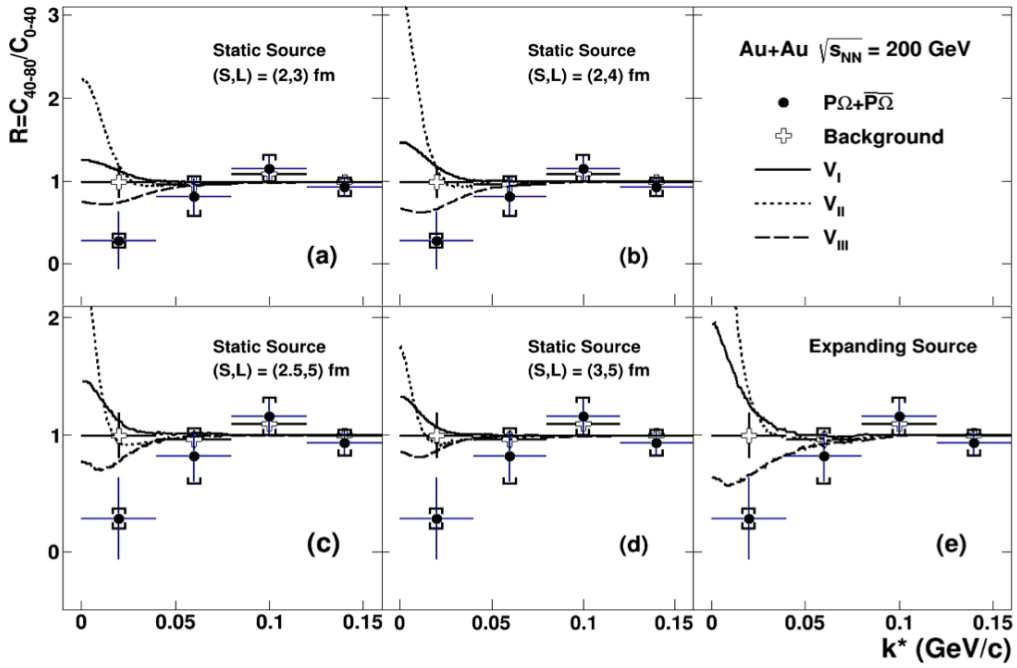

Figure 6: The solid circle represents the ratio (R) of the small system (40-80% collisions) to the large system (0-40% collisions) for pΩ and $\bar{p}\Omega$. The error bars correspond to statistical uncertainties, and caps correspond to systematic uncertainties. The open crosses represent the ratio for background candidates from the side-band of the Ω invariant mass. Predictions for the ratio of the small system to the large system for $p\Omega$ interaction potentials V_I, V_{II} and V_{III} for static sources with different source sizes (S, L) = (2,3), (2,4), (2.5, 5) and (3,5) fm, where S and L are corresponding to small and large systems, are shown in (a), (b), (c) and (d) respectively. In addition, the prediction for an expanding source is shown in (e) [38].

High-energy heavy-ion collisions provide a significant number of hyperons in each collision, which provides an excellent opportunity to study strong interactions. Measurement of

two-particle correlations at low relative momentum, with the femtoscopy method, has been used to study the space-time dynamics of the source created in heavy-ion collisions [39], [40]. In addition to this, the measurement of two-particle correlations at low relative momentum can also be used to measure final state interactions (FSI) between nucleons and hyperons. A recent study of lattice QCD calculations for heavy quark masses shows that the $N\Omega$ interaction is attractive at all distances [41]; the shape of the two-particle correlation function at low relative momentum changes significantly with the strength of the $N\Omega$ attraction [42]. However, the Coulomb interaction in the $p\Omega$ channel makes it challenging to access the strong interaction parameters directly from the measured two-particle correlation function. Therefore, a new measurement, namely the ratio of the correlation functions of peripheral (small) to central (large) collision systems, has been proposed in [42]. This ratio provides direct access to the strong interaction between proton and omega, independent of the model used for the emission source. The attractive nature of an $N\Omega$ interaction leads to the possible existence of the $N\Omega$ dibaryon. Such an $N\Omega$ dibaryon is the most interesting candidate after the H-dibaryon [43]. Several attempts have been made to estimate the binding energy of the $N\Omega$ state in different QCD-motivated models [41]. The $N\Omega$ dibaryon can be produced in high-energy heavy-ion collisions through the coalescence mechanism [44]. The measurement of the $p\Omega$ correlation function for peripheral and central Au+Au collisions at $\sqrt{s_{\rm NN}} = 200$ GeV, presented in Fig.6, provides insight into the existence of an $N\Omega$ dibaryon.

1.1.2 pp and Heavy-Ion Jet Measurements

The STAR jet program has recently focused on a new generation of measurements that are aimed at differentially studying jet production and fragmentation mechanisms in *pp* and heavy-ion collisions. In this section, we highlight recent results on jet substructure in *pp* collisions along with a measurement of correlations between jet production and the underlying event (UE) in p+Au collisions. These measurements serve a dual purpose in that they help us with studies of fundamental QCD in comparison with Monte Carlo (MC) models and theoretical calculations and as a reference for hot/cold nuclear matter effects in heavy-ion collisions.

Differential Measurements of Jet Substructure in pp Collisions

As jets are composite objects built from a parton shower and its fragmentation, they contain rich substructure information that can be exploited via jet finding algorithms [45]. These algorithms typically employ an iterative clustering procedure that generates a tree-like structure, which upon an inversion, gives access to a jet's substructure at different steps along the cluster tree. The most common toolkit for such measurements is SoftDrop grooming [46] which employs a Cambridge/Aachen re-clustering of a jet's constituents and imposes a criterion at each step as we walk backwards in the de-clustered tree

$$z_g = \frac{\min(\mathrm{p_{T,1}}, \mathrm{p_{T,2}})}{p_{T,1} + p_{T,2}} > z_{\rm cut} \left(\frac{R_g}{R_{jet}}\right)^{\beta}; R_g = \Delta R(1,2) \tag{2}$$

where $z_{cut} = 0.1$ is a momentum fraction threshold and β is the angular exponent which in our analysis is set to zero [47]. These default values for the parameters make the SoftDrop observable comparable to theoretical calculations, and at the infinite momentum limit they converge to the DGLAP splitting functions.

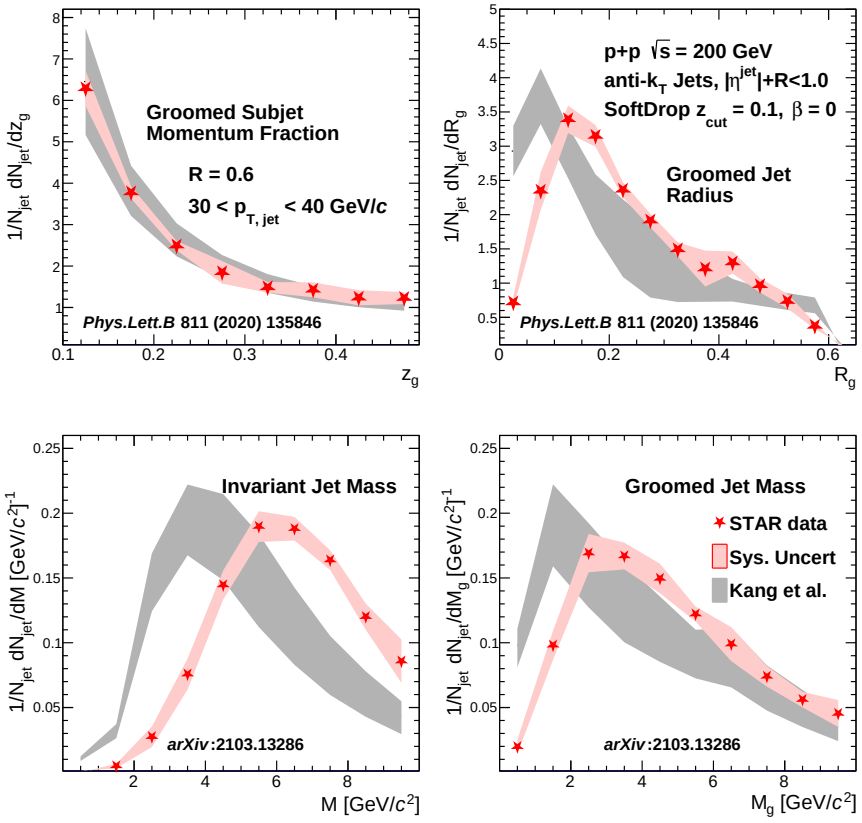

Figure 7: Comparisons of the first split SoftDrop groomed subjet momentum fraction z_g (top left), groomed jet radius R_g (top right), invariant jet mass M (bottom left) and the groomed jet mass M_g (bottom right) shown in the red markers to theoretical calculations in the shaded back regions.

STAR has recently published jet substructure measurements at the first split [48, 49] for jets of varying transverse momenta (p_{T}) and jet radius in pp collisions at $\sqrt{s} = 200$ GeV. A compilation of the different observables are shown in Fig. 7 for $R = 0.6$ jets with $30 < p_{T,jet} < 40$ GeV/c where the data are shown in the filled red star markers compared to theoretical calculations [50] in the shaded gray bands. The red band represents the total systematic uncertainty resulting from variation of the tracking efficiency, tower energy scale, hadronic correction due to tracks matched with towers and the unfolding procedure. The top panels show the SoftDrop groomed momentum fraction (z_g, top left) and the groomed jet radius (R_g, top right); we see a relatively good comparison with theory predictions which do not include any non-perturbative corrections. The calculations reproduce the z_g distribution in data for high p_{T}, large-radius jets (the publication [48] includes jets of various momenta

and radii, and the calculations do not reproduce the distributions at lower jet momenta and smaller jet radii) whereas the R_g shows significant quantitative differences with the data which can be characterized as a shape function due to non-perturbative corrections. The bottom two panels of Fig. 7 shows the first measurements of the invariant and groomed jet mass for the same jet selections as the top panels. The jet mass is sensitive to the virtuality of the jet [51] and is related to both the momentum and the angular scales [52]. The same theoretical calculation severely under-predicts the jet mass distributions primarily due to the lack of hadronization corrections and the overall small jet scales which lead to large theoretical uncertainties. The grooming procedure overall helps in reducing these non-perturbative effects and as a result, the groomed jet mass data exhibits a similar level of disagreement as that of the groomed jet radius.

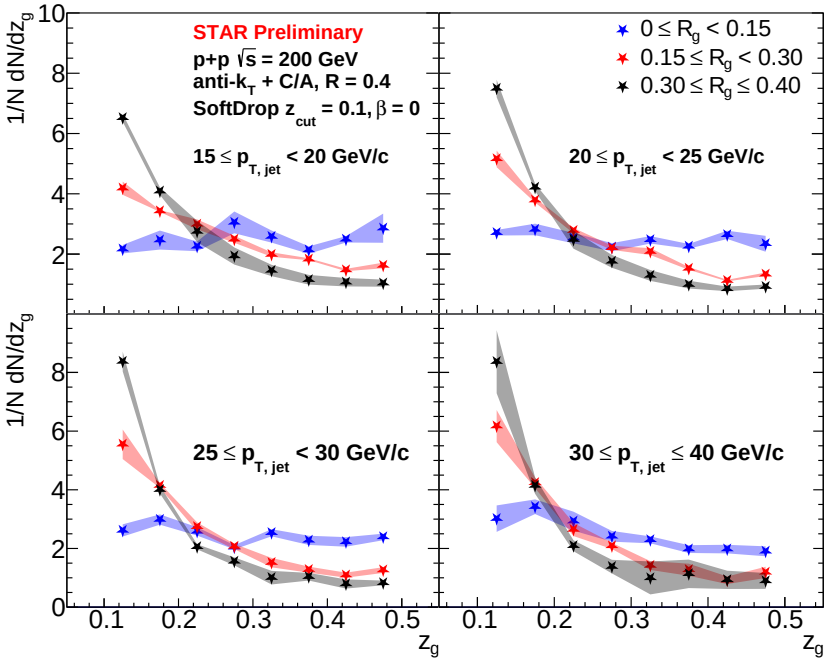

Figure 8: Differential measurements of the first split SoftDrop groomed subjet momentum fraction for jets of varying opening angle ($0 < R_g < 0.15$, $0.15 < R_g < 0.3$, $0.3 < R_g < 0.4$ in the blue, red and black markers) and transverse momenta ($15 < p_T < 20$ GeV/c in the top left to $30 < p_T < 40$ GeV/c in the bottom right).

These double differential measurements were corrected in both jet p_{T} and z_g/R_g simultaneously and show quite a significant variation in substructure for jets of a particular p_{T}. STAR has recently measured the correlations between the momentum and angular scales of jet substructure at the first split as shown in Fig. 8. The jet p_T increases from the top left to the bottom right with each panel containing three sets of data markers representing a selection on the groomed jet radius, $0 < R_g < 0.15$ (blue), $0.15 < R_g < 0.3$ (red), $0.3 < R_g < 0.4$ (black). The correlations between $z_g - R_g$ are unfolded via an 2-D iterative Bayesian procedure as implemented in the RooUnfold package [53] and followed by a boot-strap correction

for the jet energy scale. The final results are the first in jet substructure that are corrected and presented in 3-D i.e, z_g vs R_g vs $p_{\mathrm{jet,T}}$.

The data show a stark modification in the shape of the splitting z_g as R_g is varied from small to large angle. Narrow, or collinear, splits are found to have a symmetric distribution implying a near equal probability for soft or hard splittings. Wide angle splits on the contrary are strongly peaked at small values of z_g resulting in those splits containing softer emissions. The dependence on the jet p_{T} is observed to be weak compared to the R_g which essentially drives the z_g distribution for jets in our kinematics. These measurements signify the need of all three observables if one aims to tag jets with a unique substructure.

Since the jet cluster tree extends beyond a first split, one can iteratively apply the Soft-Drop procedure on the hardest surviving branch and measure the jet substructure at each split along the de-clustered tree [54]. Such measurements enable a study of the parton shower and evolution of both the momentum and angular scales within a jet. Upon applying the iterative SoftDrop procedure to the jets studied in this measurements, we reconstruct a collection of observables corresponding to the total number of splittings n and z_g^n and R_g^n at each split. We limit our measurement to the first three surviving splits within the jets and present the results fully corrected in 3-D corresponding to the jet p_{T}, z_g/R_g, and the split number n. The detector smearing effects on the $z_g/R_g, p_T^{\mathrm{jet}}$ are corrected via a 2-D Bayesian iterative unfolding via RooUnfold and the splitting hierarchy is corrected by matching the splits based on the prong that initiates that particular split at both the particle and detector level $\Delta R_{initiator} < 0.1$.

The data are shown in Fig. 9 for the first, second and third splits in the black, red and blue colored markers, respectively. The corresponding colored shaded regions behind the data markers represent total systematic uncertainty resulting from variations in the similar sources as shown in Fig. 7 with the addition of an extra systematic to the corrected data shape based on the split matching criterion varied by 0.1 ± 0.025. These first measurements detail a remarkable feature of substructure evolution along the jet shower where we observe a gradual variation in moving from the first to the third splits. The R_g at a split can also be interpreted as the available phase space for subsequent emissions/splits and is also related to the virtuality at the split. As R_g gets progressively narrower with increasing split n, the shape of z_g also changes from being peaked at smaller values i.e asymmetric splitting, to a flatter distribution with increased probability for symmetric splits. By comparing the left and right panels of Fig. 9, a weak dependence on the jet p_{T} is observed, phase space restrictions, via selecting a split, significantly impact the substructure observables.

These novel multi-dimensional measurements of jet substructure enable a critical comparison with MC event generators and quantitatively assess the impact of perturbative (parton showers) and non-perturbative (hadronization, multi-parton interactions) models and theoretical calculations with small jet and subjet scales that are close to Λ_{QCD}. With a corrected split hierarchy, we now have a measurement separated in the split formation time along a jet shower. This technique will be utilized in an upcoming heavy-ion measurements in Au+Au collisions resulting in a space-time tomography of jet quenching and parton energy loss by tagging on jets of a specific substructure.

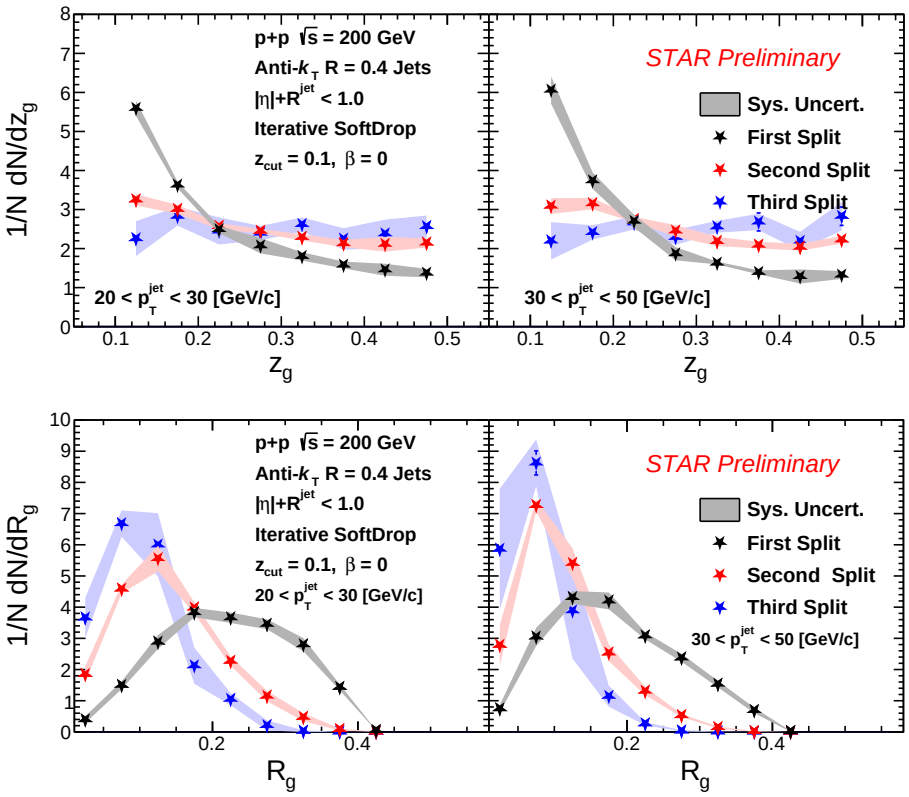

Figure 9: Measurements of the iterative SoftDrop splitting observable for the first (black markers), second (red markers) and third (blue markers) splits shown for the z_g (top panels) and R_g (bottom panels) observables for two jet momenta selections (left - $20 < p_T^{jet} < 30$ and right - $30 < p_T^{jet} < 50$ GeV/c).

Correlations of the UE and Jet Production in p+Au collisions

Jets are originated from high-Q^2 parton scatterings very early in hadronic collisions. Beside this high-Q^2 process, particles are also produced from the elastic and inelastic scatterings of multiple partons from each of the colliding beams. These processes are often described as non-perturbative and non-factorizable in comparison with the jet production, and a recent STAR measurement [55] of the canonical underlying event vs the jet momenta in pp collisions shows an anti-correlation where the particle multiplicity in the off-axis region away from the jet decreases as the jet momentum increases. This slight negative correlation is understood to be consistent with energy conservation restricting particle production in the transverse region as the leading jet becomes more energetic.

Asymmetric p+Au collisions offer a natural extension of such measurements where one can study the dependence of this anti-correlation on the event activity and the jet rapidity, i.e. if the jet is perceived to have come from the Au or p beam. The event activity (EA) is defined as the sum of ADC hits in the Au-going inner Beam Beam Counter (east iBBC) located at $\eta \in [-5, -2]$. The EA deciles are defined from the EA distribution in minimum

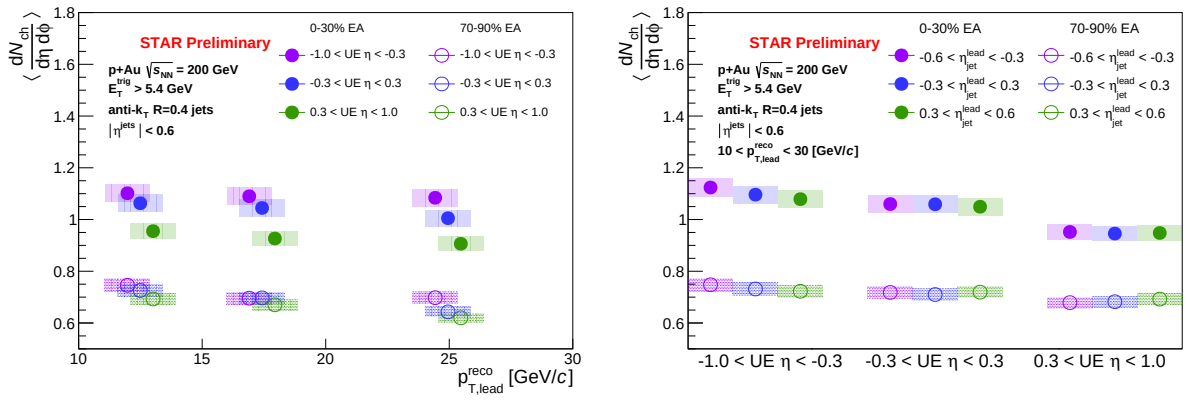

Figure 10: Average corrected charged particle multiplicity in the UE in low/high (open/filled symbols) activity p+Au collisions measured differentially as a function of the reconstructed jet momenta (left panel) and the forward, mid and backward rapidity (right panel).

bias events and high/low EA events are selected as $0-30\%/70-90\%$. Preliminary results are shown in Fig. 10 where the UE average charged particle multiplicity $\langle dN_{ch}/d\eta d\phi \rangle$ for high/low EA events (filled/open markers) are measured as a function of the leading jet p_T (left panel) and the UE η (right panel). The multiplicity is corrected for detector effects and the shaded regions represent the systematic uncertainty on the tracking efficiency. Each panel also has three different colored markers corresponding to UE η in the left and jet η in the right panel. These results are not yet corrected for the jet energy scale and resolution which will be included in the final published results. The UE mean multiplicity in p+Au collisions have a significant dependence on the EA as expected, with high EA events having large multiplicity. We also observe a slight anti-correlation on the jet momenta for the proton going direction ($0.3 < \eta < 1.0$), similar to pp collisions, along with a significant dependence on the UE η, especially in high EA events. The Au-going side has relatively similar $\langle dN_{ch}/d\eta d\phi \rangle$ within uncertainties and meaning the UE multiplicity is independent on the leading jet η.

These results, along with recent STAR preliminary measurements on semi-inclusive jet yield in high/low EA p+Au collisions, point to an early time correlation between the high Q^2 scattering leading to jet production and the low energy processes which result in the forward activity. The UE multiplicity shows very little anti-correlation with the jet momenta and is currently explored as a selection of event EA for future measurements to reduce the early time or long range effects which nominally result from selecting on forward activity.

Isobar Collisions

The isobar data collected by STAR during Run-18 is a high statistics minimum bias dataset where the primary goal was to study potential differences in chiral magnetic effects between the two colliding species, Ru and Zr, as detailed in Sec 1.2. The jet working group in STAR is involved in ongoing measurements of energy loss via inclusive charged hadrons suppression and semi-inclusive hadron-jet measurements exploiting these high statistics and

low pile-up data. Isobar data provides a motivation to study energy loss for various system sizes in comparison with Au+Au collisions and dependencies on the system geometry.

1.1.3 Heavy-flavor

Heavy-flavor (HF) quarks are produced predominately via hard scatterings of partons in p(A)+p(A) collisions. Kinematic distributions and hadronization probabilities of HF quarks in Å collisions can be different than those in pp collisions due to interactions of HF quarks with the QGP medium. Understanding these differences allows us to determine properties of the QGP. STAR has recently published two papers on heavy flavor production: 1) the measurement of inclusive J/ψ polarization in pp collisions at $\sqrt{s_{\rm NN}}$ = 200 GeV [56] and 2) observation of D_s/D^0 enhancement in Au+Au collisions at $\sqrt{s_{\rm NN}}$ = 200 GeV [57]. The former measures the J/ψ polarization in pp collisions with improved precision and over a wider $p_{\rm T}$ range, and thus provides a stricter constraint on quarkonium production mechanisms. The latter reveals that the strange-charm meson (D_s) yield is significantly enhanced in Au+Au collisions with respect to that in elementary pp /e+p/e+e collisions and confirms that coalescence is an important hadronization mechanism also for charm quarks in heavy-ion collisions. Below we describe new results from STAR on inclusive J/ψ production in p+Au collisions at $\sqrt{s_{\rm NN}}$ = 200 GeV and in Au+Au collisions at $\sqrt{s_{\rm NN}}$ = 54.4 GeV.

J/ψ production has been found to be suppressed in Au+Au collisions at RHIC top energies [58,59]. Such a suppression can be produced from color screening of the $c\bar{c}$ potential by the QGP medium, and by cold nuclear matter (CNM) effects from e.g., nuclear parton distribution functions, energy loss or absorption in the nucleus, and interaction with co-moving hadrons. Moreover, in heavy-ion collisions J/ψ can be produced from recombination of uncorrelated c and $\bar{c}$ in the QGP. Therefore, in order to precisely determine the suppression due to the color screening effect alone, it is important to quantify the CNM effects, and be able to disentangle the color-screening and recombination effects.

STAR has reported a preliminary result on the nuclear modification factor R_{pA} for inclusive J/ψ with $p_T > 4$ GeV/c and $|y| < 1$, as shown in Fig. 11. The result is extracted in the dielectron channel from the data collected from pp and p+Au collisions at $\sqrt{s_{\rm NN}}$ = 200 GeV in 2015. Compared to previous measurements, this result presents a more precise determination of the CNM effects for high-$p_{\rm T}$ inclusive J/ψ at the RHIC top energy. The measured R_{pAu} is consistent with unity, suggesting little suppression in this kinematic region due to the CNM effects. The result confirms that the color-screen effect is the main cause of the large suppression of high-p_T inclusive J/ψ observed in Au+Au collisions at $\sqrt{s_{\rm NN}}$ = 200 GeV. These data points provide a stronger constraint on theoretical calculations for J/ψ suppression due to the CNM effects and J/ψ production mechanisms in heavy-ion collisions.

STAR has also released at the 2021 Strangeness in Quark Matter conference a new preliminary result on the nuclear modification factor R_{AA} for inclusive J/ψ in Au+Au collisions at $\sqrt{s_{\rm NN}}$ = 54.4 GeV. The result is extracted in the dielectron channel from BES-II data collected in 2017. As can be seen in Fig. 12, the measured R_{AA} at $\sqrt{s_{\rm NN}}$ = 54.4 GeV is consistent with those measured at $\sqrt{s_{\rm NN}}$ = 39, 62.4 and 200 GeV [58], suggesting a partial cancellation of J/ψ suppression due to the color-screen effect by J/ψ produced from recom-

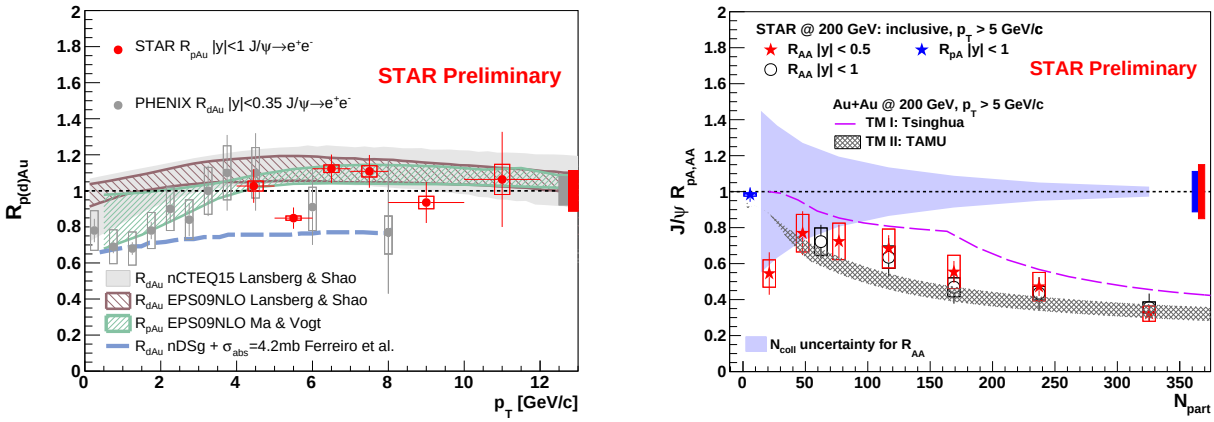

Figure 11: Left: $R_{p(d)Au}$ vs. p_{T} for inclusive J/ψ in p(d)+Au collisions at $\sqrt{s_{\mathrm{NN}}}$ = 200 GeV. Red circle: this analysis; grey circle: PHENIX R_{dAu} in $|y| < 0.35$ [60]; grey band: R_{dAu} from nCTEQ15 nuclear PDF sets [61]; brown shadowed: R_{dAu} from EPS09 NLO nuclear PDF sets [61]; green shadowed: R_{pAu} from EPS09 NLO nuclear PDF sets [62]; blue dashed line: R_{dAu} nDSg + σ_{abs} = 4.2 mb [63]. Right: R_{pAu} and R_{AA} vs. $N_{part.}$. Blue star: this analysis; red star: STAR R_{AA} $|y| < 0.5$ [59]; violet dashed line: Tsinghua model [64]; black shadowed: TAMU model [65].

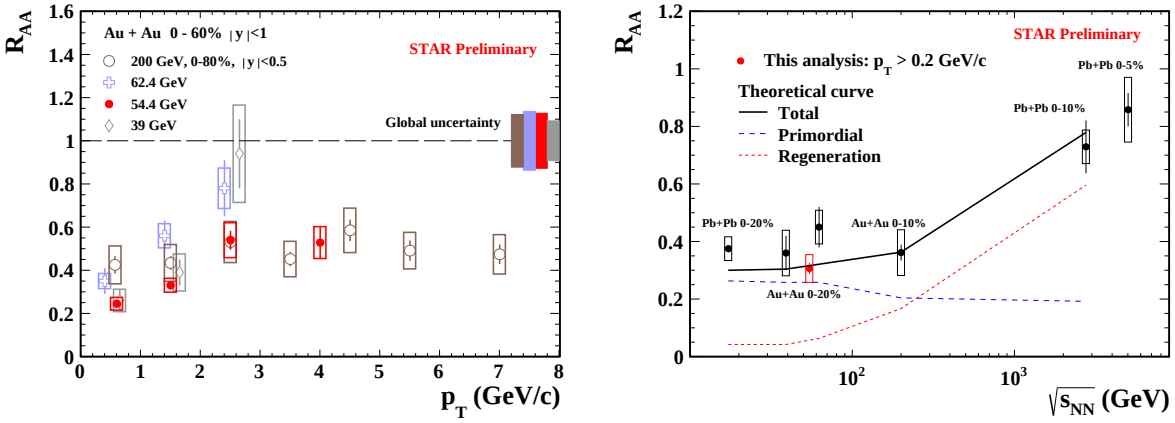

Figure 12: Left: R_{AA} vs. p_{T} for inclusive J/ψ in Au+Au collisions at $\sqrt{s_{\mathrm{NN}}}$ = 54.4 GeV (this analysis) and at 39, 62.4 and 200 GeV [58]. Right: R_{AA} vs. $\sqrt{s_{\mathrm{NN}}}$for inclusive J/ψ in Pb+Pb collisions at $\sqrt{s_{\mathrm{NN}}}$ = 17.2 GeV [66, 67], 2.76 [68] and 5.02 TeV [69], and in Au+Au collisions at 39, 62.4 and 200 GeV [58, 59].

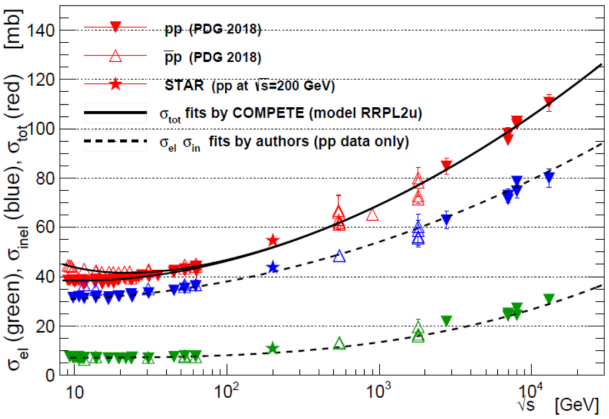

Figure 13: Comparison of STAR results on σ_{tot}, σ_{inel}, and σ_{el} with the world data for data below 1.8 TeV, the Tevatron and the LHC experiments. The COMPETE prediction for σ_{tot} is also shown (solid curve). The dashed curves represent STAR fits to σ_{inel} and σ_{el} using the same function at COMPETE. STAR data were not used in the fit.

bination. Indeed, the J/ψ yields in heavy-ion collisions from SPS [66,67], RHIC [58,59] and LHC experiments [68,69] at $\sqrt{s_{\rm NN}}$ ranging from 17.2 GeV to 5.02 TeV can be described by model calculations that incorporate both the color-screening and recombination effects [65].

1.1.4 Light Flavor and Ultra-peripheral Collisions

The Light Flavor Spectra and Ultra-peripheral Collisions (LFSUPC) physics working group is responsible for the measurements of calibrated production yields and spectra in inclusive ion-ion collisions, ultra-peripheral collisions, and exclusive *pp* collisions.

Elastic scattering plays an important role in proton-proton scattering at high energies. At the the LHC, for example, it makes up 20% of the total cross section. The *pp* elastic and total cross sections have been measured at *pp* colliders, however there exists a large energy gap between the measurements at the ISR and the LHC. The are proton-antiproton data from the Tevatron, however these are expected to have differences to the *pp* cross sections. It is important to fill the gap between the ISR and LHC to constrain the phenomenological models and to better understand the differences to the proton-antiproton data. The STAR detector was upgrades to include far-forward Roman Pots which were previously used by the PP2PP experiment. Figure 13 shows the STAR results for the elastic, inelastic, and total cross sections compared to the world data for both proton-proton and proton-antiproton collisions. The STAR results are 200 GeV are in good agreement with the trends of the world data and with the COMPETE predictions [70]

The first results from the STAR fixed-target program for Au+Au collisions at $\sqrt{s_{\rm NN}} =$ 3.0 GeV are now becoming available. Figure 14 shows the most advanced analyses from these data. The left panel of Fig. 14 shows the ϕ/K^- ratio as a function of collision energy. A significant enhancement of the ϕ yield as compared to that of the charge kaons is striking. The Grand Canonical Ensemble, which assumes a system of infinite extent, predicts significantly

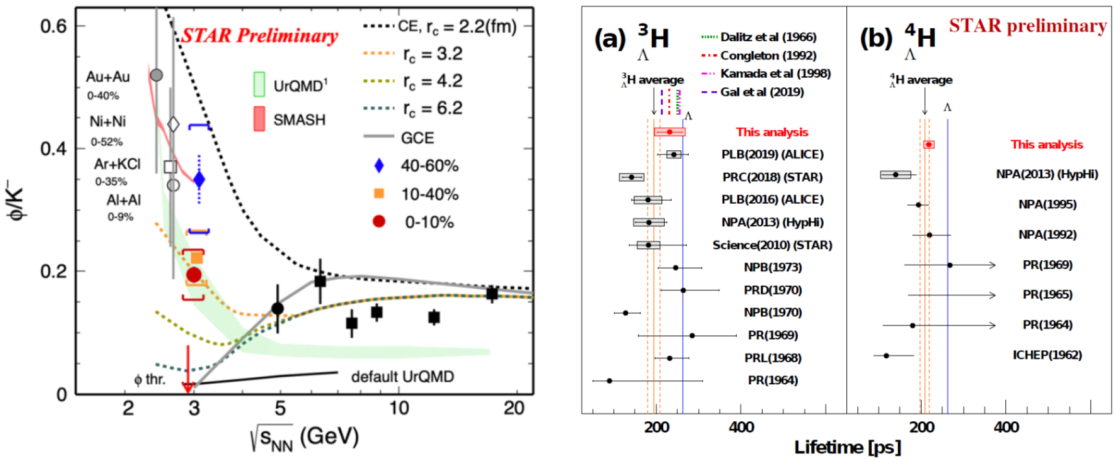

Figure 14: (Left) ϕ/K^- ratio as a function of collisions energy. The colored data points show the recent STAR measurements in centrality bins. The red arrow depicts the ϕ-meson production threshold in proton-proton collisions. The grey solid line represents a thermal model based the the Grand Canonical Ensemble (GCE) while the dashed lines represent calculations based on the Canonical Ensemble (CE) with four different parameters of strangeness correlation radius (r_c). The blue and red bands show transport model calculations using UrQMD and SMASH respectively. (Right) ${}^{3}_{\Lambda}$H (a) and ${}^{4}_{\Lambda}$H (b)measured lifetime compared to previous measurements, model calculations and the free Λ lifetime. The experimental average lifetimes and the corresponding uncertainties of ${}^{3}_{\Lambda}$H (a) and ${}^{4}_{\Lambda}$H are also shown as orange bands.

lower relative yields for the ϕ. However in the finite and ephemeral systems created in heavy-ion collisions near the nucleon-nucleon production threshold, there is a strong tendency for the strange quarks and anti-quarks to coalesce into a ϕ. This tendency had been previously noted in experiments at the GSI. The recent STAR results provide data for three different centrality ranges, which allows comparison to the lighter beam-target combinations from the GSI, to better constrain the strange quark coalescence radius. Microscopic transport models, UrQMD and SMASH, which include both resonance decays and the finite size effects, can reasonably describe the ϕ/K^- ratio at this energy (but not the K^- and ϕ yields). These results suggest a significant change in the strangeness production mechanisms at $\sqrt{s_{\rm NN}} = 3.0$ GeV as compared to that in higher energy collisions. This could shed new light on the understanding of the QCD Equation of State in the high baryon density regime.

The STAR fixed-target program covers the collision energy range where the yields of hyper-nuclei are expected to be maximized. Hyper-nuclei are understood to be created via the coalescence of hyperons with neutrons and protons. Although the hyperon yields increase approximately linearly with $ln(\sqrt{s_{NN}})$, due to the stopping of participant baryons, the density of neutrons and protons is significantly higher at these lower energies. Thus, hyper-nucleus production is expected to be maximized at $\sqrt{s_{\rm NN}} = 5$ GeV. The acceptance for hyper-nucleus detection is maximized at the lowest fixed-target energies making this lowest energy fixed-target dataset an ideal laboratory for the study of hyper-nuclei. Even with only a few hundred million Au+Au collisions at $\sqrt{s_{\rm NN}} = 3$ GeV, as compared to the

few billion at 200 GeV, we are able to achieve far more significant yields of hyper-nuclei and reduce the uncertainty on measurements of their properties. One of the first properties of interest is the lifetimes of hyper-nuclei. The question being addressed is whether incorporating a hyperon within a nucleus stabilizes or de-stabilizes the hyperon; one notes that neutrons are stabilized when bound within a nucleus. This question has been addressed both theoretically and experimentally for several decades, as seen in the right panel of Fig. 14. The preliminary results from the STAR fixed-target data for the lifetimes of ${}^{3}_{\Lambda}\mathrm{H}$ (a) and ${}^{4}_{\Lambda}\mathrm{H}$ have the highest precision of any measurement to date conclusively demonstrating the the lifetimes are significantly smaller than the free Λ lifetime. The ${}^{3}_{\Lambda}\mathrm{H}$ lifetime is consistent with theoretical calculations assuming the ${}^{3}_{\Lambda}\mathrm{H}$ is weakly bound state and including pion final state interactions.

1.2 CME Search and Isobar Run

1.2.1 Introduction

A decisive experimental test of the Chiral Magnetic Effect (CME) has become one of the major scientific goals of the heavy-ion physics program at RHIC. The existence of CME will be a leap towards an understanding of the QCD vacuum, establishing a picture of the formation of a deconfined medium where chiral symmetry is restored, and will also provide unique evidence of the strongest known electromagnetic fields created in relativistic heavy-ion collisions [71, 72]. The impact of such a discovery goes beyond the community of heavy-ion collisions and will possibly be a milestone in physics. The remaining few years of RHIC running and analyses of already collected data probably provide the only chance for dedicated CME searches in heavy-ion collisions in the foreseeable future. Significant efforts from STAR, as well as other collaborations, have been dedicated towards developing methods and observables to isolate possible CME-driven signals from non-CME background contributions in measurements of charge separation across the reaction plane. Many clever ideas have been proposed and applied to existing data. However, a general consensus is that measurements from isobar collisions, Ruthenium+Ruthenium (Ru+Ru) that has $5-9\%$ higher B-field than Zirconium+Zirconium (Zr+Zr), thus a $10-18\%$ larger CME correlation signal because of its B^2 dependence, provide the best solution. At the time of writing this BUR document, STAR has already produced all the data for the final step of the analysis, the two species are separated and the analyzers are running their codes to produce the final results. We discuss the steps of blind analysis in the following sections.

1.2.2 Modality of Isobar Running at RHIC

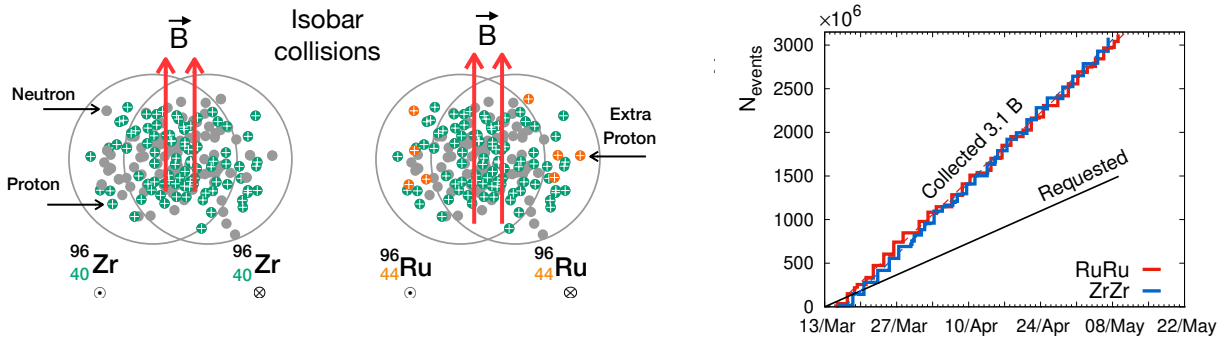

Figure 15: Left: Cartoon of the isobar collisions, about $10-18\%$ stronger B-field squared is expected in Ru+Ru collisions as compared to Zr+Zr. Right: Summary of the Isobar data collected during Run-18.

Colliding isobars, particularly Ru+Ru and Zr+Zr, to make a decisive test of CME was proposed by Voloshin in Ref [73], the same paper also proposed to use Uranium collisions to

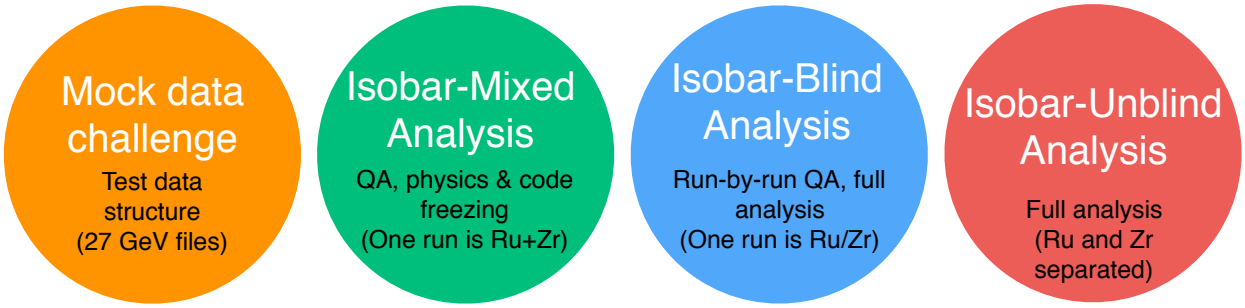

Figure 16: Cartoon taken from Ref [79], showing the steps of analysis consisting of the mock-data challenge and the three-step isobar blind analysis. This cartoon is based on the procedure for the blind analysis of isobar data that have been outlined in Ref [80]. At the time of writing of this document the two species are separated and analyzers in STAR are running their codes as a part of the last step (shown in red).

disentangle signal and background of CME. The possible difference in the signals relies on the $10-18\%$ higher B-field squared in Ru+Ru compared to Zr+Zr, due to four extra protons in each Ru nucleus [74], in contrast to about 4% difference in flow driven background [75]. Such estimates are sensitive to details of the shape, charge distribution and neutron skin thickness of the two isobar nuclei [74, 76, 77].

In the 2017-18 RHIC BUR [78] STAR proposed to collect data for two 3.5 week periods in Run-18. The projection was based on the prospect of achieving five-sigma significance in a scenario where the measurement of $\Delta\gamma$ has 80% non-CME background. This, however, relies on the assumption that the systematic uncertainties of the measurements are only a few percent, and much smaller than the statistical uncertainty. This started a large scale collaboration wide effort in synergy with the RHIC collider accelerator department to plan for the isobar running in 2018. Based on the studies of previous years of data from Au+Au and U+U collisions several major sources of systematics in the measurement of $\Delta\gamma$ were identified. The major sources include: run-to-run variation of detector response due to loss of acceptance, change in efficiency and variation in luminosity that affects the number of reconstructed tracks in the TPC. This eventually leads to uncorrectable systematic uncertainties in $\Delta\gamma$, the main observable to measure charge separation across the event plane. In order to minimize such systematics a running proposal was developed to: 1) switch species between each store and, 2) keep long stores with a level luminosity; aiming for specific rates in the coincidence measurements of beam fragments via zero-degree calorimeters. The aim was to maintain exact balance of run and detector conditions for the two species so that observations in the two systems are equally affected and can later on be largely eliminated in the ratios of observables.

1.2.3 Blinding of Datasets and Preparation for Analyses

The procedure to blind the isobar data was already in place well ahead of the actual data taking to limit the access of the data to the analysts to eliminate possible unconscious biases.

At the successful conclusion of the isobar run in 2018 STAR had collected more than 3 billion minimum-bias events for each isobar species. A total of five institutional groups agreed to perform blind analyses on the data. The analysts from each group will focus on a specific analysis described in the following section. The substantial overlap of some analyses will help cross check the results.

The details of the blinding procedure and data structure were decided by an analysis blinding committee (ABC) who are not part of the team of analysts but work in close collaboration with STAR experts who are part of the production team. The idea is to provide the analysts access to data where species-specific information are disguised or removed prior to the final step, shown in red in Fig. 16. Careful consideration was taken by the ABC to make sure only the essential information to do the analysis-specific quality assurance of the data was available to the analysts, to ensure the integrity of the CME Isobar analyses. The quality assurance, calibration and centrality determination work, that require species information, were done only by STAR experts who were not a part of the blind analysis team.

1.2.4 Methods for the Isobar Blind Analyses

The detailed procedure for the blind analyses of isobar data have been outlined in Ref [80]. Figure 16 is a cartoon that summarizes the mock-data challenge and three steps of the blind analysis.

The zeroth step shown, in the extreme left of Fig. 16 (orange circle), was the mock-data challenge; a crucial step to familiarize the analysts with the technicalities of the data structures that have been specifically designed for blind analysis, and ensure the blinding worked.

The first step shown in Fig. 16 (green circle) as the "isobar-mixed analysis" was truly the first step of the blind analysis. This was also the most challenging step from the point of view of the analysts. In this step they were provided with a data sample where each "run" comprised of events that were a mixed sample of the two species. In this step the analysts performed the full quality assurance (QA) and physics analysis of the data, documented every detail of their procedures and froze the codes. After the completion of this step, no changes to the analysis code or procedures were permissible. The only permissible change in the following step was to reject bad runs or pile-up events. However, in order to avoid unconscious bias, such rejections could not be done arbitrarily. Instead, an automated algorithm for bad run rejection was developed and corresponding codes frozen. The stability of the automated QA algorithm was tested on existing Au+Au and U+U data.

The second step shown in Fig. 16 (blue circle) is referred to as the "isobar-blind analysis". For this the analysts were provided with files each of which contained data from a single, but blinded, species. From this step on-wards, the analysts were only allowed to run their previously frozen codes. The main purpose of this step was to perform run-by-run QA of the data. The files each contained a limited number of events that could not lead to any statistically significant result. Although a pseudo-run-number was used for each file, the time ordering was preserved with a unique mapping that was unknown to the analysts. It

was important to maintain the time ordering to identify time-dependent changes in detectors and run conditions as a part of the run-by-run QA. A similar automated algorithm was also used for identifying and rejecting bad runs. After this step no more changes are allowed in terms of QA.

The final step of isobar blind analysis shown by red circle in Fig. 16 is referred to as "isobar-unblind" analysis. In this step, the species information will be revealed and the physics results will be produced by the analysts using the previously frozen codes. However, one important step is as follows. No analyzer is allowed to run his/her own code. The frozen codes should be run by a independent person. The findings from this step will be directly submitted for publication without alteration. If a mistake is found in the analysis code, the erroneous results will also accompany the corrected results.

1.2.5 Observables for Isobar Blind Analyses

The general strategy is to compare two isobar species to search for a significant difference in whatever observable used. The following sections briefly describe the procedures agreed upon as the focus of the Isobar blind analysis with comments on the outlook for isobar blind analysis: 1) measurement of higher order harmonics of γ-correlator, 2) exploiting the relative charge separation across participant and spectator planes, 3) differential measurements of $\Delta\gamma$ to identify and quantify backgrounds, 4) the use of the R-observable to measure charge separation. The first three approaches are based on the aforementioned three-particle correlator, and the last employs slightly different approaches to quantify charge separation. There is also another analysis which will be performed using the signed balance function, but this is not part of the blind analyses.

Mixed Harmonics Measurements with Second and Third Order Event Planes

In order to proceed, it is better to rewrite the conventional γ-correlator in a more general notation as $\gamma_{112} = \langle\cos(\phi_a^\alpha + \phi_b^\beta - 2\Psi_2)\rangle$. The idea is to measure charge separations across the third harmonic event plane by constructing a new correlator $\Delta\gamma_{123} = \gamma_{123}(OS) - \gamma_{123}(SS)$, where $\gamma_{123} = \langle\cos(\phi_a^\alpha + 2\phi_b^\beta - 3\Psi_3)\rangle$ was introduced by CMS collaboration in Ref [82]. Since the Ψ_3 plane is random and not correlated to B-field direction (see Fig. 17), γ_{123} is purely driven by non-CME background, the contribution of which should go as v_3/N. This is very useful to contrast signal and background scenarios by comparing measurements in the two isobaric collision systems. Since Ru+Ru has larger B-field than Zr+Zr but comparable background, the case for CME would be as follows: $(\Delta\gamma_{112}/v_2)^{\mathrm{Ru+Ru}}/(\Delta\gamma_{112}/v_2)^{\mathrm{Zr+Zr}} > 1$ and $(\Delta\gamma_{112}/v_2)^{\mathrm{Ru+Ru}}/(\Delta\gamma_{112}/v_2)^{\mathrm{Zr+Zr}} > (\Delta\gamma_{123}/v_3)^{\mathrm{Ru+Ru}}/(\Delta\gamma_{123}/v_3)^{\mathrm{Zr+Zr}}$. Figure 17 (left) shows the measurement of these observables in U+U and Au+Au collisions. Within the uncertainties of the measurements, no significant difference in the trend of $\Delta\gamma_{112}/v_2$ and $\Delta\gamma_{123}/v_3$ is observed for the two collision systems except for the very central events. Predictions from hydrodynamic model calculations with maximum possible strength of local charge conservation [75] is shown on the same plot. Overall observation indicates the backgrounds dominate the measurements and a similar analysis of the isobar data is highly anticipated.

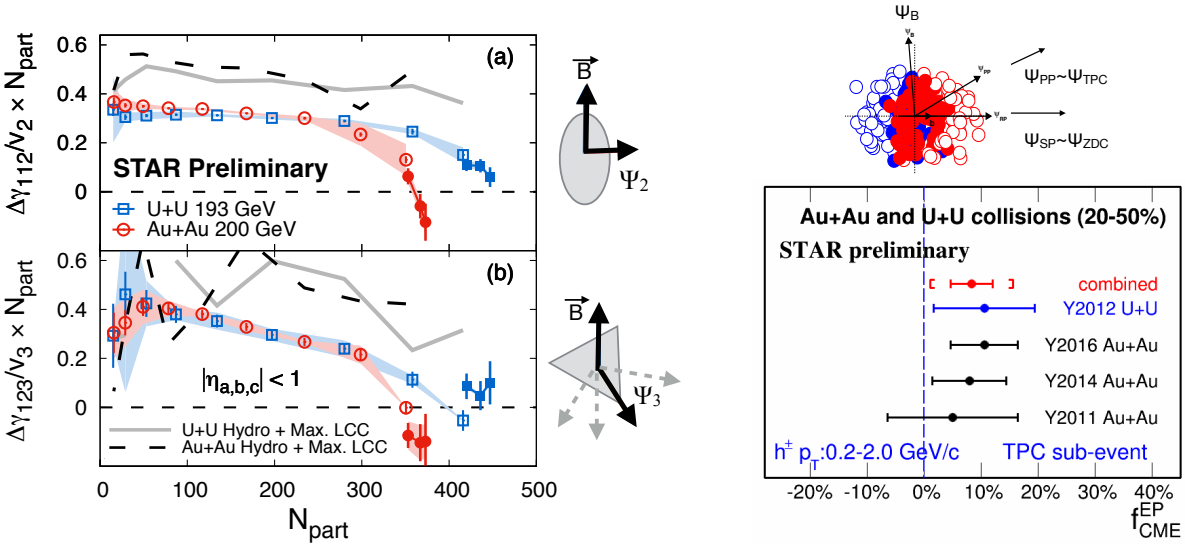

Figure 17: (Left) Measurement of charge separation along second and third order event planes in Au+Au and U+U collisions. (Right) Fraction of possible CME signal in the measurement of $\Delta\gamma$ with respect to spectator and participant planes [81].

Charge Separation Along Participant and Spectator Planes

This analysis makes use of the fact that the B-field driven signal is more correlated to the spectator plane, in contrast to flow-driven backgrounds which are maximal along the participant plane. The idea was first introduced in Ref. [83] and later on followed up in Ref. [84]. It requires measurement of $\Delta\gamma$ with respect to the plane of produced particles, a proxy for the participant plane, as well as with respect to the plane of spectators. In STAR, the two measurements can be done by using Ψ_2 from the TPC and Ψ_1 from the ZDCs, respectively. The approach is based on three main assumptions: 1) the measured $\Delta\gamma$ has contributions from signal and background, which can be decomposed as $\Delta\gamma = \Delta\gamma^{\rm bkg} + \Delta\gamma^{\rm sig}$, 2) the background contribution to $\Delta\gamma$ should follow the scaling $\Delta\gamma^{\rm bkg}({\rm TPC})/\Delta\gamma^{\rm bkg}({\rm ZDC}) = v_2({\rm TPC})/v_2({\rm ZDC})$ and, 3) the signal contribution to $\Delta\gamma$ should follow the scaling $\Delta\gamma^{\rm sig}({\rm TPC})/\Delta\gamma^{\rm sig}({\rm ZDC}) = v_2({\rm ZDC})/v_2({\rm TPC})$. The first two have been known to be working assumptions, widely used for a long time and can be used to test the case of CME [84] if $(\Delta\gamma/v_2)\,({\rm ZDC})/\,(\Delta\gamma/v_2)\,({\rm TPC}) > 1$. The validity of the last one was studied and demonstrated in Ref. [83]. Using all three equations one can extract [81] the fraction of possible CME signal $f_{\rm CME} = \Delta\gamma^{\rm sig}/\Delta\gamma$ in a fully data-driven way as shown in Fig. 17(right). This analysis will be done with the isobar data and the case for CME will be $f_{\rm CME}^{\rm Ru+Ru} > f_{\rm CME}^{\rm Zr+Zr} > 0$.

Differential Measurements of $\Delta\gamma$ to Identify and Quantify Background

Invariant mass dependence of charge separation: Differential measurements of $\Delta\gamma$ with invariant mass and relative pseudorapidity provide interesting prospects to identify and quantify the sources of flow and non-flow driven backgrounds. The idea to use invariant mass is

simple and was first introduced in Ref. [85]. Resonances are widely identified by observing structures in the invariant mass spectra of the decay daughters. Consider a pair of opposite sign pions for example, it is known that a large fraction of them come from the neutral resonances that show up in the invariant mass spectrum of $m_{inv}(\pi^+ + \pi^-)$. If we restrict the analysis to pairs of pions, differential measurements of $\Delta\gamma$ with $m_{inv}(\pi^+ + \pi^-)$ should also show similar peak like structures if background from neutral resonances dominate the charge separation. Indeed similar peak structures are observed and an analysis has been performed to extract the possible fraction of CME signals from the current measurements [86]. This analysis relies on the assumption that CME signals do not show peak like structures in $m_{inv}(\pi^+ + \pi^-)$ and also requires an assumption of m_{inv} dependence of the CME signal, therefore calls for more theoretical insight in this direction have been made.

Relative pseudorapidity dependence: The relative pseudorapidity dependence of azimuthal correlations are widely studied to identify sources of long-range components that are dominated by early time dynamics as compared to late time correlations that are prevented by causality to appear as short-range correlations. The same can be extended to charge dependent correlations which provide the impetus to explore the dependence of $\Delta\gamma$ on the pseudorapidity gap between the charge carrying particles $\Delta\eta_{ab} = |\eta_a - \eta_b|$ in $\langle\cos(\phi_a^\alpha + \phi_b^\beta - 2\Psi_{RP})\rangle$. Such measurements have been performed in STAR with Au+Au and U+U data. It turns out that the possible sources of short-range correlations due to photon conversion to $e^+ - e^-$, HBT and Coulomb effects can be identified and described as Gaussian peaks at small $\Delta\eta_{ab}$, the width and magnitude of which strongly depend on centrality and system size. Going to more peripheral centrality bins, it becomes harder and harder to identify such components as they overlap with sources of di-jets fragmentation that dominates both same-sign and opposite sign correlations. An effort to decompose different components of $\Delta\gamma$ via study of $\Delta\eta_{ab}$ can be challenging although a clear sign of different sources of correlations are visible in change of shape of individual same-sign and opposite sign measurements of γ-correlator [87].

In any case, these differential measurements of $\Delta\gamma$ in isobar collisions provide the prospect to extract the $m_{inv}(\pi^+ + \pi^-)$ and $\Delta\eta$ dependence of CME signals that will provide much deeper insights on the origin of the effect. Comparing the differential measurements in Ru+Ru and Zr+Zr it will be possible to extract the invariant mass and the relative pseudorapidity distribution of the CME signal that will provide deeper insight into the origin of the phenomenon.

Alternate Measure: The Novel R-observable

The R-observable is actually a distribution, introduced in Ref. [90], and defined as the ratio of two distribution functions of the quantity ΔS parallel and perpendicular to B-field direction defined as $R_{\Psi_m}(\Delta S) = C_{\Psi_m}(\Delta S)/C^{\perp}_{\Psi_m}(\Delta S)$. Here ΔS measures the difference in the dipole moment of the positive and negative charge in an event (see Ref. [90] for details). The shape of $R_{\Psi_2}(\Delta S)$ will be sensitive to CME as well as non-CME background. Model calculations have established several unique features of this observable: 1) presence of CME signal will lead to a concave shape of the $R_{\Psi_2}(\Delta S)$, 2) increasing strength of CME signal will increase the concavity of $R_{\Psi_2}(\Delta S)$. In the original paper [90] a second correlator $R_{\Psi_3}(\Delta S)$

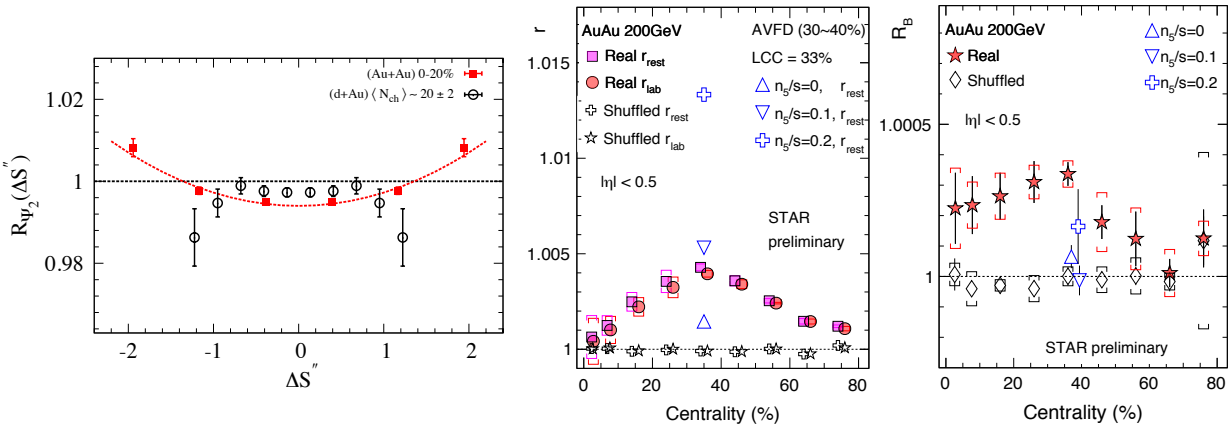

Figure 18: (Left) The R-observable shown for different collision systems, a concave shape is consistent with CME expectation [88]. (Right) The two main quantities r and R_B derived from the signed balance function, deviation from unity is consistent with CME expectations [89].

was proposed which will measure charge separation purely driven by non-CME background and may serves as a baseline. However, recent investigation has shown that due to symmetry properties of harmonics in R-variable, the results for $R_{\Psi_3}(\Delta S)$ correlator may be difficult to interpret and require further studies. Therefore, ongoing and future experimental studies from STAR will focus only on R_{Ψ_2}

The measurement of R_{Ψ_2} is shown in Fig.18. The quantity $\Delta S''$ shown is a slight variant of (ΔS) that incorporates correction for particle number fluctuations and event plane resolution. The observation of Fig.18 indicates more concave shape for R_{Ψ_2} in Au+Au whereas flat or convex shapes for p/d+Au indicates that the measurements are consistent with expectations of CME [88]. For isobar collisions, the case of CME requires an observation of a concave shape for the ratio of the observables $R_{\Psi_2}(\Delta S)^{\rm Ru+Ru}/R_{\Psi_2}(\Delta S)^{\rm Zr+Zr}$.

Alternate Measure: The Signed Balance Function

A very recently proposed observable to search for CME is via the signed balance function (SBF) [91]. The idea is to account for the ordering of the momentum of charged pairs measured by the width of SBF that is expected to be different for out-of-plane as compared to in-plane measurements captured in the ratio $r_{\rm lab}$. In addition, one can also account for the boost due to collective expansion of the system that forces all pairs to move in the same direction and measure the ratio in the pair rest frame $r_{\rm rest}$. In the presence of CME, the individual ratios, as well as the double ratio $R_B = r_{\rm rest}/r_{\rm lab}$, are expected to be greater than unity. Preliminary measurements, shown in Fig. 18 (right), from STAR in Au+Au 200 GeV data seem to be consistent with CME expectation. This observable will be studied with the isobar data but not as a part of the blind analysis. The CME expectation is: $r(\mathrm{Ru}+\mathrm{Ru}) > r(\mathrm{Zr}+\mathrm{Zr})$.

1.2.6 Benchmarking CME Observables Against EBE-AVFD Model

As the STAR Collaboration is analyzing the data from isobaric collisions with multiple CME observables, it is desirable to have a controlled study on observables so that their relative performance can be understood and calibrated. This will serve as an important reference point when interpreting isobaric data. In this section, we present a benchmark study for three CME observables, namely, the inclusive γ correlator [92], the R correlator [90, 93] and the signed balance functions [91]. The first two observables are included in STAR's blind-analysis, for which the study was conducted with frozen code that was checked into STAR official repository as part of blinding procedure. Aforementioned, the last one is not a part of blind-analysis, but has intrinsic connections [94] with the other two thus it is also presented here for completeness. For a full version of this study, please refer to [94].

The model used in this study is event-by-event anomalous-viscous fluid dynamics (EBE-AVFD) model [95–97]. It implements the anomalous transport current from CME into fluid dynamics framework to simulate the evolution of fermion currents on an event-by-event basis and to evaluate the resulting charge separation in the QGP, on top of the neutral bulk background described by the VISH2+1 hydrodynamic simulations [98] with Monte-Carlo Glauber initial conditions, followed by a URQMD hadron cascade stage [99, 100]. This new tool allows one to quantitatively and systematically investigate the various proposed measurements' responses to the CME signal and account for the resonance contributions.

For each of the two isobaric collision systems, Ru+Ru and Zr+Zr at $\sqrt{s_{\rm NN}}$ = 200 GeV, four cases of the EBE-AVFD events have been generated, with n_5/s = 0, 0.05, 0.1, and 0.2, respectively. Here n_5 is the initial axial charge density and s is the entropy density. A strong CME effect is expected when n_5/s is large. The centrality selection for all the cases focuses on 30-40% central collisions, where the potential CME signal is relatively easy to detect owing to good event plane resolutions. 200 million events were produced for each case of $n_5/s = 0$ and $n_5/s = 0.2$, and 400 million events for the each of the other two cases. To mimic the detection performance of the STAR Time Projection Chamber, simulated particles in the EBE-AVFD events are randomly rejected according to a transverse-momentum dependent tracking efficiency.

Figure 19 presents the EBE-AVFD calculations of $\gamma_{112}^{\rm OS(SS)}$ (a) and $\Delta\gamma_{112}$ (b) as functions of n_5/s for 30-40% isobaric collisions at $\sqrt{s_{\rm NN}}$ = 200 GeV. The ratios of $\Delta\gamma_{112}$ between Ru+Ru and Zr+Zr is delineated in panels (c). At each n_5/s value, $\gamma_{112}^{\rm OS}$ remains positive and $\gamma_{112}^{\rm SS}$ stays negative, both with larger magnitudes at higher n_5/s. Although the CME expects $\gamma_{112}^{\rm OS}$ and $\gamma_{112}^{\rm SS}$ to be symmetric around zero, there exist some charge-independent backgrounds such as momentum conservation and elliptic flow that shift both $\gamma_{112}^{\rm OS}$ and $\gamma_{112}^{\rm SS}$ up or down. Therefore, we shall focus on $\Delta\gamma_{112}$, which shows a finite background contribution at $n_5/s = 0$ and increases with the CME signal. The difference between Ru+Ru and Zr+Zr is better viewed with the ratio of $\Delta\gamma_{112}^{\rm Ru+Ru}/\Delta\gamma_{112}^{\rm Zr+Zr}$. This ratio is consistent with unity at $n_5/s = 0$, and increases quadratically with n_5/s as demonstrated by the 2$^{\rm nd}$-order-polynomial fit function that passes (0, 1) (dashed line). The quadratically-increasing trend is expected, because this ratio is a linear function of the CME signal fraction in $\Delta\gamma_{112}$ in a two-component perturbative framework [101], and the latter is proportional to $(n_5/s)^2$ or a_1^2. The significance

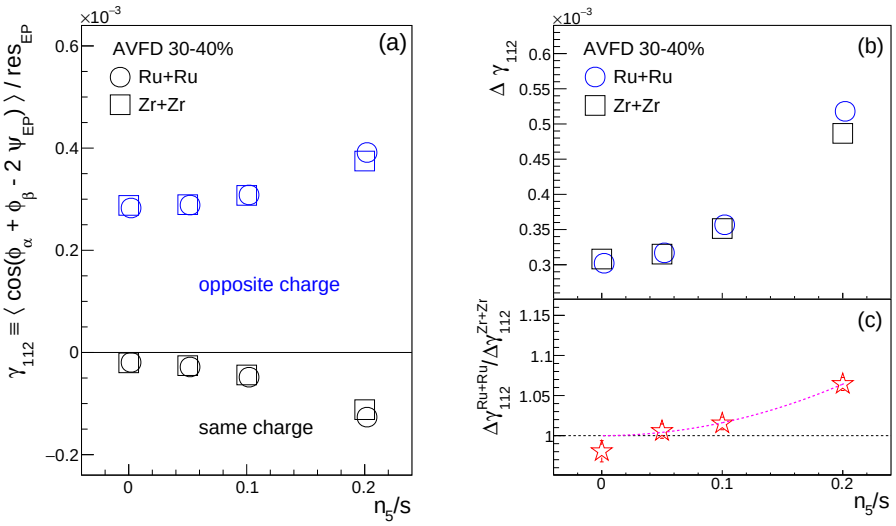

Figure 19: EBE-AVFD calculations of $\gamma_{112}^{\mathrm{OS(SS)}}$ (a) and $\Delta\gamma_{112}$ (b) as functions of n_5/s for 30-40% isobaric collisions at $\sqrt{s_{\mathrm{NN}}} = 200$ GeV, together with the ratio of $\Delta\gamma_{112}$ (c) between Ru+Ru and Zr+Zr. In panel (c), the 2$^{\mathrm{nd}}$-order-polynomial fit function illustrates the rising trend starting from (0, 1).

values of the $\Delta\gamma_{112}^{\mathrm{Ru+Ru}}/\Delta\gamma_{112}^{\mathrm{Zr+Zr}}$ ratio, along with other ratios to be discussed, are stored in Table 4.

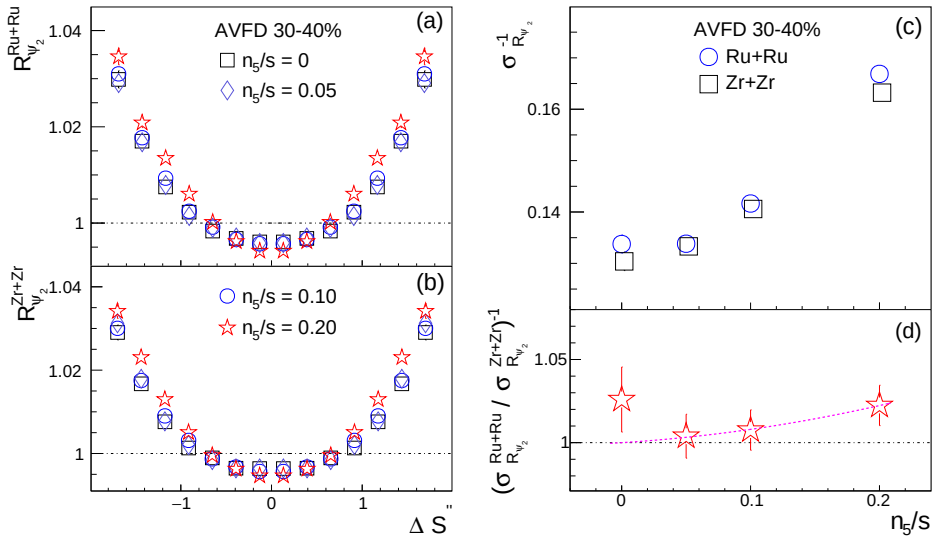

Figure 20: Distributions of $R(\Delta S_2^{''})$ from EBE-AVFD events of 30-40% Ru+Ru (a) and Zr+Zr (b) at 200 GeV with different n_5/s inputs. Panel (c) depicts σ_{R2}^{-1} vs n_5/s, extracted from panels (a) and (b), and the σ_{R2}^{-1} ratios between Ru+Ru and Zr+Zr are shown in panel (d), where the 2$^{\mathrm{nd}}$-order-polynomial fit function shows the rising trend starting from (0, 1).

Table 4: The statistical significance of $(O^{\mathrm{Ru+Ru}}/O^{\mathrm{Zr+Zr}}-1)$ for different experimental observables. N_{event} is the number of events used for each isobaric system of 30-40% centrality in the simulation. See [94] for discussions on observables that are listed but not discussed in this document.

n_5/s	N_{event}	$\Delta\gamma_{112}$	$\Delta\delta$	κ_{112}	r_{lab}	σ_{R2}^{-1}
0	2×10^8	−1.50	−2.89	−1.21	−0.77	1.33
0.05	4×10^8	0.62	−6.16	1.37	0.47	0.29
0.10	4×10^8	1.91	−16.81	3.43	3.11	0.62
0.20	2×10^8	7.73	−42.96	14.07	5.96	1.84

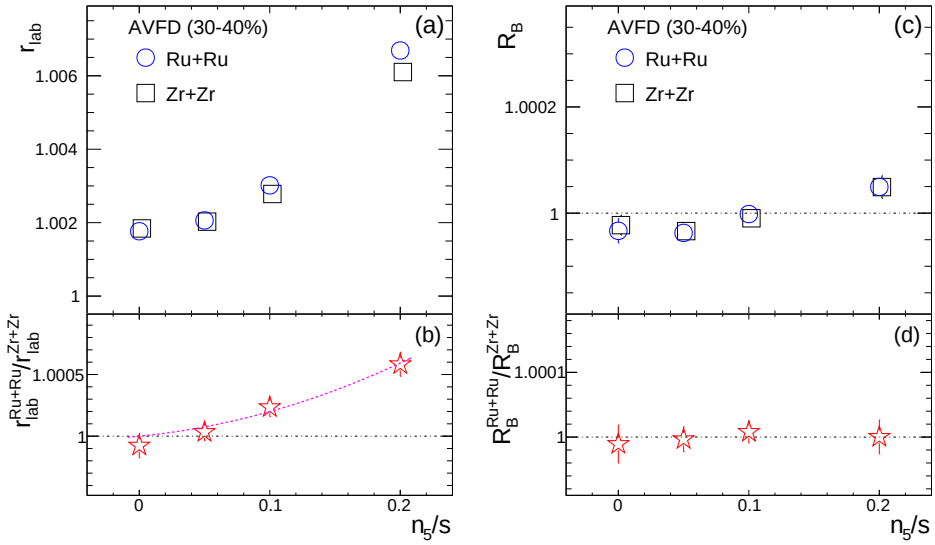

Figure 21: r_{lab} (a) and R_{B} (c) as function of n_5/s from the EBE-AVFD model for 30-40% Ru+Ru and Zr+Zr collisions at $\sqrt{s_{\mathrm{NN}}}$ = 200 GeV, with their ratios between Ru+Ru and Zr+Zr in panels (b) and (d), respectively. In panel (b), the 2$^{\mathrm{nd}}$-order-polynomial fit function demonstrates the rising trend starting from (0, 1).

A similar frozen-code analysis is performed for the $R(\Delta S_2)$ correlator, and the results are presented in Figure 20. Panels (a) and (b) show the $R(\Delta S_2^{''})$ [90] distributions from EBE-AVFD events of 30-40% Ru+Ru and Zr+Zr collisions, respectively, at $\sqrt{s_{\mathrm{NN}}}$ = 200 GeV with different n_5/s inputs. As n_5/s increases, the $R(\Delta S_2^{''})$ distribution becomes more concave, qualitatively representing more CME contributions. To quantify the distribution shape, the Gaussian width (σ_{R2}) is obtained by fitting each $R(\Delta S_2^{''})$ distribution with an inverse Gaussian function, and the resultant σ_{R2}^{-1} values are depicted in panel (c), increasing with n_5/s. The σ_{R2}^{-1} ratios between Ru+Ru and Zr+Zr are shown in panel (d). We fit the σ_{R2}^{-1} ratios with a 2$^{\mathrm{nd}}$-order polynomial function starting from (0, 1).

Figure 21 presents the sensitivity study for the signed balance functions. This approach is not part of the STAR blind analysis, but follows the same procedure as used in the Quark Matter 2019 Conference proceedings [89]. The observables r_{lab} and R_{B} [91] are exhibited

in panels (a) and (c) as function of n_5/s from the EBE-AVFD model for 30-40% Ru+Ru and Zr+Zr collisions at $\sqrt{s_{\rm NN}}$ = 200 GeV. The corresponding ratios between Ru+Ru and Zr+Zr are shown in panels (b) and (d), respectively. $r_{\rm lab}$ increases with the CME signal in each isobaric collision. The $r_{\rm lab}$ ratio between the two systems should roughly obey a 2$^{\rm nd}$-order polynomial function that starts from (0, 1). This relation is demonstrated with the corresponding fit in Fig. 21(b). Panel (d) does not show a clear trend for the ratio of $R_{\rm B}^{\rm Ru+Ru}/R_{\rm B}^{\rm Zr+Zr}$, which is not a complete surprise: R_B looks for a higher-order effect in the difference between $r_{\rm lab}$ and $r_{\rm rest}$, and thus requires much more statistics than $r_{\rm lab}$.

To summarize, in this study [94], we have established the relation between these methods via analytical derivation, and employed both simple Monte Carlo simulations and the EBE-AVFD model to verify the equivalence between the kernel components of these observables (not shown in this document). Our study supports the assumption that the CME signal and the background contributions can be linearly added up in such kernel components. We have extracted their sensitivities to the difference between Ru+Ru and Zr+Zr collisions at $\sqrt{s_{\rm NN}}$ = 200 GeV from 30-40% central events generated by EBE-AVFD. $\Delta\delta$ and κ_{112} may render better sensitivities than other observables, which could be a model-dependent feature instead of a universal truth, and needs to be further scrutinized by data. The same significance level has been corroborated for $\Delta\gamma_{112}$, $r_{\rm lab}$ and σ_{R2}^{-1}, if put on an equal footing. In the implementation of the STAR frozen codes, slight differences in the kinematic cuts cause the apparently worse sensitivity of σ_{R2}^{-1} than the other observables. This study provides a reference point to gauge the STAR isobaric-collision data.

1.2.7 Prospect of CME Search Beyond the Isobar-era

It is important to discuss the strategy for CME search beyond the isobar-era. While it is true that such a strategy needs to be finalized based on the outcome of the isobar program, we would like to get started by considering two possible scenarios at top RHIC energy: 1) isobar program results in a significance of 3σ and below, 2) isobar program results in a significance of 3σ and above.

In the first scenario one can infer from the projection plot of Fig. 22 that the upper limit of the fraction of CME signal should be less than or equal to 8%. Under such a scenario can STAR perform a follow up measurement to achieve a decisive 5σ significance and establish a conclusive evidence of CME? It turns out such a measurement is possible even with a single Au+Au 200 GeV dataset during the year 2023-25 running of STAR concurrently with sPHENIX. Current CME related analyses of the aforementioned Au+Au 200 GeV extraction using elliptic flow and charge separation with respect to spectator and participant planes yields 4% statistical uncertainty with 2.4 B events ($2-3\sigma$ significance). In order to get 5 σ significance with the same analysis one needs to have a statistical uncertainty of order 1.6% which would require about $(4/1.6)^2 \times 2.4 = 15$ Billion events. Therefore, as per the previous estimates of anticipated 20 Billion events that can be collected by STAR during Run-23 and 25, one can achieve more than 5σ significance on the upper limit of a possible CME signal fraction in the measurement of charge separation. This estimate does not account for two important facts that can lead to higher significance and a decisive measurement. The

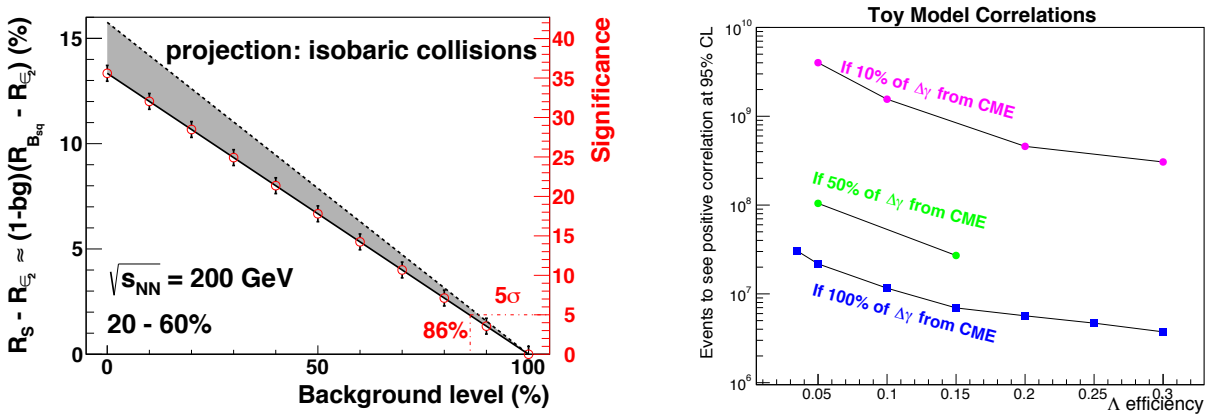

Figure 22: (Left) Projection plot taken from a previous beam user request document [78] indicating the anticipated significance in the measurement of charge separation as a function of the CME signal fraction prepared using 2.5 B simulated events. (Right) Estimation of the number of events required to see positive correlation between net Λ helicity with out-of-plane charge separation sensitive to local parity violation at 95% confidence level, plotted against the efficiency of $\Lambda(\bar{\Lambda})$ reconstruction (see [102] for details).

first is that the magnitude of the projected B-field on the reaction plane is higher in Au+Au collisions as compared to isobar collisions. The second one is that the iTPC upgrade enhances the charge particle multiplicity by 50% and therefore triplet($\sim dN/d\eta^3$) (pair $\sim dN/d\eta^2$) statistics by a factor of 3.4 (2.3). So the final conclusion is that even if isobar program results in a 3 σ measurement running STAR in 2023-25 will result in a $> 5\sigma$ measurement if about 20 Billion events are collected. This conclusion assumes that the systematic uncertainty can be controlled to be smaller than the statistical uncertainty, i.e. below 2%. Also, this estimation does not include the systematics due to effect of sub-event gap which is being studied in STAR.

For the second scenario ($> 3\sigma$ measurement from isobar program) we will also be able to establish an upper limit of the fraction of CME signal. For example, in Fig. 22 we see that a 5σ significance will establish 13% CME signal and a discovery of the CME phenomenon in heavy-ion collisions. The impact of such a discovery will be a significant milestone. Running STAR in 2023-25 concurrently with sPHENIX would be essential to perform dedicated precision measurements to further investigate and characterize the phenomenon.

A topic that may be addressed with future data is event-by-event correlations between CME charge separation and other parity-odd features of the event. One such analysis is motivated by the idea that the local parity violation (characterized in each event by a net topological charge Q) that is expected to work with the spectator-produced magnetic field to given the CME should also cause a net helicity of $\Lambda(\bar{\Lambda})$ with the same handedness in each event as the charge separation relative to the B-field.

We are looking for evidence of an event-by-event correlation between these two parity-odd effects as suggested in [102]. To do this, we first need to measure the charge separation

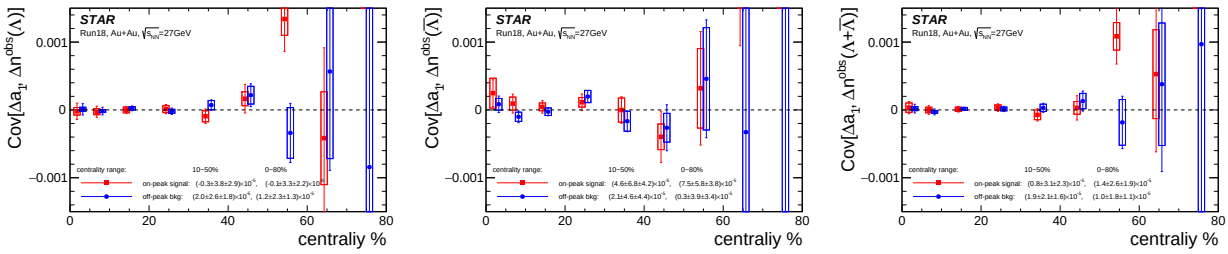

Figure 23: The covariance between Δa_1 and measured Δn for Λ (Left), $\bar{\Lambda}$ (Middle), and the sum of them (Right) as functions of centrality. The red markers come from the $\Lambda(\bar{\Lambda})$ mass peak region with purity correction and blue markers come from the side bands for pure background.

with respect to the first-order reaction plane in each event which we can characterize by the azimuthal correlator ($\Delta a_1 \equiv \langle \sin(\phi^+ - \Psi_{\rm RP})\rangle - \langle \sin(\phi^- - \Psi_{\rm RP})\rangle$). We next need to determine the imbalance in the handedness of $\Lambda(\bar{\Lambda})$, $\Delta N = N_{\rm L} - N_{\rm R}$. A measured correlation between Δa_1 and ΔN would be strong evidence for the CME and underlying local parity violation, and would extend the measurement into other parity-odd effects. Note also that the flow-related backgrounds that plague charge-separation measurements are not expected to affect ΔN or this correlation measurement. We use a similar toy model to that used in [102] to estimate the number of events required to see non-zero correlations between Δa_1 and ΔN at the 95% confidence level as a function of the efficiency of $\Lambda(\bar{\Lambda})$ reconstruction for various cases with different CME signal fraction in the $\Delta\gamma$ measurement (see Fig. 22(right)). The chief unknown in this estimate is the extent to which strange quarks may be counted as light quarks and so will have a net handedness imparted by the parity-odd domain.

Although Fig. 22(right) suggests that this will be a topic that may require the large datasets of future runs, these event number estimates have a large uncertainty, making it very useful to perform such an analysis with existing data both to search for a correlation signal and as an exercise of the analysis method.

To explore this correlation, we have analyzed the Run-18 Au+Au collision data at $\sqrt{s_{NN}} = 27$ GeV. The $\Lambda(\bar{\Lambda})$ baryons are reconstructed by their decay daughter tracks and identified by topological cuts. Each Λ handedness is estimated by decay kinematics. After a purity correction, N_L and N_R are calculated for both Λ and $\bar{\Lambda}$ in each event, and then Δn (normalized ΔN, $\Delta n = \frac{N_L - N_R}{\langle N_L + N_R \rangle}$) is calculated. The observable Δa_1 can be calculated from primordial particles' azimuthal angles w.r.t. the first-order EP measured by the Event Plane Detector (EPD). The covariance between Δn and Δa_1 is then calculated for the event sample. In this exploratory measurement, the covariance is consistent with zero, and so no correlations have been observed beyond statistical fluctuations (see Fig. 23).

Regardless of the outcome of the measurements with the isobar program, that will be performed at the top RHIC energy, one question will remain. What happens at lower collision energy? In this context a new idea has emerged. The newly installed event-plane detector (EPD) upgrade provides a new capability at STAR towards CME search at lower collision energy and for the BES-II program [103]. The idea is simple, at lower energies the EPD

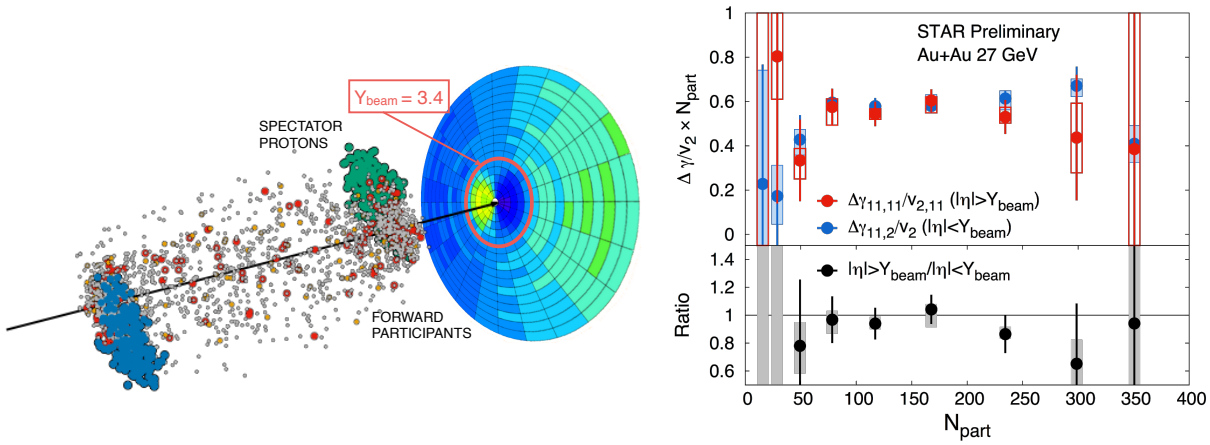

Figure 24: Prospect of CME search with the BES-II data. (Left) Single simulated UrQMD event and EPD detector acceptance that covers beam rapidity and detects both forward participants and spectators in 27 GeV Au+Au collisions that have large directed flow which changes sign at $\eta = Y_{\rm bean} = 3.4$. (Right) γ-correlators scaled by v_2 across different event-planes and double ratio of spectator/participant event plane results which would be above unity for finite CME scenario.

acceptance ($2.1 < |\eta| < 5.1$) falls in the region of beam rapidity ($Y_{\rm beam}$) and can measure the plane of strong directed flow (Ψ_1) of spectator protons, beam fragments and stopped protons, therefore strongly correlated to the B-field direction (See Fig. 24). The next step is to measure $\Delta\gamma$ with respect to Ψ_1 and compare it with the measurement of $\Delta\gamma$ along Ψ_2 planes from outer regions of EPD and TPC at mid-rapidity that are relatively more weakly correlated to the B-field directions. A test of CME scenario will be to see if a large difference is observed in the measurements. First preliminary measurements from STAR as shown in Fig, 24 are dominated by uncertainty, but seem to show good prospects for the CME search at lower energies. With the higher statistics data from the BES-II (7.7-19.6 GeV) and fixed target programs more precise measurements are possible.

1.3 Cold QCD Highlights

1.3.1 Introduction

The goal of the STAR Cold QCD program is to probe the spin and flavor structure of the proton and understand the role of spin in Quantum Chromodynamics, exploiting the unique capability of RHIC to provide longitudinally and transversely polarized pp collisions at multiple energies. Measurements with longitudinal beam polarizations have given new insights into the helicity structure of the proton, while measurements with transverse polarizations have provided new ways to probe polarized parton distribution functions in the collinear and transverse momentum dependent frameworks. This program is complemented by studies of polarized pp elastic scattering and central exclusive production, in which a far-forward proton is detected intact.

Since 2009, RHIC STAR has completed several highly successful polarized pp runs both at $\sqrt{s} = 200$ GeV and $\sqrt{s} = 500/510$ GeV. Moreover, p+Au and p+Al datasets with a transversely polarized proton beam have been recorded in 2015 at $\sqrt{s} = 200$ GeV to address important physics problems, including the underlying non-perturbative mechanism responsible for large forward transverse single spin asymmetries, the ridge phenomenon and the possible onset of gluon saturation effects. Table 5 summarizes the STAR sampled luminosity and the luminosity averaged beam polarization as measured by the hydrogen jet (H-jet) polarimeter.

Table 5: Summary of polarized pp and p+A running periods at RHIC since 2009, including center-of-mass energy, STAR's integrated luminosity and the average beam polarization for blue (B) and yellow (Y) beams from the H-jet polarimeter.

Year	System	$\sqrt{s}$ (GeV)	Recorded Lumi. (pb^{-1})	Polarization Orientation	B/Y $\langle P \rangle$ (%)
2009	pp	200	25	Longitudinal	55/55
2009	pp	500	10	Longitudinal	39/39
2011	pp	500	12	Longitudinal	48/48
2011	pp	500	25	Transverse	48/48
2012	pp	200	22	Transverse	61/56
2012	pp	510	82	Longitudinal	50/53
2013	pp	510	300	Longitudinal	51/52
2015	pp	200	52	Transverse	53/57
2015	pp	200	52	Longitudinal	53/57
2015	pAu	200	0.45	Transverse	60/–
2015	pAl	200	1	Transverse	54/–
2017	pp	510	320	Transverse	55/55

Since the last PAC meeting, there have been four publications in Phys. Rev. D and nine new preliminary releases that are highlighted in the following section. Additionally, STAR

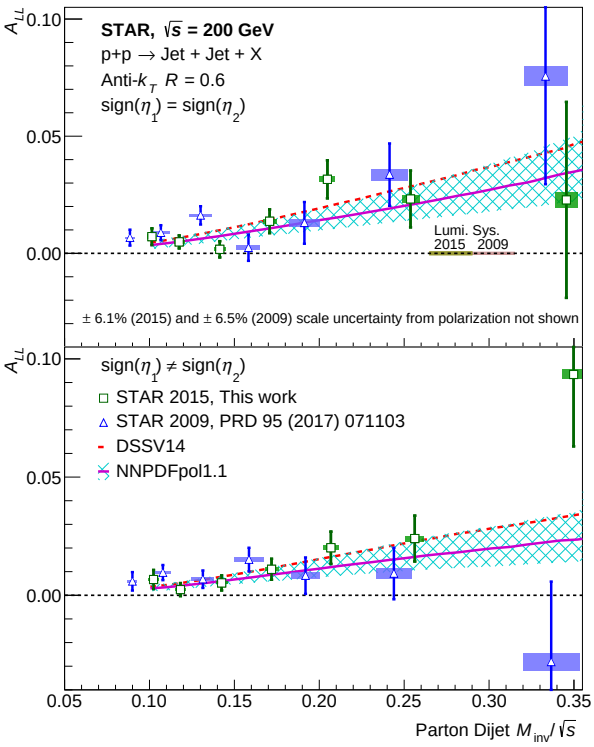

Figure 25: A_{LL} versus $M_{inv}/\sqrt{s}$ for dijets with the sign(η_1) = sign(η_2) (top) and sign(η_1) $\neq$ sign(η_2) (bottom) event topologies [104]. The square markers show the present data, whereas the triangle markers show the data of Ref. [105]. The results are compared to theoretical predictions for dijets from DSSV14 [106] and NNPDFpol1.1 [107] with its uncertainty.

has one analysis, Run-13 inclusive jet and dijet A_{LL} at mid-rapidity, that just formed its God Parent Committee.

1.3.2 Longitudinal Program

STAR has recently completed and published in PRD Letters its results for the high precision inclusive jet and dijet longitudinal double-spin asymmetries, A_{LL}, from Run-15 pp collisions at $\sqrt{s} = 200$ GeV [104], which was selected for an *Editors' Suggestion*. These results are sensitive to the gluon helicity distribution in the proton, especially for the medium gluon momentum fractions in the range from $x \simeq 0.05$ to $x \simeq 0.5$. Figure 25 shows the new results of dijet A_{LL} together with the Run-9 results of Ref. [105] and the expected A_{LL} values for the DSSV14 [106] and NNPDFpol1.1 [107] parton distributions. The results are in good agreement with previous measurements at $\sqrt{s} = 200\,\text{GeV}$ and with the theoretical evaluations of prior world data. They have better precision and thus provide further evidence that $\Delta G(x, Q^2)$ is positive for $x > 0.05$.

Dijet measurements at larger pseudorapidity and higher center-of-mass energy probe lower values of partonic momentum fraction x, a region where the gluon helicity distribution is still poorly constrained. The first measurement of A_{LL} for intermediate pseudorapidity dijets [108] used Run-9 data at $\sqrt{s} = 200$ GeV. Figure 26 shows preliminary results for intermediate pseudorapidity dijet A_{LL} using Run-12 STAR pp data at $\sqrt{s} = 510$ GeV. The higher collision energy of the Run-12 preliminary results will provide lower kinematic reach in partonic momentum fraction x relative to the Run-9 results, and further constrain the

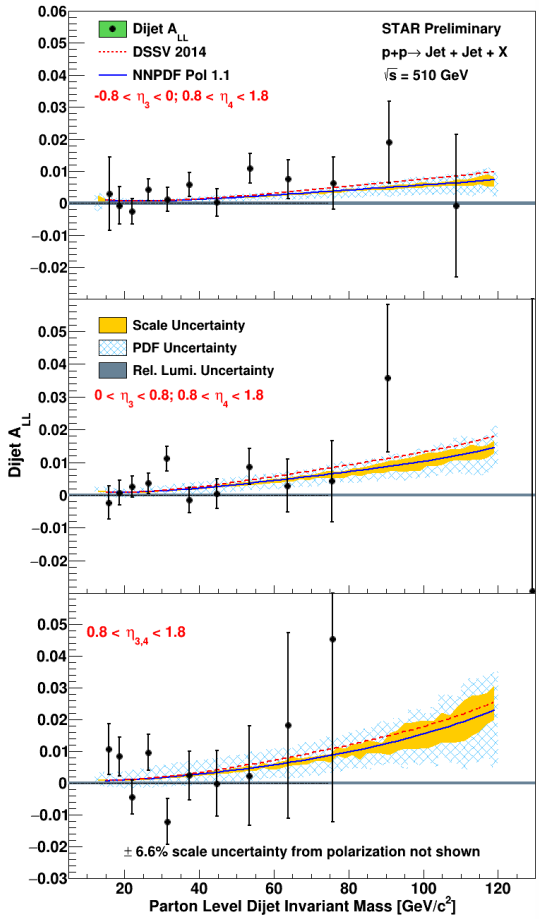

Figure 26: Preliminary results of A_{LL} as a function of parton-level invariant mass for dijets from Run-12 data at 510 GeV with the East Barrel-Endcap (top), West Barrel-Endcap (middle) and Endcap-Endcap (bottom) event topologies [109]. The curves represent theoretical predictions of A_{LL} for the DSSV14 [106] and NNPDFpol1.1 [107] parton distributions.

low-x behavior of $\Delta G(x, Q^2)$.

The longitudinal spin transfer, D_{LL}, of Λ and $\bar{\Lambda}$ are expected to be sensitive to the helicity distributions of the strange quark and anti-quark and the longitudinal polarized fragmentation functions. The left panel of Fig. 27 shows new D_{LL} preliminary results based on the Run-15 dataset at 200 GeV [110], which have about two times larger statistics than previously published results from the Run-9 dataset [111]. The new results cover transverse momenta up to 8.0 GeV/c, and are consistent with zero within uncertainty.

1.3.3 Transverse Program

There have been three new preliminary results released and two publications from the transverse spin program since the last PAC meeting. The highlights include new preliminary results for the Collins asymmetries for a charge hadron in a jet [112], interference fragmentation function (IFF) asymmetries for di-pion [113], and hyperon transverse spin transfer [110] in $\sqrt{s} = 200$ GeV pp collsions. Moreover, the A-dependence of transverse single spin asymmetries (TSSA) for π^0 at forward rapidity in pp p+Au and p+Al at 200 GeV, and isolated π^0 & EM-jet TSSA in pp collisions at 200 GeV and 500 GeV are now both published in Phys.

Rev. D [114, 115].

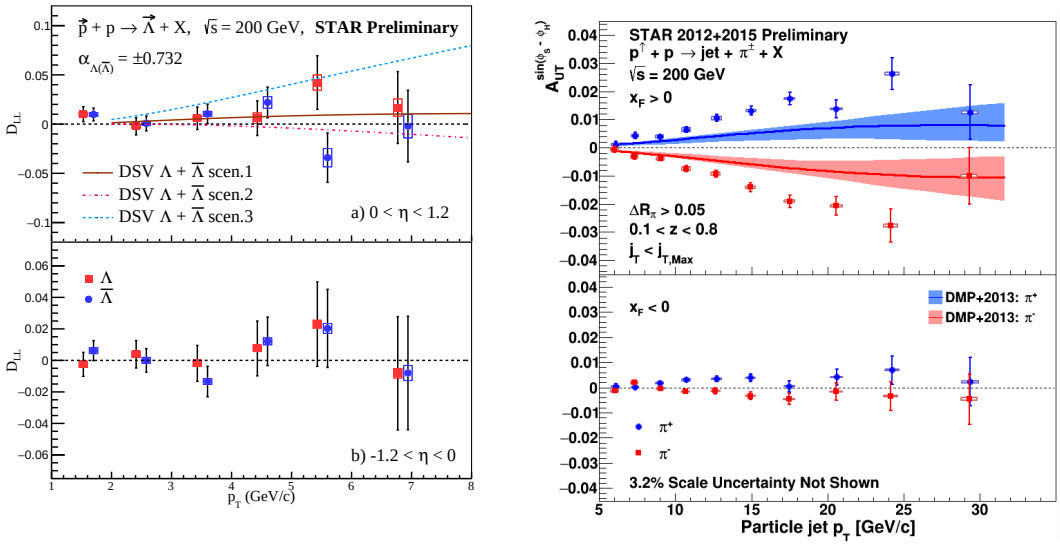

Figure 27: Left: Preliminary results of longitudinal spin transfer, D_{LL}, of Λ(red) and $\bar{\Lambda}$(blue) from Run-15 pp dataset [110]. The top and bottom panels are for the positive and negative η with respect to the polarized beam, respectively. The results for the $\bar{\Lambda}$ have been shifted to larger p_T slightly for clarity. Right: Preliminary results for the the combined Run-12 and Run-15 Collins asymmetry plotted for identified π^+ (blue) and π^- (red) particles as a function of jet p_T for jets that scatter forward relative to the polarized beam ($x_F > 0$) on top panel and those scatter backward ($x_F < 0$) on lower panel [112]. The full range of both z and j_T are integrated over. Theoretical evaluations from [116] with their uncertainties are presented for π^+ (blue) and π^- (red).

In the soft-collinear-effective theory framework, the Collins asymmetry combines the collinear quark transversity in the proton with the transverse momentum dependent Collins fragmentation function [117–119], and thus provides a cleaner probe of the Collins fragmentation function than that in semi-inclusive deep inelastic scattering (SIDIS). This also enables tests of evolution, universality and factorization breaking in the TMD formalism. The right panel of Fig. 27 shows the combined Run-12 and Run-15 preliminary Collins asymmetries for charged pions within jets with jet $p_{\rm T}$ dependence. The measured asymmetries at positive x_F are larger than theoretical predictions [119] which are based on the transversity and Collins fragmentation function from SIDIS and e^+e^- processes with TMD approach.

In transversely polarized proton collisions, di-hadron production is also sensitive to transversity. The coupling of transversity to the di-hadron fragmentation function creates azimuthal modulations which leads to observed asymmetries. STAR has released new preliminary results on di-pion ($\pi^+\pi^-$) correlation asymmetry [113] based on the Run-15 $\sqrt{s} =$ 200 GeV dataset, as shown in Fig. 28, as $A_{UT}^{sin(\phi_{RS})}$ versus the di-pion invariant mass, $M_{inv}^{\pi^+\pi^-}$, in the forward pseudorapidity region ($\eta^{\pi^+\pi^-} > 0$). The asymmetry signal is enhanced near the ρ mass ($M_{inv}^{\pi^+\pi^-} \approx 0.78 GeV/c^2$), consistent with the theory prediction. The statisti-

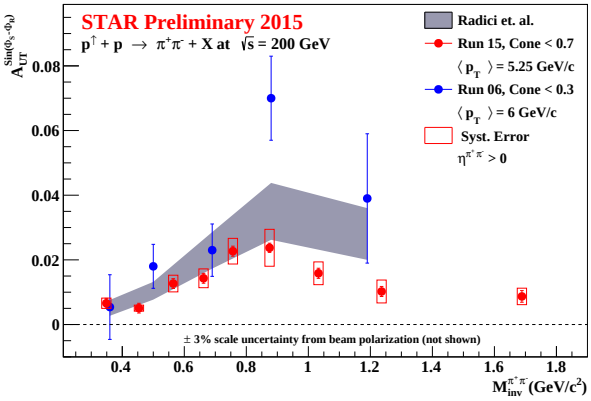

Figure 28: Preliminary results of di-hadron asymmetry $A_{UT}^{sin(\phi_{RS})}$ as a function of $M_{inv}^{\pi^+\pi^-}$, integrated over $p_T^{\pi^+\pi^-}$ in forward pseudo-rapidity region ($\eta^{\pi^+\pi^-} > 0$) at $\sqrt{s}$= 200 GeV from Run-15 together with previously published Run-6 data. The error bars represent the statistical uncertainty, while the boxes represent the systematic uncertainty.

cal precision of the 2015 result is significantly improved compared to the previous Run-6 measurement.

Transverse Spin transfer, D_{TT}, of hyperons in pp collisions can provide a connection to the transversity distribution of the $s(\bar{s})$ quark in the proton and the polarized fragmentation functions. STAR has published its first measurement of the transverse spin transfer of Λ and $\bar{\Lambda}$ hyperons at $\sqrt{s} = 200$ GeV based on the Run-12 pp dataset [121]. A new D_{TT} preliminary result using the Run-15 pp dataset has been released [110]. The Run-15 dataset is about twice as large as the Run-12 dataset, allowing for better statistical precision. The left panel of Fig. 29 shows the preliminary Run-15 results for D_{TT} versus $\Lambda(\bar{\Lambda})$ p_T. The new results are consistent with zero within uncertainties, and also are consistent with model predictions.

A new STAR publication reports on the transverse single spin asymmetry (TSSA) for forward neutral pions produced in polarized proton collisions with protons (pp), aluminum nuclei (p+Al) and gold nuclei (p+Au) at $\sqrt{s} = 200$ GeV are measured with the FMS in Run-15 [114]. The measured asymmetries, presented in the right panel of Fig. 29, are found to rise with transverse momentum at $x_F < 0.5$, while they flatten or fall at larger x_F. The results are consistent with a weak nuclear A dependence. Moreover, a further observation is that the TSSA is significantly larger for isolated π^0s than for non-isolated π^0s, which are accompanied by additional jet-like fragments.

The TSSA of neutral pions in pp collisions at both $\sqrt{s} = 200$ GeV and 500 GeV from FMS data are shown in Fig. 30. The 200 GeV data are from Run-15, while the 500 GeV data are from the Run-11. The results have been published [115]. A continuous increase of the TSSA with Feynman-x indicates a weak dependence on the center-of-mass energy. Pions with no nearby particles ("isolated"), which may not arise from conventional parton fragmentation, tend to have a higher TSSA than non-isolated pions, which suggests that a different mechanism (i.e., diffractive) other than the Sivers or Collins effects is required to explain these results. The theoretical calculations presented in the plot are based on the TMD and collinear twist-3 functions from a recent global analysis [122], which also includes previous forward π^0 and charged hadron TSSA data from RHIC in the fit. The theoretical calculation differs from our measurement and only provides a reasonable description of the non-isolated π^0 in the low-x_F region.

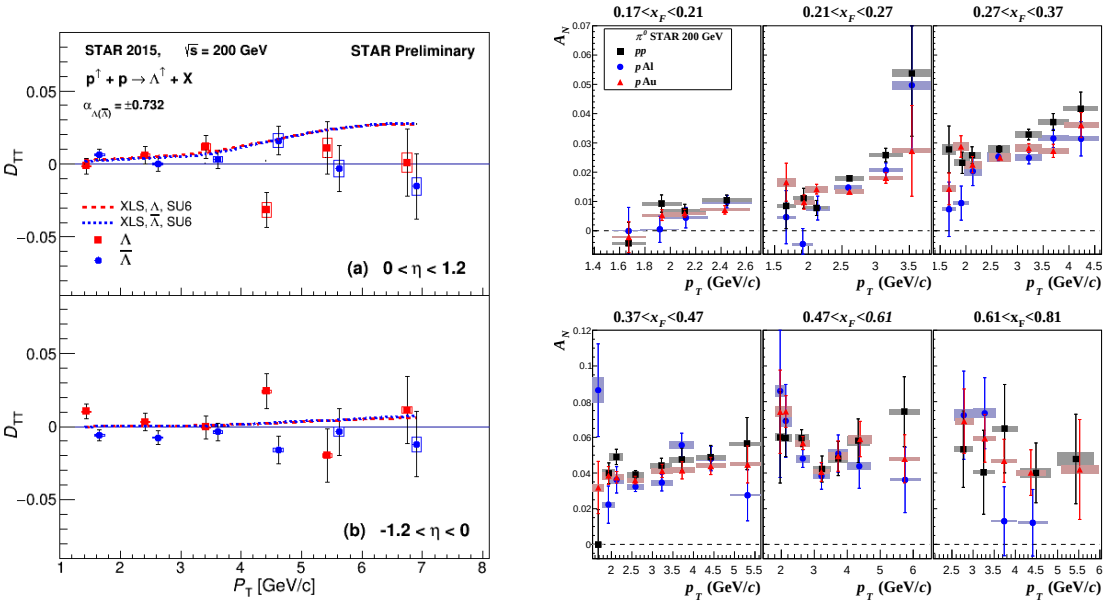

Figure 29: Left: Preliminary results of D_{TT} versus $\Lambda(\bar{\Lambda})$ p_{T} from the Run-15 pp dataset at $\sqrt{s}$ = 200 GeV [110]. The upper panel is for positive η with respect to the polarized beam and the lower for negative η. The results are compared with a model calculation [120]. The Λ results have been offset to smaller p_{T} for clarity. Right: Transverse single spin asymmetry for forward π^0 production as a function of transverse momentum for six Feynman x_T regions [114]. The results for three collisions systems are shown, the black squares are for pp blue circles for p+Al and red triangles for p+Au collisions. The statistical uncertainties are shown with vertical error bars and the filled boxes indicate the horizontal and vertical systematic uncertainties.

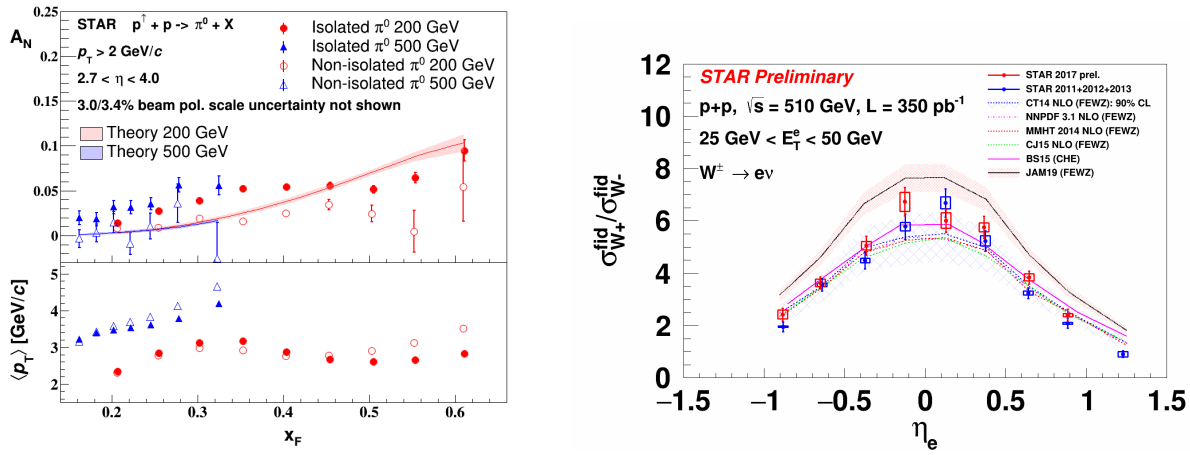

Figure 30: Left: Results for the transverse single-spin asymmetry as function of Feynman-x for the isolated and non-isolated π^0 in transversely polarized pp collisions at $\sqrt{s} = 200$ and 500 GeV [115]. Theory curves based on a recent global fit [122] are also shown. The average $p_{\rm T}$ of the π^0 for each x_F bin is shown in the lower panel. Right: Comparison of W^+ and W^- cross-section ratio as a function of lepton pseudorapidity for the Run-17 dataset to the recently published combined Runs-11, 12 and 13 datasets [123]. The central values correspond to the mean value of η_e distribution for that bin. The error bars represent the statistical uncertainty and the rectangular boxes represent the systematic uncertainty. These measurements are compared to various theory frameworks, which use several different PDF inputs.

1.3.4 Unpolarized Program

Since the last PAC meeting STAR has published one paper on the W and Z cross sections and their ratios for the combined Run-11, Run-12, and Run-13 $\sqrt{s} = 500/510$ GeV pp datasets [123]. The W^+/W^- cross-section ratio is a unique measurement that is sensitive to the unpolarized $\bar{d}/\bar{u}$ quark distribution and will provide insight and constraints to its x dependent distribution. This STAR measurement is complementary to the Drell-Yan results from NuSea [124] and SeaQuest [125], covering the overlapping x region of about $0.1 - 0.35$ at higher $Q^2 (= M_W^2)$. The W^+/W^- cross-section ratio measured with Run-17 dataset at $\sqrt{s} = 510$ GeV has been released as preliminary [126]. Figure 30 shows the ratio plotted as a function of lepton pseudorapidity for the combined Run-11, 12 and 13 published results and the Run-17 preliminary result.

Measurements of the differential inclusive jet cross section in pp collisions can be incorporated into global fits to provide constraints on the unpolarized gluon PDFs. Differential inclusive jet cross section results at $\sqrt{s} = 200$ GeV and 510 GeV from STAR's Run-12 dataset have been released as preliminary [127, 128]. The measurement at $\sqrt{s} = 200$ GeV, as seen in Fig. 31, corresponds to a range of $x_T \equiv \frac{2p_T^{\rm jet}}{\sqrt{s}}$ from 0.067 up to 0.5, allowing for the possibility of constraining the unpolarized gluon PDF at high-x. The measurement at $\sqrt{s} = 510$ GeV, shown in Fig. 32, is sensitive to lower x values of the gluon PDF compared to the 200 GeV measurement.

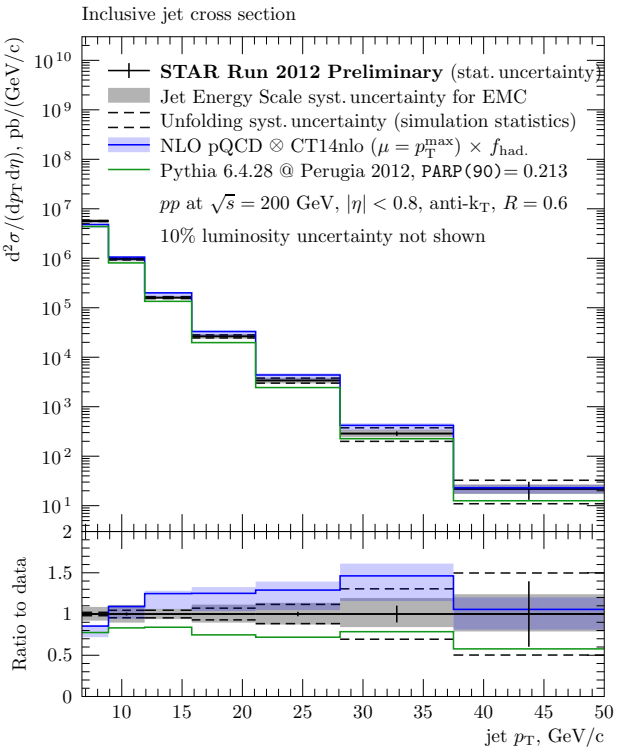

Figure 31: Differential inclusive jet cross section for pp collisions at $\sqrt{s} = 200$ GeV as a function of jet p_T corrected for underlying event. The measurement is compared to a prediction from the PYTHIA Monte Carlo generator. Another comparison is to a prediction of the NLO pQCD theory with a bin-by-bin correction for effects of the hadronization estimated using the same PYTHIA generator.

The azimuthal correlation of forward di-hadrons produced in pp and p+A collisions provides an essential tool to access the underlying gluon dynamics in the nonlinear evolution region. STAR has released preliminary results for the measurement of azimuthal correlations of di-π^0 produced in the forward direction ($2.6 < \eta < 4.0$) in pp, p+Al and p+Au collisions at $\sqrt{s} = 200$ GeV from the Run-15 dataset [129]. A clear suppression of the correlated yields of back-to-back pairs is observed in p+Al and p+Au compared with the reference pp collisions. The larger suppression found in p+Au than p+Al collisions exhibits the saturation scale, Q_s^2, dependence on A. The observed suppression of back-to-back pairs as a function of event activity and p_T from Fig. 33 points to the non-linear gluon dynamics arising at high parton densities.

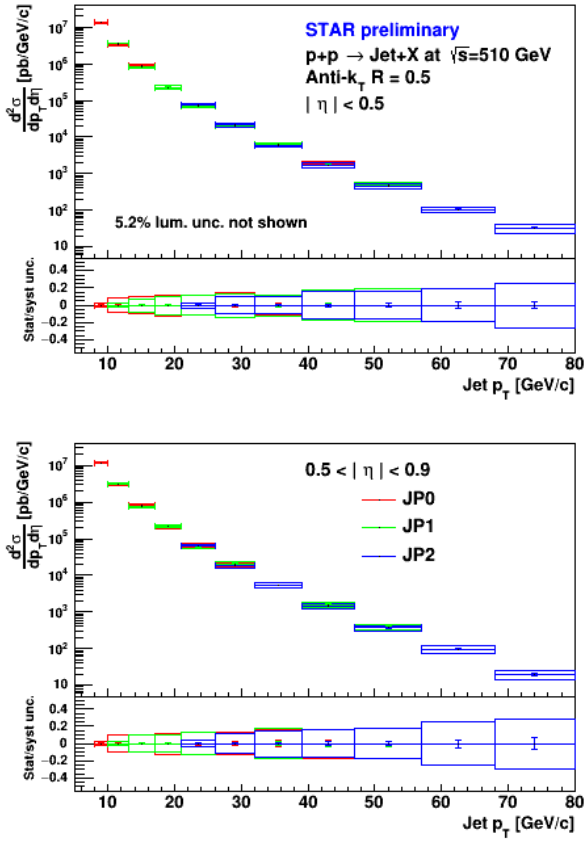

Figure 32: Differential inclusive jet cross section, $\frac{\mathrm{d}^2\sigma}{\mathrm{d}p_T\,\mathrm{d}\eta}$, as a function of particle jet transverse momentum p_T for JP0, JP1 and JP2 triggered samples within two η regions, $|\eta| < 0.5$ and $0.5 < |\eta| < 0.9$. The results show excellent agreement between triggers, which indicates an accurate simulation of the trigger efficiency used in detector effect unfolding.

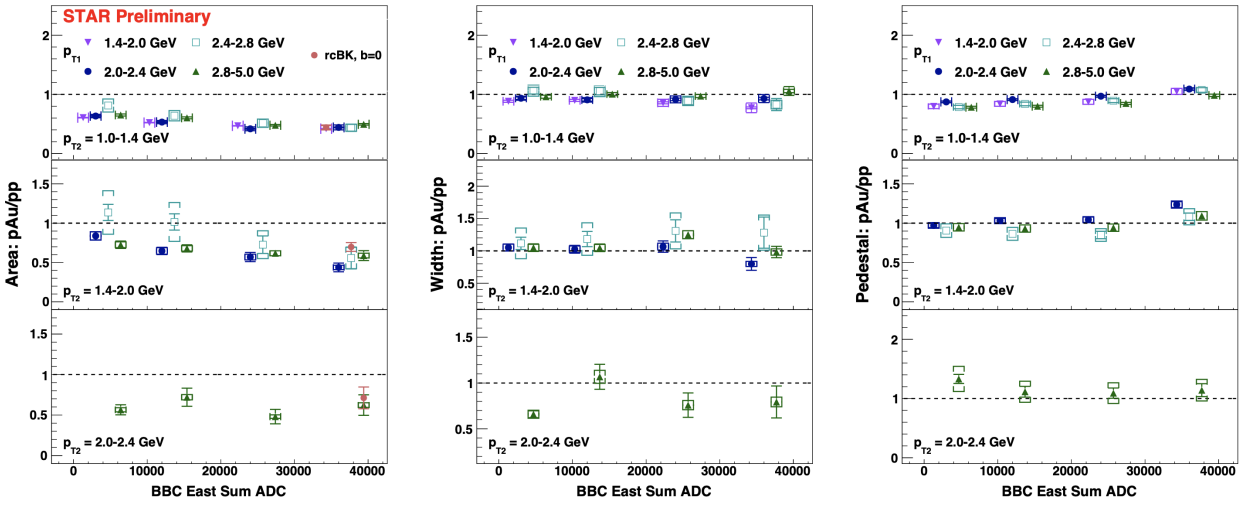

Figure 33: Comparison of back-to-back di-π^0 ratios of pair yields, the width, and the level of pedestal in p+Au and minBias pp collisions as a function of di-π^0's p_T and event activity. Energy deposited at east Beam-Beam Counter (BBC) quantifies the "event activity". The measured area ratio is compared with theory predictions based on rcBK model [130].

1.4 Run-21 Performance

In this section, we review the BES-II collider and fixed-target performance to date, detailing which of the Run-21 physics priorities have been completed. Careful study of these performance metrics will be used to make projections about the required time to complete the remaining Run-21 physics priorities. As our projections indicate that we are highly likely to complete the Run-21 priorities within the allotted run-time, we also propose an additional physics topic which could be addressed if time is available toward the end of Run-21 operations.

The highest priority for Run-21 was to complete the BES-II physics program. Most of the BES-II collider and fixed-target systems had been completed during 2018-2020. The only remaining dataset to be collected was the 7.7 GeV collider system. This had been chosen to be run last as it was expected to be the most difficult from an operations point of view. Tests of the 7.7 GeV collider program had been performed in 2019 (without electron cooling) and in 2020 (with electron cooling), and projections using the best performance from 2020 suggested that, conservatively, it would require 28 weeks to complete the 7.7 GeV collider system. STAR optimistically projected that the 7.7 GeV collider system would be completed in 11-20 weeks, and proposed a prioritized physics program that could make use of additional beam-time if available (see Table 6).

Table 6: Physics Priorities for Run-21

Priority	Beam Energy	$\sqrt{s_{NN}}$	System	Events	Weeks	Goals
1	3.85	7.7	Au+Au	100 M	11-20	Complete BES-II
2a	3.85	3.0	Au+Au	300 M	3 days	Fluctuations
2b	44.5	9.1	Au+Au	50 M	1 day	Stopping
2b	70	11.5	Au+Au	50 M	1 day	Stopping
2b	100	13.7	Au+Au	50 M	1 day	Stopping
3a	100	200	O+O	400 M	4 days	Small systems (min bias)
3a	100	200	O+O	200 M	4 days	Small systems (central)
3b	8.65	17.3	Au+Au	250 M	2.5	Additional BES-II energy
3c	3.85	3.0	Au+Au	2 B	3	Double hyper-nucleus search

1.4.1 Performance to Date

Priority 1:
STAR started taking physics data for the 7.7 GeV collider program on January 31st, and completed the event statistics goal on May 1st. This was a total of 90 days (or 12.8 weeks) of data taking. The 7.7 GeV run did prove to be very technically challenging. At the start of data taking in early February, the good event rates were only half of those that had been achieved the year before. Optimizations and improvements included: using the Tandem (as opposed to EBIS) to achieve the maximum intensity at injection, including a beta-squeeze

ten minutes into the fill (made possible by the reduction of the beam emittance due to the electron cooling), optimizing the longitudinal matching for injection from the AGS to RHIC, developing a new “low tune" for RHIC, and implementing dampers. After this month of optimizations, the store-average good event rate reached 30 Hz, which was a factor of five better than was achieved in 2010, and a factor of two better than the best rates achieved in the 2020 tests. The key run-averaged performance metrics are detailed in Table 7, and compared to those achieved for the other BES-II collider energies. Although the store-average good event rate reached 30 Hz in the later half of the run, the run-averaged value was 22 Hz, which was close to the most optimistic projection. The second most significant performance metric is the average hours of data taking per day. This metric is influenced by the store length, the up-time of the collider, the up-time of the experiment, and the faction of time dedicated to other programs (CeC and APEX) and maintenance. STAR had estimated 12-15 hours per day of data taking. Over the course of the run, an average of 13 hours per day was achieved, however, it should be noted that an average of 1.5 hours per day had been dedicated to CeC and APEX during the 90 days of 7.7 GeV running; therefore the average hours per day was also close to the most optimistic projection. Data quality assurance is performed on a run-by-run basis by the shift crews, on a daily basis by remote QA shifters using fast offline production, and on a weekly basis by the physics working groups.

Table 7: Achieved and projected experiment performance criteria for the BES-II Au+Au collider program.

Collision Energy (GeV)	7.7	9.2	11.5	14.6	17.1	19.6	27
Performance in BES-I	2010	NA	2010	2014	NA	2011	2011
Good Events (M)	4.3	NA	11.7	12.6	NA	36	70
Days running	19	NA	10	21	NA	9	8
Data Hours per day	11	NA	12	10	NA	9	10
Fill Length (min)	10	NA	20	60	NA	30	60
Good Event Rate (Hz)	7	NA	30	23	NA	100	190
Max DAQ Rate (Hz)	80	NA	140	1000	NA	500	1200
Performance in BES-II (**achieved**)	2021	2020	2020	2019	2021	2019	2018
Required Number of Events	100	160	230	300	250	400	NA
Achieved Number of Events	**101**	**162**	**235**	**324**	TBD	**582**	**560**
fill length (min)	**30**	**45**	**25**	**45**	50	**60**	**120**
Good Event Rate (Hz)	**22**	**33**	**80**	**170**	265	**400**	**620**
Max DAQ rate (Hz)	**600**	**700**	**550**	**800**	1300	**1800**	**2200**
Data Hours per day	**13**	**13**	**13**	**9**	15	**10**	**9**
Projected number of weeks	11-20	8.5-14	7.6-10	5.5	2.5	4.5	NA
weeks to reach goals	**12.8**	**14.6**	**8.9**	**8.6**	TBD	**5.1**	**4.0**

Priority 2:
The second priority really breaks down in two distinct fixed-target physics programs. The first (indicated as Priority 2a in Table 6) required 300 M minimum bias events from fixed-target collisions using the 3.85 GeV Au beam. This study used the same beam energy as the 7.7 GeV collider program, therefore it was efficient to run immediately after the 7.7 GeV program was completed as the reconfiguration of the collider was minimal. The fixed-target program did need a long beta star lattice and used only twelve bunches in the yellow ring, and STAR needed to reconfigure its trigger. All of these changes were completed efficiently, and within three hours of the completion of the 7.7 GeV collider run, STAR was taking physics data for the 3.85 GeV fixed-target run. The key physics goals for this 3.85 GeV run are fluctuation measurements, therefore, strict requirements were placed in consistency of operations and minimization of pile-up. These operational requirements limited the store length to two hours, shorter than the expected four hours, which resulted in the 3.3 days instead of the expected 3.0 days. On a positive note, the eTOF detector system, which is critical for this energy, was live for 99.6% of all events recorded.

The second part of the priority 2 fixed-target program (indicated as Priority 2b in Table 6) required 50 M events at three higher energies (44.5, 70, and 100 GeV). Changing the collider from low-energy to high-energy operations required reconfiguring the injection kickers, the abort kickers, conditioning the RHIC magnets to run at full current, and developing three new energies with 5 m beta star lattices. Developing the high rigidity 100 GeV beam for fixed-target operations proved especially challenging as the 1.8 mm vertical shift in the beam necessary to graze the target was at the limit of the capabilities of the collider and maintaining the optimal luminosity required maximum use of the BBQ kicker, injection mismatch, and IBS scattering to produce the largest emittance 100 GeV Au beam ever seen. In total, the reconfiguration, beam development, and data taking took a little over three days (with data taking times of 12, 12, and 10 hours for each of the three beams). Each of these three energies completed data taking with a single store. Overall performance was exactly as expected. A summary of the Run-21 fixed-target performance is compared to the expected metrics and to previous years runs in Table 8

Priority 3a:
The O+O system at $\sqrt{s_{\rm NN}}$= 200 GeV provides a small system for flow and correlation studies. The events request was divided into a 400 M events request for minimum bias data and a 200 M event request for central collisions (top 5%). There is ample luminosity for O+O collisions at full energy to fill the STAR DAQ bandwidth, therefore a few operational choices were made to increase the quality of the recorded data. First, the beams were collided with a 1.65 mrad angle, which helps by limiting the vertex distribution to $\pm$ 30 cm in z. Second, the luminosity was limited by slightly adjusting the offsets of the beams in y to limit the minimum bias trigger rate to 4 kHz to minimize the pile-up. This program was started on May 8th. For the minimum bias part of the program achieved an average of 14 hours per day of data taking, and good events rates of 7.5 M events per hour, as expected for a program that efficiently filled the STAR DAQ bandwidth. We finished the minimum bias

Table 8: Achieved and projected experiment performance criteria for the BES-II Au+Au fixed-target program.

Beam Energy	$\sqrt{s_{NN}}$ (GeV)	Expected Duration	Actual Duration	Proposed Events	Recorded Events	Year
3.85	3.0	4 days	3.5 days	100 M	258 M	2018
3.85	3.0	3 days	3.3 days	300 M	307 M	**2021**
3.85	3.0	3 weeks	TBD	2 B	TBD	**2021**
4.59	3.2	2 days	46 hours	200 M	200.6 M	2019
5.75	3.5	1 day	23 hours	100 M	115.6 M	2020
7.3	3.9	0.5 days	12 hours	50 M	52.7 M	2019
7.3	3.9	1 day	29 hours	100 M	117 M	2020
9.8	4.5	1 day	31 hours	100 M	108 M	2020
13.5	5.2	1 days	21 hours	100 M	103 M	2020
19.5	6.2	1 days	22 hours	100 M	118 M	2020
26.5	7.2	parasitic	2 days	none	155 M	2018
26.5	7.2	parasitic	3.5 days	none	317 M	2020
26.5	7.2	parasitic	TBD	none	TBD	2021
31.2	7.7	0.5 days	11.5 hours	50 M	50.6 M	2019
31.2	7.7	1 day	26 hours	100 M	112 M	2020
44.5	9.1	0.5 days	12 hours	50 M	53.9 M	**2021**
70	11.5	0.5 days	12 hours	50 M	51.7 M	**2021**
100	13.7	0.5 days	10 hours	50 M	50.7 M	**2021**

event statistics requirements on Sunday May 16th with 404 M good events. For the central collisions, the luminosity was increased by a factor of five by reducing the vertical offset of the beams. There was still sufficient luminosity to fill the STAR DAQ bandwidth. As it was important the hardware trigger did not bias the top 5% of centrality events, which will be selected in offline analysis, the trigger efficiency was only 45%. We completed the central collision dataset on May 21st (5 days) with 212 M good events. It had been expected to take 4-5 days to complete the central collisions goals. Upon completion of the physics goals for the O+O system, the field for the STAR solenoid was flipped and another three days (shared with CeC) of minimum bias were taken. These data are needed to carefully study the alignment, calibrations, and corrections needed to maximize the tracking accuracy of the STAR TPC. Data taking for O+O was completed on May 24th.

1.4.2 Projections to Complete the Run-21 Physics Priorities

Priority 3b:
The Au+Au system at $\sqrt{s_{\rm NN}}$ = 17.3 GeV adds an energy to the BES-II collider program where there is a larger than average gap between adjacent energies, and hence μ_B, and where there is hint of a change in the ratios of the light nuclei which could suggest an increase

in neutron fluctuations. The projections for the key metrics are interpolated from those achieved to the 14.6 and 19.6 GeV collider systems (see Table 7). RHIC needed less than one day to reconfigure the injection and abort kickers and to tune the 17.3 GeV collisions. The collider optimization occurred faster than expected and the RHIC was exceeding the expected good event rate within a day of starting operations at this energy. Data taking is expected to take 17-21 days. Four days of CeC, APEX, machine set-up, and maintenance have been included in the data taking time estimates. It is projected that data for the 17.3 GeV Au+Au system will be completed by June 10-14th.

Priority 3c:
STAR will return to 3.85 GeV fixed target running toward the end of Run-21. The driving physics goal for this period is the search for the doubly-strange hyper-nucleus. As this is a rare particle search and not a fluctuations measurement, the conduct of operations will be optimized for the total number of recorded events and not for reduction of pile-up. Data taking is expected to take 23-28 days (mostly depending on the weather in June and July). Two and a half days of CeC, APEX, and maintenance have been included in the data taking time estimate. It is projected that data for this 3.85 GeV fixed-target system will be completed by July 3-10th (July 10th would be a hard stop in preparation for warm-up).

Priority X:
In previous years, STAR has recorded 26.5 GeV fixed-target data parasitically while CeC is running. This typically only occurs once CeC has reached consistent running. This has not yet happened to date, however it is expected that toward the end of Run-21 operations there will be several days of stable CeC operations, at which time we are likely to record 26.5 GeV fixed-target data.

1.5 Additional Physics Opportunity for Run-21

Pinning Down the Precise Role of Geometry on Collectivity with Central d+Au Collisions

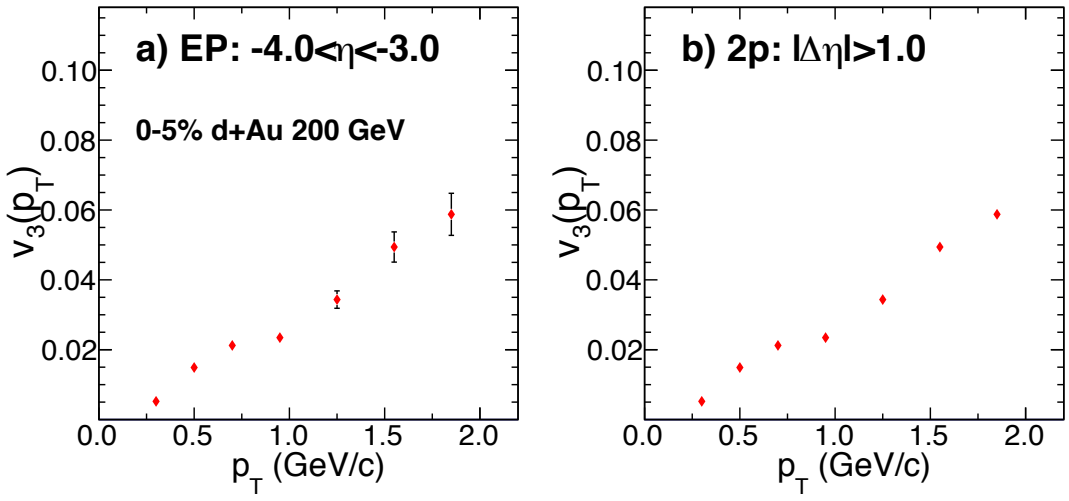

Figure 34: Projection for v_3 with forward and midrapidity acceptance in high multiplicity d+Au collisions utilizing the extended pseudorapidity capability of iTPC and EPDs.

The first striking evidence of collective behavior in small collision systems was observed in the pattern of anisotropy of particle emissions in rare high activity pp collisions at the LHC [131]. This, followed by measurements in p+Pb collisions [132–134], started a strong debate on whether such correlations originate at a very early stages due to collective behavior of gluons inside colliding protons, or whether they originate at a late stage due to the formation of a fluid like medium. Measurements of azimuthal anisotropy coefficients (v_n) in most central (0-5%) small collision systems ^3He+Au [135], d+Au [136,137] and p+Au [138] with different initial shapes from RHIC have confirmed that even in small collision systems fluid-dynamic final state effects are essential to drive collectivity [139]. Such results from the PHENIX experiment using the combination of particles form mid-rapidity ($|\eta| < 0.35$) and another from forward rapidity ($1 < \eta < 3$, Au-going side) indicate a specific ordering of triangular harmonic anisotropy $v_3(^3He + Au) > v_3(d + Au) \sim v_3(p + Au)$. This hints at the possibility that a more triangular initial geometry is produced in $^3He + Au$ collisions (compared to d+Au and p+Au) as expected from a nucleon based initial state model [140].

However, recent STAR preliminary results using two particle correlations with both particles at mid-rapidity ($|\eta| < 1$) show $v_3(^3He + Au) \sim v_3(d + Au) \sim v_3(p + Au)$ [141] implying no system dependence of triangularity indicating fluctuations or geometry at the sub-nucleonic scale drives anisotropy. This qualitative difference of system dependence of v_3 measurements between STAR and PHENIX kinematics is very striking. With the anticipated high statistics d+Au run by triggering on central events at RHIC it will be possible to

perform measurements of v_n using acceptance similar to both previous PHENIX and STAR measurements and answer:

- How will v_3 measurements in d+Au change from mid-rapidity to forward rapidity?
- How will forward v_3 measurements in d+Au from STAR compare to the same from PHENIX?

Figure 34 shows a projection plot for v_3 using particles from forward and midrapidity acceptance in high multiplicity d+Au collisions utilizing the extended pseudorapidity capability of STAR. The two panels show estimates for v_3 in two-particle correlation approach by using : 1) tracks from TPC+iTPC ($|\eta| < 1.5$) and hits from EPDs ($2.1 < |\eta| < 5.1$), 2) pairs of tracks from TPC+iTPC ($|\eta| < 1.5$) and using a relative pseudrapidity gap of $|\Delta\eta| > 1$. To start with we assume STAR will collect data at the rate of 2.2 kHz and a combined RHIC×STAR down time of 50% (12 hour/day) for three days of running during Run-21. The desired run conditions will be such that the coincidence rate of ZDCs will be about 10 kHz. The idea is to dedicate the first day entirely on collecting minimum bias events. This will lead to the accumulation of about 1(day)×86400(sec.)×0.5(downtime) ×2200(rate) ×1.0 (bandwidth) ≈ 95 Million events. On the second and the third day, we plan to split the bandwidth equally into collecting min-bias and high multiplicity events with a dedicated trigger. Following the same estimates of rate, we can collect 95 million events for the two case. Therefore over all three days, we will be able to accumulate 190 Million min-bias events and 95 Million high multiplicity events. With such statistics and aforementioned measurements it will possible to revisit the v_n measurements in STAR and PHENIX kinematics and understand the apparent discrepancy between the previous measurements.

2 Physics with $p^{\uparrow}p^{\uparrow}$ and $p^{\uparrow}$+A Collisions at 510 and 200 GeV

The exploration of the fundamental structure of strongly interacting matter has always thrived on the complementarity of lepton scattering and purely hadronic probes. As the community eagerly anticipates the future Electron Ion Collider (EIC), an outstanding scientific opportunity remains to complete "must-do" measurements in *pp* and *p*+A physics during the final years of RHIC. These measurements will be essential if we are to fully realize the scientific promise of the EIC, by providing a comprehensive set of measurements in hadronic collisions that, when combined with future data from the EIC, will establish the validity and limits of factorization and universality. Much of the Run-22 and Run-24 physics program outlined here is, on the one hand, unique to proton-proton and proton-nucleus collisions and offers discovery potential on its own. On the other hand, these studies will lay the groundwork for the EIC, both scientifically and in terms of refining the experimental requirements of the physics program, and thus are the natural next steps on the path to the EIC. When combined with data from the EIC these STAR results will provide a broad foundation to a deeper understanding of fundamental QCD.

The separation between the intrinsic properties of hadrons and interaction-dependent dynamics, formalized by the concept of factorization, is a cornerstone of QCD and largely responsible for the predictive power of the theory in many contexts. While this concept and the associated notion of universality of the quantities that describe hadron structure have been successfully tested for unpolarized and, to a lesser extent, longitudinally polarized parton densities, its experimental validation remains an unfinished task for much of what the EIC is designed to study – the three-dimensional structure of the proton and the physics of dense partonic systems in heavy nuclei. To establish the validity and limits of factorization and universality, it is essential to have data from *both* lepton-ion and proton-ion collisions, with experimental accuracy that makes quantitative comparisons meaningful.

Beginning in Run-22, STAR will be in a unique position to provide this essential *pp* and *p*+A data. A full suite of forward detectors will be installed this year, providing excellent charged-particle tracking at high pseudorapidity ($2.5 < \eta < 4$) for the first time, coupled with both electromagnetic and hadronic calorimetry. This will enable STAR to explore the interesting regimes of high-x (largely valence quark) and low-x (primarily gluon) partonic physics with unparalleled precision. In addition, mid-rapidity detector upgrades motivated primarily by the BES-II program, in particular the iTPC, will substantially extend STAR's already excellent kinematic reach and particle identification capabilities beyond those that existed during previous *pp* and *p*+A runs.

For the case of *pp* spin physics, it is important to recognize the complementary roles that will be played by Run-22 at 510 GeV and Run-24 at 200 GeV. The combination of 510 GeV *pp* collisions and the STAR Forward Upgrade will provide access to forward jet physics at perturbative scales, thereby enabling measurements at the highest and lowest x values. In parallel, mid-rapidity measurements at 510 and, especially, 200 GeV will interpolate between the high and low x values, with significant overlaps to probe evolution effects

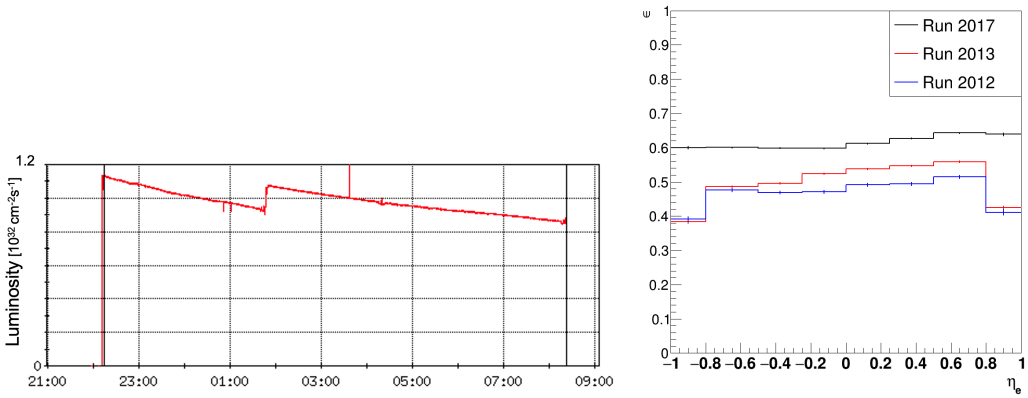

Figure 35: Example of the leveled luminosity profile for a fill from Run-17 at 510 GeV (left). The right panel shows the impact of the luminosity leveling on the W boson reconstruction efficiency. Luminosity leveling was applied during Run-17 but not for Run-12 and Run-13. A higher W efficiency is clearly seen in Run-17 with the luminosity leveling applied. The more uniform efficiency in Run-17 for two outer lepton-η bins is the result of a different cut at $|\eta| < 0.9$ to remove the detector edge effects.

and provide cross-checks. Together, the two runs will allow STAR to measure fundamental proton properties, such as the Sivers and transversity distributions, over nearly the entire range $0.005 < x < 0.5$.

Run-24 will also provide outstanding opportunities to probe fundamental questions regarding QCD in cold nuclear matter. The STAR Forward Upgrade will enable an extensive suite of measurements probing the quark-gluon structure of heavy nuclei and the regime of low-x non-linear gluon dynamics, as predicted by saturation models. STAR will also explore how a nucleus, serving as a color filter, modifies the propagation, attenuation, and hadronization of colored quarks and gluons.

For these reasons, STAR requests at least 16 weeks of polarized pp data-taking at $\sqrt{s} =$ 510 GeV in Run-22. All data-taking will involve proton beams polarized transversely relative to their momentum direction in order to focus on those observables where factorization, universality, and/or evolution remain open questions, with spins aligned vertically at the STAR IR. Based on the latest guidance from CAD, and mindful of 'lessons learned' in previous pp runs at full energy (see Fig. 35), we will ask for luminosity-leveling of the collision rate to maximize the efficiency of our main tracking detectors. Assuming we will have running conditions similar to those achieved in Run-17, we expect to sample at least 400 pb^{-1} for our rare / non-prescaled triggers. Reducing the Run-22 run time from 20 to 18 cryo-weeks would have a significant impact on our physics program described in section 2.1.1. Along with the luminosity loss associated with fewer running weeks, STAR will be commissioning its newly installed, and critical for the proposed program, forward detector suite which will result in additional luminosity being subtracted from physics running. In total, this would result in at least 15% less sampled luminosity, as the loss will occur near the end of the run when the detectors and RHIC will be operating most efficiently.

STAR also requests at least 11 weeks of polarized pp data-taking at $\sqrt{s} = 200$ GeV and 11 weeks of polarized p+Au data-taking at $\sqrt{s_{NN}} = 200$ GeV during Run-24. All of the running will involve vertically polarized protons. Based on recent CAD guidance, we expect to sample at least 235 pb^{-1} of pp collisions and 1.3 pb^{-1} of p+Au collisions. These totals represent 4.5 times the luminosity that STAR sampled during transversely polarized pp collisions in Run-15, and 3 times the luminosity that STAR sampled during transversely polarized p+Au collisions in Run-15. Effectively, we request approximately equal nucleon-nucleon luminosities for pp and p+Au which is essential to optimize several critical, and in many cases luminosity-demanding, measurements that require comparisons of the same observable in (polarized or unpolarized) pp and p+Au collisions, described further in Section 2.2. Any significant reduction of the available running period, e.g. 20 instead of 28 weeks, would almost certainly result in the impossibility of fulfilling the unique physics goals in Run-24.

2.1 Run-22 Request for $p^{\uparrow}p^{\uparrow}$ Collisions at 510 GeV

2.1.1 Inclusive Transverse Spin Asymmetries at Forward Rapidities

The experimental study of spin phenomena in nuclear and particle physics has a long history of producing important, and often surprising, results. Attempts to understand such data have pushed the field forward, forcing the development of both new theoretical frameworks and new experimental techniques. Recent and ongoing detector upgrades at STAR, at mid- and forward-rapidity, coupled with the versatility of RHIC, will allow us to gain new insights into long-standing puzzles, and to probe more deeply the complexities of emergent behavior in QCD.

Results from PHENIX and STAR have shown that large transverse single-spin asymmetries (TSSA) for inclusive hadron production, first seen in pp collisions at fixed-target energies and modest p_{T}, extend to the highest RHIC center-of-mass energies, $\sqrt{s} = 510$ GeV, and surprisingly large p_{T}. Figure 36 summarizes the world data for the inclusive neutral pion asymmetries A_N as a function of Feynman-x. The asymmetries are seen to be nearly independent of $\sqrt{s}$ over the very wide range of roughly 19 to 500 GeV.

To understand the observed TSSAs, one needs to go beyond the conventional leading-twist (twist-2) collinear parton picture for the hard-scattering processes. Two theoretical formalisms have been developed to try to explain these sizable asymmetries in the QCD framework: transverse-momentum-dependent (TMD) parton distribution and fragmentation functions, such as the Sivers and Collins functions; and transverse-momentum-integrated (collinear) quark-gluon-quark correlations, which are twist-3 distributions in the initial state proton or in the fragmentation process. For many of the experimentally accessible spin asymmetries, several of these functions can contribute, and need to be disentangled in order to understand the experimental data in detail, in particular the observed p_T dependence. These functions manifest their spin dependence either in the initial state–for example, the Sivers distribution and its twist-3 analog, the Efremov-Teryaev-Qiu-Sterman (ETQS) function [142]–or in the final state via the fragmentation of polarized quarks, such as in the Collins function and related twist-3 function $\hat{H}_{FU}(z, z_z)$.

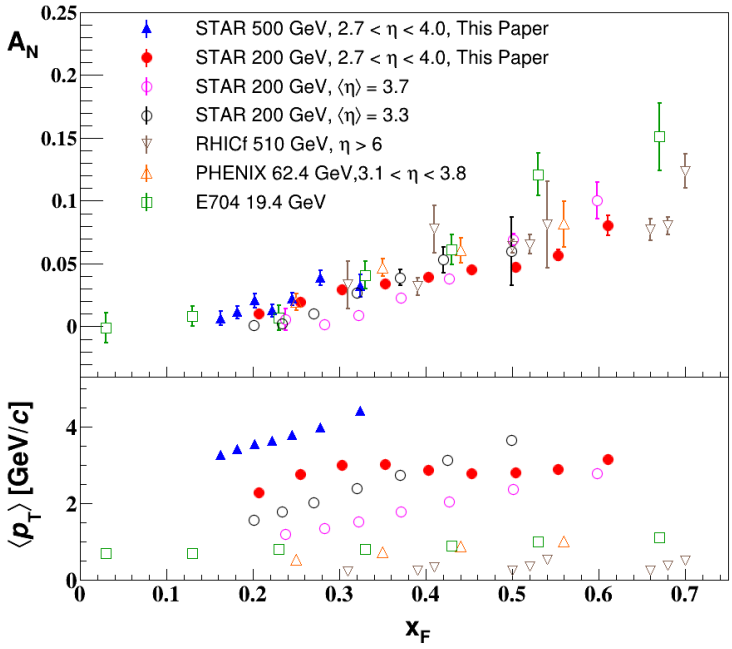

Figure 36: Transverse single-spin asymmetry A_N measurements for neutral pion in pp collisions at different center-of-mass energies as a function of Feynman-x [115].

Incorporating the fragmentation term within the collinear twist-3 approach demonstrated the ability of this formalism to describe the large values of A_N for π^0 production observed at RHIC [143]. In this work, the relevant (non-pole) 3-parton collinear fragmentation function $\hat{H}_{FU}(z, z_z)$ was fit to the RHIC data. The so-called soft-gluon pole term, involving the ETQS function $T_{q,F}(x_1, x_2)$, was also included by fixing $T_{q,F}$ through its well-known relation to the TMD Sivers function $f_{1T}^{\perp}$. The authors obtained a very good description of the data due to the inclusion of the non-pole fragmentation function and based on this work they were able to make predictions for π^+ and π^- production asymmetries A_N at the forward rapidities covered by the STAR upgrades, $2.5 < \eta < 4$. The results are shown in Fig. 37 for $\sqrt{s}$= 200 and 500 GeV for two rapidity ranges, $2 < \eta < 3$ and $3 < \eta < 4$.

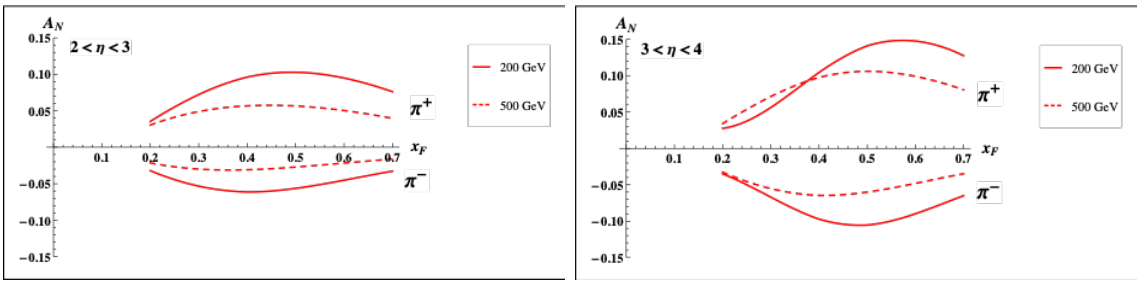

Figure 37: Predictions for A_N for π^+ and π^- production over the ranges $2 < \eta < 3$ (left) and $3 < \eta < 4$ (right) at $\sqrt{s} = 200$ GeV (solid lines) and 500 GeV (dashed lines).

In Run-22, with the full suite of forward tracking detectors and calorimetry installed, STAR will for the first time be able to map out inclusive charged-hadron asymmetries up to the highest energies achievable at RHIC and at these forward rapidities in the Feynman-x region $0.2 < x_F < 0.7$. The expected separation power between positively and negatively charged hadrons in the pseudorapidity region $2.5 < \eta < 4$ with the STAR forward upgrade is presented in Figure 38 and the expected p_{T} resolution as a function of particle p_{T} is presented in Fig. 39.

It would be very interesting to confirm that inclusive charged-hadron asymmetries are indeed largely independent of center-of-mass energy. The measurements of A_N for charged hadrons, together with analogous data (from Run-22 as well as previous STAR runs) on A_N for direct photons and neutral pions, should provide the best dataset in the world to constrain the evolution and flavor dependence of the twist-3 ETQS distributions and to determine if the 3-parton collinear fragmentation function $\hat{H}_{FU}$ is the main driver of the large forward inclusive asymmetries.

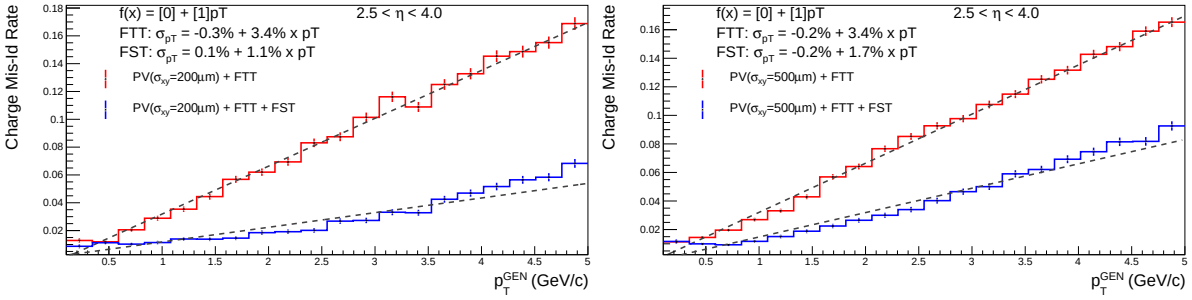

Figure 38: The expected charge mis-identification rate as a function of particle p_{T} in the pseudorapidity region $2.5 < \eta < 4$ with the STAR forward upgrade assuming a transverse primary vertex resolution of 200 μm (left) and 500 μm (right). The results in blue correspond to full tracking system including both sTGC and silicon detectors and the red ones include sTGC only.

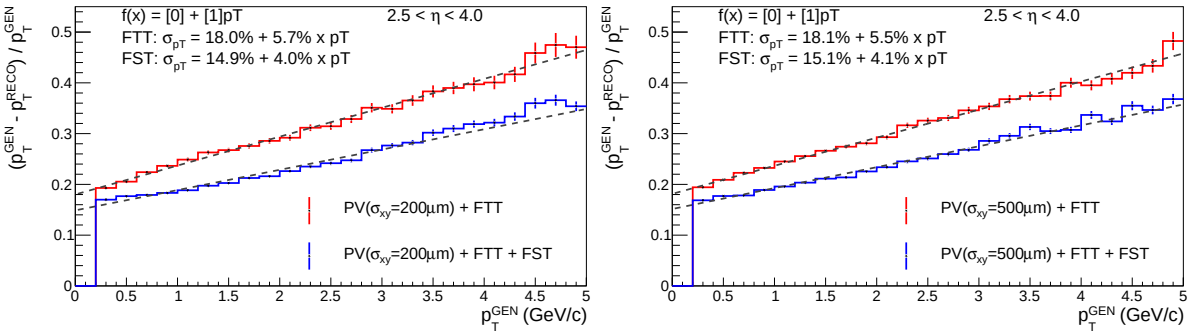

Figure 39: The expected p_{T} resolution as a function of particle p_{T} in the pseudorapidity region $2.5 < \eta < 4$ with the STAR forward upgrade for a transverse primary vertex resolution of 200 μm (left) and 500 μm (right). The results in blue correspond to full tracking system including both sTGC and silicon detectors and the red ones include sTGC only.

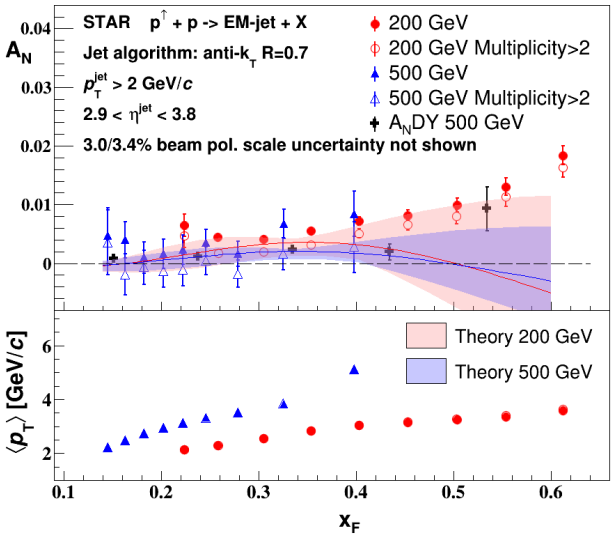

Figure 40: New STAR results on inclusive electromagnetic jets TSSA in pp collisions at both 200 and 500 GeV [115].The results that require more than two photons observed inside a jet are shown as open symbols. Theory curves [144] for TSSA of full jets at rapidity $\langle y \rangle = 3.25$ for 200 GeV (red) and $\langle y \rangle = 3.57$ for 500 GeV (blue) are also shown. The average $p_{\rm T}$ of the jet for each $x_{\rm F}$ bin is shown in the lower panel.

2.1.2 Sivers and Efremov-Teryaev-Qiu-Sterman Functions

There is great theoretical interest in testing the relation between the ETQS correlation functions and the Sivers function. As discussed above, both the Sivers and the ETQS functions encapsulate partonic spin correlations within the proton, but they are formally defined in different frameworks. While the Sivers function is a TMD quantity that depends explicitly on spin-dependent transverse partonic motion k_T, the ETQS function is a twist-3 collinear distribution, in which SSAs are generated through soft collinear gluon radiation.

Measurements of forward jet production from the ANDY collaboration [145] indicated rather small asymmetries. This was argued to be consistent with the idea that the twist-3 parton correlation functions for up and down valence quarks should cancel, because their behavior reflects the Sivers functions extracted from fits to the SIDIS data that demonstrate opposite sign, but equal magnitude, up and down quark Sivers functions. Preliminary STAR results on charge-tagged dijets at mid-rapidity [146] (see Fig. 43) support this interpretation, with the caveat that the measured observable (a spin-dependent $\langle k_T \rangle$) is defined in the TMD, and not the twist-3, framework. Moreover, recently published STAR results for forward inclusive electromagnetic jets [115] also show small TSSA as seen in Fig. 40. The results have been analyzed with the generalized parton model approach [147], and when incorporated in the reweighing procedure of the quark Sivers functions extracted from SIDIS data they significantly improved its uncertainty at larger momentum fraction x (see Fig. 41).

To better test quantitatively the relation between the twist-3 and TMD regimes, one can measure spin asymmetries for jets which are *intentionally* biased towards up or down quark jets via detection of a high-z charged hadron within the jet. Figure 42 shows the flavor of initial partons for positively and negatively charged leading hadrons in the rapidity range $2.6 < \eta < 4.1$ for different regions of Feynman-x based on PYTHIA Minimum Bias studies for pp at 510 GeV. For $x_F > 0.2$ one can see a significant enhancement of the u-quark contribution for positively charged leading hadrons, and the d-quark contribution for

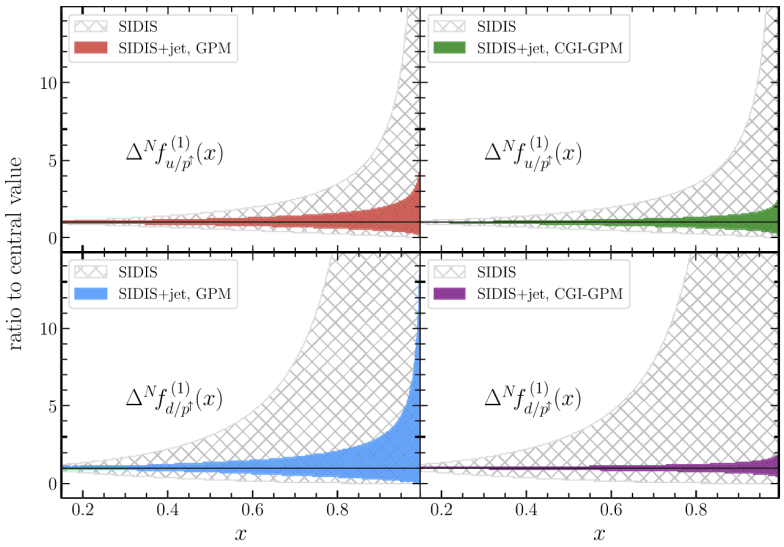

Figure 41: Comparison between the Sivers function first moments normalized to the corresponding central value from SIDIS data and their reweighted counterparts that incorporate new STAR results on electromagnetic jets [115] extracted in [147] in the generalized parton model (left panels) and color gauge invariant generalized parton model (right panels) framework. In both plots, results for u (upper panels) and d (lower panels) quarks are shown.

negatively charged ones.

Higher-twist calculations of jet asymmetries based on the Sivers function predict sizeable effects for these flavor-enhanced jets. With the suite of new forward detectors installed at STAR, full jet reconstruction, along with identification of a high-z hadron of known charge sign (see Fig. 38 and Fig. 39), will be possible at high pseudorapidity. Using realistic simulation of the forward calorimeter, and requiring a charged hadron with $z > 0.5$, the expected statistical uncertainties of asymmetries has been extracted and are presented in the left panel of Fig. 43. The simulations have assumed an integrated luminosity of 350 pb^{-1} at $\sqrt{s} = 510$ GeV. No tracking or hadron reconstruction has been included, and the trigger effects have been accounted for by applying jet p_T thresholds (4, 6, 7.5 GeV/c) for jet-patch triggers in two pseudo-rapidity regions spanning $2.5 < \eta < 3.5$ and $3 < \eta < 4$ respectively. A similar measurement is also expected at 200 GeV. Figure 43 (left) also compares the Run-22 projections to the single spin asymmetries calculated by the ETQS function, based on the SIDIS Sivers functions.

In a TMD framework, the Sivers effect manifests itself as a correlation (a triple product) between the transverse momentum of a parton ($\overrightarrow{k}_T$) with momentum fraction x, and the transverse spin ($\overrightarrow{S}$) of a polarized proton moving in the longitudinal ($\overrightarrow{p}$) direction. Thus, for transversely polarized protons, the Sivers effect probes whether the k_T of the constituent quarks is preferentially oriented in a direction perpendicular to both the proton momentum and its spin. Momentum conservation then implies that the two jets in the final state will

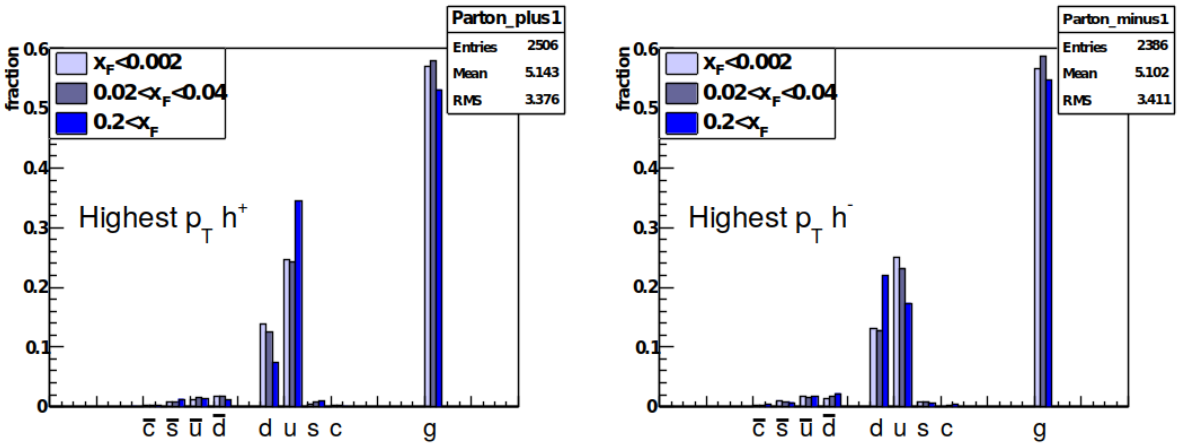

Figure 42: Flavor of initial partons for events with positively (left) and negatively (right) charged leading hadrons in the rapidity range $2.6 < \eta < 4.1$ for different regions of Feynman-x based on PYTHIA Minimum Bias studies for pp at 510 GeV. For $x_F > 0.2$ one can see an enhancement of the u-quark contribution for positively charged leading hadrons, and the d-quark contribution for negatively charged ones.

not emerge back-to-back on average, but instead will 'tilt' in the direction of the summed k_T of the initial state partons. Moreover, the (average) tilt of interest will reverse direction under a 'flip' of the proton spin; a spin-dependent $\langle k_T \rangle$ can then be extracted by associating the azimuthal opening angle of the jet pair with this tilt.

STAR carried out an earlier measurement of this transverse single-spin asymmetry using a dijet dataset with $\sim$1 pb^{-1} of integrated luminosity [148], and found it to be consistent with zero within 2σ. An ongoing and much improved analysis based on Run-12 and Run-15 has past STAR paper preview process, and the preliminary results can be found in [146]. Perhaps most significantly, the jets were sorted according to their net charge Q, calculated by summing the signed momentum of all particle tracks with $p > 0.8$ GeV, to minimize underlying event contributions, yielding jet samples with enhanced contributions from u quarks (positive Q) and d quarks (negative Q), with a large set near $Q = 0$ dominated by gluons. Simple kinematics allow for conversion from the spin-dependent 'tilt' of the dijet pair to a value of k_T on an event-by-event basis; these are then sorted by the Q of the jet and binned by the summed pseudorapidities of the outgoing jets, $\eta^{\text{total}} \equiv \eta_3 + \eta_4$. Because the contributions of different partons (u, d, all else) to $\langle k_T \rangle$ vary with both Q and also η^{total}, in a way that can be estimated robustly using simulation, the data can be inverted to yield values of $\langle k_T \rangle$ for the individual partons, though with coarser binning in η^{total}. Figure 43 (right) shows the preliminary results for the spin-dependent $\langle k_T \rangle$ values for u, d and $gluon + sea$.

With the new forward detectors in place, along with the enhanced reach in η afforded by the iTPC, this technique can be expanded in Run-22 to cover pseudorapidities at STAR from roughly -1 to 4, though with a gap at $1.5 < \eta < 2.5$. Despite this gap, values of $\langle k_T \rangle$ can be extracted for u and d quarks for η^{total} ranging from ~ -1.5 to as high as 7 with reasonable

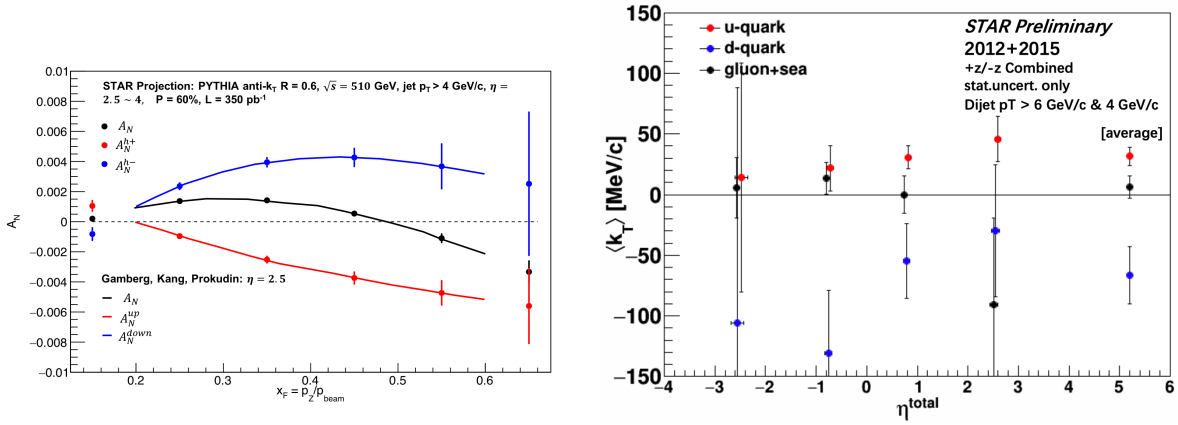

Figure 43: Left: Up quark (red line), down quark (blue line) and all jet (black line) single spin asymmetries as a function of x_F as calculated by the ETQS function, which is based on the SIDIS Sivers functions, for 200 GeV center-of-mass energy proton collisions – the 510 GeV results are expected to be qualitatively similar. Overlaid on the theory curves are the expected experimental sensitivities for jet asymmetries tagging in addition a positive hadron with z above 0.5 (red points), a negative hadron with z above 0.5 (blue points) or all jets (black) as a function of x_F at 510 GeV. Right: Preliminary results for the spin-dependent $\langle k_T \rangle$ values for u, d and $gluon + sea$ from the dijet Sivers measurement as a function of the sum of dijet pseudorapidities $\eta_1 + \eta_2 \sim \ln(\frac{x_1}{x_2})$ [146].

statistics. This latter regime will probe $2 \to 2$ hard scattering events in which $x_1 \gg x_2$, *i.e.*, a sample enriched in valence quarks interacting with low-x gluons. Such measurements, exploiting the full kinematic reach of STAR, will not only allow precise determinations of the average transverse partonic motion, $\langle k_T \rangle$, exhibited by individual partonic species in the initial state, but will provide important information on the x dependence of the proton Sivers functions.

Collisions at $\sqrt{s} = 510$ GeV will also allow STAR to continue our successful program to study the evolution and sign change of the Sivers function. By focusing on interactions in which the final state involves only weakly interacting particles, and hence the transverse partonic motion (in a TMD framework) or the collinear gluon radiation (in twist-3) must be in the initial state, one can test for the predicted sign change in A_N relative to interactions in which these terms must appear in the final state, such as SIDIS measurements. Following the low statistics Run-11 proof-of-principle measurement, STAR has measured A_N in W and Z in Run-17, which had about 14 times more integrated luminosity than Run-11. Figure 44 compares the reconstructed Z mass between combined Runs-11+12+13 and Run-17. From the comparison one can see a consistent mass spectrum and the clearly visible Z mass peak. Additionally, from the number of reconstructed Z events shown, one can see the effect of that the higher efficiency in Run-17 (see Fig. 35), due to the luminosity leveling, has on the data. The Run-17 preliminary Z and $W^{\pm}$ A_N results plotted as a function of reconstructed boson rapidity are shown in Figs. 45 and 46, respectively. The systematic uncertainties assigned to the W A_N preliminary results were estimated by varying the various cut criteria, in particular the lepton E_T cut, according to the Barlow criteria. Additionally the contribution from the

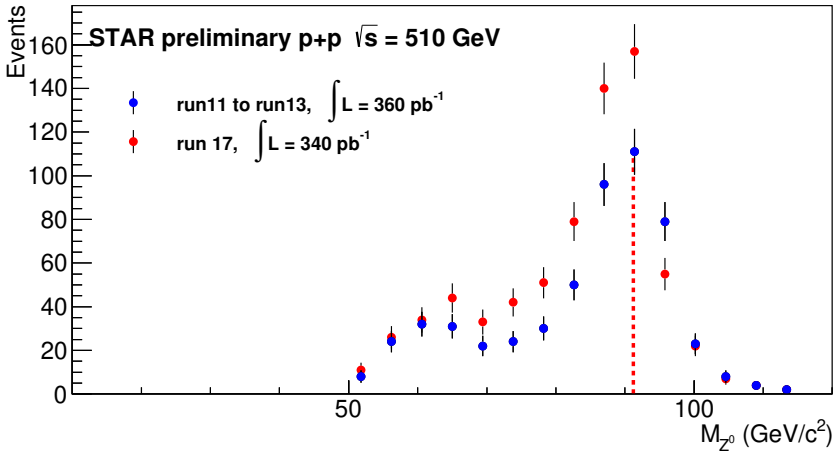

Figure 44: Preliminary results for the reconstructed Z boson mass for Run-11+12+13 (blue markers) and Run-17 (red markers).

transversal helicity function, g_{1T}, which has a cos azimuthal modulation was estimated by extracting the asymmetry A_N from a simultaneous sin / cos fit to the measured azimuthal modulations. With the increased precision provided by Run-17 we find smaller asymmetries than were suggested by Run-11. As a result it is critical that we increase the statistics of our dataset with Run-22 to improve the precision of our asymmetry measurements in order to provide a conclusive test of the Sivers' function sign change.

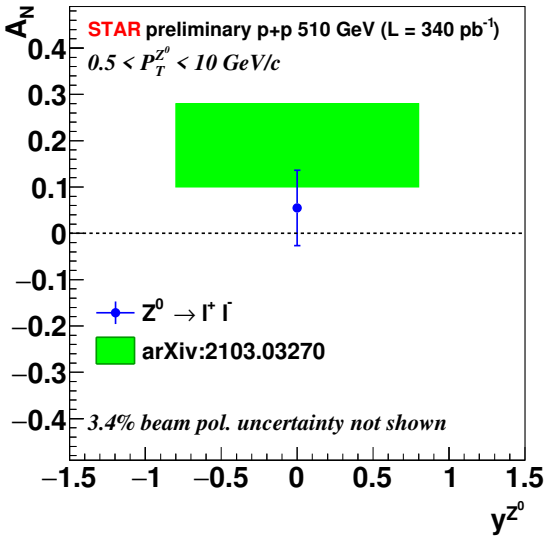

Figure 45: Preliminary results for the transverse single-spin asymmetries of Z boson as a function of rapidity for Run-17. The green band is a theoretical prediction from [149], folding in data on the sea-quark Sivers functions.

The improved tracking capabilities provided by the iTPC upgrade will allow us to push our mid-rapidity $W^{\pm}$ and Z measurements to larger rapidity $y_{W/Z}$, a regime where the asymmetries are expected to increase in magnitude and the anti-quark Sivers' functions remain largely unconstrained. In addition to the noted extension of our kinematic reach, an

additional 16 weeks of beam time at $\sqrt{s} = 510$ GeV in Run-22 would increase our dataset by about a factor of 2. This experimental accuracy would significantly enhance the quantitative reach of testing the limits of factorization and universality in lepton-proton and proton-proton collisions.

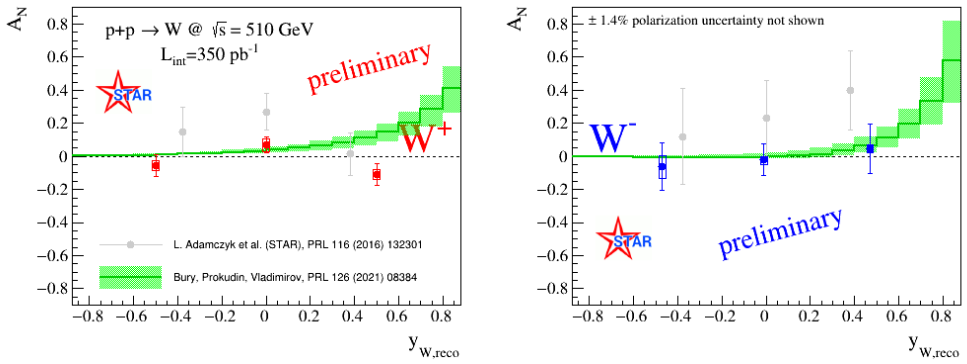

Figure 46: Preliminary results for the transverse single-spin asymmetries of $W^{\pm}$ bosons as a function of their rapidity for Run-17 compared to the Run-11 results [150]. The green lines and boxes are theoretical predictions from [149] using data from SIDIS, pion-induced polarized Drell-Yan, and $W^{+/-}/Z^0$-boson A_N STAR measurements from Run-11.

2.1.3 Transversity, Collins Function and Interference Fragmentation Function

A complete picture of nucleon spin structure at leading twist must include contributions from the unpolarized and helicity distributions, as well as those involving transverse polarization, such as the transversity distribution [151–153]. The transversity distribution can be interpreted as the net transverse polarization of quarks within a transversely polarized proton. The difference between the helicity and transversity distributions for quarks and antiquarks provides a direct, x-dependent connection to nonzero orbital angular momentum components in the wave function of the proton [154]. Recently, the first lattice QCD calculation of the transversity distribution has been performed [155]. In addition, the measurement of transversity has received substantial interest as a means to access the tensor charge of the nucleon, defined as the integral over the valence quark transversity: $\delta q^a = \int_0^1 [\delta q^a(x) - \delta \overline{q}^a(x)]\, dx$ [152, 156]. Measuring the tensor charge is very important for several reasons. First, it is an essential and fundamental quantity to our understanding of the spin structure of the nucleon. Also, the tensor charge can be calculated on the lattice with comparatively high precision, due to the valence nature of transversity, and hence is one of the few quantities that allow us to compare experimental results on the spin structure of the nucleon directly to *ab initio* QCD calculations. Finally, the tensor charge describes the sensitivity of observables in low-energy hadronic reactions to beyond the standard model physics processes with tensor couplings to hadrons. Examples are experiments with ultra-cold neutrons and nuclei.

Transversity is difficult to access due to its chiral-odd nature, requiring the coupling of

this distribution to another chiral-odd distribution. Semi-inclusive deep-inelastic scattering (SIDIS) experiments have successfully probed transversity through two channels: asymmetric distributions of single pions, convoluting the TMD transversity distribution with the TMD Collins fragmentation function, and azimuthally asymmetric distributions of di-hadrons, coupling transversity to the so-called "interference fragmentation function" (IFF) in the framework of collinear factorization. Yet in spite of a wealth of lepton-scattering data, the kinematic reach of existing SIDIS experiments limits the precision with which the proton's transversity can be extracted, as the range of Bjorken-x values that can be accessed does not extend above $x \sim 0.3$.

In hadronic collisions, the k_T integrated quark transversity distribution may be accessed mainly via two channels. The first is the single spin asymmetry of the azimuthal distribution of hadrons in high energy jets [117]. In the jet+hadron channel, the collinear transversity distribution couples to the TMD Collins function [117,118]. This makes pp collisions a more direct probe of the Collins fragmentation function than Collins asymmetries in SIDIS [117], where a convolution with the TMD transversity distribution enters. This also makes the Collins asymmetry in pp collisions an ideal tool to explore the fundamental QCD questions of TMD factorization, universality, and evolution. The second channel is the single spin asymmetry of pion pairs, where transversity couples to the collinear interference fragmentation function [157]. STAR mid-rapidity IFF data [158] have been included in the first extraction of transversity from SIDIS and proton-proton IFF asymmetries [159]. In addition, transverse spin transfer, D_{TT}, of Λ hyperons in pp collisions is also expected to be able to provide sensitivity for the strange quark transversity through the polarized fragmentation functions. The strange quark transversity is not constrained at all currently. The first D_{TT} measurement of Λ and $\bar{\Lambda}$ hyperons at $\sqrt{s} = 200$ GeV has been performed with the Run-12 pp dataset [121], and current results didn't indicate a sizable spin transfer yet. The iTPC upgrade will help to reach near-forward pseudo-rapidity $\eta<1.5$ for the spin transfer measurements.

The universality of TMD PDFs and fragmentation functions in pp collisions has been an open question. General arguments [160,161] have shown that factorization can be violated in hadron-hadron collisions for TMD PDFs like the Sivers function, though very recent calculations indicate the violations might be quite small [162,163]. In contrast, while there is no general proof that the Collins effect in pp collisions is universal to all orders, explicit calculations [117,118,164,165] have shown that diagrams like those that violate factorization of the Sivers function make no contribution to the Collins effect at the one- or two-gluon exchange level, thereby preserving its universality at least to that level.

Comparisons of the transversity distributions extracted from the Collins and IFF channels will allow STAR to study the size and nature of any factorization breaking effects for TMD observables in hadronic collisions. Likewise, comparisons with the transversity, Collins and IFF distributions extracted from SIDIS collisions will shed light on universality and constrain evolution effects. The measurement of evolution effects in TMD distributions is particularly important because, unlike the collinear case, TMD evolution contains a non-perturbative component that cannot be calculated directly. Measurements at $\sqrt{s}$ of 200 and 510 GeV will

provide additional experimental constraints on evolution effects and provide insights into the size and nature of TMD observables at the future Electron-Ion Collider.

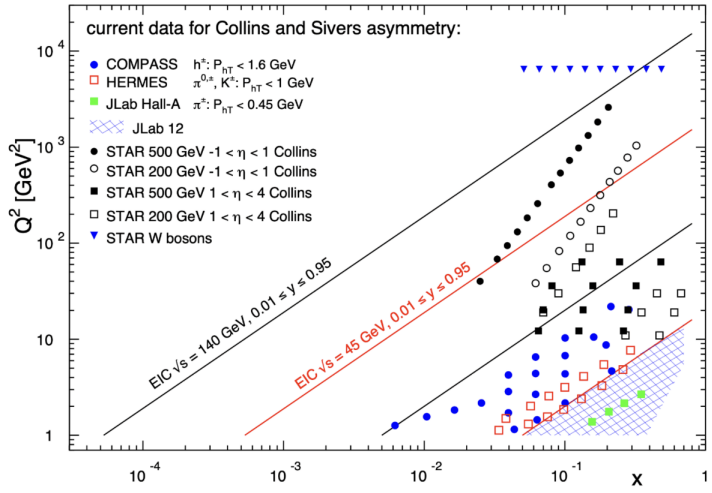

Figure 47: $x - Q^2$ coverage of RHIC measurements compared to existing Collins and Sivers effect measurements in SIDIS and the future coverage of the EIC.

Extending measurements of di-hadron and Collins asymmetries to the forward direction during Run-22 will allow access to transversity in the region $x > 0.3$. This valence quark region is not currently probed by any experiments and is essential for the determination of the tensor charge, which receives 70% of its contributions from $0.1 < x < 1.0$. In addition, probing transversity in pp collisions also provides better access to the d-quark transversity than is available in SIDIS, due to the fact that there is no charge weighting in the hard scattering QCD $2 \to 2$ process in pp collisions. This is a fundamental advantage of pp collisions, as any SIDIS measurement of the d-quark transversity has to be on a bound system, *e.g.* He-3, which ultimately requires nuclear corrections to extract distributions. The high scale we can reach in 510 GeV collisions at RHIC has allowed STAR [166] to demonstrate, for the first time, that previous SIDIS measurements at low scales are in fact accessing the nucleon at leading twist. Figure 47 shows the $x - Q^2$ coverage spanned by the RHIC measurements compared to the future EIC, JLab-12, and the current SIDIS world data.

Another fundamental advantage of pp collisions is the ability to access gluons directly. While gluons cannot be transversely polarized in a transversely polarized spin 1/2 hadron, they can be linearly polarized. Similarly, there exists an equivalent of the Collins fragmentation function for the fragmentation of linearly polarized gluons into unpolarized hadrons [167]. The linear polarization of gluons is a largely unexplored phenomenon, but it has been a focus of recent theoretical work, in particular due to the relevance of linearly polarized gluons in unpolarized hadrons for the p_T spectrum of the Higgs boson measured at the LHC. Polarized proton collisions with $\sqrt{s} = 510$ GeV at RHIC, in particular for asymmetric parton scattering if jets are detected in the backward direction, are an ideal place to study the

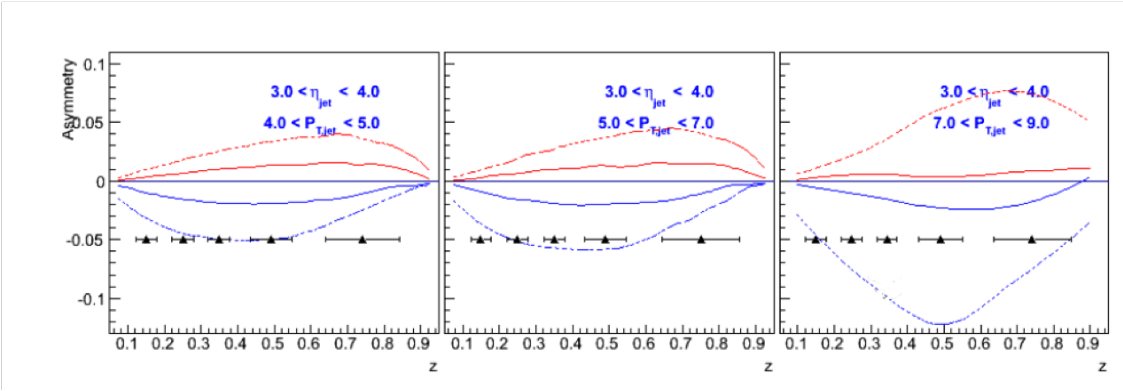

Figure 48: Expected h^- Collins asymmetry uncertainties at $3 < \eta < 4$ (black points) from a sampled luminosity of 350 pb^{-1} at $\sqrt{s} = 510$ GeV, compared to positive (red) and negative (blue) pion asymmetries based on the Torino extraction (full lines) and the Soffer bound (dashed lines) as a function of hadron z for bins in jet p_T. Most uncertainties are smaller than the height of the triangles.

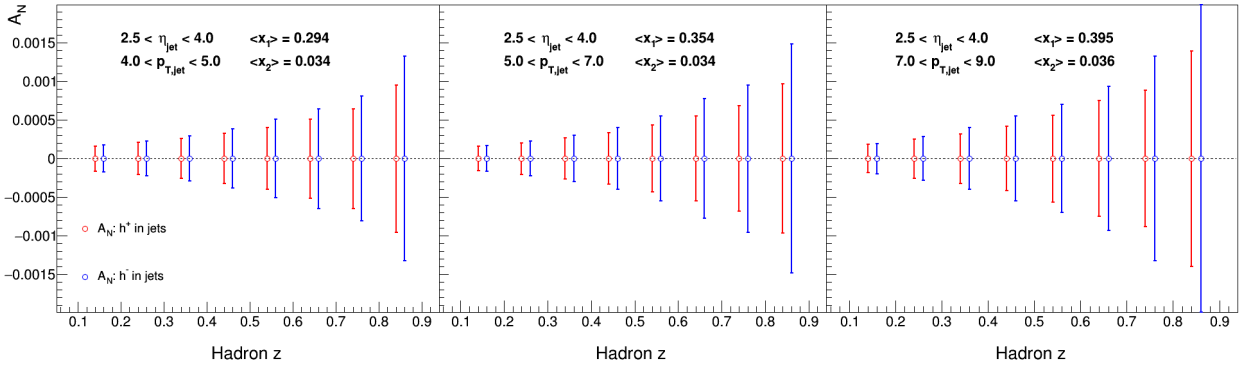

Figure 49: Expected $h^{\pm}$ Collins asymmetry uncertainties at $2.5 < \eta < 4$ for the three momentum bins shown in Fig. 48, based on a sampled luminosity of 350 pb^{-1} at $\sqrt{s} = 510$ GeV.

linearly polarized gluon distribution in polarized protons. (Note that the distributions of linearly polarized gluons inside an unpolarized and a polarized proton provide independent information). A first measurement of the "Collins-like" effect for linearly polarized gluons has been done by STAR with data from Run-11 [166], providing constraints on this function for the first time.

Figure 48 shows projected h^- Collins asymmetry uncertainties along with $\pi^+/-$ Collins asymmetries from theory calculations at 510 GeV with the Forward Upgrade during Run-22. Figure 49 shows STAR's expected $h^{\pm}$ Collins asymmetry corresponding to the kinematic regions shown in Fig. 48, but with a zoomed in vertical scale. As indicated on the figure, jets with $2.5 < \eta < 4$ and $4 < p_T < 9$ GeV/c will explore transversity in the important region $0.3 < x < 0.5$ that has not yet been probed in SIDIS. A realistic momentum smearing of final state hadrons as well as jets in this rapidity range was assumed and dilutions due to

beam remnants (which become substantial at rapidities close to the beam) and underlying event contributions have been taken into account. For the expected p_T measurement resolution and charged-hadrons separation with the forward upgrade refer to Fig. 38 and Fig. 39, respectively. As no dedicated particle identification at forward rapidities will be available for these measurements, only charged hadrons were considered. This mostly reduces the expected asymmetries due to dilution by protons (10-14%) and a moderate amount of kaons (12-13%). As anti-protons are suppressed compared to protons in the beam remnants, especially the negative hadrons can be considered a good proxy for negative pions ($\sim$78% purity according to PYTHIA6). Given their sensitivity to the down quark transversity via favored fragmentation, they are particularly important since SIDIS measurements, due to their electromagnetic interaction, are naturally dominated by up-quarks. We have estimated our statistical uncertainties based on an accumulated luminosity of 350 pb^{-1}, which leaves nearly invisible uncertainties after smearing. These expected uncertainties are compared to the asymmetries obtained from the transversity extractions based on SIDIS and Belle data [168] as well as from using the Soffer positivity bound for the transversity PDF [169]. More recent global fits have slightly different central up and down quark transversity distributions. But due to the lack of any SIDIS data for $x > 0.3$, the upper uncertainties are compatible with the Soffer bounds. This high-x coverage will give important insights into the tensor charge, which is essential to understand the nucleon structure at leading twist.

Although the studies presented here are for the Collins asymmetries, the resulting statistical uncertainties will be similar for other measurements using azimuthal correlations of hadrons in jets. One important example is the measurement of "Collins-like" asymmetries to access the distribution of linearly polarized gluons. As described earlier, the best kinematic region to access this distribution is at backward angles with respect to the polarized proton and at small jet p_T. Figure 48 shows that a high precision measurement of the distribution of linearly polarized gluons down to $x \sim 0.005$ will be performed concurrently.

It is important to recognize that these hadron-in-jet measurements with the STAR Forward Upgrade will provide very valuable experience detecting jets close to beam rapidity that will inform the planning for future jet measurements in similar kinematics at the EIC.

While the STAR Forward Upgrade will provide sensitivity to transversity to the highest x, concurrent mid-rapidity measurements (see Fig. 47) will provide the most precise information as a function of x, z, j_T, and Q^2 to probe questions of TMD factorization, universality, and evolution. The left panel of Fig. 50 shows published STAR measurements of the Collins asymmetry vs. pion z in 500 GeV Run-11 pp collisions [166]. The results, which represented the first ever observation of the Collins effect in pp collisions, are consistent at the 2σ level with model predictions, with and without TMD evolution, derived from fits to e^+e^- and SIDIS data [117,170]. However, greater precision is clearly necessary for a detailed universality test, as well as to set the stage for the EIC.

STAR Run-17 sampled about 14 times the luminosity that we recorded in Run-11. In Run-22, we propose to record another dataset equivalent to 16 times the sampled luminosity from Run-11. Furthermore, during Run-22 the iTPC will improve the dE/dx particle identification compared to the previous years. Studies using the dE/dx distributions seen in

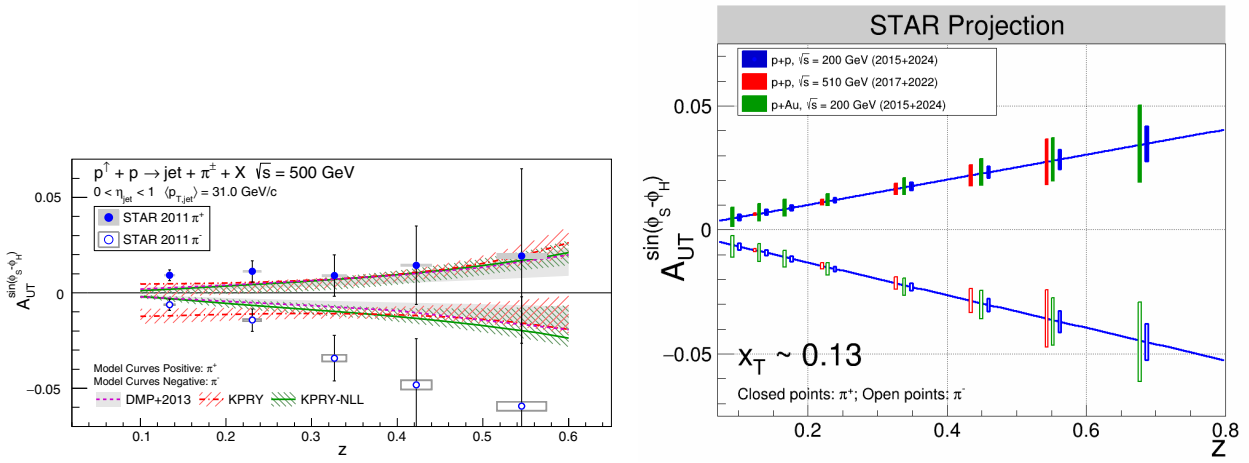

Figure 50: The left panel shows STAR measurements of the Collins asymmetry vs. pion z in 500 GeV pp collisions from Run-11, compared to several model calculations. See [166] for details. The right panel shows projected statistical uncertainties for STAR Collins asymmetry measurements at $0 < \eta < 0.9$ in pp at $\sqrt{s} = 200$ and 510 GeV and p–Au at $\sqrt{s_{\rm NN}} = 200$ GeV. The points have arbitrarily been drawn on the solid lines, which represent simple linear fits to the STAR preliminary 200 GeV pp Collins asymmetry measurements from 2015. (Note that only one bin is shown spanning $0.1 < z < 0.2$ for 510 GeV pp whereas three bins are shown covering the same z range for the 200 GeV measurements).

our 200 GeV pp data from Run-15 and the actual dE/dx resolution improvements that have been achieved during BES-II indicate the iTPC will yield a $20-25\%$ increase in the effective figure-of-merit for pions with $|\eta| < 0.9$. The right-hand panel of Fig. 50 shows the projected STAR statistical uncertainties for the Collins asymmetry at $0 < \eta < 0.9$ in 510 GeV pp collisions once the Run-17 and Run-22 datasets are fully analyzed. It's also important to recognize that the iTPC will also enable STAR to measure the Collins asymmetry over the region $0.9 < \eta < 1.3$ during Run-22, in addition to the projections that are shown in Fig. 50.

The statistical precision of transversity measured in 510 GeV pp collisions using IFF asymmetries are expected to be comparable to the statistical improvements from Run-11 [158] to Run-17 + Run-22 shown for the Collins effect data in Fig. 50.

2.1.4 Probing Unpolarized Distributions in the Proton

STAR can also provide important information related to unploarized quark distributions and constrain unpolarized TMD PDFs by measuring the spin integrated W and Z cross sections. As discussed in Sec. 1.3, the W^+/W^- cross-section ratio is sensitive to the $\bar{d}/\bar{u}$ quark distribution, providing complimentary information to Drell-Yan experiments [124,125]. Recent results from STAR [123] have been shown to not only have an impact on constraining the $\bar{d}/\bar{u}$ quark distribution, but other quark distributions as well [171]. Figure 51 shows the uncertainty on PDF distributions where STAR data was included in the global analysis relative to the uncertainties were it was not. This global analysis shows about 30% relative

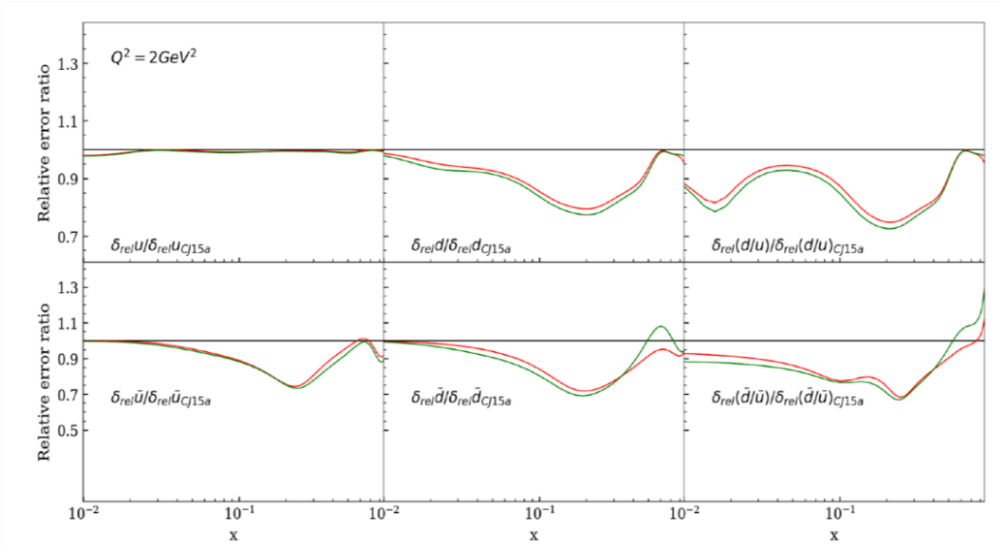

Figure 51: CJ collaboration global analysis comparing the uncertainties on unpolarized PDF distributions where STAR data was included in the analysis relative to the uncertainties where it was not [171].

uncertainty reduction in the region $0.2 < x < 0.3$. An additional 16 weeks of running during Run-22 would yield similar statistics as was achieved in Run-17. Combining our already measured datasets with what would be collected during Run-22 would provide a precision measurement of W^+/W^- consisting of about 1000 pb^{-1}. Furthermore, STAR's Z differential cross section as a function of the boson p_T can serve as input to constrain unpolarized TMD PDFs. Figure 52 shows preliminary results for the Run-11, 12, 13, and 17 combined datasets.

2.1.5 Spatial Imaging of the Nucleon

Diffractive and Ultra Peripheral processes at RHIC are an essential tool that can elucidate the origin of single-spin asymmetries in polarized pp collisions and access the orbital motion of partons inside the proton. Also at the EIC diffractive processes have been identified as the golden tool to study several key physics programs

- What is the spatial distribution of quarks and gluons inside the nucleon?
- What is the role of orbital motion of sea quarks and gluons in building the nucleon spin?
- Saturation in nuclei.

Diffraction: The essential characteristics of diffraction in QCD are summarized by two facts:

- The event is still called diffractive if there is a rapidity gap. Due to the presence of a rapidity gap, the diffractive cross-section can be thought of as arising from an

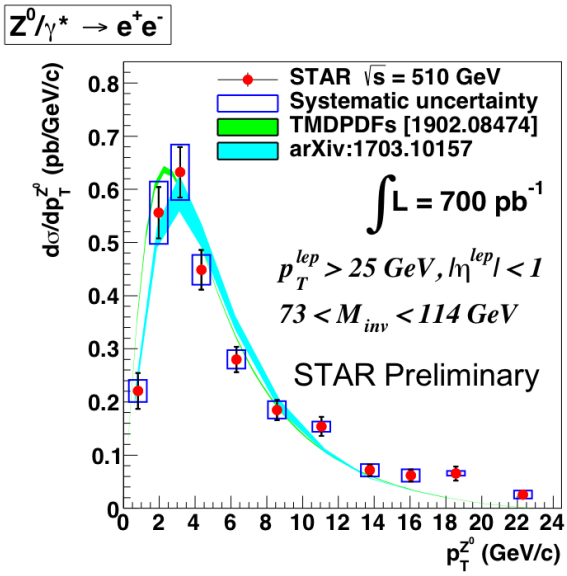

Figure 52: Z differential cross section as a function of boson p_{T} for combined Run-11, 12, 13, and 17 datasets.

exchange of several partons with zero net color between the target and the projectile. In high-energy scattering, which is dominated by gluons, this color neutral exchange (at the lowest order) consists of at least two exchanged gluons. This color singlet exchange has historically been called the pomeron, which had a specific interpretation in Regge theory. A crucial question in diffraction is the nature of the color neutral exchange between the protons. This interaction probes, in a novel fashion, the nature of confining interactions within hadrons.

- The proton/nuclear target is not always an opaque "black disk" obstacle of geometric optics. A projectile that interacts more weakly due to color-screening and asymptotic freedom is likely to produce a different diffractive pattern from a larger, more strongly interacting, projectile.

HERA discovered that 15% of the total ep cross-section is given by diffractive events (for details see [172] and references therein), basically independent of kinematics. At RHIC center-of-mass energies diffractive scattering events constitute $\sim$ 25% of the total inelastic pp cross-section [173]. As described above diffraction is defined as an interaction that is mediated by the exchange of the quantum numbers of the vacuum, as shown in Fig. 53. Experimentally these events can be characterized by the detection of a very forward scattered proton and jet (singly diffractive) or two jets (doubly diffractive) separated by a large rapidity gap. Central diffraction, where two protons, separated by rapidity gaps, are reconstructed along with a jet at mid-rapidity, is also present, but suppressed compared to singly and doubly diffractive events. To date, there have been no data in pp collisions studying spin effects in diffractive events at high $\sqrt{s}$ apart from measuring single spin asymmetries in elastic pp scattering [174–177].

A discovery of large transverse single spin asymmetries in diffractive processes would open a new avenue to study the properties and understand the nature of the diffractive

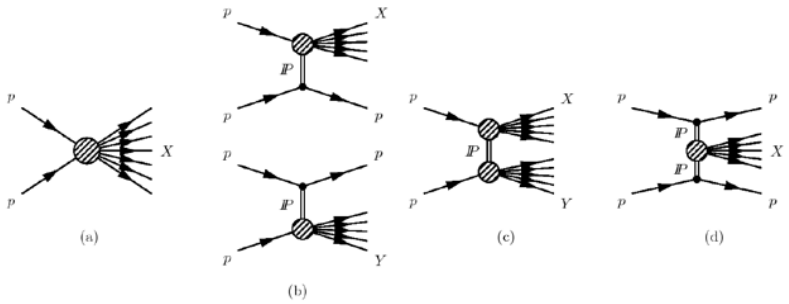

Figure 53: Schematic diagrams of (a) non-diffractive, $pp \to X$, (b) singly diffractive, $pp \to Xp$ or $pp \to pY$, (c) doubly diffractive, $pp \to XY$, and (d) centrally diffracted, $pp \to pXp$, events.

exchange in pp collisions. One of the primary observables of STAR to access transverse spin phenomena has been forward neutral pion production in transversely polarized pp collisions at both $\sqrt{s} = 200$ and 500 GeV. Figure 30 shows the isolated and non-isolated transverse single spin asymmetries A_N for π^0 detected in the STAR FMS at $2.5 < \eta < 4.0$ as a function of x_F, where the neutral pion A_N is larger for isolated pion than when it is accompanied by additional nearby photons [115]. A similar observation was seen in STAR's 200 GeV p+A results [114].

All these observations might indicate that the underlying subprocess causing a significant fraction of the large transverse single spin asymmetries in the forward direction are not of $2 \to 2$ parton scattering processes but of diffractive nature. PYTHIA-8 [178] was used to evaluate the fraction of hard diffractive events [179] contributing to the inclusive π^0 cross-section at forward rapidities. Figure 54 shows the hard diffractive cross-section for π^0 production at $\sqrt{s} = 200$ GeV and 500 GeV for a rapidity range of $2.5 < \eta < 4.0$ with and without applying several experimental cuts, i.e. the proton in the STAR Roman Pot acceptance. While the information from Roman Pots will not be available in Run-22, the diffractive processes will be studied by requiring the rapidity gaps. The prediction from this PYTHIA-8 simulation is that 20% of the total inclusive cross-section at forward rapidities is of diffractive nature. This result is in agreement with measurements done over a wide range of $\sqrt{s}$ (see Fig. 12 in Ref. [172]).

In 2015 STAR collected data in $\sqrt{s} = 200$ GeV transversely polarized pp collisions, where an isolated π^0 is detected in the forward pseudorapidity range along with the forward-going proton, which scatters with a near-beam forward pseudorapidity into Roman Pot detectors. The sum of the π^0 and the scattered proton energies is consistent with the incident proton energy of 100 GeV, indicating that no further particles are produced in this direction. Correlations between the π^0 and scattered proton have been presented [180], along with single-spin asymmetries which depend on the azimuthal angles of both the pion and the proton. This is the first time that spin asymmetries have been explored for this process, and a model to explain their azimuthal dependence is needed.

The STAR Forward Upgrade will be a game changer for diffractive measurements at RHIC. It will allow the reconstruction of full jets both at $\sqrt{s} = 200$ GeV and 510 GeV. Measuring spin asymmetries for diffractive events as function of $\sqrt{s}$ might reveal surprises, which will inspire new physics opportunities for EIC, i.e SSA in polarized e+A collisions.

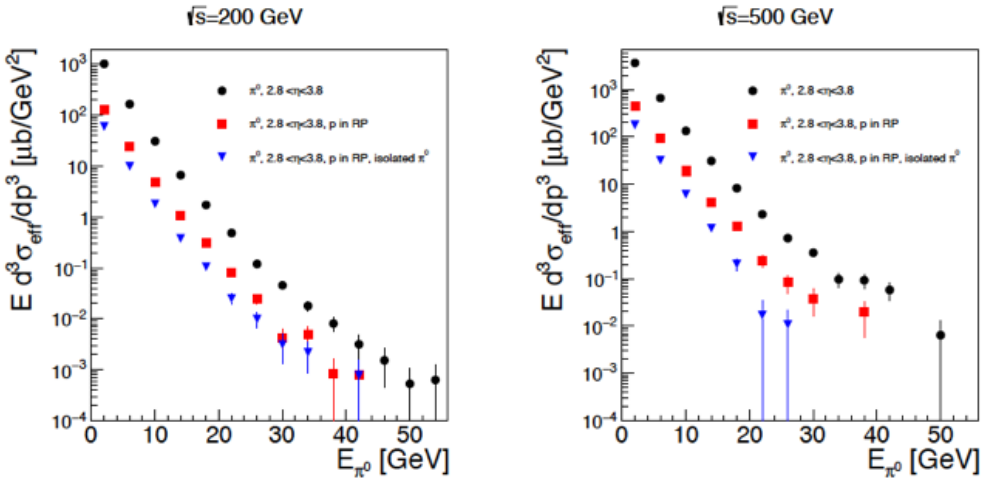

Figure 54: Estimate of the cross-section for hard diffractive processes at $\sqrt{s} = 200$ GeV and 500 GeV using PYTHIA 8. The different points reflect different analysis cuts applied: π^0 in rapidity $2.8 < \eta < 3.8$ (black), one proton is required to be detected in the STAR Roman Pot acceptance (red) and an isolation cut of 35 mrad around the π^0 (blue).

2.2 Run-24 Request for Polarized pp and p+A Collisions at 200 GeV

Run-24, with polarized pp and p+Au collisions at $\sqrt{s_{\rm NN}} = 200$ GeV, will likely be the last RHIC spin/cold QCD run. This run will provide STAR with the unique opportunity to investigate these 200 GeV collision systems with the Forward Upgrade providing full tracking and calorimetry coverage over the region $2.5 < \eta < 4$ and the iTPC providing enhanced particle identification and expanded pseudorapidity coverage at mid-rapidity. These powerful detection capabilities, when combined with substantially increased sampled luminosity compared to Run-15, will enable critical measurements to probe universality and factorization in transverse spin phenomena and nuclear PDFs and fragmentation functions, as well as low-x non-linear gluon dynamics characteristic of the onset of saturation. This will provide unique insights into fundamental QCD questions in the near term, and essential baseline information for precision universality tests when combined with measurements from the EIC in the future.

We therefore request at least 11 weeks of polarized pp data-taking at $\sqrt{s} = 200$ GeV and 11 weeks of polarized p+Au data-taking at $\sqrt{s_{\rm NN}} = 200$ GeV during Run-24. Effectively, we request approximately equal nucleon-nucleon luminosities for pp and p+Au which is essential to optimize several critical measurements that require comparisons of the same observable in (polarized or unpolarized) pp and p+Au collisions described in the following sections.

All of the running will involve vertically polarized protons. Based on recent C-AD guidance, we expect to sample at least 235 pb^{-1} of pp collisions and 1.3 pb^{-1} of p+Au collisions. These totals represent 4.5 times the luminosity that STAR sampled during transversely polarized pp collisions in Run-15 and 3 times the luminosity that STAR sampled during transversely polarized p+Au collisions in Run-15.

In addition, collection of this high statistics p+Au dataset enables the unique opportunity

to search for some recently predicted novel fluid configurations, such as toroidal vortex structures [181].

2.2.1 Spin Physics with Polarized pp and p+A Collisions at 200 GeV

Section 1.3 described several very mature STAR analyses and recent publications that are based on the transversely polarized pp and p+Au datasets that we recorded during 2015. Run-24 will enable STAR to probe these questions with a far more capable detector and much larger datasets than were available during Run-15. With the overlapping kinematic coverage for both pp and p+A data, this program is critical to set the stage for related future measurements at the EIC. Here we give brief descriptions of several of the opportunities presented by Run-24.

Forward Transverse Spin Asymmetries

Section 1.3.3 presents some results that STAR recently published in a pair of papers discussing forward transverse spin asymmetries in pp p+Al and p+Au collisions measured with the Forward Meson Spectrometer (FMS). One paper focuses on the dynamics that underlie the large asymmetries that have been seen to date. Figure 30 shows that A_N for forward π^0 production in pp collisions at 200 and 500 GeV is substantially larger when the π^0 is isolated than when it is accompanied by additional nearby photons. The same analysis also shows that A_N for inclusive electromagnetic jets (EM-jets) in 200 and 500 GeV collisions is substantially larger than that for EM-jets that contain three or more photons and that the Collins asymmetry for π^0 in EM-jets is very small. The other paper focuses on the nuclear dependence of A_N for π^0 in $\sqrt{s_{NN}} = 200$ GeV collisions. It presents a detailed mapping of A_N as functions of x_F and p_T for all three collision systems. Figure 29 shows the observed nuclear dependence is very weak. The same analysis shows that isolated *vs.* non-isolated π^0 behave similarly in p+Al and p+Au collisions as they do in pp collisions.

These two papers provide a wealth of new data to inform the ongoing discussion regarding the origin of the large inclusive hadron transverse spin asymmetries that have been seen in pp collisions at forward rapidity over a very broad range of collision energies. Nonetheless, the STAR Forward Upgrade will be a game changer for such investigations. It will enable measurements of A_N for $h^{+/-}$, in addition to π^0. It will enable isolation criteria to be applied to the $h^{+/-}$ and π^0 that account for nearby charged, as well as neutral, fragments. It will enable full jet asymmetry and Collins effect measurements, again for $h^{+/-}$ in addition to π^0, rather than just EM-jet measurements. It will permit all of these measurements to be performed at both 510 GeV, as discussed in Sects. 2.1.1 and 2.1.2, and at 200 GeV. In addition, all of these observables can be tagged by forward protons detected in the STAR Roman pots or by requiring rapidity gaps to identify the diffractive component of the observed transverse spin asymmetries. For pp there will be considerable overlap between the kinematics at the two energies, but the 510 GeV measurements will access higher p_T, while the 200 GeV measurements will access higher x_F. Moreover, at 200 GeV we will also perform the full suite of measurements in p+Au to identify any nuclear effects. Figure 37 shows one

set of predictions for the inclusive $\pi^{+/-}$ A_N in 200 and 500 GeV pp collisions, while Fig. 43 shows the predictions for the one hadron-in-jet measurement that will help to isolate the Sivers effect contribution at 200 GeV.

Moreover, it is important to stress that the 200 GeV running with the Forward Upgrade will give the unique opportunity for jet reconstruction studies at the exact same rapidity that is critical for the future EIC. The data will provide an extraordinary possibility to exercise new reconstruction techniques incorporating AI/ML methods and train the next generation of scientists.

Sivers Effect

Section 2.1.2 describe the first ever observation of the Sivers effect in dijet production. Such measurements are crucial to explore questions regarding factorization of the Sivers function in dijet hadroproduction [160–163]. Those results were derived from 200 GeV transverse spin data that STAR recorded in Run-12 and Run-15 (total sampled luminosity ~ 75 pb^{-1} for the two years combined). Nonetheless, the uncertainties remain large, as can be seen in Fig. 43. Run-24 data will reduce the uncertainties for $|\eta_3 + \eta_4| < 1$ by a factor of two. The increased acceptance from the iTPC will reduce the uncertainties at $|\eta_3 + \eta_4| \approx 2.5$ by a much larger factor, while the Forward Upgrade will enable the measurements to be extended to even larger values of $|\eta_3 + \eta_4|$. When combined with the 510 GeV data from Run-17 and Run-22 (see Sect. 2.1.2), the results will provide a detailed mapping *vs.* x for comparison to results for Sivers functions extracted from SIDIS, Drell-Yan, and vector boson production.

Transversity and Related Quantities

As described in Sect. 2.1.3, measurements of the Collins asymmetry and IFF in pp collisions at RHIC probe fundamental questions regarding TMD factorization, universality, and evolution. Data from 200 GeV pp collisions will play an essential role toward answering these questions. Figure 47 shows that 200 GeV pp collisions interpolate between the coverage that we will achieve during Run-22 at high-x with the Forward Upgrade and at low-x with the STAR mid-rapidity detectors. They will also provide a significant overlapping region of x coverage, but at Q^2 values that differ by a factor of 6. This will provide valuable information about evolution effects, as well as cross-checks between the two measurements. Furthermore, for most of the overlapping x region, 200 GeV pp collisions will also provide the greatest statistical precision (see for example Fig. 50), thereby establishing the most precise benchmark for future comparisons to ep data from the EIC.

The high statistical precision of the Run-24 data will enable detailed multi-dimensional binning for the Collins asymmetry results. This is particularly valuable because, as emphasized in [117, 118], hadron-in-jet measurements in pp collisions provide a direct probe of the Collins fragmentation function since they combine it with the *collinear* transversity distribution. In general, the observed asymmetries are functions of jet (p_T, η), hadron (z, j_T), and Q^2. However, the physics interpretations associated with these variables separate, with p_T

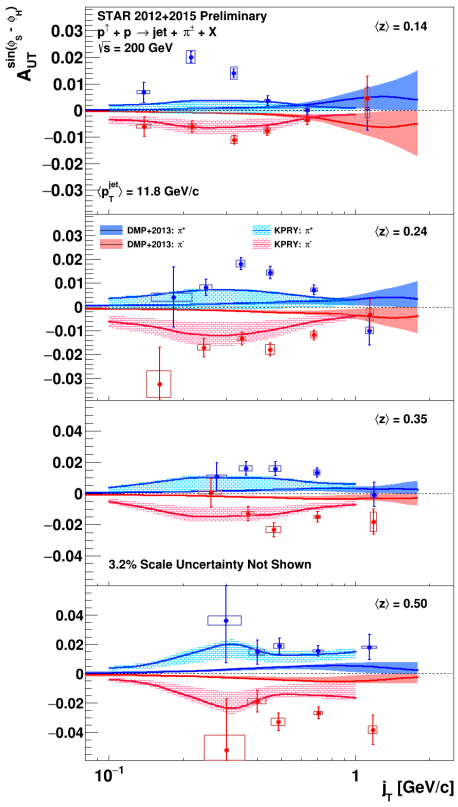

Figure 55: Preliminary Run-12 and Run-15 results for the Collins asymmetry for charged pions in 200 GeV pp collisions as a function of z and j_T, integrated over $9.9 < p_T < 31.6$ GeV/c and $0 < \eta < 0.9$. Theoretical evaluations from [116] with their uncertainties are presented for π^+ (blue) and π^- (red).

and η primarily coupling to the incident quark x and the polarization transfer in the hard scattering, while z and j_T characterize the fragmentation kinematics. Thus, A_{UT} *vs.* p_T, as shown in Fig. 27 for the preliminary Run-12 and Run-15 analysis, provides information about the transversity distribution. In parallel, the (z, j_T) dependence, integrated over a wide range of jet p_T, as shown in Fig. 55 for the preliminary Run-12 and Run-15 results, provides a detailed look at the Collins fragmentation function. Note that STAR finds the maximum value of A_{UT} shift to higher j_T as z increases which is not seen in the current theory evaluations [116]. The statistical uncertainties in Figs. 27 and 55 will be reduced by a factor of about 2.5 when Run-12, Run-15 and Run-24 data are combined together.

The Run-15 Collins analysis has also, for the first time, measured the Collins effect for charged kaons in pp collisions, as shown in Fig. 56. The asymmetries for K^+, which like π^+ have a contribution from favored fragmentation of u quarks, are about 1.5-sigma larger than those for π^+ in Fig. 27, while those for K^-, which can only come from unfavored fragmentation, are consistent with zero at the 1-sigma level. These trends are similar to those found in SIDIS by HERMES [182] and COMPASS [183], and provide additional insight into the Collins fragmentation function. This same analysis with Run-24 data will yield statistical uncertainties a factor of 3 smaller than those in Fig. 56. This is a much greater improvement than would be expected from the increase in sampled luminosity thanks to the improved dE/dx resolution provided by the iTPC. In addition, the iTPC will enable the measurements in Figs. 27, 55, and 56 to be extended to an additional higher η bin ($0.9 < \eta < 1.3$).

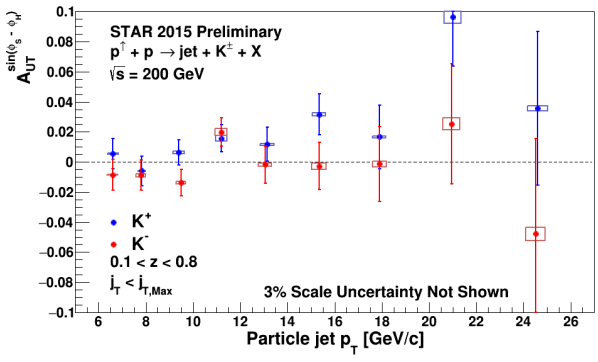

Figure 56: Preliminary Run-15 results for the $K^{+/-}$ Collins asymmetries *vs.* jet p_T for $0 < \eta < 0.9$ in 200 GeV pp collisions.

RHIC has the unique opportunity to extend the Collins effect measurements to nuclei. This will provide an alternative look at the universality of the Collins effect in hadron-production by dramatically increasing the color flow options of the sort that have been predicted to break factorization for TMD PDFs like the Sivers effect [160, 161]. This will also explore the spin dependence of the hadronization process in cold nuclear matter. STAR collected a proof-of-principle dataset during the 2015 p+Au run that is currently under analysis. Those data will provide a first estimate of medium-induced effects. However, the small nuclear effects seen by STAR for forward inclusive π^0 A_N (see Fig. 29) indicate that greater precision will likely be needed. Figure 50 shows the projected Run-15 and Run-24 statistical uncertainties for the p+Au Collins asymmetry measurement at $\sqrt{s_{\rm NN}} = 200$ GeV, compared to those for the pp at the same energy.

Ultra-peripheral Collisions

The formalism of generalized parton distributions (GPDs) provides a theoretical framework which addresses some of the above questions [184–187]. Constraints on GPDs have mainly been provided by exclusive reactions in DIS, e.g. deeply virtual Compton scattering. RHIC, with its unique capability to collide transversely polarized protons at high energies, has the opportunity to measure A_N for exclusive J/Ψ production in ultra-peripheral collisions (UPCs) [188]. In such a UPC process, a photon emitted by the opposing beam particle (p or A) collides with the polarized proton. The measurement is at a fixed $Q^2 \sim M^2_{J/\psi} \approx 10$ GeV^2 and $10^{-4} < x < 10^{-1}$. A nonzero asymmetry would be the first signature of a nonzero GPD E_g for gluons, which is sensitive to spin-orbit correlations and is intimately connected with the orbital angular momentum carried by partons in the nucleon and thus with the proton spin puzzle.

The Run-15 p$^\uparrow$–Au data allowed a proof-of-principle of such a measurement. A trigger requiring back-to-back energy deposits in the Barrel Electromagnetic Calorimeter selected J/Ψ candidates. The e^+e^- mass distribution after selection cuts is shown in the left of Fig. 57, and the pair p_T distribution of the J/ψ mass peak is shown on the right of that figure. The data are well described by the STARlight model [189] (colored histograms in the figure), including the dominant γ+p$\uparrow\to J/\psi$ signal process and the γ+Au$\to J/\psi$ and $\gamma+\gamma\to e^+e^-$

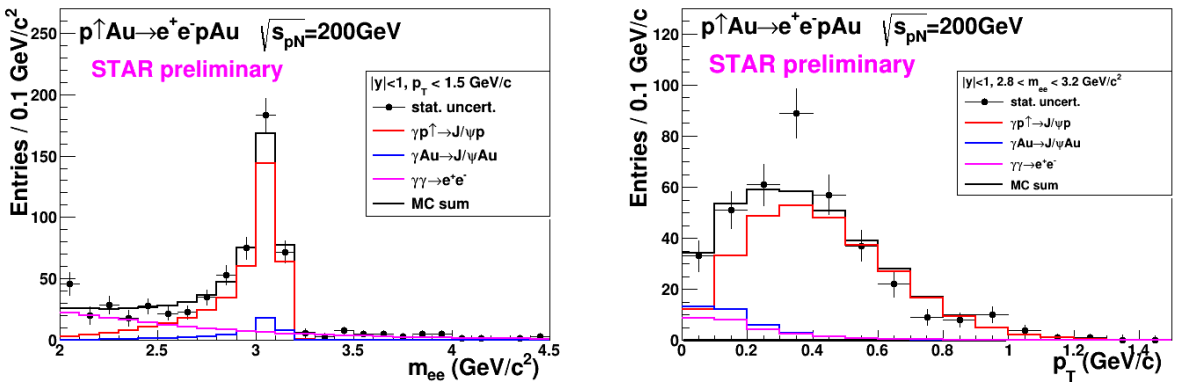

Figure 57: Mass distribution of selected e^+e^- pairs (left), and p_T distribution of the J/ψ mass peak (right). The colored histograms are the indicated processes modelled by STARlight and the sum fit to the data.

background processes. The left of Fig. 58 shows the STAR preliminary measurement (solid circle marker) of the transverse asymmetry A_N^γ for the J/ψ signal, which have a mean photon-proton center-of-mass energy $W_{\gamma p} \approx 24$ GeV. The result is consistent with zero. Also shown is a prediction based on a parameterization of E_g [190]; the present data provide no discrimination of this prediction.

This measurement can be greatly improved with a high statistics transversely polarized p↑–Au Run-24. The integrated luminosity for the Run-15 measurement was 140 nb^{-1}; the Run-24 will provide 1.3 pb^{-1}, allowing a sizeable reduction of statistical uncertainty in the same $W_{\gamma p}$ range. However, the Forward Upgrade and iTPC will also provide a significant extension of the $W_{\gamma p}$ range of the measurement. The right panel of Fig. 58 shows the accepted cross section for γ+p$^\uparrow \to J/\psi$ for various detector pseudorapidity ranges. With the full detector, the sensitive cross section is a factor of five times the central barrel alone and the expected asymmetry is substantially larger. The projected statistical uncertainty on A_N^γ as shown in the left of Fig. 58 (open square marker) will be ≈ 0.02, offering a powerful test of a non-vanishing E_g. Also, the accepted region has a lower mean $W_{\gamma p} \approx 14$ GeV. Predictions based on E_g parameterizations such as shown in the figure have a larger asymmetry at lower $W_{\gamma p}$, with increased possibility of a nonzero result. Alternatively, the increased statistics will allow a measurement of A_N^γ in bins of $W_{\gamma p}$.

The UPC cross section scales with Z^2 of the the nucleus emitting the photon; for protons this is $1/79^2$ relative to Au nuclei, which makes analogous measurements in pp collisions extremely luminosity-hungry. Therefore, the p+Au run is important for this measurement.

2.2.2 Physics Opportunities with Unpolarized proton-Nucleus Collisions

Our quest to understand QCD processes in Cold Nuclear Matter (CNM) centers on the following fundamental questions:

- Can we experimentally find evidence of a novel universal regime of non-linear QCD

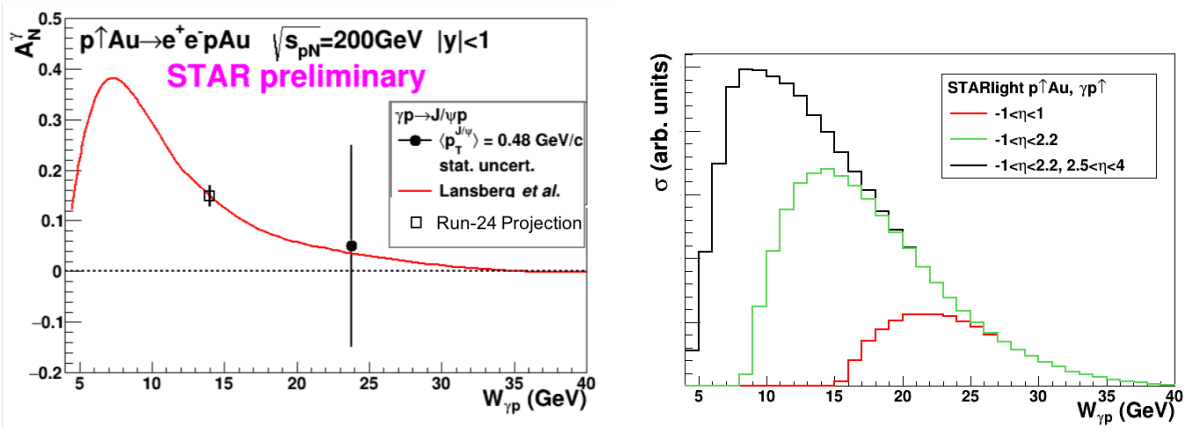

Figure 58: Left: The measured J/ψ transverse asymmetry A_N^γ and a prediction based on a parameterization of E_g. Right: The accepted cross section for γ+p↑→ J/ψ for various detector pseudorapidity η ranges; the black curve shows the result for the full STAR detector with the Forward Upgrade and the iTPC.

dynamics in nuclei?

- What is the role of saturated strong gluon fields, and what are the degrees of freedom in this high gluon density regime?
- What is the fundamental quark-gluon structure of light and heavy nuclei?
- Can a nucleus, serving as a color filter, provide novel insight into the propagation, attenuation and hadronization of colored quarks and gluons?

Various aspects of these questions have been addressed by numerous experiments and facilities around the world, most of them at significantly lower center-of-mass energies and kinematic reach than RHIC. Deep inelastic scattering on nuclei addresses some of these questions with results from, for instance, HERMES at DESY [191–193], CLAS at JLab [194], and in the future from the JLab 12 GeV. This program is complemented by hadron-nucleus reactions in fixed target p+A at Fermilab (E772, E886, and E906) [195] and at the CERN-SPS.

In the following we propose a measurement program unique to RHIC to constrain the initial state effects in strong interactions in the nuclear environment. We also highlight the complementarity to the LHC p–Pb program and stress why RHIC data are essential and unique in the quest to further our understanding of nuclei. The uniqueness of the RHIC program is based on the flexibility of the RHIC accelerator to run collisions of different particle species at very different center-of-mass energies. This in combination with the enhanced STAR detector capabilities in Run-24 allows to disentangle nuclear effects in the initial and final state as well as leading twist shadowing from saturation effects in a kinematic regime where all these effects are predicted to be large. Most of the discussed measurements critically rely on the Forward Upgrade.

Nuclear parton distribution functions: A main emphasis of the Run-15 and later p+A runs is to determine the initial conditions of the heavy ion nucleus before the collision to support the theoretical understanding of the A–A program both at RHIC and the LHC. In the following, the current status of nPDFs will be discussed, including where the unique contributions of RHIC lie, in comparison to the LHC and the future EIC.

Our current understanding of nuclear parton distribution functions (nPDFs) is still very limited, in particular, when compared with the rather precise knowledge of PDFs for free protons collected over the past 30 years. Figure 59 shows an extraction of nPDFs from available data, along with estimates of uncertainties. All results are shown in terms of the nuclear modification ratios, i.e., scaled by the respective PDF of the free proton. The yellow bands indicate regions in x where the fits are not constrained by data [196] and merely reflect the freedom in the functional form *assumed* in the different fits. Clearly, high precision data at small x and for various different values of Q^2 are urgently needed to better constrain the magnitude of suppression in the x region where non-linear effects in the scale evolution are expected. In addition, such data are needed for several different nuclei, as the A-dependence of nPDFs cannot be predicted from first principles in pQCD and, again, currently relies on assumptions. Note that the difference between DSSZ [197] and EPS09 for the gluon modification arise from the different treatment of the PHENIX midrapidity $\pi^0 R_{dAu}$ data [198], which in the EPS09 [199] fit are included with an extra weight of 20. The $\pi^0 R_{dAu}$ data are the only data, which can probe the gluon in the nucleus directly, but these data also suffer from unknown nuclear effects in the final state (see [200]). Therefore, it is absolutely critical to have high precision data only sensitive to nuclear modification in the initial state over a wide range in x and intermediate values of Q^2 (away from the saturation regime) to establish the nuclear modification of gluons in this kinematic range.

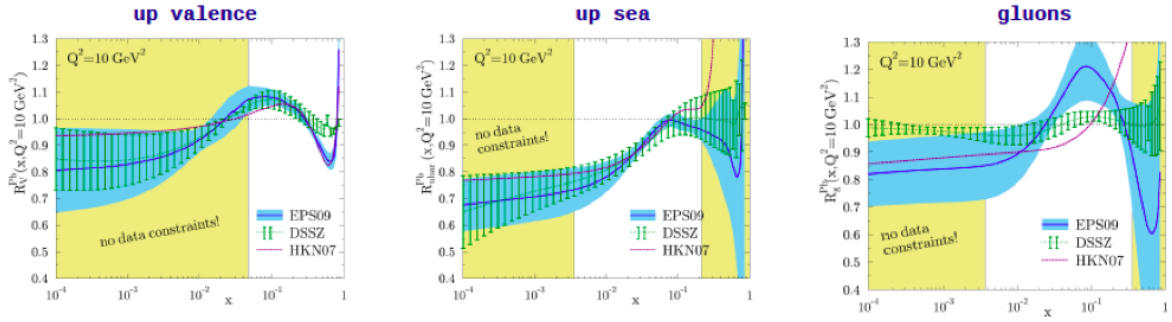

Figure 59: Summary of the most recent sets of nPDFs. The central values and their uncertainty estimates are given for the up valence quark, up sea quark, and the gluon. The yellow bands indicate regions in x where the fits are not constrained by any data (taken from Ref. [196]).

It is important to realize that the measurements from RHIC are compelling and essential even when compared to what can be achieved in p–Pb collisions at the LHC. Due to the

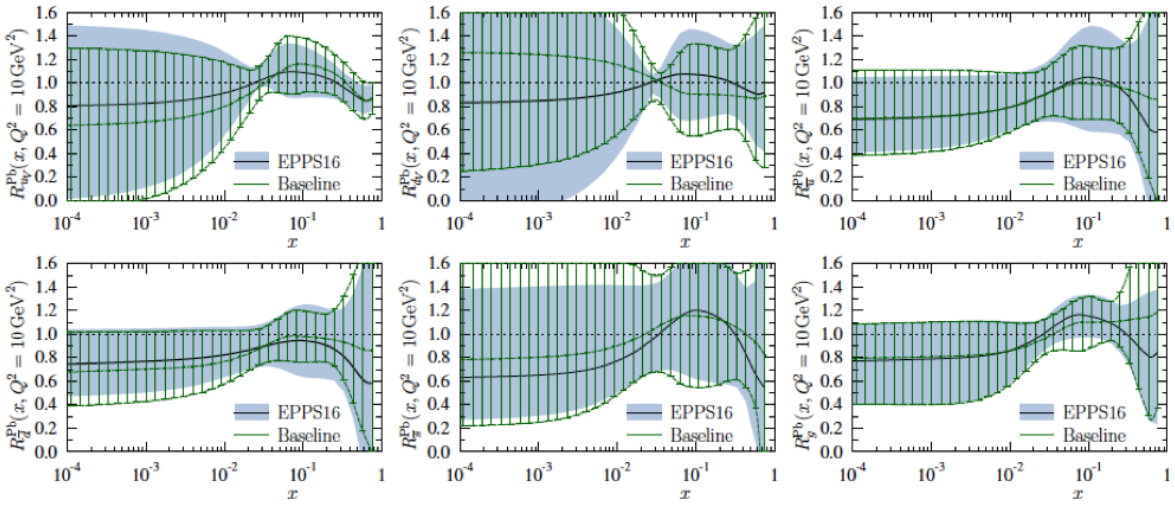

Figure 60: The nuclear modifications at $Q^2 = 10$ GeV^2 from the EPPS-16 fit (black central line and light-blue bands) compared with the Baseline fit (green curves with hatching) which uses only the data included in the EPS09 fit.

higher center-of-mass system energy most of the LHC data have very high Q^2, where the nuclear effects are already reduced significantly by evolution and are therefore very difficult to constrain. Two recent articles [201, 202] assessed the impact of the available LHC Run-I p+Pb data on determinations of nPDFs. The rather moderate impact of these data is illustrated in Fig. 60. Note that the extra weight factor of 20 for the PHENIX midrapidity $\pi^0 R_{dAu}$ data [198] in the original EPS09 [199] fit was removed in all of the new fits, leading to a much smaller nuclear modification factor for gluons, especially at medium to high x.

RHIC has the *unique* capability to provide data in a kinematic regime (moderate Q^2 and medium-to-low x) where the nuclear modification of the sea quark and the gluon is expected to be sizable and currently completely unconstrained. In addition, and unlike the LHC, RHIC has the potential to vary the nucleus in p+A collisions and as such also constrain the A-dependence of nPDFs.

Extraction of this information is less ambiguous if one uses processes in which strong (QCD) final-state interactions can be neglected or reduced. Such golden channels would include: a measurement of R_{pA} for Drell-Yan production at forward pseudo-rapidities with respect to the proton direction ($2.5 < \eta < 4$) to constrain the nuclear modifications of sea-quarks; and of R_{pA} for direct photon production in the same kinematic regime to constrain the nuclear gluon distribution. Data for the first measurement of R_{pA} for direct photon production have already been taken during the p+Au and p+Al Run-15, with recorded luminosities by STAR of $L_{pAu} = 0.45$ pb^{-1} and $L_{pAl} = 1$ pb^{-1}, respectively. The anticipated statistical precision for p+Au runs in Run-15 and projections for the Run-24 are shown in Fig. 61. The Forward Upgrade with its tracking at forward rapidities will also provide the possibility to measure R_{pA} for positive and negatively charged hadrons. Approximately equal nucleon-nucleon luminosities for pp and p+Au are important for the optimization of

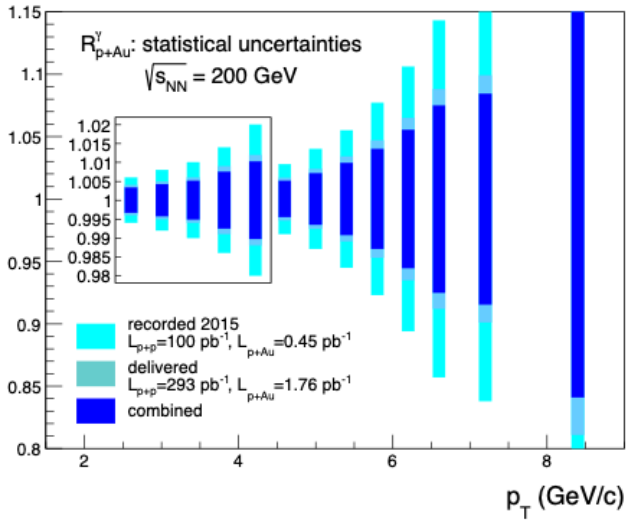

Figure 61: Projected statistical uncertainties for R_{pA} for direct photons in Run-15 (light blue) and Run-24 (blue) and the sum of both (dark blue). The recorded luminosity for Run-15 was $L_{pAu} = 450$ nb^{-1} and $L_{pp} = 100$ pb^{-1}. The delivered luminosity for Run-24 is assumed to be $L_{pAu} = 1.8$ pb^{-1} and $L_{pp} = 300$ pb^{-1}.

R_{pA} measurements as they directly compare the same observable—yields—in both collision systems.

Figure 62 (left) shows the significant impact of the Run-15 and Run-24 R_{pA} for direct photon production on the corresponding theoretical expectations and their uncertainties obtained with the EPPS-16 set of nPDFs. The uncertainty bands are obtained through a re-weighting procedure [203] by using the projected data shown in Fig. 61 and randomizing them according to their expected statistical uncertainties around the central values obtained with the current set of EPPS-16 nPDFs. Figure 62 (right) shows how these measurements will help significantly in further constraining the nuclear gluon distribution in a broad range of x that is roughly correlated with accessible transverse momenta of the photon, i.e., few times $10^{-3} < x <$ few times 10^{-2}. The relevant scale Q^2 is set be $\sim p_T^2$ and ranges from 6 GeV^2 to about 40 GeV^2. Like all other inclusive probes in pp and p+A collisions, e.g., jets, no access to the exact parton kinematics can be provided event-by-event but global QCD analyses easily account for that. After the p+Au Run-24, the statistical precision of the prompt photon data will be sufficient to contribute to a stringent test of the universality of nuclear PDFs when combined with the expected data from the EIC (see Figure 2.22 and 2.23 in Ref [204]).

Figure 63 shows the kinematic coverage in x–Q^2 of past, present, and future experiments capable of constraining nuclear parton distribution functions. The shown experiments provide measurements that access the initial state parton kinematics on an event-by event basis (in a leading order approximation) while remaining insensitive to any nuclear effects in the final state. Some of the LHC experiments cover the same x-range as DY at forward pseudo-rapidities at RHIC but at a much higher scale Q^2, where nuclear modifications are already significantly reduced [202, 205, 206]. At intermediate Q^2, DY at STAR will extend the low-x reach by nearly one decade compared to EIC.

The biggest challenge of a DY measurement is to suppress the overwhelming hadronic background: the total DY cross-section is about 10^{-5} to 10^{-6} smaller than the corresponding

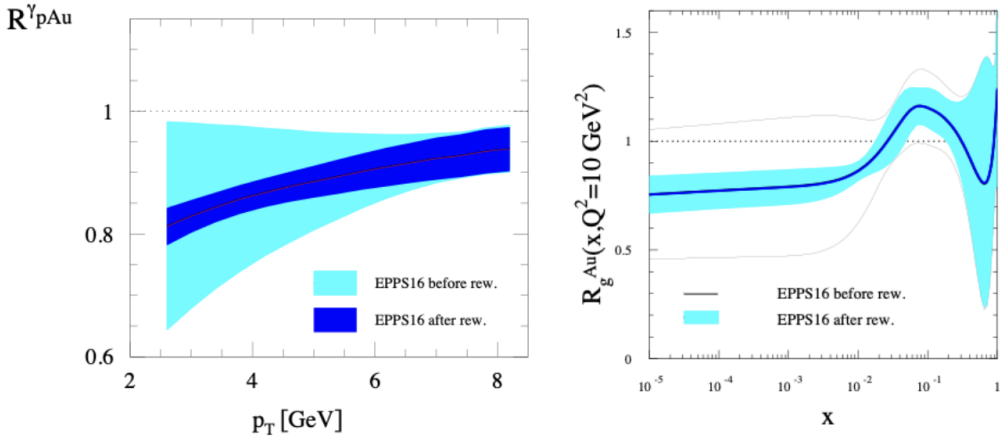

Figure 62: (left) The impact of the direct photon R_{pA} data measured in Run-15 (blue band) and for the anticipated statistics for the future p+Au Run-24 (dark blue band) compared with the current uncertainties (cyan band) from EPPS-16. (right) The impact of the direct photon R_{pA} data measured in Run-15 and for the anticipated statistics for the future Run-24 p+Au run on EPPS-16. The impact is shown on the nuclear suppression factor R_g of nPDF to the proton PDF, the grey bands represent the uncertainties before including the RHIC pseudo data.

hadron production cross-sections. Therefore, the probability of misidentifying a hadron track as a lepton has to be suppressed to the order of 0.1% while maintaining reasonable electron detection efficiencies. To that end, we have studied the combined electron/hadron discriminating power of the Forward Upgrade. It was found that by applying multivariate analysis techniques to the features of EM/hadronic shower development and momentum measurements we can achieve hadron rejection powers of 200 to 2000 for hadrons of 15 GeV to 50 GeV with 80% electron detection efficiency.

The same procedure as for the direct photon R_{pA} was used to study the potential impact of the DY R_{pA} data for the EPPS-19 sets of nPDFs. We expect again a significant impact on the uncertainties of R_{pA} DY upon including the projected and properly randomized data. Clearly, the DY data from RHIC will be instrumental in reducing present uncertainties in nuclear modifications of sea quarks. Again, these data will prove to be essential in testing the fundamental universality property of nPDFs in the future when EIC data become available.

STAR's unique detector capabilities will provide the first data on J/Ψ-production in ultra-peripheral collisions. This measurement provides access to the spatial gluon distribution by measuring the t-dependence of $d\sigma/dt$. As follows from the optical analogy, the Fourier-transform of the square root of this distribution yields the source distribution of the object probed. To study the gluon distribution in the gold nucleus, events need to be tagged where the photon is emitted from the proton. For both observables a measurement with different nuclei is required to pin down the A-dependence of nPDFs. The J/Ψ-production in ultra-peripheral collisions requires significantly more statistics than accumulated to date.

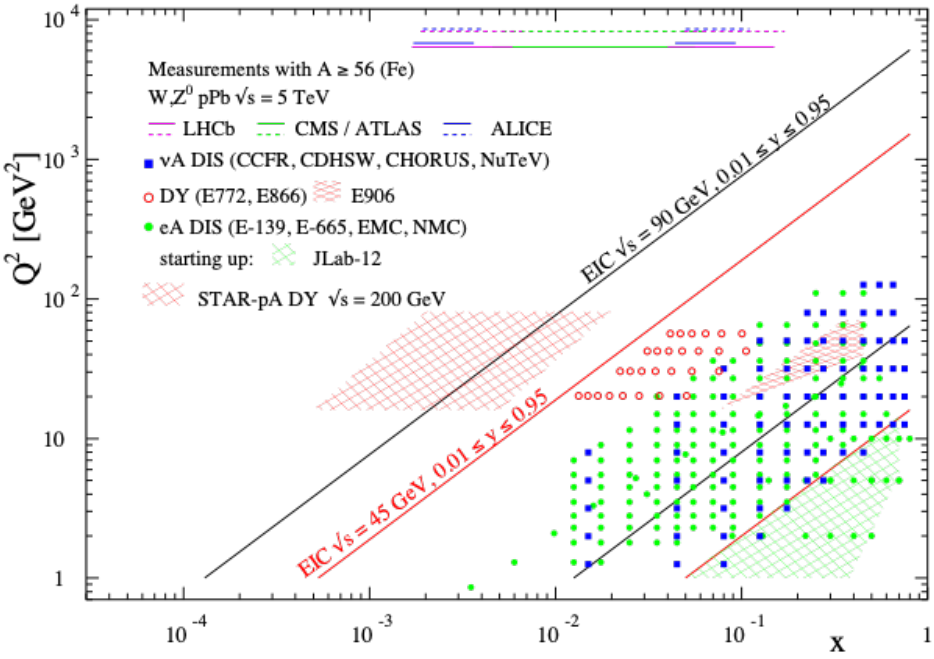

Figure 63: The kinematic coverage in $x - Q^2$ of past, present and future experiments constraining nPDFs with access to the exact parton kinematics event-by-event and no fragmentation in the final state.

Gluon Saturation

Our understanding of the proton structure and of the nuclear interactions at high energy would be advanced significantly with the definitive discovery of the saturation regime [207–213]. Saturation physics would provide an infrared cutoff for perturbative calculations, the saturation scale Q_s, which grows with the atomic number of the nucleus A and with decreasing value of x. If Q_s is large it makes the strong coupling constant small, $\alpha_s(Q_s^2) << 1$ allowing for perturbative QCD calculations to be under theoretical control.

It is well known that PDFs grow at small-x. If one imagines how such a high number of small-x partons would fit in the (almost) unchanged proton radius, one arrives at the picture presented in Fig. 64: the gluons and quarks are packed very tightly in the transverse plane. The typical distance between the partons decreases as the number of partons increases, and can get small at low-x (or for a large nucleus instead of the proton). One can define the saturation scale as the inverse of this typical transverse inter-parton distance. Hence Q_s indeed grows with A and decreasing x.

The actual calculations in saturation physics start with the classical gluon fields (as gluons dominate quarks at small-x) [214–220], which are then evolved using the nonlinear small-x BK/JIMWLK evolution equations [221, 222, 222–230]. The saturation region can be well-approximated by the following formula: $Q_s^2 \sim (A/x)^{1/3}$. Note again that at small enough x the saturation scale provides an IR cutoff, justifying the use of perturbative calculations. This is important beyond saturation physics, and may help us better understand small-x evolution of the TMDs.

While the evidence in favor of saturation physics has been gleaned from the data collected at HERA, RHIC and the LHC, the case for saturation is not sealed and alternative

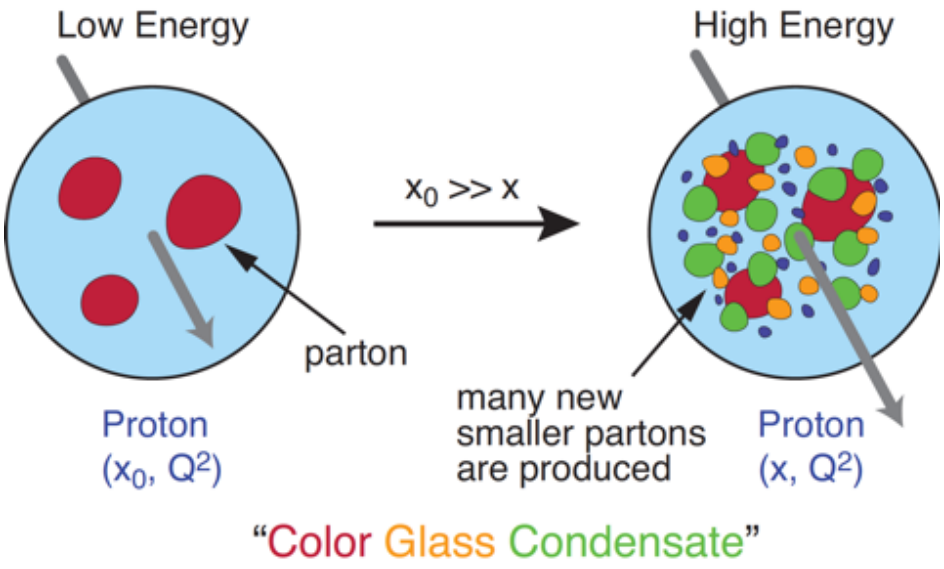

Figure 64: Proton wave function evolution towards small-x.

explanations of these data exist. The EIC is slated to provide more definitive evidence for saturation physics [231]. To help the EIC complete the case for saturation, it is mandatory to generate higher-precision measurements in p+Au collisions at RHIC. These higher-precision measurements would significantly enhance the discovery potential of the EIC as they would enable a stringent test of universality of the CGC. We stress again that a lot of theoretical predictions and results in the earlier Sections of this document would greatly benefit from saturation physics: the small-x evolution of TMDs in a longitudinally or transversely polarized proton, or in an unpolarized proton, can all be derived in the saturation framework [232] in a theoretically better-controlled way due to the presence of Q_s. Hence saturation physics may help us understand both the quark and gluon helicity PDFs as well as the Sivers and Boer-Mulders functions.

The saturation momentum is predicted to grow approximately like a power of energy, $Q_s^2 \sim E^{\lambda/2}$ with $\lambda \sim 0.2 - 0.3$, as phase space for small-x (quantum) evolution opens up. The saturation scale is also expected to grow in proportion to the valence charge density at the onset of small-x quantum evolution. Hence, the saturation scale of a large nucleus should exceed that of a nucleon by a factor of $A^{1/3} \sim 5$ (on average over impact parameters). RHIC is capable of running p+A collisions for different nuclei to check this dependence on the mass number. This avoids potential issues with dividing say p–Pb collisions in N_{part} classes [233]. Figure 65 shows the kinematic coverage in the $x-Q^2$ plane for p+A collisions at RHIC, along with previous e+A measurements and the kinematic reach of an EIC. The saturation scale for a Au nucleus is also shown. To access at RHIC a kinematic regime sensitive to saturation with $Q^2 > 1$ GeV^2 requires measurements at forward rapidities. For these kinematics the saturation scale is moderate, on the order of a few GeV^2, so measurements sensitive to the saturation scale are by necessity limited to semi-hard processes.

Until today the golden channel at RHIC to observe strong hints of saturation has been

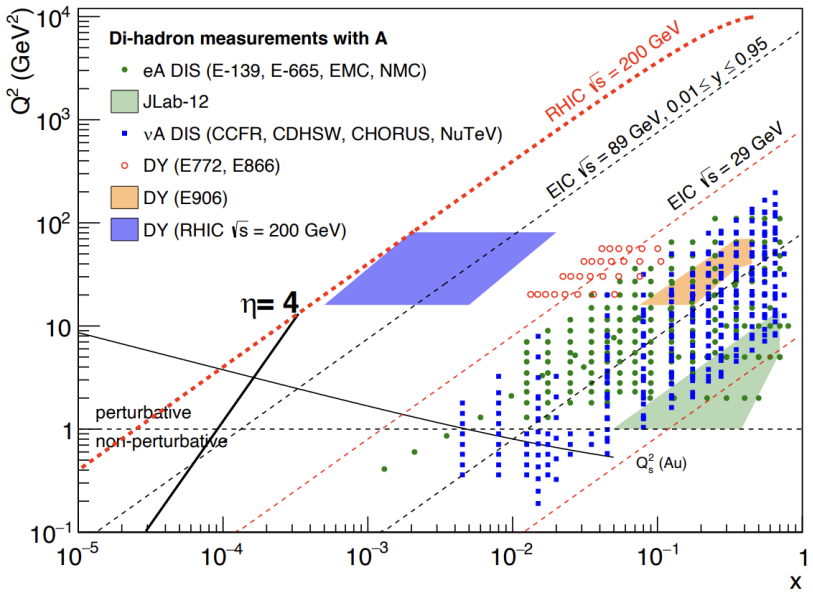

Figure 65: Kinematic coverage in the $x - Q^2$ plane for p+A collisions at RHIC, along with previous e+A measurements, the kinematic reach of an electron-ion collider, and estimates for the saturation scale Q_s in Au nuclus and the line illustrating the range in x and Q^2 covered with hadrons at rapidity $\eta = 4$.

the angular dependence of two-particle correlations, because it is an essential tool for testing the underlying QCD dynamics [233]. In forward-forward correlations facing the $p(d)$ beam direction one selects a large-x parton in the $p(d)$ interacting with a low-x parton in the nucleus. For $x < 0.01$ the low-x parton will be back-scattered in the direction of the large-x parton. Due to the abundance of gluons at small x, the backwards-scattered partons are dominantly gluons, while the large-x partons from the $p(d)$ are dominantly quarks. The measurements of di-hadron correlations by STAR and PHENIX [234, 235], have been compared with theoretical expectations using the CGC framework based on a fixed saturation scale Q_s and considering valence quarks in the deuteron scattering off low-x gluons in the nucleus with impact parameter $b = 0$ [236,237]. Alternative calculations [238] based on both initial and final state multiple scattering, which determine the strength of this transverse momentum imbalance, in which the suppression of the cross-section in d+Au collisions arises from cold nuclear matter energy loss and coherent power corrections have also been very successful to describe the data.

The p+Au Run-15 at RHIC has provided unique opportunities to study this channel in more detail at STAR. The high delivered integrated luminosities allow one to vary the trigger and associated particle p_T from low to high values and thus crossing the saturation boundary as shown in Fig. 65 and reinstate the correlations for central p+A collisions for forward-forward π^0's. Studying di-hadron correlations in p+A collisions instead of d+A collisions has a further advantage. In reference [239], the authors point out that the contributions from double-parton interactions to the cross-sections for $dA \to \pi^0\pi^0 X$ are not negligible. They find that such contributions become important at large forward rapidities, and especially in the case of d+A scattering. Figure 33 shows the results for the di-hadron correlations for π^0 from the 2015 pp and p+Au run. Shown is the ratio of the area, the width and the level of pedestal of the backward peak for p+Au and pp as function of the p_T of the trigger and the

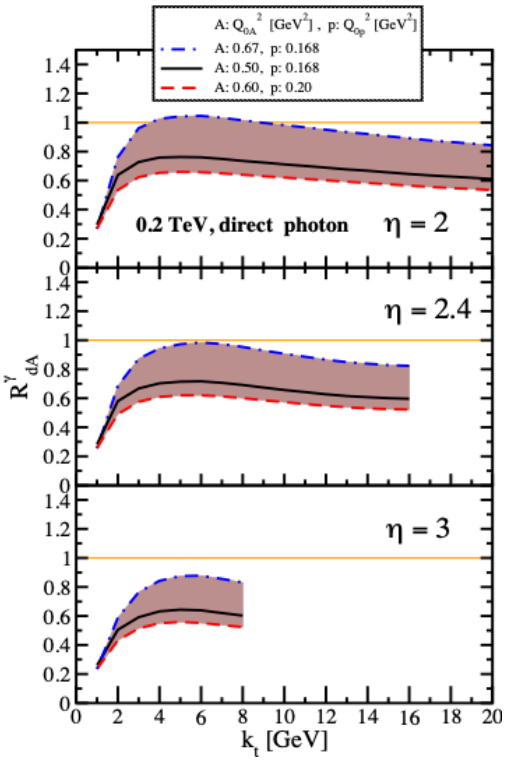

Figure 66: Nuclear modification factor for direct photon production in $p(d)$–A collisions at various rapidities at RHIC $\sqrt{s} = 200$ GeV. The curves are the results obtained from Eq. (12) in Ref. [240] and the solution to rcBK equation using different initial saturation scales for a proton Q_{op} and a nucleus Q_{oA}. The band shows our theoretical uncertainties arising from allowing a variation of the initial saturation scale of the nucleus in a range consistent with previous studies of DIS structure functions as well as particle production in minimum-bias pp, p+A and A–A collisions in the CGC formalism, see Ref. [240] for details.

associated π^0 and the activity in the collision as measured by the BBC.

The results show basically no change in the width of the backward peak and the background/pedestal the peak is sitting on shows only up to a 20% increase in p+Au to pp. However, the area of the backward peak shows a large suppression with increasing activity in the collision. For fixed activity the biggest suppression is observed for the smallest trigger p_T in combination with the smallest p_T for the associated π^0. This behaviour is consistent with different calculations based on the CGC formalism. This result is the first clean observable, which cannot yet be explained in a different framework than CGC and as such a clear hint for non-linear effects.

It is important to note that for the measurements to date in $p(d)$–A collisions both initial and final states interact strongly, leading to severe complications in the theoretical treatment (see [241, 242], and references therein). As described in detail in the Section above in p+A collisions, these complications can be ameliorated by removing the strong interaction from the final state, by using photons and Drell-Yan electrons. The Run-15 p+A run will for the first time provide data on R_{pA} for direct photons and therefore allow one to test CGC based predictions on this observable as depicted in Fig. 66 (taken from Ref. [240]). The higher delivered integrated luminosity for the upcoming p+Au Run-24 together with the Forward Upgrade will enable one to study more luminosity hungry processes and/or complementary probes to the di-π^0 correlations, i.e. di-hadron correlations for charged hadrons, photon-jet, photon-hadron and di-jet correlations, which will allow a rigorous test of the calculation in the CGC formalism. It is important to stress that the comparison of these correlation probes in pp and p+Au requires approximately equal nucleon-nucleon luminosities for these

two collision systems for optimal measurements. It is noted that these results are crucial for the equivalent measurements at an EIC, which are planned at close to identical kinematics, because only if non-linear effects are seen with different complementary probes, i.e., ep and p+A one can claim a discovery of saturation effects and their universality.

We use direct photon plus jet (direct γ+jet) events as an example channel to indicate what can be done in Run-24. These events are dominantly produced through the gluon Compton scattering process, g+q $\rightarrow \gamma$+q, and are sensitive to the gluon densities of the nucleon and nuclei in pp and p+A collisions. Through measurements of the azimuthal correlations in p+A collisions for direct γ+jet production, one can study gluon saturation phenomena at small-x. Unlike di-jet production that is governed by both the Weizsäcker-Williams and dipole gluon densities, direct γ+jet production only accesses the dipole gluon density, which is better understood theoretically [240, 243]. On the other hand, direct γ+jet production is experimentally more challenging due to its small cross-section and large background contribution from di-jet events in which photons from fragmentation or hadron decay could be misidentified as direct photons. The feasibility to perform direct γ+jet measurements with the Forward Upgrade in unpolarized pp and p+Au collisions at $\sqrt{s_{\rm NN}} = 200$ GeV has been studied. PYTHIA-8.189 [244] was used to produce direct γ+jet and di-jet events. In order to suppress the di-jet background, the leading photon and jet are required to be balanced in transverse momentum, $|\phi^{\gamma} - \phi^{jet}| > 2\pi/3$ and $0.5 < p_T^{\gamma}/p_T^{jet} < 2$. Both the photon and jet have to be in the forward acceptance $1.3 < \eta < 4.0$ with $p_T > 3.2$ GeV/c in 200 GeV pp collisions. The photon needs to be isolated from other particle activities by requiring the fraction of electromagnetic energy deposition in the cone of $\Delta R = 0.1$ around the photon is more than 95% of that in the cone of $\Delta R = 0.5$. Jets are reconstructed by an anti-k_T algorithm with $\Delta R = 0.5$. After applying these selection cuts, the signal-to-background ratio is around 3:1 [245]. The expected number of selected direct γ+jet events is around 1.0M/0.9M at $\sqrt{s_{\rm NN}} = 200$ GeV in p+Au collisions for the proposed Run-24. We conclude that a measurement of direct photon-jet correlation from p+Au collisions is feasible, which is sensitive to the gluon density in $0.001 < x < 0.005$ in the Au nucleus where parton saturation is expected.

The Final State

Nuclear fragmentation functions: In spite of the remarkable phenomenological successes of QCD, a quantitative understanding of the hadronization process is still one of the great challenges for the theory. Hadronization describes the transition of a quark or gluon into a final state hadron. It is a poorly understood process even in elementary collisions. RHIC's unique versatility will make it possible to study hadronization in vacuum and in the nuclear medium, and additionally with polarized beams (see Sect. 2.2.1 for the latter).

It has long been recognized that the hadron distributions within jets produced in pp collisions are closely related to the fragmentation functions that have typically been measured in e^+e^- collisions and SIDIS. The key feature of this type of observable is the possibility to

determine the relevant momentum fraction z experimentally as the ratio of the hadron to the jet transverse momentum. Recently [246] a quantitative relationship has been derived in a form that enables measurements of identified hadrons in jets in pp collisions to be included in fragmentation function fits on an equal footing with e^+e^- and SIDIS data. Furthermore, hadrons in pp jets provide unique access to the gluon fragmentation function, which is poorly determined in current fits [247], in part due to some tension found in the inclusive high p_T pion yields measured by the PHENIX and ALICE collaborations. Here, the proposed measurements can provide valuable new insight into the nature of this discrepancy.

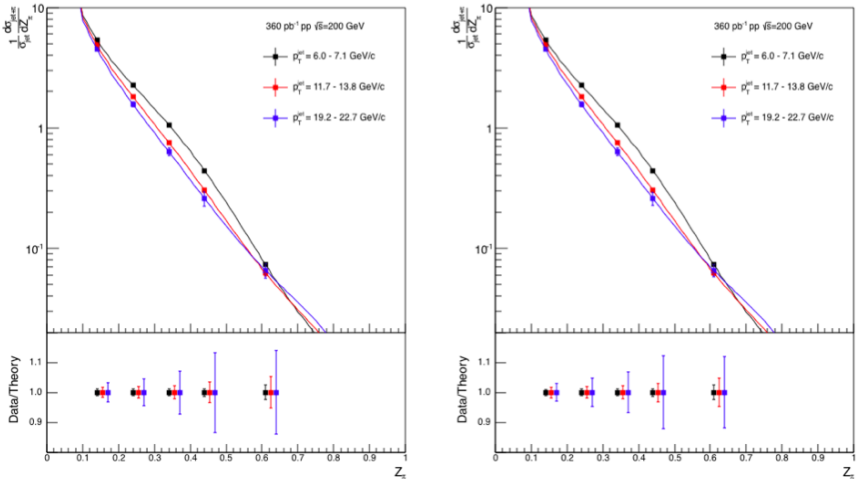

Figure 67: Anticipated precision for identified π^+(left) and π^-(right) within jets at $|\eta| < 0.4$ in 200 GeV pp collisions for three representative jet p_T bins. The data points are plotted on theoretical predictions based on the DSSV14 pion fragmentation functions [246, 247]. Kaons and (anti)protons will also be measured, over the range from $z < 0.5$ at low jet p_T to $z < 0.2$ at high jet p_T, with uncertainties a factor of ∼3 larger than those for pions.

This development motivated STAR to initiate a program of identified particle fragmentation function measurements using pp jet data at 200 and 500 GeV from Run-11, Run-12, and Run-15. Figure 67 shows the precision that is anticipated for identified π^+ and π^- in 200 GeV pp collisions for three representative jet p_T bins after the existing data from Run-12 and Run-15 are combined with future 200 GeV pp data from Run-24. Identified kaon and (anti)proton yields will also be obtained, with somewhat less precision, over a more limited range of hadron z. Once the Run-17 data are fully analyzed, the uncertainties for 510 GeV pp collisions will be comparable to that shown in Fig. 67 at high jet p_T, and a factor of ∼ 2 larger than shown in Fig. 67 at low jet p_T. Identified hadron yields will also be measured multi-dimensionally vs. j_T, z, and jet p_T, which will provide important input for unpolarized TMD fits.

Data from the HERMES experiment [191, 193, 248] have shown that production rates of identified hadrons in semi-inclusive deep inelastic e–A scattering differ from those in ep scattering. These differences cannot be explained by nuclear PDFs, as nuclear effects of strong interactions in the initial state should cancel in this observable. Only the inclusion of

nuclear effects in the hadronization process allows theory to reproduce all of the dependencies (z, x, and Q^2) of R_{eA} seen in SIDIS, as shown in Fig. 68.

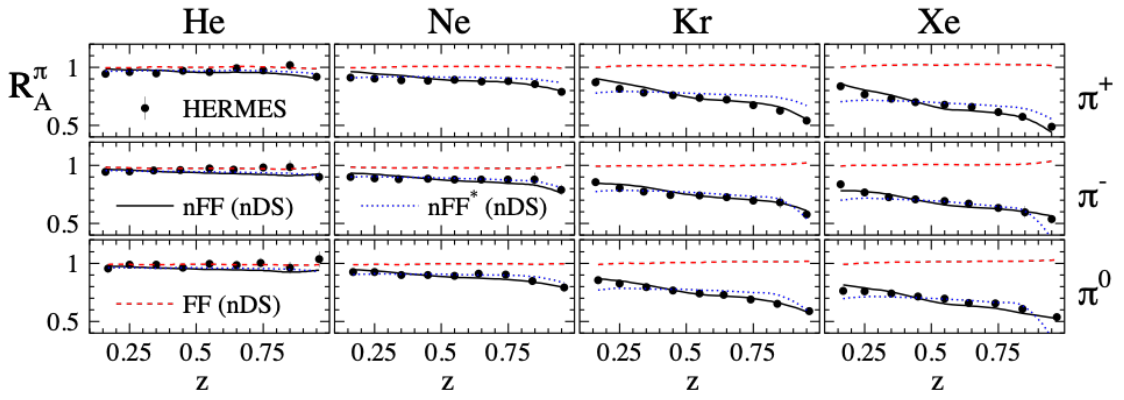

Figure 68: R_{eA} in SIDIS for different nuclei in bins of z as measured by HERMES [191, 193, 248]. The solid lines correspond to the results using effective nuclear FF [200] and the nDS medium modified parton densities [249]. The red dashed lines are estimates assuming the nDS medium modified PDFs but standard DSS vacuum FFs [250, 251] and indicate that nPDFs are insufficient to explain the data

It is critical to see if these hadronization effects in cold nuclear matter persist at the higher $\sqrt{s}$ and Q^2 accessed at RHIC and EIC – both to probe the underlying mechanism, which is not understood currently, and to explore its possible universality. The combination of pp jet data from RHIC and future SIDIS data from EIC will also provide a much clearer picture of modified gluon hadronization than will be possible with EIC data alone. Using the Run-15 200 GeV p+Au data, STAR will be able to make a first opportunistic measurement of these hadron-jet fragmentation functions in nuclei, but the precision will be limited. Additional pp and p+Au data will be needed in Run-24 in order to provide a sensitive test for universality, as shown in Fig. 69.

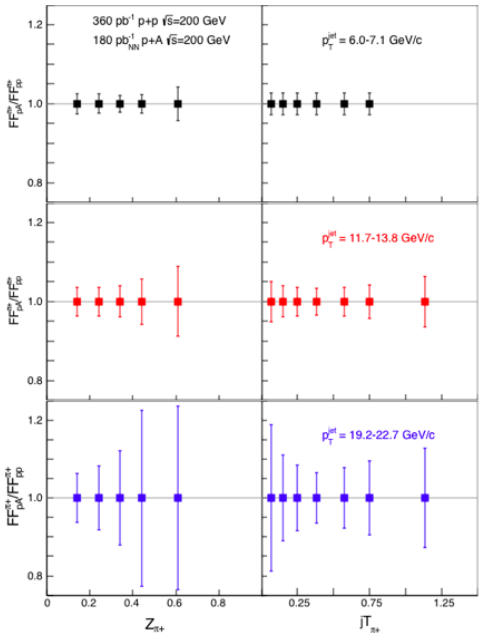

Figure 69: Anticipated precision for measurements of π^+ fragmentation functions in p+App at $|\eta| < 0.4$ vs. z and j_T in Run-24 for three representative jet $p_{\rm T}$ bins. Uncertainties for π^- will be similar to those shown here for π^+, while those for kaons and (anti)protons will be a factor of ~ 3 larger. Note that, to be species independent, the nucleon-nucleon equivalent luminosity is specified for p+Au.

2.2.3 Novel QGP Droplet Substructure in p+A Collisions

In addition to cold QCD effects, a high-statistics measurement of p+Au collisions will be highly valuable to explore novel fluid configurations that have recently been predicted [181]. In particular, the data is needed to discover vortex rings or tubes at midrapidity, included by shear in the asymmetric initial state.

Physical Effect and Observable

It has been suggested [252] that p+A collisions at RHIC form the "smallest QGP droplets." This claim is often based on anisotropic yields, which resemble those from Å collisions that are attributed to hydrodynamic collective flow. Indeed, with well-chosen initial conditions and tuned parameters, three-dimensional viscous hydro calculations can reproduce the measured anisotropies from small, asymmetric collisions [138] at RHIC. However, a claim of QGP formation in such small systems would be much more compelling if it were based on more than one observable, especially since other, non-hydrodynamic mechanisms contribute to v_n in these systems, e.g. [17].

As Helmholtz observed more than 150 years ago [253], vortex rings are ubiquitous in hydrodynamic systems subject to initial conditions characterized by a "push down the middle," such as a smoker blowing a ring. Clear observation of this novel phenomenon would constitute important evidence that the smallest systems at RHIC truly do form a fluid sys-

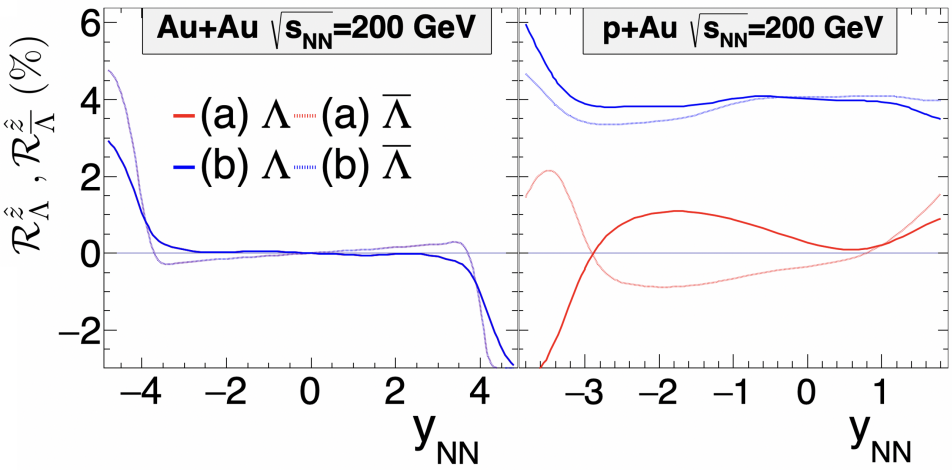

Figure 70: The "ring parameter" $\overline{\mathcal{R}}^{z}_{\Lambda}$ for $b = 0$ Au+Au and p+Au collisions at top RHIC energy. Blue (red) curves correspond to a scenario in which a toroidal vortex structure is (is not) generated by shear forces in the initial state. Solid (dashed) curves correspond to Λ ($\overline{\Lambda}$; note that baryon current is locally conserved in these collisions, so small differences between Λ and $\overline{\Lambda}$ are expected at finite baryon density. From [181].

tem.

This signature probes aspects of particular and fundamental importance to the RHIC program, as well. The vortex ring structure is sensitive to the degree and timescale of equilibration in these small systems, as well as the extreme shear fields in the initial state [254]. Fluctuations in the vortical fields probe hydrodynamic structures at the smallest possible scales, as they arise directly from rotational derivatives in the "surface" of the flux tube.

The experimental signature of toroidal vortex structure is the so-called "ring parameter" [181]:

$$\overline{\mathcal{R}}^{z}_{\Lambda} \equiv \left\langle \frac{\vec{S}'_{\Lambda} \cdot (\hat{z} \times \vec{p}'_{\Lambda})}{|\hat{z} \times \vec{p}'_{\Lambda}|} \right\rangle, \tag{3}$$

where $+\hat{z}$ is the direction of the proton beam, and the average is taken over all particles and events. This is the average polarization relative to the hyperon production plane. Rings will be most clear for central collisions, but the detailed centrality dependence of the effect is currently under investigation [254]. We focus on 0-10% centrality.

Figure 70 shows $\overline{\mathcal{R}}^{z}_{\Lambda}$ calculated [181] for completely central Au+Au and p+Au collisions at $\sqrt{s_{NN}} = 200$ GeV. Calculations were done with MUSIC [255], a three-dimensional relativistic viscous hydrodynamics simulation that locally conserves baryon number, and calculation of the thermal vorticity along the freezeout hypersurface.

Initial condition (a) corresponds to the usual Bjorken "boost-invariant" flow profile used in most Å simulations, whereas condition (b) features strong shear fields generated in the initial condition, leading to observable vortex toroids. Both initial conditions generate identical $dN/d\eta$ distributions, but the latter is argued [181] to be more natural.

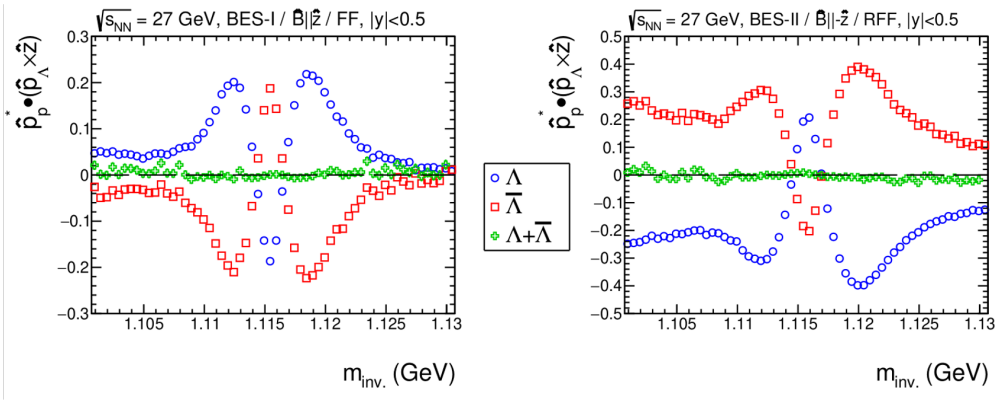

Figure 71: Production-plane polarization (modulo an overall scaling by $\frac{8\pi}{\alpha_\Lambda}$) for Λ (blue) and $\overline{\Lambda}$ (red) candidates, as a function of invariant mass. The data comes from STAR measurements of Au+Au collisions at $\sqrt{s_{NN}}$ in the BES-I (left) and BES-II (right) campaigns. STAR's solenoidal magnetic field was directed to the West and East, respectively, for these two datasets. For the BES-I data, hyperon candidates were identified with "standard" topological cuts, whereas the candidates shown in BES-II were identified using the new KFParticle package.

Statistics required

The statistical requirement to discover these toroidal vortex structures may be estimated by STAR's previous hyperon polarization measurements. The uncertainty on global polarization measurements $\delta\overline{P}_\Lambda \propto N_\Lambda^{-1/2} \cdot R_{\rm EP}^{-1}$, where N_Λ is the total number of hyperons in the analysis, and $R_{\rm EP}$ is the event plane resolution [103]. Because there is no event plane involved in the production plane polarization, on the other hand, the uncertainty on the ring observable goes as $\delta\overline{\mathcal{R}}_\Lambda^z \propto N_\Lambda^{-1/2}$. For the same-magnitude signal, then, $\overline{\mathcal{R}}_\Lambda^z$ enjoys an effective $R_{\rm EP}^{-2}$ "statistical advantage" over $\overline{P}_\Lambda$. Since STAR measured [256] $\overline{P}_\Lambda \approx 1\%$ at $\sqrt{s_{NN}} = 11$ GeV with 3.5σ significance, with the same number of hyperons in the analysis, we should be able to measure $\overline{\mathcal{R}}_\Lambda^z \sim 1\%$ with 7σ significance. The 11-GeV analysis involved 6M Λs, and we estimate 0.02 Λs per central $(0-10\%)$ p+Au collision at $\sqrt{s_{NN}} = 200$ GeV. Therefore, the 7σ measurement will require $6M/0.02 = 300M$ central p+Au collisions.

The need for both field configurations

Also crucial to this measurement is that data must be collected with both polarities of STAR's magnetic field. This is because of large and highly nontrivial decay-topology-dependent detector effects, which will give a "false" production plane polarization signal. The magnitude of the artifact is an order of magnitude larger than the physical signal of interest, and it is highly sensitive to momentum, PID, and topological cuts. We could not feel confident applying such large and complex "correction factors" based solely on detector simulations, if we claim a completely novel signature with far-reaching physical implications. Fortunately, the sign of this artifact flips with the magnetic field polarity.

Figure 71 illustrates these points. Au+Au collisions at $\sqrt{s_{NN}} = 27$ GeV were recorded by STAR using opposite polarities of the magnetic field. For Λs, the quantity $\hat{p}_{\rm p} \cdot (\hat{p}_\Lambda \times \hat{z})$, where $\vec{p}_{\rm p}$ is the daughter proton momentum, is proportional to $\overline{\mathcal{R}}_\Lambda^z$. For $\overline{\Lambda}$s, the quantity

$\hat{p}_{\overline{\mathrm{p}}} \cdot (\hat{p}_{\overline{\Lambda}} \times \hat{z})$, where $\vec{p}_{\mathrm{p}}$ is the daughter proton momentum, is proportional to $-\overline{\mathcal{R}}^z_{\overline{\Lambda}}$.

A rapidity cut symmetric about midrapidity ($|y| < 0.5$ was used; for a symmetric system, the physical production plane polarization vanishes by symmetry– any nonvanishing value results purely from topologically-sensitive efficiency effects.

Consider first the Λ curve from BES-I, the blue points in the left panel. Clearly, the effect has a nontrivial dependence on invariant mass; note even the asymmetry about $m_{\mathrm{inv}} = m_\Lambda$. Equally clearly, it is large, corresponding to values $\overline{\mathcal{R}}^z_\Lambda = \frac{8}{\pi\alpha_\Lambda}\hat{p}_{\mathrm{p}} \cdot (\hat{p}_\Lambda \times \hat{z}) \approx 50\%$, an order of magnitude larger than the predicted value of physical effect of interest.

In terms of topologically-sensitive efficiency effects, substituting $\Lambda \to \overline{\Lambda}$ is equivalent to flipping the sign of the magnetic field. The red datapoints in the left panel are a perfect mirror image to the blue points in that panel, as indicated by the vanishing green points, which are the sum. Further note that naive interpretation of the data in the left panel would suggest that the vortical ring values for the hyperons and antihyperons ($\overline{\mathcal{R}}^z_\Lambda$ and $\overline{\mathcal{R}}^z_{\overline{\Lambda}}$) would be identical in magnitude and sign.

The right panel shows the same colliding system, but measured during the BES-II campaign with the opposite orientation of STAR's magnetic field. As expected from the above discussion, $\overline{\mathcal{R}}^z_\Lambda = -\overline{\mathcal{R}}^z_{\overline{\Lambda}}$. The shape and magnitude of the artifact is different from the BES-I case, however, because a different method has been used to identify hyperon candidates. This illustrates the cut-dependence of the artifact.

In short, for reliable extraction of the ring vorticity measure, STAR must measure p+Au collisions with both field orientations, in order to cancel the complex efficiency-driven artifacts. Finally, we point out that this sort of cancellation is not unique to this observable. Indeed, there is an analogous effect for the global polarization, which precludes extracting the *first*-order azimuthal dependence of $\overline{P}_\Lambda$; there, the artifact is of order 100%, compared to the physical and measured value of $\sim 2\%$ [257].

Distinction from other effects

For symmetric collisions (e.g. Au+Au), the quantity $\overline{\mathcal{R}}^z_\Lambda$ must be antisymmetric about midrapidity. However, at very forward/backward rapidities, circular vorticity has been reported in hydrodynamic [258–262] and transport [15, 263–268]. This effect, also visible in the left panel in figure 70, arises from strong temperature gradients and edge effects in three-dimensional space. It is of very different origin than the ring voriticity of interest here.

Finally, production plane polarization at large x_{F} has been observed (primarily) in p+p and (in some) p+A collisions [269–274] at energies up to $\sqrt{s_{NN}} = 41$ GeV. This effect, which is believed to be completely hadronic in origin but remains incompletely understood, is distinguishable from the hydrodynamically-driven ring vorticity discussed here by its rapidity dependence, which is strongly forward-focused, as well as the fact that $\overline{\Lambda}$s do not display production plane polarization at all. Thus, in addition to double-checking topologically-dependent efficiency artifacts (discussed above), it is important that STAR will measure the effect both for hyperons and antihyperons to distinguish hydrodynamic from hadronic phenomena.

3 Exploring the Microstructure of the QGP (Run-23 and Run-25 Au+Au)

The completion of RHIC's scientific mission involves the two central goals of (i) mapping out the phase diagram of the QCD, and (ii) probing the inner workings of the QGP by resolving its properties at short length scales [275]. The complementarity of the RHIC and LHC facilities to study the latter is scientifically as essential as having more than one experiment independently study the microstructure of the QGP. With several years of operating the iTPC upgrade and the soon-to-be installation and operation of the forward detectors, the STAR collaboration will be in an excellent position to take advantage of its vastly improved detection capabilities. Combine this with the prospect of a substantial increase in beam luminosities and RHIC will be uniquely positioned to fully engage in a detailed exploration of the QGP's microstructure. Through careful discussions in its physics working groups, the STAR collaboration has identified a number of topics that together make a compelling case to take data during Runs 23-25 alongside sPHENIX, and successfully complete RHIC's scientific mission. In this section, we present a selection of those topics that will take full advantage of both STAR and RHIC's unique capabilities and address the following important questions about the inner workings of the QGP.

- What is the precise temperature dependence of the shear η/s, and bulk ζ/s viscosity?
- What is the nature of the 3-dimensional initial state at RHIC energies? How does a twist of the event shape break longitudinal boost invariance and decorrelate the direction of an event plane?
- How is global vorticity transferred to the spin angular momentum of particles on such short time scales? And, how can the global polarization of hyperons be reconciled with the spin alignment of vector mesons?
- What is the precise nature of the transition near $\mu_B = 0$, and where does the sign-change of the susceptibility ratio χ_6^B/χ_2^B take place?
- What is the electrical conductivity, and what are the chiral properties of the medium?
- What can we learn about confinement and thermalization in a QGP from charmonium measurements?
- What are the underlying mechanisms of jet quenching at RHIC energies? What do jet probes tell us about the microscopic structure of the QGP as a function of resolution scale?

The event statistics projections that are used in this section will rely on the CAD's recently update 2023E and 2025E Au+Au luminosities [276] and are listed in Table 9. For each year we presume 24 weeks of RHIC operations, and based on past run operations an overall average of 85% × 60% (STAR×RHIC) uptime, respectively. The minimum-bias

rates assume a conservative 1.5 kHz DAQ rates which will allow sufficient bandwidth for specialized triggers which are listed as integral luminosities. In order to achieve the projected luminosities, the collaboration will look into optimizing the interaction rates at STAR by allocating low and high luminosity periods within fills. Such periods, in which low interaction rates are sampled in the early part of a fill and high interaction rates typically in the later part, will allow us to collect clean, low pile-up, minimum bias events, while at the same time not burn beam luminosities that could affect interaction rates for sPHENIX. Clean minimum bias events will improve tracking efficiencies which in turn are expected to benefit many of the proposed correlation analyses. Optimization of the available bandwidth for high-p_T triggers would allow us to push for lower p_T thresholds, thus further reducing biases. The impact of such an optimization will lead to some reduction in the projected rates, while still enabling a significant improvement in the precision and kinematic reach of current STAR measurements, and making important measurements that are yet more differential possible.

year	minimum bias [$\times 10^9$ events]	high-p_T int. luminosity [nb^{-1}] all vz	|vz|<70cm	|vz|<30cm
2014 2016	2	27	19	16
2023 2025	20	63	56	38

Table 9: STAR minimum bias event statistics and high-p_T luminosity projections for the 2023 and 2025 Au+Au runs. For comparison the 2014/2016 event statistics and luminosities are listed as well.

At RHIC it is possible to build detectors that can span from mid-rapidity to beam rapidity – with the two recent upgrades STAR is able to achieve this unique capability. STAR's BES-II upgrade sub-systems comprised of the inner Time Projection Chamber (iTPC, $1.0 < |\eta| < 1.5$) , endcap Time Of Flight (eTOF, $1 < \eta < 1.5$) and Event Plane Detector (EPDs, $2.1 < |\eta| < 5.1$), that are all commissioned and fully operational since the beginning of 2019 [103, 277, 278]. As will be discussed in Section 4, the STAR collaboration is constructing a forward rapidity ($2.5 < \eta < 4$) upgrade that will include charged particle tracking and electromagnetic/hadronic calorimetry [279]. For charge particle tracking the aim is to construct a combination of silicon detectors and small strip thin gap chamber detectors. The combination of these two tracking detectors will be referred to as the forward tracking system (FTS). The FTS will be capable of discriminating the hadron charge sign. It should be able to measure transverse momentum of charged particles in the range of $0.2 < p_{\rm T} < 2$ GeV/c with $20-30\%$ momentum resolution. In what follows, we will refer to the combination of the existing TPC ($|\eta| < 1$) and the iTPC upgrade as iTPC ($|\eta| < 1.5$) for simplicity.

The impetus for running STAR during the year of 2023-2025 in terms of bulk correlation measurements in Au+Au 200 GeV collisions comes from gains via: i) extended acceptance and ii) enhanced statistics. In the first subsections, we briefly describe how these two op-

portunities can be exploited to perform correlations measurements that are unique to the physics goals of the RHIC heavy-ion program.

Next, thanks to a reduced material budget between the beam and the iTPC, STAR will be uniquely positioned to perform dielectron measurements with which we propose to probe degrees of freedom of the medium and its transport properties. For that we will use the high precision dilepton excess yield, i.e. l^+l^- invariant mass distribution after subtraction of dilepton sources produced after freeze-out, and contributions from the initial collisions such as Drell-Yan and correlated charm-anticharm pairs. Furthermore, we propose to study the virtuality, Wigner function and final-state magnetic field in the QGP. For the latter photon-photon collisions in ultra-peripheral, peripheral,and midcentral reactions and p+A (all centralities) in both channels e^+e^-, $\mu^+\mu^-$ will be measured with high accuracy.

In the last subsections, we address our proposed charmonium measurements and motivate the importance of STAR's proposed program of precise jet measurements to explore the micro-structure of the QGP.

Figure 81 shows the kinematic projection plot for the STAR past (until 2015), current, and with Run23+25 hard probes measurements. The corresponding STAR measurements are compared with the LHC (published) measurements.

3.1 Correlation Measurements Utilizing Extended Acceptance

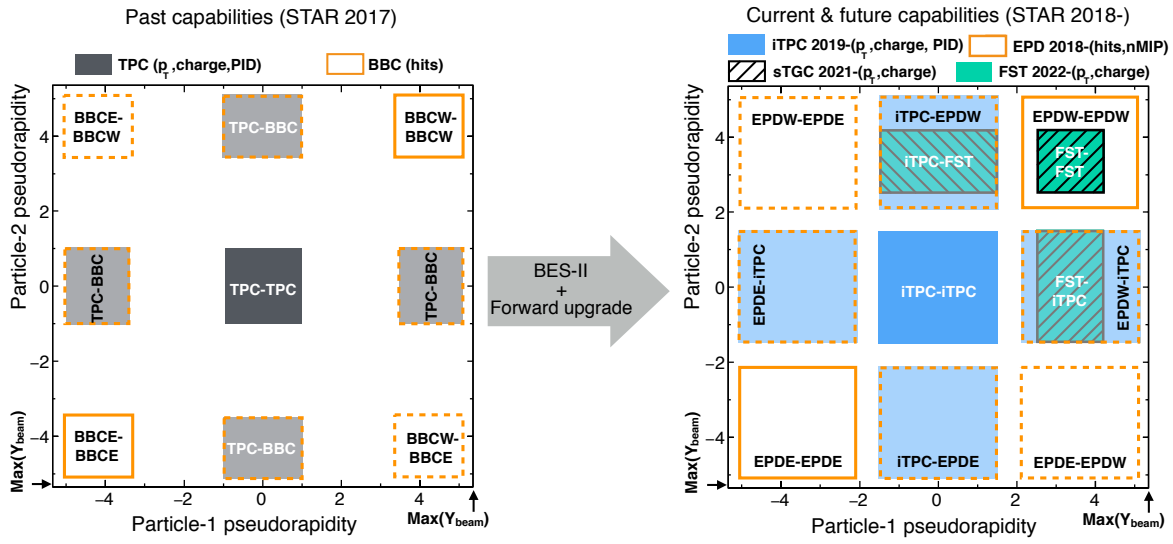

Figure 72: A visual representation of two-particle phase space in pseudorapidity covered by STAR detectors with respect to the region allowed by maximum beam rapidity (Y_{beam}=5.36 at 200 GeV Au+Au collisions) of RHIC. Left and right panels show the capabilities before and after BES-II and forward upgrades of the STAR detector, respectively. Note that in addition to a larger pair acceptance, the EPD granularity is over an order of magnitude larger than that of the BBC, and individual EPD tiles are shown to be separable into 1, 2, 3 MIP responses.

Figure 72 demonstrates how STAR, with the BES-II and forward upgrades, will extend the two-particle phase-space (in terms of η_1 and η_2 with respect to beam rapidity) many times enabling us to perform correlation measurements over a wide window of relative pseudorapidity. Since many of the important correlation measures are based on two-particle correlations, this enhanced phase-space will provide STAR with many advantages: 1) an increase in the number of pairs resulting in better precision, 2) a reduction in different sources of the non-flow backgrounds by increasing the pseudorapidity separation. Many multi-particle correlations will also benefit from the increase in triplets, quadruplets and so on due to the overall increased acceptance. With this unique extended pseudorapidity reach our goal is to perform correlation measurements to enable a deeper understanding of the largely unexplored three-dimensional structure of the initial state, and further improve the extraction of temperature dependent transport properties of the subsequent fluid-like medium produced in heavy ion and small system collisions at RHIC through data-model comparison such as the Bayesian analysis performed in Ref [280].

Two key sets of measurements are of interests: 1) the pseudorapidity dependence of azimuthal correlations, 2) the pseudorapidity dependence of global hyperon polarization.

Pseudorapidity-dependent Azimuthal Correlations to Tightly Constrain the Temperature Dependence of Viscosity

The idea of tightly constraining the temperature dependent viscosity of the QGP was envisioned in the 2015 Long Range Plan for Nuclear Science [275]. The QCD matter formed at RHIC shows nearly perfect fluidity characterized by the smallest viscosity to entropy ratio η/s known in nature. One major aim is to perform precision measurements to constrain the temperature dependence of the shear η/s (T) and bulk ζ/s (T) viscosities. Recent state-of-the-art Bayesian analyses of flow and spectra data within sophisticated event-by-event hydrodynamics models has show strong evidence for temperature dependence of η/s and ζ/s [280–282], but the uncertainties are still quite large. On the other hand, hydrodynamic simulations have demonstrated that since the temperature of the produced fireball in HICs vary with the rapidity, the measurement of the rapidity dependence of flow harmonics can provide additional constraint on the η/s (T) and ζ/s (T) [283]. For this, RHIC measurements have an advantage over the LHC since the smaller beam rapidity at RHIC provides stronger variations of the temperature with rapidity. The beam energy scan at RHIC provides an additional handle on temperature to map η/s (T), and ζ/s (T) over a wide range of temperatures. Indeed, the hydrodynamic simulation of Ref. [283] indicates that η/s (T) at lower temperatures, near its possible minimum ($T = T_c$), can be better constrained by RHIC measurements. Results from such simulations are shown in Fig. 73. In this simulation, a number of QCD-motivated parameterizations of the temperature dependence of the shear viscosity were assumed, as shown in Fig. 73 (left).

Existing data from the PHOBOS collaboration suffer from large uncertainties, therefore only limited constraints on the temperature dependence of the transport parameters can be achieved. The BES-II upgrade (with iTPC) and the forward upgrade (FTS) of STAR will provide precise estimations of different azimuthal correlation observables: $v_n(\eta)$ and

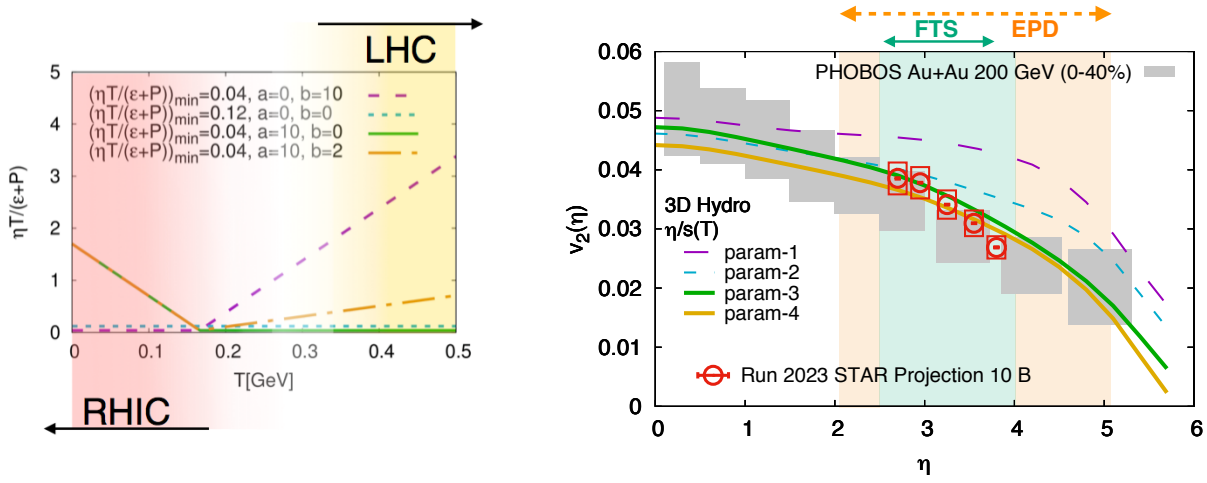

Figure 73: (Left) Different parameterizations of the temperature dependence of the shear viscosity to entropy η/s (T) (at zero chemical potential) used in the hydrodynamical simulation of Ref. [283]. Interestingly, it has been demonstrated in Ref. [284] that the region of lowest η/s is the one that can be probed at RHIC. (Right) Effects on the elliptic flow co-efficient v_2 due to different parameterizations of the viscosity parameter, indicating better constraints on η/s (T) can only be performed by measurements at forward rapidities at RHIC. The interpretation of the existing PHOBOS data is limited by the large uncertainties. Projections for STAR measurements are shown on the same plot.

other higher-order ($n > 2$) flow coefficients $v_n(\eta)$, its fluctuations $\sigma(v_n)/v_n$ that have never been measured at forward rapidity, are essential in terms of constraining η/s (T) near its possible minimum. These quantities previously measured at mid-rapidity with previous data are not enough for discriminating different parameterization of η/s (T) as shown in the hydrodynamic simulation of Ref. [283]. While transverse momentum integrated quantities at forward rapidity can constrain the shear viscosity, measurement of the p_{T} of particles at forward rapidity (i.e. forward tracking) is essential to constrain the bulk viscosity ζ/s – in particular the information of $\langle p_T \rangle$ is needed to constrain ζ/s(T). With the forward tracking systems it will be possible to measure the p_{T} dependence of v_n in Au–Au collisions in 2023.

Pseudorapidity-dependent Azimuthal Correlations to Constrain the Longitudinal Structure of the Initial State

Initial-state longitudinal fluctuations and the fluid dynamical response of the medium formed in heavy ion collisions can lead to de-correlations of the direction of the reaction planes Ψ_n (which determines the orientation of the harmonic anisotropies) with pseudorapidity (see Fig. 74). Such effects are often referred to as a torque or twist of the event shape [287–289] that eventually leads to a breaking of longitudinal/boost/rapidity invariance. The magnitude of the de-correlation is determined by the details of the dynamics of initial state, and the distribution of nucleons and partons inside the colliding nu-

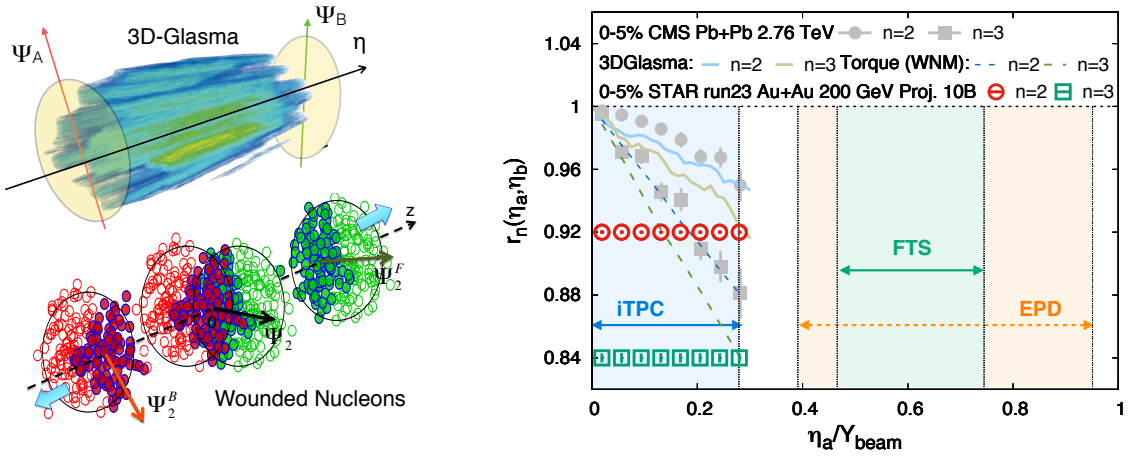

Figure 74: (Left) Cartoon to demonstrate the de-correlation of event planes in the longitudinal direction of a collision from a gluon saturation based 3D-Glasma model [285] and a wounded nucleon model (WNM) [286, 287]. (Right) The longitudinal de-correlation of the elliptic anisotropy plane as a function of pseudorapidity in units of beam rapidity. CMS results are compared to predictions from two models in the left with STAR projection for Run-23 (using preliminary Run-19 results) from an anticipated 10 B min-bias events. The colored regions show that the current and future capabilities at STAR (with iTPC+EPD+FTS) can extend such measurements with good precision by covering a large fraction of the beam rapidity at 200 GeV – this demonstrates the unique strength to STAR to study the physics of 3D initial state.

clei. Several promising observables have been proposed to study this effect, Fig. 74 shows one which can be expressed as $r_n(\eta_a, \eta_b) = V_{n\Delta}(-\eta_a, \eta_b)/V_{n\Delta}(\eta_a, \eta_b)$, where $V_{n\Delta}(\eta_a, \eta_b)$ is the Fourier coefficient calculated with pairs of particles taken from three different pseudorapidity regions $-\eta_a$, η_a and η_b. The observable $r_n(\eta_a, \eta_b)$ was originally introduced and measured by CMS collaboration in Ref. [290] and also been measured by the ATLAS collaboration in [291]. An observable using three-particle correlations that is sensitive to this effect is the relative pseudorapidity dependence of the three-particle correlator $C_{m,n,m+n}(\eta_a, \eta_b, \eta_c) = \langle \cos(m\phi_1(\eta_a) + n\phi_2(\eta_b) - (m+n)\phi_3(\eta_c)) \rangle$ [292]. Another, very similar to r_n in terms of design but involving four-particle correlations, is: $R_{n,n|n,n}(\eta_a, \eta_b)$ [293]. As shown in Fig. 74, CMS measurements of r_n show strong de-correlation ($\sim$ 16% for n=3, $\sim$ 8% for n=2) in central events within the range of their acceptance. In the 3D-Glasma model of initial state, the breaking of boost invariance is determined by the QCD equations which predict the evolution of gluons in the saturation regime with Bjorken-x. At the LHC such models predict weaker de-correlation as compared to when the initial state is described by wounded nucleon models. The 3D-Glasma model does a good job in explaining the r_2 data from CMS [285] but over-predicts the r_3 results. One expects the nature of the initial state to change from LHC to RHIC, in particular the region of Bjorken-x probed is very different. It is therefore extremely important to utilize the enhanced acceptance of the STAR detector with a Au+Au 200 GeV run to study this effect. In Fig. 74 STAR's projections using preliminary Run-19 results to estimate the uncertainties for 10 B events

are shown for the measurement of r_n within the acceptance $|\eta| < 1.5$. The colored regions show that the current and future capabilities at STAR (with iTPC+EPD+FTS) can extend such measurements using observables $r_n, C_{m,n,m+n}, R_{n,n|n,n}$ with good precision by covering either an equal (iTPC only) or larger (iTPC+FTS+EPDs) fraction of the beam rapidity at 200 GeV compared to the LHC measurements. This unique measurement capability will help pin down the nature of the 3-D initial state of heavy ion collisions. It will also help constrain different models of QCD that predict the rapidity (or Bjorken-x) dependence of valance quark and gluon distributions inside colliding nuclei as has been demonstrated by theoretical calculations in Ref. [285, 294].

Search for Collectivity in Photo-nuclear ($\gamma + Au$) Processes

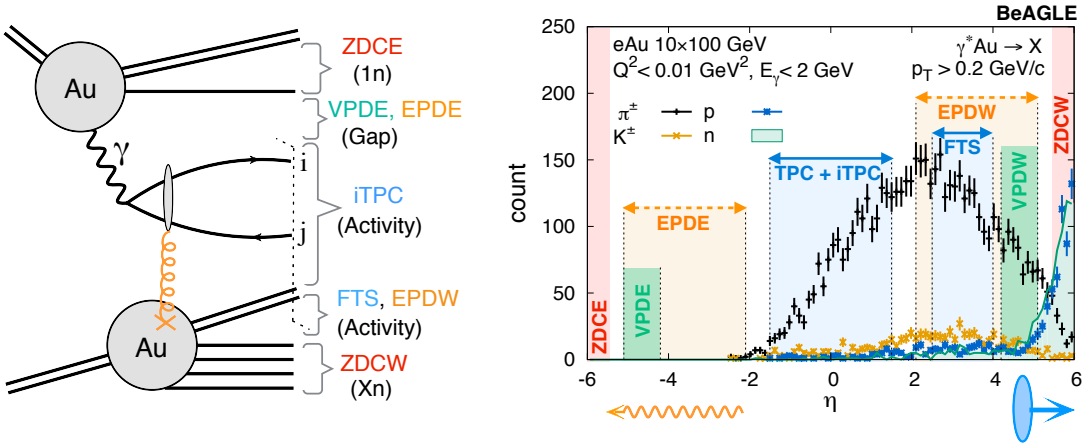

Figure 75: (Left) $\gamma + Au$ process in ultra-peripheral heavy ion collisions associated with a large rapidity asymmetry; the large acceptance of the STAR detector can be used to trigger these events to study bulk observables and search for collectivity, the same can be done in low virtuality e+Au collisions to search for collectivity at the EIC.(Right) Pseudorapidity distribution of different particles using the state-of-the-art BeAGLE [295, 296] event generator for EIC in e+Au events. By restricting virtuality and energy of the photon (γ^*) we try to mimic the kinematics of a $\gamma + Au$ (Au+Au UPC) event. The purpose of this plot is to demonstrate how different STAR detectors will be used to identify such UPC processes at the kinematics similar to that at EIC.

Until the EIC at BNL is built, high-energy photoproduction processes (low virtuality limit of deep inelastic scattering) as shown in Fig.75, can be studied using ultra-peripheral ion collisions (UPCs) that occur when two heavy ion interact at large impact parameters. Such collisions can be considered as γ+A collisions but unlike at the EIC, the photons involved in UPCs are quasi-real. Do we expect to see collectivity in such collisions? If observed, this will address an important question. Origin of collectivity in small collision systems has been argued to be driven by the formation of a medium that evolves hydrodynamically. However, due to the phenomenon of saturation, intrinsic correlations for gluons in the colliding hadrons/nuclei have been shown by theoretical models such as color glass conden-

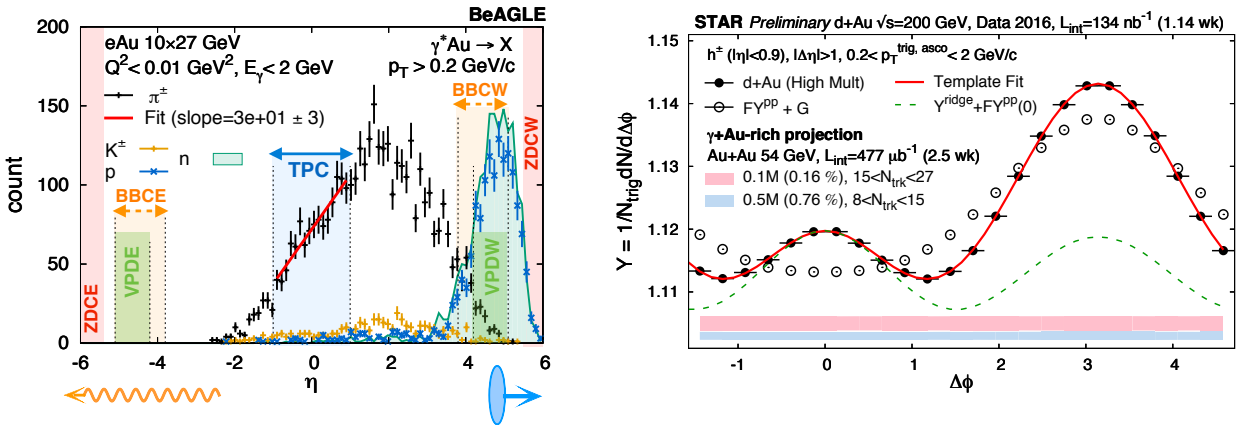

Figure 76: (Left) $\gamma + Au$ processes simulated using BeAGLE event generator in the low virtuality limits ($Q^2 < 0.01$ GeV/c^2) of DIS by restricting the energy of photons to be $E_\gamma < 2$ GeV and ion energy to be 27 GeV. The pseudorapidity distributions thus produced is used to apply cuts on detectors in STAR to identify $\gamma + Au$ candidates in 54 GeV Au+Au collisions. (Right) STAR preliminary data on per-trigger yield estimated using di-hadron correlations in d+Au (hadornic) 200 GeV collisions. The correlation function in pp collisions (open circle) is used as a template to fit the same in relatively higher multiplicity d+Au collisions (solid circle) and to extract the long-range ridge-like component. The red and blue band show projections for $\gamma + Au$ enriched events for two different multiplicity bins. The aim is to use the correlation function from the low multiplicity $\gamma + Au$ to perform template fit in the high multiplicity bin. Our exploratory analysis with 54 GeV data indicates about 0.16-0.76% of minbias events are $\gamma + Au$ events. With the anticipated 20 Billion Au+Au 200 GeV events collected in Run-23 and Run-25, about 300 times more $\gamma + Au$ candidates can be collected, implying a reduction of the red and blue bands by a factor of 17.

sate (CGC) to contribute to collectivity – experimentally such contributions have not been decisively established. The general consensus is that correlations predicted by both hydrodynamics and CGC contribute to collectivity – although no experimental measurement has been proposed that can disentangle the contribution from the two effects. No studies have convincingly demonstrated that in γ+A collisions a hydrodynamic medium can be formed. Observation of collectivity in $\gamma + Au$ (or future e+A), therefore, may very well be the first evidence of purely initial-state gluon driven contribution to such phenomenon as argued in the theoretical work of ref [297]. This will be an important step to understanding the role of gluon saturation or color coherence in driving collectivity, and also pioneer several new measurements in this direction a the BNL EIC.

The search for collectivity in ultra-peripheral (UPC) 5.02 TeV Pb+Pb collisions, by triggering γ+A events, has recently been initiated by the ATLAS collaboration at the LHC where interesting hints of long-range ridge like correlations have been observed [298]. However, RHIC has similar ion energies when compared to the future EIC. This gives STAR the necessary motivation to propose a program to search for the collectivity in $\gamma + A$ events at RHIC. This is interesting as γ+A UPC events have much synergy with low virtuality events in e+A collisions at the EIC and in many ways this provides a chance to better un-

derstand the origin of collectivity. It must be noted the proposed program with STAR will have several unique strengths to both complement and extend such a search for collectivity at lower collision energies due to: a wider acceptance compared to beam rapidity ($Y_{\rm beam}$), better momentum resolution to measure the soft part of the spectrum, and better particle identification capabilities. As shown in Fig.75, our goal is to trigger on the $\gamma + Au$ process in ultra-peripheral heavy ion collisions associated with a large rapidity asymmetry. The figure also demonstrates how the combination of the inner Time Projection Chamber (iTPC), the new highly granular Event-Plane Detectors (EPD) and the forward tracking system (FTS) and Zero-Degree Calorimeters (ZDC) can be used isolate $\gamma + Au$ events from peripheral Au+Au events (symmetric in η with no gaps). By triggering on these events our aim will be to study bulk observables ($dN/dydp_T(\pi^{\pm}, K^{\pm}, p/\bar{p})$) and long range ridge-like azimuthal correlations to search for collectivity.

A handful of datasets exist on the disk with the appropriate event trigger selection for such a process. For example, Fig.76 show a feasibility study using the dataset of Au+Au collisions at 54 GeV (year 2017) and 200 GeV (year 2019). In order to mimic the kinematics of Fig.76(left) we apply asymmetric cuts on the energy deposition of neutrons in ZDCs (1nXn). For example, if the ZDC east is restricted to have a single neutron hit, while no restriction is placed on the ZDC west we trigger on $\gamma + Au$ candidates with east going photons, and vice versa. We also apply similar asymmetric cuts in the BBCs to get purer samples. After collecting $\gamma + Au$-rich candidates we study di-hadron correlations in such events and compare with the same from hadronic events with same activities. We select two such windows of event activity based on cuts on numbers of tracks in TPC ($15 < N_{trk}^{|\eta|<0.5} < 27$ and $1 < N_{trk}^{|\eta|<0.5} < 8$). According to our estimates the percentage of possible $\gamma + Au$ candidates are about 0.17% and 0.83% of min-bias events in those two windows of multiplicity. Fig.76 shows STAR preliminary data on the per-trigger yield in di-hadron correlations in d+Au events where a clear ridge can be seen after template fitting. On the same plot we show projections of uncertainties for the di-hadron correlations in possible $\gamma + Au$-rich events using Au+Au 54 GeV data. With the new forward detector capability and new datasets in the future Au+Au 200 GeV (year 2023 and 2025) run of RHIC with a dedicated trigger selection, we should be able to make measurements at the kinematics similar to that at EIC as shown in Fig.76. Based on the feasibility studies with 54 GeV data, we estimate about $0.16 - 0.76\%$ of minbias candidates to be potential $\gamma + Au$ candidates (purity of such events are still under investigation). Therefore, event without any dedicated trigger, 20 Billion minbias Au+Au events can already give us 32-152 Million potential $\gamma + Au$ candidates. This will significantly reduce the uncertainties shown by the red and blue projection bands in Fig.76. This will enable us to perform differential measurements of di-hadron correlations with different combinations of trigger and associated transverse momenta.

Pseudorapidity Dependence of Global Hyperon polarization

The global polarization of hyperons produced in Au+Au collisions has been observed by STAR [256]. The origin of such a phenomenon has hitherto been not fully understood.

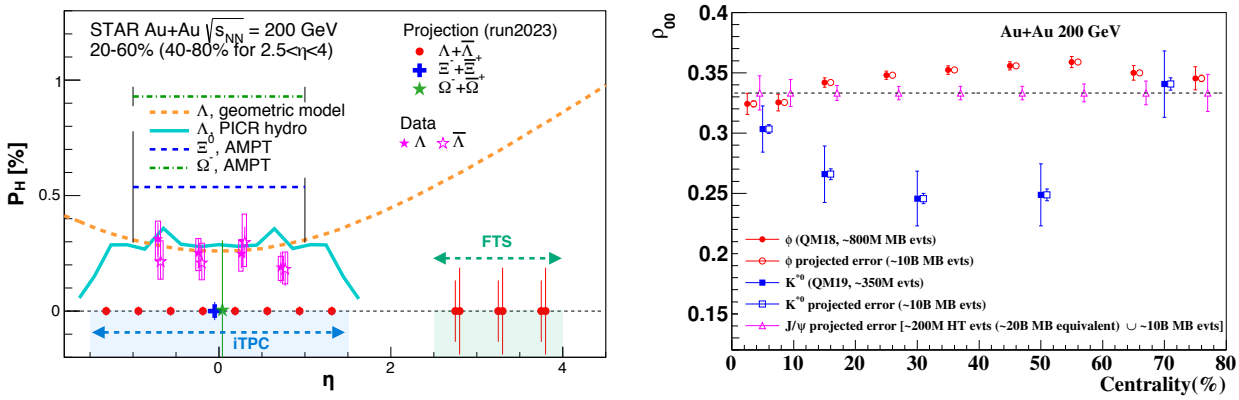

Figure 77: (Left) Projections (along with preliminary data) for differential measurements of $\Lambda(\bar{\Lambda}$ polarization over the extend range of pseudorapidity with the iTPC and FTS detectors of STAR that will help resolve tension between different theoretical model predictions (shown by curves) of polarization with η. In addition, projections for the measurements of spin-1/2 Ξ and spin-3/2 Ω particles are also shown. (Right) Spin alignment co-efficient ρ_{00} as a function of centrality, with projected errors based on $\sim$ 10 billion minimum bias events. The enhanced statistics Run-23, combined with the excellent dilepton capabilities of STAR, will enable us to measure J/ψ alignment along with increasing the significance of the ϕ and K^{*0} measurements.

Several outstanding questions remain. How exactly is the global vorticity dynamically transferred to the fluid-like medium on the rapid time scales of a collision? Then, how does the local thermal vorticity of the fluid gets transferred to the spin angular momentum of the produced particles during the process of hadronization and decay? In order to address these questions one may consider measurement of the polarization of different particles that are produced in different spatial parts of the system, or at different times. A concrete proposal is to: 1) measure the $\Lambda(\bar{\Lambda})$ polarization as a function of pseudorapidity and 2) measure it for different particles such as Ω and Ξ. Both are limited by the current acceptance and statistics available as recently published by STAR [299]. However, as shown in Fig. 77 with the addition of the iTPC and FTS, and with high statistics data from Run-23 it will be possible to perform such measurements with a reasonable significance. iTPC (+TPC) has excellent PID capability to measure all these hyperons. Although the FTS has no PID capability we can do combinatorial reconstruction of $\Lambda(\bar{\Lambda}$ candidates via displaced vertices. A similar analysis was performed and published by STAR using the previous FTPC [300]. In order to make a conservative projection we assume similar momentum resolution of $10-20\%$ for single charged tracks, similar overall tracking efficiency, charge state identification capability for the FTS and FTPC (see the forward upgrade section for exact numbers). We also assume the FTS, with it's novel-tracking framework, will be able to measure a minimum separation of 20 cm between the all pairs of one positive and one negative track (a possible decay vertex) from the main vertex of the event. This will give rise to about 5% efficiency of $\Lambda(\bar{\Lambda})$ reconstruction with about $15-20\%$ background contribution from $K^0_S \rightarrow \pi^+ + \pi^-$ [300]. With this we can make projections for a polarization measurement in Au+Au 200 GeV $40-80\%$ assuming 10 Billion minimum-bias events as shown in Fig. 77. The two different error bars

correspond to lower and upper limits considering current uncertainties on the efficiency of charged track reconstruction and the final efficiency of Λ reconstruction. Currently theoretical models predict contradictory trends for the pseudorapidity dependence of Λ polarization. If the initial local orbital angular momentum driven by collision geometry [301] plays a dominant role it will lead to increases of polarization with pseudorapidity. On the other hand if the local thermal vorticity and hydrodynamic evolution [302] play a dominant role it will predict decreasing trend or weak dependence with pseudorapidity. Such tensions can be easily resolved with the future proposed measurement during Run-23.

3.2 Correlation Measurements Utilizing the Enhanced Statistics

Over the past years the STAR collaboration has pursued dedicated measurements of Au+Au collisions at $\sqrt{s_{\rm NN}}$ = 200 GeV that have major discovery potential but are intrinsically statistics hungry. Attempts have been made to combine datasets from several years to increase the significance of such measurements. This can result in run-to-run variations and systematics in detector responses that sometimes are tedious to correct. A single stable long run with similar detector conditions, as anticipated during Run-23, can avoid such issues. In the following section, and also in section 1.2.7, we propose correlation measurements that will utilize the enhanced statistics from Run-23 and can lead to high-impact results. To start we assume STAR will collect data at the rate of 1.5 kHz and a combined RHIC×STAR uptime of 50% (12 hour/day) for 24 weeks of running during Run-23. This will lead to the accumulation of about $24 \times 7 \times 86400 \times 0.5 \times 1500 \approx 10$ billion events.

Global Spin Alignment of J/ψ

Surprisingly large signals of global spin alignment of vector mesons such as $\phi(1020)$ and $K^{*0}(892)$ have been measured via the angular distribution of one of their decay products. These experimental observations of vector meson spin alignment have yet to be interpreted satisfactorily by theory calculations. It has been realized that the mechanism driving the global polarization of hyperons can have its imprint on vector meson spin alignments albeit the observed strength of signals for the two measurements cannot be reconciled. In fact the large quantitative difference between the measurements of $\phi(1020)$ and $K^{*0}(892)$ spin alignment as shown in Fig. 77 (right) cannot be simultaneously explained by conventional mechanisms of spin-orbit coupling, driven by angular momentum, without invoking strong force fields. It is argued that the strong force field makes a dominant contribution to the spin-alignment coefficient ρ_{00} of ϕ, while for K^{*0}, the contribution is diminished due to the mixing of quark flavors (averaging-out of different meson fields) [303, 304]. Therefore, the current preliminary experimental data from STAR (Fig. 77, showing $\rho_{00}(\phi) > \rho_{00}(K^{*0})$) support the role of strong force field as a key mechanism that leads to global spin alignment. However, a stringent test of such a prediction can be performed by measuring the spin alignment of J/ψ. This is because similar arguments apply for both ϕ and J/ψ, i.e. like s and $\bar{s}$, the strong field component also couples to c and $\bar{c}$ quarks leading to larger ρ_{00} for J/ψ. In Fig. 77(right) we present the projected uncertainties for ρ_{00} of J/ψ estimated for various

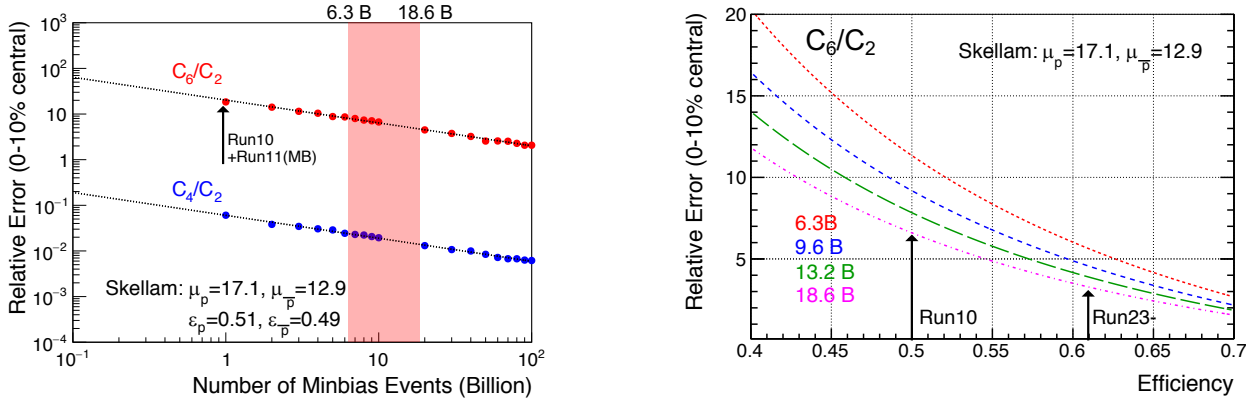

Figure 78: Projection for measurement of ratio of sixth order over second order cumulants of net-proton distribution.

centralities assuming: 1) 10 billion min-bias events for low p_T J/ψ measurements and, 2) 200 million events implementing High Tower (HT) triggers with the Barrel Electromagnetic Calorimeter for the high p_T J/ψ. Both assume 24 weeks running anticipated in Run-23. It is worth to mention that apart from J/ψ spin alignment, such a large statistics dataset will also allow addition differential study of global spin alignment of ϕ and K^{*0} and help to further elucidate the mechanism behind vector meson spin alignment.

Sixth Order Cumulant of Net-proton Distributions

LQCD calculations [5, 305] predict a sign change of the susceptibility ratio χ_6^B/χ_2^B with temperature (T at $\mu_B = 0$) taking place in the range of 145-165 MeV. The observation of this ratio going from positive to negative values is considered to be a signature of a crossover transition. Interestingly, as shown in Section 1.1.1, values of net-proton C_6/C_2 are found to be negative systematically from peripheral to central Au+Au 200 GeV collisions within large statistical uncertainties. The observation of negative C_6/C_2 is intriguing and so far only hinted at in the 200 GeV data, the current result has less than 2.3σ significance for 30-40% centrality in terms of statistical uncertainties. The current systematic uncertainty is of similar order as the statistical uncertainty and if based off of combining datasets from Run-10 and Run-11. As shown in the projection plot of Fig. 78 it is possible to establish definitive observation of negative C_6/C_2 at 200 GeV with nearly 10 billion minimum-bias events to be collected during the Run-23 with 15% increase in the reconstruction efficiency and enhanced acceptance of the iTPC detector upgrade. A similar measurement can be performed at the LHC for vanishing baryon chemical potential, while only STAR measurements can explore the finite μ_B region. Our measurement at $\sqrt{s_{NN}}$ =200 GeV has the potential to establish the first experimental observation of QCD chiral crossover transition at $\mu_B \approx 20$ MeV.

Strong Interaction Measurements

The strong interaction between baryons leads to a residual force; the most common example is NY. The same force is responsible for binding $n - p$ into d. So far, understanding the

strong interaction has been limited to the effective theories related to nucleons and the scattering experiments, which are very challenging due to the short lifetime of resonances (a few cm decay length). One of the current challenges is to evaluate the strong interaction between hyperons, as experimentally still very little is known about NY and YY interactions. Hypernuclei (a hyperon bound inside an atomic nucleus) are proof of a positive, attractive interaction of NY. Measurements of NN and NY interactions have crucial implications for the possible formations of bound states. Studies of the strong interaction potential via two-particle correlations in momentum space measured in relativistic heavy-ion and elementary collisions have proven to be useful to gain access to the interactions between exotic and rare particles. Possible combinations can be: $p\Lambda$, $p\Sigma$, $p\Omega$, $p\Xi$, $\Lambda\Lambda$, $\Xi\Xi$. In contrast to $p\Lambda$, the nature of $p\Sigma$, $p\Omega$, $\Lambda\Lambda$ still need experimental verification. Even if scattering experiments are available, they are not very conclusive.

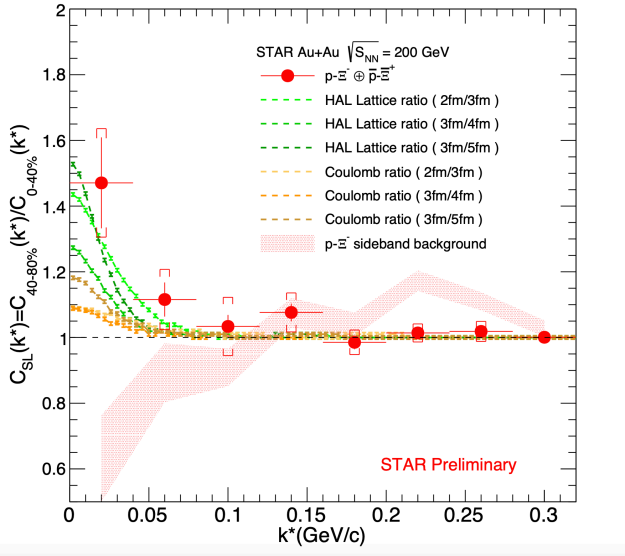

Figure 79: Solid circles represent the ratio (R) of the small system (40-80% collisions) to the large system (0-40% collisions) for proton–Ξ and $\bar{p}$–Ξ correlations. The bars correspond to the statistical uncertainties. The shaded area represents R for background candidates from the side-band of the Ξ invariant mass. Coulomb-induced R are shown in yellow and orange colors. HAL Lattice predictions of R are shown in green.

Figure 79 shows the preliminary $p\Xi$ correlations function. All available statistics, 3 billion events accumulated over all previous runs, were used for the $p\Xi$ and $p\Omega$ cases. Combining such datasets leads to the run-to-run variations resulting in larger total systematic uncertainties in the detector responses. A single stable long run with similar detector settings during the Run-23 will avoid such issues. Statistical uncertainties of the current measurements remain high, and the number of points that build the correlation function is minimal. This means that the current results are not conclusive enough to study in detail the parameters of the strong interaction. Since the effect of the Coulomb interaction, seen via two-particle

correlation, is expected to cancel in the ratio of two correlation functions, the extraction of the strong interaction parameters can be performed with larger datasets by measuring the correlation signal for central and mid-central+peripheral collisions. The collection of 10 billion events from Run-23 will make possible the construction of correlation functions of the $p\Xi$ case with double the number of points and smaller statistical uncertainties than the current measurement. The $p\Omega$ system is more statistics hungry, and we expect that we will require 20 billion events, from combining Run-23 and Run-25, before we can double of the number of points that build the correlation signal. Previous STAR measurements of $p\Omega$ correlations show that the parameters of the strong interaction can be studied. However, with higher data collections, more precise and detailed studies would be possible. The description of the $\Lambda\Lambda$ interaction is still an open issue. Such a description is fundamental since it plays a decisive role in understanding the nature of hyperons that appear in neutron stars. If many hyperons appear close to each other and their fraction becomes significant, the YY interactions are expected to play an essential role in describing the equation of state of the dense system. An alternative way to study hypernuclei is two-particle momentum correlations of $\Lambda\Lambda$ pairs produced in hadron-hadron collisions thanks to femtoscopy. Figure 80 shows primary $\Lambda\Lambda$ (left) and $\Xi\Xi$ (right) correlation functions. For current $\Lambda\Lambda$ and $\Xi\Xi$ systems also data from all previous runs were combined. Due to differences between individual runs, a significant source of systematic uncertainties exist now, and it will disappear with all 10 billion events collected during the Run-23 for the $\Lambda\Lambda$ case. More critical seems to be the increased statistics for the $\Xi\Xi$ case, and having 20 billion events from Run-23 and Run-25 enables the reduction of statistical uncertainties significantly and makes it possible to determine parameters of the strong interaction with higher precision. Having combined data from the Run-23 and Run-25 will also allow the hypotheses about possible bound states to be verified.

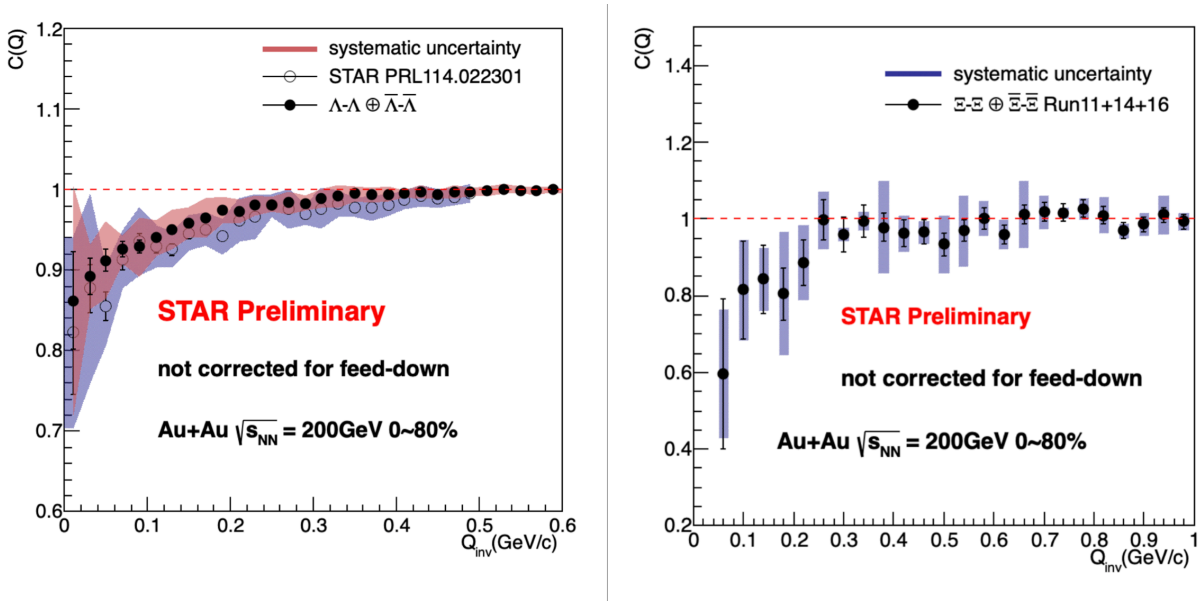

Figure 80: Left: combined $\Lambda\Lambda$ and $\bar{\Lambda}\bar{\Lambda}$ preliminary correlation functions with systematic uncertainties compared with already published previous STAR results. Right: combined $\Xi\Xi$ and $\bar{\Xi}\bar{\Xi}$ correlation functions with systematic uncertainties.

3.3 Hard Probes: Jets and Heavy Flavor

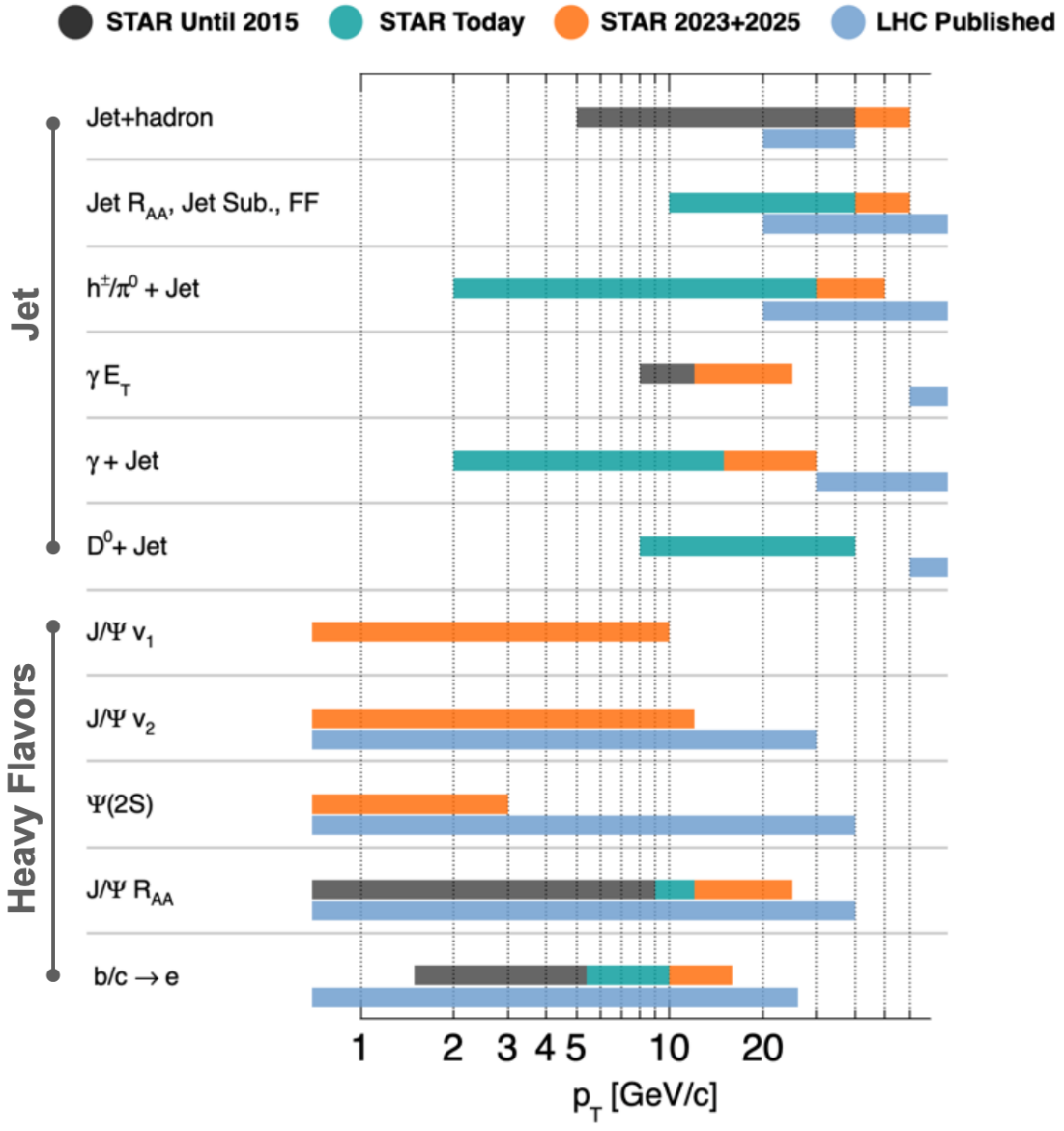

Figure 81: The kinematic coverage of the STAR Hard Probes measurements (past, current, and future projection) are shown with the corresponding comparison to the LHC (published) measurements. The details on the projection for precision measurements can be found in section. 3.3.

Measurements of fully reconstructed jets and heavy flavor particles over a broad kinematic range at RHIC are essential to meet the goal outlined in the NSAC 2015 Long Range Plan (LRP), to "probe the inner workings of the QGP" [275].

A diagrammatic representation of STAR's kinematic coverage for various measurements

related to hard probes is shown in Figure 81. The different colored horizontal bars showcase STAR measurements that were available at the time of the 2015 NSAC-LRP (black), ongoing measurements and recently released results (green) and projections for future data-taking in years 2023 and 2025 (orange). The current high statistics STAR Au+Au collision datasets available were recorded in 2014 and 2016, the integrated luminosities sampled by STAR's BEMC triggers are shown in Table 9. STAR's capabilities are compared with the corresponding LHC (light blue) published measurements. This overview reveals our ability to investigate the QGP over a wide range of temperatures and medium properties produced in heavy-ion collisions. Some of the flagship measurements are listed along the different rows grouped into two topics related to 'Jets' and 'Heavy Flavors', where the x-axis represents a p_{T} scale. The Run-23+25 RHIC heavy-ion runs will enable an expanded kinematic range of fully reconstructed jets and open heavy flavor measurements through the semi-leptonic decay channel, providing an overlap with the LHC data. They will also facilitate measurements of low transverse momentum J/ψ elliptic flow (v_2) to study the recombination mechanism in more detail, J/ψ directed flow (v_1) that will allow us to study the initial tilt of the bulk medium and suppression of the loosely bounded ψ(2S) state to explore the temperature profile of the medium.

The dependence of jet energy loss on the jet p_{T} and/or resolution or angular scale tagged by jet substructure observables, are key tools in discriminating various jet quenching mechanisms [306–309]. In addition, the measurement of jet acoplanarity is a sensitive probe of transverse momentum broadening and medium-induced radiative effects [310], particularly for jets at low p_{T} which are accessible at STAR by selecting a given momentum transfer via a photon trigger. Such a measurement is also minimially affected by background arising from vacuum Sudakov radiation at RHIC energies [311, 312], potentially enabling a precise extraction of in-medium jet scattering.

Measurements of open heavy flavor and quarkonium production in heavy-ion collisions provide important information about the properties of the created medium. Production of open heavy flavor hadrons, J/ψ and Υ mesons in Au+Au collisions at RHIC was found to be suppressed compared to the production in pp collisions. The suppression of open heavy flavor production at high p_{T} is due to energy loss of heavy quarks in the QGP, while the suppression of quarkonium states is due to a screening of the $Q\bar{Q}$ potential by the medium color charges. In addition, J/ψ production can be affected by recombination of charm quarks in a later stage of the collision evolution. The regeneration mechanism is expected to contribute mostly at the low J/ψ transverse momentum range. Furthermore, recent theoretical calculations suggest that measurements of the directed flow of heavy flavors particles can be used to shed light on the initial geometry and the magnetic field information created during heavy-ion collisions [313, 314].

STAR's unique geometry allows collection of events over a wide range of vertex positions along the beam direction (vz) for jet and heavy flavor analyses, thereby efficiently sampling the provided RHIC luminosity. Optimization of the vz range used in the various analyses involves a balance between statistical precision and complexity of corrections, with the latter predominantly contributing to the systematic uncertainties of the measurement. Recent

STAR jet measurements in Au+Au collisions have employed two classes of z-vertex cuts: the inclusive charged-particle jet analysis [315] utilizes $|\mathrm{vz}| < 30$ cm, whereas the γ_{dir}+jet analysis utilizes $|\mathrm{vz}| < 70$ cm. With the γ_{dir}+jet measurement successfully utilizing the broad vz range with controlled systematic precision, we are exploring similar event selections maximizing the available statistics for future jet measurements, including the inclusive/differential jet analyses. In Section 3 we present the sampled integrated luminosity in 2023 and 2025 for both the 30 cm and 70 cm vz cuts. The following physics performance projections are based on the 70 cm cut, using the cumulative sampled integrated luminosity for Run-14, Run-16, and 2023 and 2025 together. For $|\mathrm{vz}| < 70$ cm, this total is 53.3 nb^{-1}, which is roughly a factor 7 increase in trigger statistics relative to the current analyses based on Run-14 data.

The following paragraphs in this section will highlight some of these measurements in greater detail.

3.3.1 Precision Jet Measurements to Study the QGP Micro-Structure

To quantify the effect of the marked increase in integrated luminosity, we utilize two mature jet measurements currently in progress and discuss their expected improvement with enhanced integrated luminosity. These analyses are the semi-inclusive distribution of charged-particle jets recoiling from a high-E_{T} direct-photon trigger ($\gamma_{\mathrm{dir}} + \mathrm{jet}$); and the differential measurement of energy loss for jet populations selected by varying a substructure metric. Since these analyses are mature, their analysis methodologies and correction schemes are optimized, so that their projections based on increased statistics are meaningful. We do not imply that these will be the only flagship measurements that STAR will make with the 2023/2025 datasets; we will additionally continue to focus, for instance, on fully reconstructed jets and utilizing substructure observables, including those not yet developed. However, these analyses are most mature at present, and therefore provide the most accurate projections of gain in precision.

Semi-inclusive $\gamma_{\mathrm{dir}} + \mathrm{jet}$ Measurements

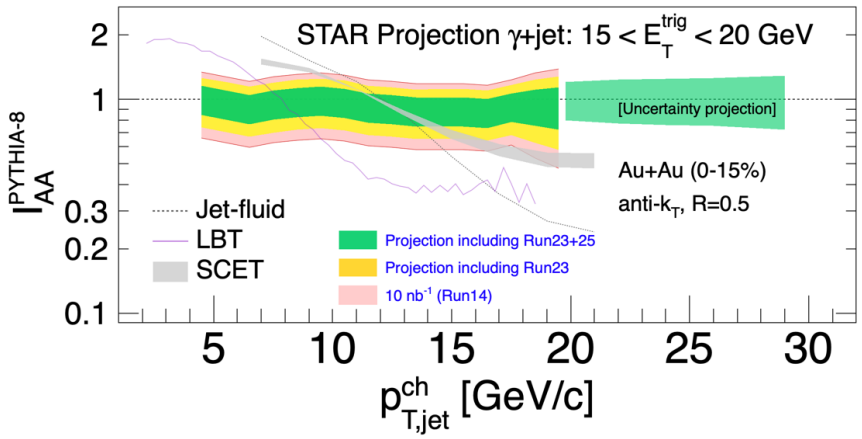

Figure 82: Projections for the I_{AA} for semi-inclusive anti-k_{T}, $R = 0.5$ jets recoiling from a direct-photon trigger with $15 < E_{\mathrm{T}} < 20$ GeV for central (0-15%) Au+Au collisions at $\sqrt{s_{\mathrm{NN}}} = 200$ GeV. The colored bands show the cumulative uncertainty for the current analysis and projections for future analysis with the higher statistics datasets.

Figure 82 shows I_{AA} for fully-corrected semi-inclusive distributions of charged-particle jets (anti-k_{T}, $R = 0.5$) recoiling from a direct-photon trigger with $15 < E_{\mathrm{T}} < 20$ GeV in central Au+Au collisions at $\sqrt{s_{\mathrm{NN}}} = 200$ GeV, for the current analysis based on 10 nb^{-1} [316] within $|\mathrm{vz}| < 70$ cm. The projected uncertainties for Run-23 and Run-25 (75 nb^{-1} including the previous years and Run-23 and Run-25) are shown in the yellow and green colored bands respectively. Significant reduction in the uncertainty band is seen to result from the increase in integrated luminosity, together with a significant increase in kinematic reach. An additional Run-25 not only reduces the uncertainty but also improves the precision measurement of high jet $p_{\mathrm{T,jet}}$as evident by the extended green band along the x-axis.

The revised luminosity projection of 75 nb^{-1} reduces the systematic uncertainty band by a factor of $1/\sqrt{7.5}$ from the current measurement since systematic uncertainty of this measurement, dominated by the unfolding procedure, is correlated with the statistical precision. Due to this correlation, the improvement shown in Fig. 82 should be regarded as a conservative estimate of the improvement in precision of this measurement channel with the projected integrated luminosity increase.

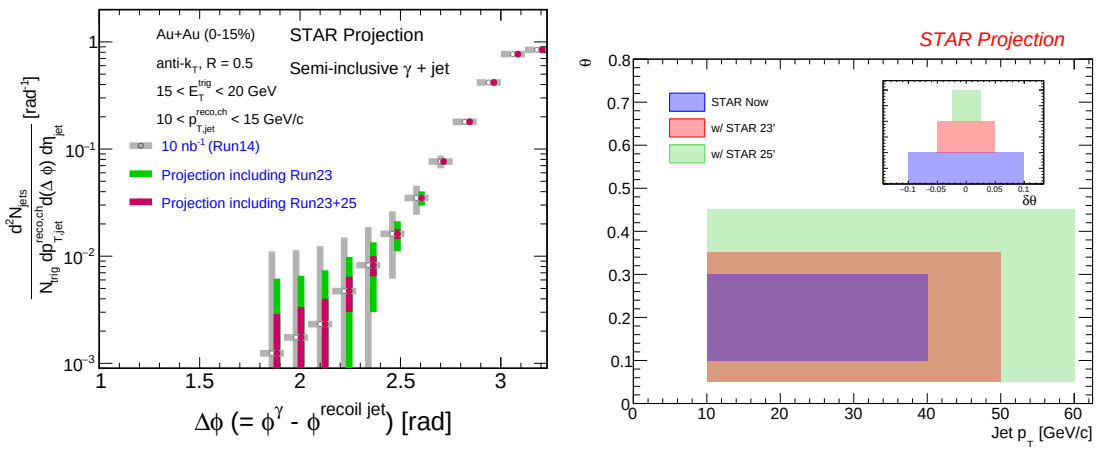

Figure 83: Left: Projections for the acoplanarity for semi-inclusive anti-k_{T}, $R = 0.5$ jets recoiling from a direct-photon trigger with $15 < E_{\mathrm{T}} < 20$ GeV for central (0-15%) Au+Au collisions at $\sqrt{s_{\mathrm{NN}}} = 200$ GeV. The colored bands show the cumulative uncertainty for the current analysis and projections for future analysis with the higher statistics datasets. Right: The subjet opening angle as a function of jet $p_{\mathrm{T,jet}}$ in 0-20% central Au+Au collisions for various scenarios of data-taking. The inset is the corresponding resolution of θ. Blue, red, and green represent current ($10\mathrm{nb}^{-1}$), with Run-23, and with Run-23+Run-25, respectively.

The p_{T} broadening due to medium effects not only modifies the shape but also introduces a decorrelation between the di-jet angular distributions. The vacuum QCD process (Sudakov radiation) makes such measurements challenging in heavy-ion collisions, although at RHIC the Sudakov effect is smaller than at the LHC as it depends on the virtuality Q^2 [311, 312]. A detailed study is needed to understand both these effects (medium-induced and vacuum radiation) at a wide range of jet $p_{\mathrm{T,jet}}$ both at RHIC and the LHC energies. Such measurements are crucial to probe $\hat{q}$ and/or quest for the predicted large-angle jet scattering off of quasi-particles in the QGP [317].

In this direction, STAR is undertaking a preliminary study using γ_{dir}+jet and π^0+jet with $11 < E_{\mathrm{T}} < 15$ GeV and a charged-particle jet (anti-k_{T}, $R = 0.2$ and 0.5) with $10 < p_{\mathrm{T,jet}}^{\mathrm{ch}} < 15$ GeV/c. The analysis techniques pertaining to this measurement are being studied extensively to achieve precision on systematic uncertainty. Such measurements with higher energy triggers (γ_{dir} and π^0) $E_{\mathrm{T}}^{\mathrm{trig}}$ and $p_{\mathrm{T,jet}}$ are crucial to study the inner working of the QGP. This is limited by the current statistics, particularly to study recoil jets at a large $\Delta\phi$ angle. A similar study at the LHC is also ongoing using h+jet measurements [318].

The left plot of Fig. 83 shows the semi-inclusive distribution of the azimuthal separation between a direct-photon trigger with $15 < E_{\mathrm{T}} < 20$ GeV and a charged-particle jet (anti-k_{T}, $R = 0.5$) with $10 < p_{\mathrm{T,jet}}^{\mathrm{ch}} < 15$ GeV/c, in central Au+Au collisions at $\sqrt{s_{\mathrm{NN}}} = 200$ GeV with only statistical uncertainties. The azimuthal smearing of this observable due to uncorrelated background is small, and such acoplanarity measurements are therefore strongly statistics-dominated [319, 320]. The grey points are from the current preliminary measurement based on 10 nb^{-1}, whereas the green and red points correspond to including Run-23 and Run-

23+25 (75 nb^{-1}), respectively. A marked increase in measurement precision is projected, with corresponding qualitative increase in physics impact.

Differential Measurements of Energy Loss Tagged with a Substructure Metric

Systematic exploration of parton energy loss controlled for variations in the jet shower forms an integral part of the jet program at STAR. Since parton showers are inherently probabilistic, a jet population contains patterns of radiation varying in both angle and momentum fraction which can be extracted via jet substructure measurements designed with jet constituents' angle and/or momentum via algorithms or correlations. By selecting jets based on their substructure, STAR can differentially measure jet-medium interactions for various types of energy loss e.g. color coherence, dead cone, etc. In other words, the STAR jet program for Run-23+Run-25 will focus on jet substructure as a jet-tagger.

Theory calculations show significant differences between energy loss signatures for jets perceived by the medium as a single or multiple color charges [308]. The integrated luminosity from the Run-23+Run-25 datasets not only provide a substantial increase in statistics in the current measurements of jet substructure, they also increase the available phase space for rare processes such as wide angle emissions from high-p_{T} jets. This enables STAR to extend our current measurements of differential energy loss, with a resolution of $\delta\theta = 0.1$ to finer resolution $\delta\theta \approx 0.025$ in the jet opening angle, measured via reconstructed subjets as shown in Fig. 83 (right) and also extend to jets of higher momenta. By extending to high energy splittings within jets, at varied opening angles, we can probe earlier formation times whereby vacuum-like emissions and medium induced radiations are expected to occur.

Given the unique nature of jet-medium interactions at RHIC, with the jet and sub-jet scales sufficiently closer to the medium scale, the aforementioned measurements bolster the importance of the STAR jet program with the goal of extracting the microscopic properties of the QGP as outlined in the 2015 LRP.

3.3.2 Deconfinement and Thermalization With Charmonia Measurements

An important observable for studying the properties of the deconfined medium is the second order flow harmonic of the Fourier expansion of the azimuthal distribution of the produced hadrons, the elliptic flow coefficient v_2. As in the case of light hadrons, a positive v_2 of D-mesons and electrons from heavy-flavor hadron decays was observed at RHIC energies of 54.4 and 200 GeV. Which suggests that charm quarks may (partially) thermalize and participate in the bulk medium collective evolution. On the other hand, the v_2 of heavier J/ψ reported by STAR based on the 2010 Au+Au 200 GeV data sample was found to be consistent with zero, albeit within large statistical uncertainties and systematic uncertainties due to non-flow effects. The precision of the measurement was also not enough to distinguish between theoretical model calculations that assume only primordial J/ψ production and ones that include additional J/ψ production via recombination. This calls for a larger sample of heavy-ion data at 200 GeV, as will be provided by RHIC in 2023 and 2025, in order to observe a possible non-zero J/ψ v_2 at RHIC energies and put more constraints on the J/ψ

production models especially regarding its regeneration. Particularly important for these studies is STAR's potential to measure low transverse momentum J/ψ with a very good precision. This excellent low-p_{T} performance at STAR can be achieved thanks to its low material budget and great particle identification capabilities.

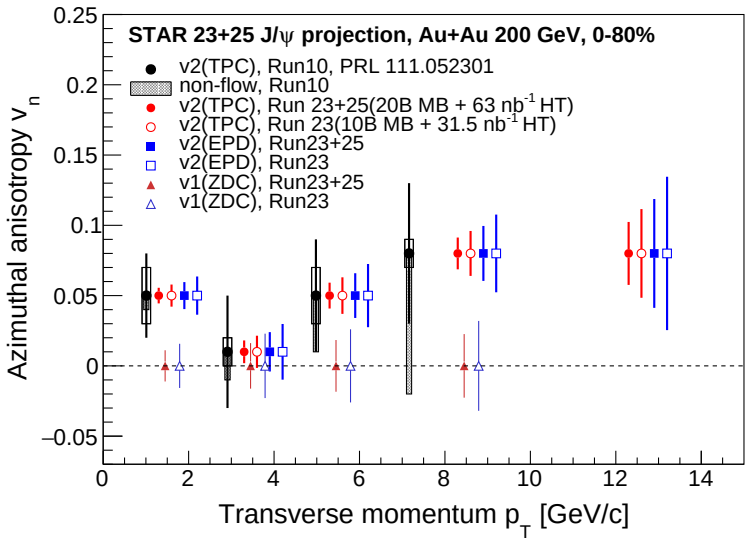

Figure 84: Projections for the J/ψ ($J/\psi \to e^+e^-$) directed (v_1) and elliptic (v_2) flow vs J/ψ p_{T} in 0-80% Au+Au collisions at 200 GeV, assuming 20 B MB events and HT triggered events corresponding to an integrated luminosity of 63 nb^{-1} with $|\mathrm{V_Z}| < 30$ cm.

Moreover, the second order Event Plane (EP) can be reconstructed using the new Event Plane Detectors (EPD) installed before Run-18. It is expected that using the forward EPD will significantly decrease the contribution from the non-flow effects and consequently the measurement's systematic uncertainties. Also, an inverse of the EP resolution enters directly the J/ψ v_2 uncertainty calculation. Thanks to the EPD, the resolution of the EP reconstruction at forward rapidity for the J/ψ v_2 measurement at STAR will improve. Figure 84 presents statistical projections for the J/ψ v_2 measurement in 0-80% central Au+Au collisions assuming 20 B MB events and HT triggered events corresponding to an integrated luminosity of 63 nb^{-1}. Both cases of the second order EP reconstruction, using the forward EPD and mid-rapidity TPC detectors, are considered and shown. A clear significant improvement in the precision of the J/ψ v_2 can be seen across the whole experimentally accessible J/ψ p_{T} coverage of the previous measurement. In addition, the new larger dataset would allow to extend the measured p_{T} range beyond 10 GeV/c.

Studies of the directed flow, v_1, as a function of rapidity provide crucial information to understand the initial tilt of the medium produced in heavy-ion collision [313, 314]. Heavy quarks are produced in the early stage of a heavy-ion collision and thus are of particular interest for the medium initial asymmetry studies. STAR recently reported the first measurement of D-meson v_1 in Au+Au collisions at 200 GeV where the magnitude of the heavy-flavor meson v_1 is about 25 times larger than the v_1 for charged kaons. With the

2023-2025 data, STAR would have a unique opportunity to also study the v_1 of a bound $c\bar{c}$ state, the J/ψ mesons, for which even larger directed flow can be expected [321]. In addition to STAR's excellent capability to reconstruct low-p_{T} J/ψ, as discussed above, the iTPC detector completed in 2018 will improve the momentum resolution and extend the pseudorapidity coverage. This will provide better precision for the slope extraction of the v_1 vs y measurement, that quantifies the strength of directed flow. The expected precision of a J/ψ v_1 measurement vs p_{T} at STAR in 2023-2025, assuming 20 B MB events and HT triggered events corresponding to an integrated luminosity of 63 nb^{-1}, in 0-80% central Au+Au collisions at 200 GeV is shown in Fig. 84. Together with the J/ψ v_2 measurements, v_1 would provide a more complete picture of the J/ψ production mechanism as well as the medium properties in heavy-ion collisions at RHIC.

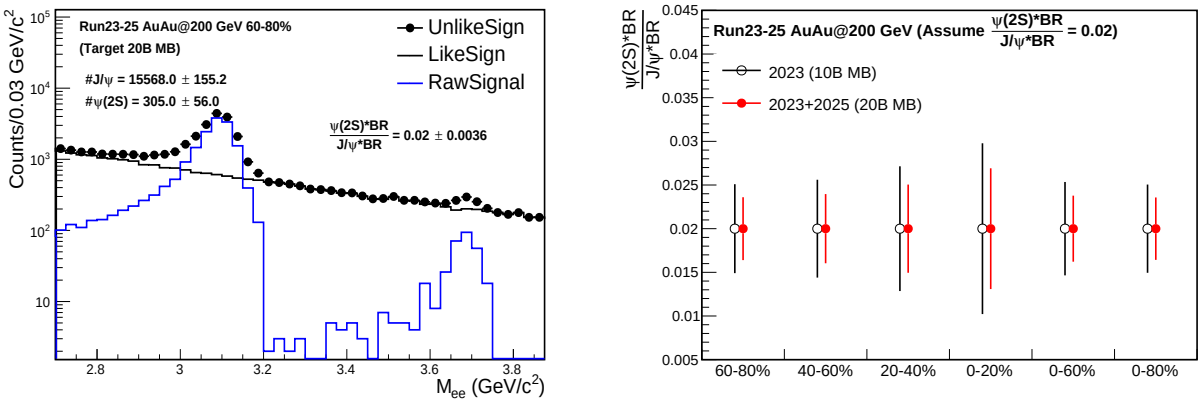

Figure 85: Projections for the J/ψ and ψ(2S) signals in 60-80% Au+Au collisions at 200 GeV and the yield ratio in various centrality bins. The improvement of momentum and dE/dx resolution thanks to the iTPC upgrade have not been taken into account.

ψ(2S) is the most loosely bounded quarkonium state currently accessible to heavy-ion collision experiments. Its dissociation temperature is predicted to be around, or below, the critical temperature, and is much less than that of J/ψ and Υ states. It is therefore more likely to be dissociated in the early stage and in the core of the fireball, and those ψ(2S) that are measured may have significant contributions from regeneration at a later stage in the evolution of the fireball. The relative suppression of ψ(2S) and J/ψ is sensitive to the temperature profile of the fireball produced in heavy-ion collisions and its space-time evolution. It is also argued that the charmonium formation process from a $c\bar{c}$ pair may be affected by both the QGP and the initial strong external magnetic field, altering the relative yields among different charmonium states [322, 323]. The measurement of ψ(2S) is much more difficult than that of J/ψ due to a much smaller production cross-section and dilepton decay branching ratio, resulting in a very low signal-to-background ratio. The ALICE Collaboration successfully measured the relative suppression of ψ(2S) and J/ψ in Pb+Pb collisions at forward rapidity [324], and the ATLAS and CMS Collaborations published the relative suppression in Pb+Pb collisions at mid-rapidity and high p_T [325,326]. Attempts to measure

ψ(2S) suppression in heavy-ion collisions at RHIC have not been successful to date. The low material budget and excellent particle identification capability of STAR together with the combined large data sample in 2023 and 2025 will provide a unique opportunity to measure the suppression of ψ(2S) at low p_T and mid-rapidity in heavy-ion collisions. Figure 85 shows the projections of ψ(2S) signal and the yield ratio of ψ(2S) and J/ψ from 20 B MB events in Au+Au collisions. Here the $\psi(2S)/J/\psi$ ratio is assumed to be 0.02, and the performance of detectors from existing data before STAR iTPC upgrade is used for the projection. As shown in the figure, the ψ(2S) signal significance will be around 3σ level in the 0-20% centrality bin. This significance could become even smaller depending on the level of further suppression for ψ(2S) compared to J/ψ. Despite the improvement of momentum and dE/dx resolution thanks to the STAR iTPC upgrade, it is crucial to have both the 2023 and 2025 data for a significant ψ(2S) measurement.

3.4 Electromagnetic Probes and Ultra-periheral collisions

3.4.1 Probing the degrees of freedom of the medium and its transport properties:

At $\mu_B \sim 0$ Lattice QCD works and can be directly tested against experimental results. In case the measured in-medium spectral function merges into the QGP description this would indicate a transition from hadrons into a structure-less quark-antiquark continuum, thus providing the manifestation of chiral symmetry restoration. We will continue to search for a direct signature of chiral symmetry restoration via chiral ρ-a_1 mixing. The signal is predicted to be detectable in the dilepton intermediate mass range. Difficulties are related to the fact that correlated charm-anticharm and QGP saturate the invariant mass region of 1.1 — 1.3 GeV/c^2. Therefore an accurate measurement of the excess dilepton yield, i.e. dilepton yield after subtraction of the cocktail of contributions from final-state decays, Drell-Yan and those from correlated heavy-flavor decays, up to invariant mass of 2.5 GeV/c^2 is required. The challenging analysis on charmed-decayed dielectron is ongoing from the datasets taken with the Heavy Flavor Tracker at STAR [327]. Thus deeper understanding of origin of thermal radiation in Au+Au collisions at $\sqrt{s_{\rm NN}}$ = 200 GeV from ∼zero mass up to 2.5 GeV/c^2 will become possible with rigorous theoretical efforts and improved dielectron measurements. Figure 86 shows the expected statistical and systematic uncertainties of the dielectron excess mass spectrum with all the detector upgrades and for the anticipated total Run-23/Run-25 statistics of 20×10^9 events.

Another application of dileptons is to use them to measure transport coefficients. The electrical conductivity can be directly obtained as the low-energy limit of the EM spectral function. We aim to extract such information by studying excess dielectron yields at the low-energy regime of the dilepton spectra and the conductivity peak at small invariant masses, i.e. at low invariant mass and low p_T^{ee}. Low field run could be profitable, however already now leptons with p_T^e down to 60 MeV/c could be measured. Measurement of Drell-Yan in p+A collisions at low p_T would provide an important reference to constrain the dilepton cocktail.

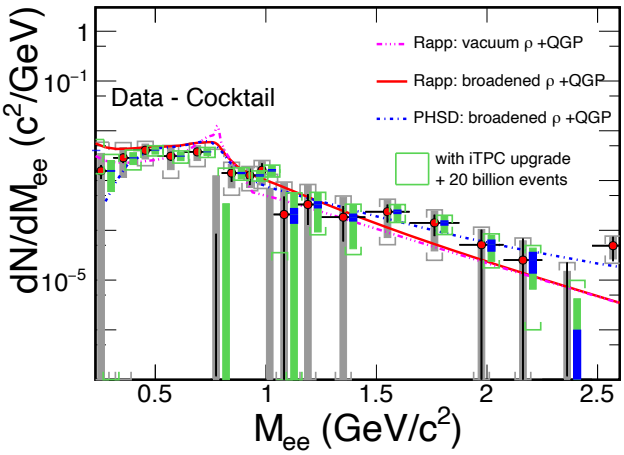

Figure 86: The expected statistical and systematic uncertainties on the dielectron excess mass spectrum with the iTPC upgrade compared to the current TPC case. The data are from our measurements in $\sqrt{s_{\rm NN}}$ = 200 GeV Au+Au collisions [328]. Model comparisons are also shown. The boxes represent systematic uncertainties from data and the brackets represent the total systematic uncertainties including those from cocktails. The grey ones are for the current case while the green ones are for the Run-23+Run-25 case. The blue bands represent statistical uncertainties from 20 billion minimum-bias events with the iTPC upgrade.

To gain a deeper understanding of the microscopic origin of the excess radiation, we will

- separate early from later time radiation by measuring dilepton elliptic flow (v_2) as a function of dilepton mass;
- identify the source of dilepton radiation by studying dilepton polarization versus invariant mass (helicity angle);
- measure precisely the lifetime of the interacting fireball. As an observable we will use integrated low-mass yield but also compare explicit model calculations with various $\tau_{fireball}$;
- extract an average radiating source temperature from the fit of a Boltzmann distribution to the invariant mass slope in the range 1.1 - 2.5 GeV/c^2 spectrum. The higher the invariant mass, the stronger the QGP contribution to the spectrum, the higher the chance to measure temperature of the QGP.

Last, but not least, concerning direct-photon emission, the existing difference, on the order of a factor of two, between the low momentum spectra from PHENIX and STAR in 200 GeV Au+Au collisions, has to be resolved. In order to clarify the direct photon puzzle we will measure with precision the direct virtual photon yield as well as its elliptic flow coefficient. We will particularly focus on low p_T η measurement which might be instrumental in clarifying this long standing question.

3.4.2 Studying the Photon Wigner Function and Final-state Magnetic Fields in the QGP

The unsuccessful description of STAR data by the STARLight model led to the attribution of the broadening to the possible residual magnetic field trapped in an electrically conducting QGP [329]; which is key information to the study of the chiral magnetic effect.

Similarly, ATLAS quantified the effect via the acoplanarity of lepton pairs in contrast to the measurements in UPC and explained the additional broadening by multiple electromagnetic scatterings in the hot and dense medium [330], which is analogous to the medium $P_\perp$-broadening effects for jet quenching.

These descriptions of the broadening in hadronic collisions are based on the assumption that there is no impact parameter dependence of the transverse momentum distribution for the electromagnetic production. Recent lowest-order QED calculations, in which the impact parameter dependence is recovered, could reasonably describe the broadening observed by STAR and ATLAS without any in-medium effect. To solve the puzzle, we propose to precisely study the initial $P_\perp$-broadening for the dilepton pair in ultra-peripheral collisions. Different neutron emission tags serve as the centrality definition, and will allow us to explore the broadening baseline variation with impact parameter. Furthermore, the differential spectrum as a function of pair $P_\perp$, rapidity, and mass enable us to study the Wigner function of the initial electromagnetic field, which provide the information to extract the momentum and space correlation of EM field.

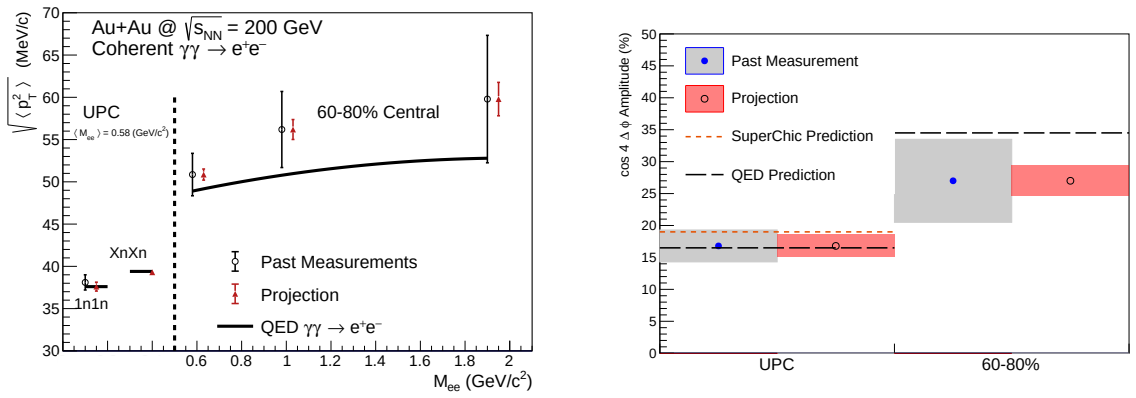

Figure 87: (Color online) Projections for measurements of the $\gamma\gamma \to e^+e^-$ process in peripheral and ultra-peripheral collisions. Left: The $\sqrt{\langle p_T^2 \rangle}$ of di-electron pairs within the fiducial acceptance as a function of pair mass, M_{ee}, for $60-80\%$ central and ultra-peripheral Au+Au collisions at $\sqrt{s_{\rm NN}}$ = 200 GeV. Right: The projection of the $\cos 4\Delta\phi$ measurement for both peripheral $(60-80\%)$ and ultra-peripheral collisions.

As shown in Fig. 87, comparing with the latest QED calculation, there still exists additional broadening in peripheral collisions, although the significance is only about 1σ, which still leave room for the medium effect. In Run-23 and Run-25, as projected in the figure, we

could judge the existence of additional broadening with much higher precision and further constrain the strength of final-state magnetic field in the QGP.

Precision measurement of the amplitude of the recently observed $\cos 4\Delta\phi$ modulation of the $\gamma\gamma \to e^+e^-$ process will allow precision mapping of the photon Wigner function and provide additional constraints on possible final-state effects, thereby complementing the $P_\perp$ broadening measurement. Figure 87 right panel shows the projected precision for a measurement of the $\cos 4\Delta\phi$ modulation in Run-23+25. The modulation is a direct result of the mismatch in initial and final spin configuration of the $\gamma\gamma \to e^+e^-$ process. Any final-state effect that modifies the $P_\perp$ will necessarily reduce the amplitude of the modulation. Assuming the same central value as previously measured, evidence for suppression of the $\cos 4\Delta\phi$ modulation will be visible at the $> 3\sigma$ level (stat. & syst. uncertainty). Precision measurement of the $\cos 4\Delta\phi$ modulation in Run-23+25 may also allow a first direct experimental measurement of the impact parameter dependence of this new observable (by comparing UPC and $60-80\%$). Assuming the same central values as previously measured, the improved precision will provide evidence for impact parameter dependence at the $> 3\sigma$ level (stat. & syst. uncertainty). Assuming the central value predicted by QED would lead to a $> 5\sigma$ difference between the UPC case and the $60-80\%$ case.

3.4.3 Ultra-peripheral Au+Au Collisions: Probe Gluon Distribution Inside the Nucleus

STAR recently observed a significant $\cos 2\Delta\phi$ azimuthal modulation in $\pi^+\pi^-$ pairs from photonuclear ρ^0 and continuum production. The structure of the observed modulation as a function of the $\pi^+\pi^-$ pair transverse momentum, $P_\perp$, appears related to the diffractive pattern. Recent theoretical calculations [331], which implemented linearly polarized photons interacting with the saturated gluons inside a nucleus, have successfully described the qualitative features of the observed modulation(see Fig. 88), and indicate that the detailed structure of the $\cos 2\Delta\phi$ modulation vs. $P_\perp$ is sensitive to the nuclear geometry and gluon distribution. Data from Run-23+25 would allow the additional statistical reach needed to perform multi-differential analysis, providing stronger theoretical constraints. Specifically, multi-differential analysis of the $\cos 2\Delta\phi$ modulation with respect to pair rapidity and pair mass are needed. Multi-differential analysis with respect to pair mass is needed to separate the ρ^0 production from the continuum Drell-Soding production. Multi-differential analysis with respect to the pair rapidity is needed to quantitatively investigate how the double-slit interference mechanism effects the structure of the observed azimuthal modulation. Additional statistical precision is also needed for measurement of the higher harmonics. Similar measurements with $J/\Psi \to e^+e^-$ can be performed and such measurements at higher mass provide better comparison with more reliable QCD calculation.

Ultraperipheral Å collisions, where photons generated by the Lorentz-boosted electromagnetic field of one nucleus interact with the gluons inside the other nucleus, can provide certain 3D gluonic tomography measurements of heavy ions, even before the operation of the future EIC. STAR has performed experimental measurements of the photoproduction

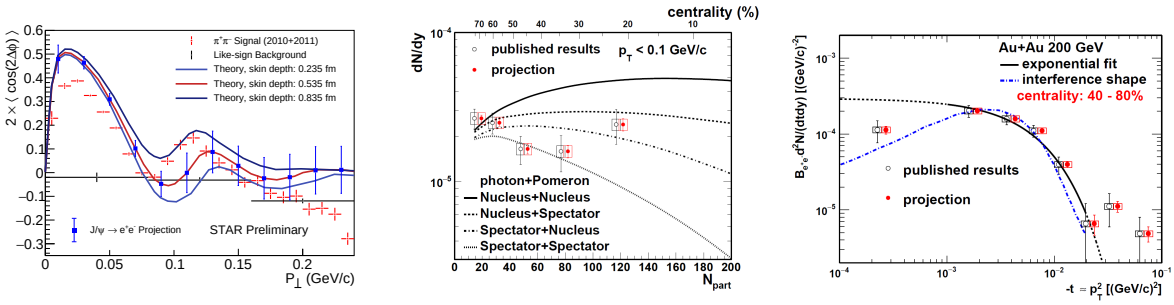

Figure 88: Left: Measurement of the $\cos 2\Delta\phi$ modulation of $\pi^+\pi^-$ pairs from photonuclear ρ^0 and continuum production compared to theoretical predictions [331]. Projections are shown for a similar measurement of the azimuthal modulation of e^+e^- pairs from photonuclear production of the J/ψ. Center: Projection of the dN/dy of photoproduced J/ψ in non-UPC events vs. the event centrality ($N_{\rm part}$) compared to various theoretical production scenarios. Right: Projection of the t spectra of photoproduced J/ψ in $40-80\%$ central collisions.

of J/ψ at low transverse momentum in non-UPC heavy-ion collisions [332], accompanying the violent hadronic collisions. A detailed study with p_T distributions has shown that the $|t|$ distribution in peripheral collisions is more consistent with the coherent diffractive process than the incoherent process. Although models [333, 334] incorporating different partial coherent photon and nuclear interactions could explain the yields, it remains unclear how the coherent process happens and whether final-state effects play any role [335]. Resolving this puzzle with high statistical data and detailed $|t|$ distributions at different centralities at RHIC as projected for Run-23+25 in Fig. 88 may be important for understanding what defines the coherentness of the photoproduction, how vector mesons are formed in the process and how exclusive the similar process has to be in future EIC experiments with forward neutron veto/tagging.

4 Forward Upgrade

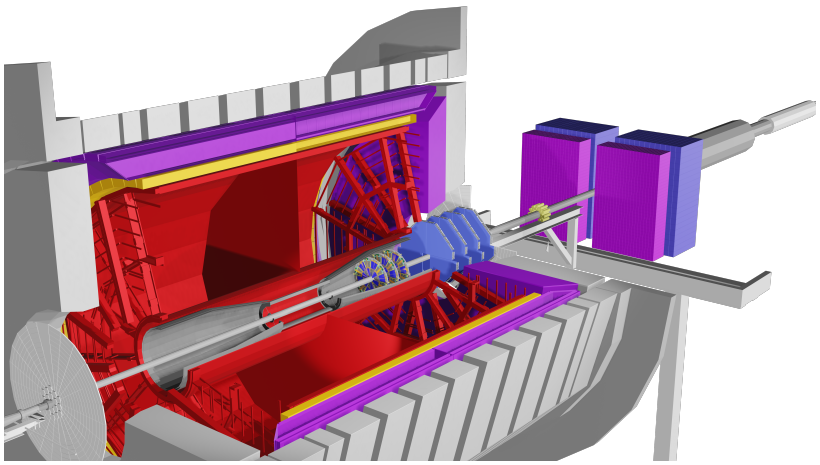

Figure 89: A view of the detectors comprising the STAR forward upgrade, rendered by simulation.

STAR is finalizing construction of the forward detector system, realized by combining tracking with electromagnetic and hadronic calorimeters, in preparation for first data taking in Run-22. It will have superior detection capability for neutral pions, photons, electrons, jets, and leading hadrons within the pseudorapidity range $2.5 < \eta < 4$.

The design of the Forward Calorimeter System (FCS) was driven by consideration of detector performance, integration into STAR, and cost optimization. For the electromagnetic calorimeter, components of the refurbished PHENIX sampling EMCal were used, while the hadronic calorimeter has been newly constructed as a sandwich iron/scintillator plate sampling type, based on extensive STAR Forward Upgrade and EIC Calorimeter Consortium R&D. The existing Event Plane Detector (EPD) will be used as a trigger detector, especially for di-electron triggers. Both calorimeters share the same cost-effective readout electronics, with SiPMs as photo-sensors. The FCS system will have very good electromagnetic ($\sim 10\%/\sqrt{E}$) and hadronic ($\sim 50\%/\sqrt{E} + 10\%$) energy resolution.

In addition, a Forward Tracking System (FTS) is being constructed. The FTS will be capable of discriminating hadron charge sign for transverse spin asymmetry and Drell-Yan measurements in pp and p+A collisions. In heavy ion collisions, measurements of charged-particle transverse momenta over the range $0.2 < p_{\mathrm{T}} < 2$ GeV/c with 20-30% momentum resolution are required. To keep multiple scattering and photon conversion backgrounds under control, the material budget of the FTS must be small. Hence, the FTS design is based on three Silicon mini-strip detectors that consist of disks with a wedge-shaped design to cover the full azimuth and $2.5 < \eta < 4.0$; they are read out radially from the outside to minimize the material. The Si-disks are combined with four small-strip Thin Gap Chamber (sTGC) wheels following the ATLAS design [336, 337]. The three Si mini-strip disks will be located in the region $z = 146.6 - 173.7$ cm, while the four sTGC wheels will be placed 30 cm apart starting from $z = 273$ cm. The Si-Disks readout is based on APV chips and will reuse

the readout chain of the IST, which was part of the STAR HFT. For the sTGC the readout will be based on the ATLAS VMM3 chip [338].

4.1 Status

Following a successful Director's Review in November 2018, the FCS consortium submitted an NSF Major Research Instrumentation (MRI) proposal for construction of the EMCAL and HCAL and associated electronics. The MRI was approved in Summer 2019 and work began in earnest on all aspects of the upgrade. In August 2020, another successful Director's Review was conducted on the status of the upgrades. No serious issues were found. By the end of 2020, construction of both the EMCAL and HCAL had been successfully completed; they are now being commissioned as part of the ongoing Run-21. The Silicon Tracker and sTGC Tracker systems are expected to finish construction in June 2021, and will be installed in STAR prior to the start of Run-22.

4.2 Forward Calorimeter System

The platform that supports the HCAL and EMCAL was installed in 2019, followed by installation and stacking of the refurbished PHENIX EMCAL blocks.

Production of the HCAL absorber blocks at Chapman Lake Instrumentation and Gatto Industrial Plating was completed in late summer 2020, with all parts delivered to BNL. All of the 18,200 scintillating tiles have been produced and polished at ACU, Valparaiso, UCLA and OSU. Front-end electronics boards were designed and tested at Indiana University, sent out for commercial production, then QA'ed at IU and UKY. Other parts have been fabricated, tested, and calibrated at Rutgers, Temple, BNL and UCLA. HCAL construction started on the platform in Fall 2020, and successfully finished by the end of 2020 on schedule despite following COVID19 restrictions, as seen in Fig. 90.

For both the EMCAL and HCAL, front-end electronics cards with SiPM sensors were installed, calibrated, and commissioned with very few failures, and are now fully working. Seventy-eight DEP/ADC readout boards and three DEP/IO boards for trigger processing have been produced and installed in five crates at STAR. They are connected to DAQ PCs and are currently being used to take data during Run-21. About 0.5% of channels were found to have issues, and will be fixed during the upcoming shutdown.

LED systems were also installed for both the EMCAL and HCAL. They are being used for mapping verification, as shown in Fig. 91, and for short- and long-term gain stability monitoring, as well as determining temperature compensation for the SiPM voltages. Radiation damage monitoring has started and small increases in the dark current have been observed, which fall well within the expected range.

A signal splitter for the west EPD has been designed, and two prototype boards were produced. These were installed in late May 2021 for testing and for timing adjustments during the remaining weeks of Run-21. A total of 24 boards (plus spares) will be produced and installed prior to Run-22.

Figure 90: A view of the installed forward EMCAL, with the HCAL behind, left and right of the beam pipe.

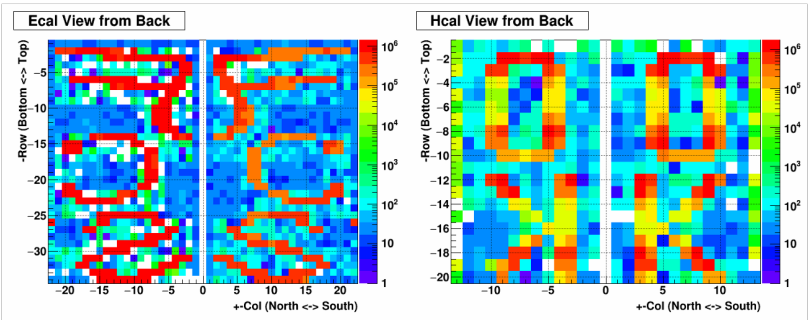

Figure 91: An event display of FCS EMCal and HCal with voltage patterns loaded for mapping checks.

4.3 Forward Silicon Tracker

The Forward Silicon Tracker (FST) consists of three disks, each with 12 wedge-shaped detector modules. Each module is separated into two sections along the radial direction, with Silicon mini-strip sensors mounted on different sides of the module respectively. These modules will be mounted on an aluminum support structure and inserted into the inner cone of the STAR TPC. Two prototype detector modules were assembled and their efficiency and resolution were verified with cosmic ray (see Figure 92). Mass production of detector modules started after a FST production readiness review in Aug. 2020. As of May 2021, about 40 detector modules have been fully assembled and tested successfully at Fermilab and at the University of Illinois at Chicago. Six of these have arrived at BNL for initial installation tests; the rest will be shipped in the first week of June. The support structure and its associated installation tooling have been fabricated and assembled in the STAR clean

room. Mounting detector modules onto the support structure has started, together with the full set of cabling and cooling tube connections. The cooling and DAQ systems, which were used previously for the HFT-IST sub-system, have been incorporated into the FST and their performance has been verified. The operation of the entire detector will be verified by running the cooling and DAQ systems with the fully assembled detector in the clean room in June-July before installation into STAR in August, 2021. Despite all the complications and challenges imposed by COVID19, the Forward Silicon Tracker upgrade project has stayed on schedule and the detector is expected to be ready for physics data taking in Run-22.

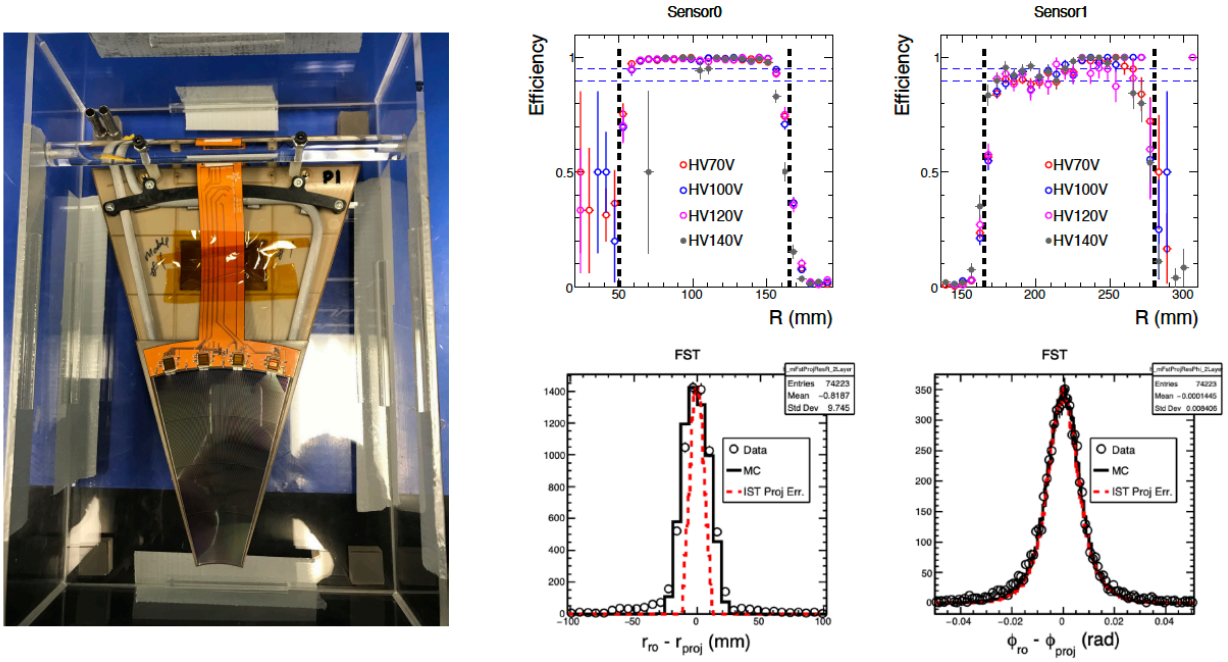

Figure 92: Left: a photograph of a FST detector module in the storage box with the Silicon sensor in the inner section facing up. Right: measured FST detector module performance from cosmic ray testing. Shown on the top are the efficiencies for the inner (left) and outer sensor (right) respectively. Shown in the bottom are the residual distributions between the measured and projected positions in the radial and azimuthal directions, respectively.

4.4 Forward sTGC Tracker

The sTGC system for the forward upgrade has been designed by collaborators from Shandong University (SDU), who also oversee the mass production and testing of the sTGC modules. A 60×60 cm^2 sTGC module was produced, and was found to have a position resolution of 140 microns and a detector efficiency of 97.3%. This module was shipped to BNL and installed at STAR for data taking this year. Due to space constraints around the beam pipe, the final sTGC modules have been designed to have a pentagon shape (see Figure 93). Four pentagon pre-production modules were assembled in August 2020. Following an sTGC production readiness review in Nov. 2020, comments and suggestions received from

the review committee were addressed. Mass production of pentagon modules started in March 2021; 20 pentagon sTGC stations have been produced as of mid-May this year.

High detector efficiencies and low leakage currents have been demonstrated for the produced stations. Final position resolutions will be measured using the new read-out electronics, which is based on the ATLAS VMM3a chip developed for a similar detector. The strips of each sTGC layer will be read out by 24 Front-End Boards (FEBs), so a total of 96 FEBs are needed for the four sTGC layers. The signals are sent to a Readout Board Driver (ROD) and interfaced to STAR DAQ. The electronics design and fabrication was carried out by USTC. The FEB design is complete and final production is ongoing. RDO construction is finished, as is design of the installation and mounting frames. The required n-pentane gas system and interlocks have been designed and approved at BNL. The 60×60 cm^2 sTGC module equipped with both the old TPX electronics boards and new VMM3a-chip based FEBs, has been operated with the n-pentane gas system, and fully integrated to STAR DAQ. Slow control system has been developed and working smoothly. Online QA plots are also in place.

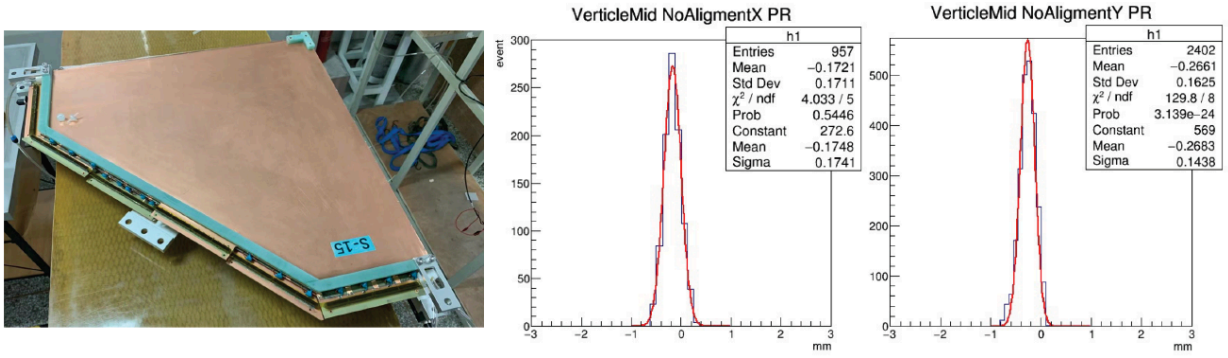

Figure 93: Left: a photograph of a pentagon-shaped sTGC module. Middle and right: residual distributions between the measured and projected positions of the 60×60 cm^2 sTGC prototype in the x and y directions, respectively, from cosmic ray testing.

In order to mitigate the effect of COVID19 and stay on schedule, more engineers for module production were hired at SDU. Module production is now completed. The first 4 modules out of 20 (16 for full sTGC system and 4 for spares) were shipped to BNL towards the end of May. Obvious damages were seen for all the 4 modules. We determined that the 4 modules could still be repaired at SDU, therefore, will be shipped back to SDU. We are also re-designing shipping frames to mitigate the effect from improper handling in the shipping process. All the other 16 sTGC modules will be shipped to BNL with the new frames by the end of June. The 4 modules, after shipped back to SDU and repaired, will be shipped back to BNL in July.

In addition to the FEBs and one ROD used for our 60×60 cm^2 sTGC prototype integration test at STAR, three more FEBs and 17 additional RODs (16 RODs needed for the full system) were received at BNL in May. Towards the end of June, 35 additional FEBs will be ready and shipped to BNL from USTC. The rest of FEBs will be shipped to BNL in

mid-July.

For the sTGC installation, 4 sTGC modules will be mounted onto a frame to form a disk, therefore, 4 frames will be needed to hold the full system. The frames should have arrived at the end of May, however, due to the delay in the procurement, they are now expected to arrive in July 19. The sTGC modules and FEBs will be mounted onto the frames by mid-August. Cooling manifolds and ducting installation and testing, cabling and gas line installation, gas system test, and full system test will be followed. The sTGC assembly will be completed by the end of August, and will be installed to STAR in early October. We will have two weeks to test the full sTGC system at its final location before sTGC platform is removed. With all the careful planning, we believe the sTGC will be ready for Run-22. However, the delay in procurement of the frames to hold the sTGC modules and unpredicted damages to our first 4 pentagon-shaped sTGC modules in the shipping process make our schedule very tight.

4.5 Software

Much of the software needed for the Forward Calorimeter System has already been developed, including DAQ, online monitoring, trigger algorithm simulation and verification, slow control and alarming, and recording the detector status to the STAR database. Offline codes for fitting pulse shapes, cluster finding, and cluster analysis are working. From test data taken with 200 GeV Au+Au collisions during Run-19, π^0 and MIP peaks in the EMCAL were successfully reconstructed and identified, as shown in Fig. 94 and Fig. 95. Data have also been collected from 200 GeV O+O collisions during the ongoing Run-21 using the fully assembled FCS, and are being analyzed to set final calibrations.

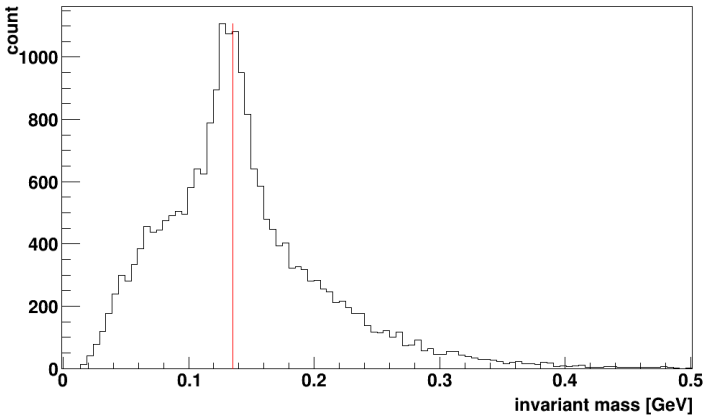

Figure 94: Reconstructed π^0 peak from 200 GeV Au+Au collisions taken during Run-19.

Sets of trigger algorithms for the FCS have been developed, based on simulations performed by Texas A&M. FPGA codes have been written, loaded to the DEP/IO boards, their timing adjusted and verified, and are currently being used for data taking during the

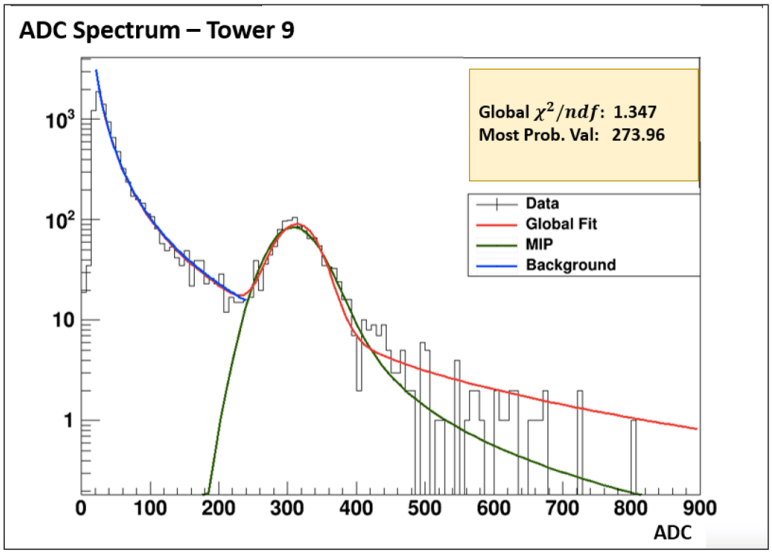

Figure 95: Reconstructed MIP peak from 200 GeV Au+Au collisions taken during Run-19.

ongoing Run-21. We will continue to work on refining the algorithms, as it was found that more powerful logic is available on the FPGAs than is used in current algorithms.

Preliminary versions of slow control, DAQ, and online monitoring software for the tracking detectors have also been developed and tested. Track reconstruction algorithms utilizing hits from the four sTGC planes and the three Si layers have been developed, and good performance has been demonstrated. The tracking algorithm is based on modern techniques: it depends on GENFIT, a general purpose tracking toolkit, and on the iLCSoft KiTrack, a Cellular Automata library, which is used to seed track finding. Other components of the offline software needed for the tracking detectors are being developed and tested.

5 Future Opportunities

Experience from the BES-II has shown us that the excellent performance from RHIC may allow us to take short opportunistic datasets that enable unique physics programs with minimal extra running time. With this in mind we outlined in Section 1.5 a request for a short d+Au run in Run-21 if time permits. If this is not possible, STAR remains interested in taking this data if the opportunity arrives in 2023-2025 after collection of our higher priority datasets outlined in the rest of the BUR. Below we outline two other opportunistic programs, both are of great interest to STAR and the larger nuclear physics community.

5.1 Fixed-target Measurements Using Light Beam and Target Combinations

Although the proposed fixed-target Au+Au energy scan has been completed, if the opportunity exists for further measurements, light beam and target combinations could help to clarify the role and mechanisms of nucleon stopping. Indeed, STAR was recommended to consider installing a beryllium target, that being the lowest Z feasible solid target which could work with the target apparatus. This was not done previously because changing the target requires opening the STAR beampipe and removing the existing target, and that could not be done until the Au+Au energy scan had been completed. Both the collider and STAR have demonstrated that fixed-target runs can be quickly tuned, as the demands on collider operations are modest, and efficiently run, as the collider can control and deliver sufficient intensity to fill the STAR DAQ bandwidth and the experiment can cleanly trigger on these events.

It is possible that fixed-target collisions using light beam and target combinations could also benefit the Space Radiation Protection community. Cosmic rays are a serious concern to astronauts, electronics, and spacecraft. Although 90% of the cosmic ray flux is comprised of energetic protons and another 9% is Helium nuclei, the remaining 1%, which is made up of nuclei from Li to Fe, is not negligible both because the energy loss is proportional to Z^2 and because additional damage is done by the energetic light nuclei (p, d, t, ^3He, and ^4He) produced through the fragmentation of the target and projectile nuclei. Light ion cross section measurements represent the largest uncertainty in space radiation estimates. The energy spectrum of cosmic rays in the solar system is concentrated at energies below 1 GeV/n. Extensive measurements have been made using the dedicated NSRL facility at the booster, and at other lower energy facilities. However, the Space Radiation Community has recently identified higher energy systems, using beams from 3 to 50 GeV/n on C, Al, and Fe targets as one of the next areas of need. The requirements would be to measure the cross section for light nucleus (p, d, t, ^3He, and ^4He) production through fragmentation of the target and projectile. STAR has very good particle identification for all of these particle species using both dE/dx and time-of-flight, however the acceptance is only in the target-side of the rapidity distribution. For symmetric systems this is not a problem. For asymmetric systems this would require both light-on-heavy and heavy-on-light combinations. Efforts are underway to determine if the STAR detector has sufficient acceptance in p_T and

y to meet the needs of the Space Radiation Protection community. If it is determined that the measurements that could be made at RHIC using the STAR detector would meet those needs, STAR is likely to propose brief energy scans using He, Si, and Fe beams on light targets in years 23, 24, and 25. Such measurements could not be made in 2022 because the timeline to prepare for the Run-22 is very brief and there is not be adequate time to open the STAR beampipe and replace the targets.

5.2 Shape Tomography of Atomic Nuclei Using Collective Flow Measurements

The success of the hydrodynamic framework of heavy-ion collisions permits us today to perform quantitative extractions of the transport properties of the QGP via the state-of-the-art multi-system Bayesian analysis approaches [280–282]. Such extractions rely largely on a correct description of the initial condition of the QGP prior to the hydrodynamic expansion. Recent experimental data in ^{238}U+^{238}U [16] (see also Figs. 3) and ^{129}Xe+^{129}Xe [339–341] collisions, as well as dedicated theoretical studies [31, 342–344], have indicated the importance of nuclear deformation on the measured anisotropic flow. However, the effects of nuclear deformation are not yet considered in these Bayesian approaches. For a reliable extraction of transport properties and initial-state from the flow data, we need to ensure that the uncertainty associated with the structure of the colliding ions is under control in the hydrodynamic models, especially since all species for which high statistics of events have been collected at RHIC and the LHC are expected to present some deformations in the ground state, as indicated in Table 10). Note that the deformation values are often obtained via global analysis of nuclear structure data and to some extent are model dependent.

	β_2	β_3	β_4
^{238}U	0.286 [27]	0.078 [345]	0.09 [346]
^{208}Pb	0.05 [27]	0.04 [347]	?
^{197}Au	-(0.13-0.16) [346, 348]	?	-0.03 [346]
^{129}Xe	0.16 [346]	?	?
^{96}Ru	0.05-0.16 [27, 346]	?	?
^{96}Zr	0.08 [27]	?	0.06 [346]

Table 10: Some estimates of the deformation values β_2, β_3, and β_4 for the large nuclei collided at RHIC and the LHC with references given, mostly on global analysis of $B(En)$ transition data over a broad range of nulclei.

It is straightforward to see why the geometry of heavy-ion collisions is sensitive to nuclear deformation. We refer to the cartoon in Figure 96. A nucleus can be modeled through a nucleon density of Woods-Saxon form:

$$\rho(r,\theta,\phi) = \frac{\rho_0}{1+e^{[r-R(\theta,\phi)]/a}},\ R(\theta,\phi) = R_0\left(1+\beta_2[\cos\gamma Y_{2,0}+\sin\gamma Y_{2,2}]+\beta_3 Y_{3,0}+\beta_4 Y_{4,0}\right), \tag{4}$$

where $Y_{n,m}(\theta,\phi)$ is the standard real form of the spherical harmonics and the nuclear surface $R(\theta,\phi)$ includes only the most relevant deformation components from nuclear structure physics, quadrupole $n=2$, octupole $n=3$ and hexadecapole $n=4$. The angle $0 \leq \gamma \leq \pi/3$ controls the triaxiality of the quadruple deformation or the three radii R_a, R_b, R_c of the ellipsoid, with $\gamma = 0$ corresponds to prolate ($R_a = R_b < R_c$), and $\gamma = \pi/3$ corresponds to oblate ($R_a < R_b = R_c$). In central heavy-ion collisions, the shape of the deformed ions determines the geometry of overlap. The entire mass distribution is probed simultaneously, and one can use multi-particle correlation observables to probe it. This way of probing nuclear densities is different from the standard techniques of low-energy physics, where the β_n is inferred from the orientation-averaged form factor data from e+A and hadron+A scatterings and multipole transition probabilities, $B(En)$, between low-lying rotational states. The $B(En)$ method is also sensitive to whether the rotor undergoes rigid or wavelike (irrotational) rotations, while heavy ion collisions only care about the spatial distribution of nucleons. Furthermore, the time scales involved in high-energy heavy ion collisions are much shorter ($< 10^{-24}$s), than the typical timescale of the EM transition involved in the rotational bands (typically on the order of 10^{-21}s). As we shall also argue below, a remarkable question is whether the manestification of nuclear deformation – collective features of the nuclear many-body system – is the same across energy scales.

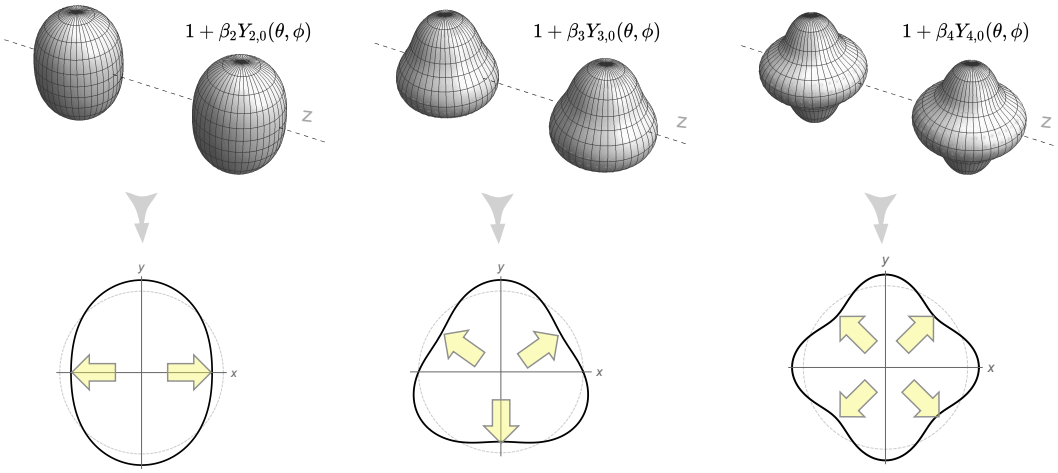

Figure 96: A cartoon of a collision of nuclei with quadruple (left), octupole (middle) and hexadecapole (right) deformations including only the $Y_{n,0}$ mode and with $\beta_n = 0.25$ (we ignore the large Lorentz contraction in the z-direction). The bottom row shows how the initial condition of the medium formed after the collision looks like in the transverse plane. The yellow arrows indicate the direction of maximum pressure gradients along which the medium expands with the largest velocity, leading to final state harmonic flow v_n with n-fold symmetry.

The presence of multipoles, β_n, in the colliding ions modifies nontrivially the corresponding spatial anisotropy, ε_n, of the produced QGP, and consequently the final-state flow harmonic, v_n. For $n=2$ both the mean-squared eccentricity and the mean-squared elliptic

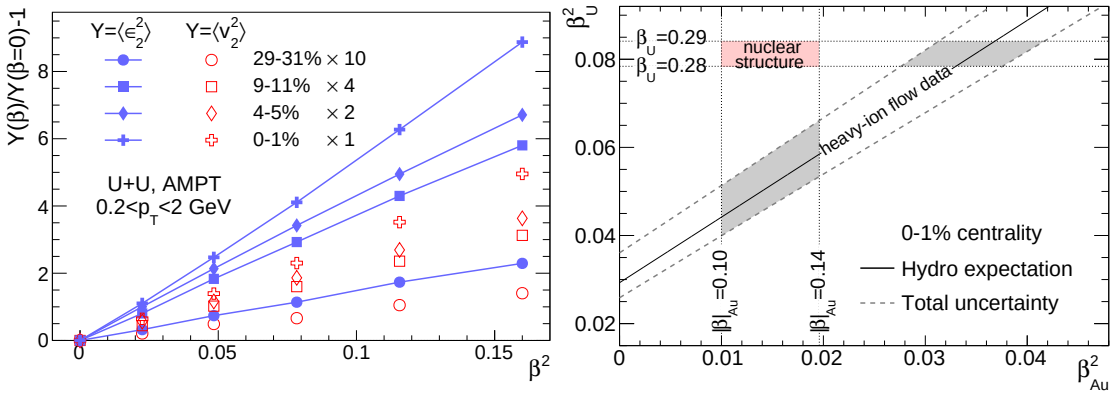

Figure 97: Left panel: $\langle v_2^2(\beta)\rangle / \langle v_2^2(0)\rangle - 1 = b/a\ \beta_2^2$ (empty symbols) and $\langle \epsilon_2^2(\beta_2)\rangle / \langle \epsilon_2^2(0)\rangle - 1 = b'/a'\ \beta_2^2$ (full symbols) as a function of β_2^2 in U+U collisions from the AMPT model. Different symbols correspond to different centrality classes. Right panel: $\beta_{2,\mathrm{U}}^2$ as a function of $\beta_{2,\mathrm{Au}}^2$. The region between the dashed lines is consistent with the hydrodynamic expectation based on Eq. (6) and STAR v_2 data in 0–1% centrality. Figures taken from Ref. [350].

flow are simple functions of the quadruple deformation parameter [344, 349] (see Fig. 97)

$$\left\langle \epsilon_2^2 \right\rangle = a' + b'\beta_2^2, \qquad \left\langle v_2^2 \right\rangle = a + b\beta_2^2, \tag{5}$$

where the a' and a are mean-squared eccentricity and elliptic flow without deformation, $a' = \langle \epsilon_2^2 \rangle_{|\beta_2=0}$ and $a = \langle v_2^2 \rangle_{|\beta_2=0}$, while the b' and b describe the parametric dependence of the deformation-enhanced component of eccentricity and elliptic flow, respectively. Interestingly, the response coefficients for the deformation-independent and deformation-dependent components are not the same, i.e. $k_a \equiv a/a' \neq b/b' \equiv k_b$, which opens up the possibility to test hydrodynamics using β_2 as a new control variable. The value $b' \approx 0.2$ reflects a simple phase space factor accounting for the average over all random orientations, and is found to be nearly independent of the colliding systems. The strict quadratic dependence of Eq. 5 leads to a very robust equation relating the β_2 between any pair of collision systems, X+X and Y+Y, that are close in mass number [349]:

$$\beta_{2,\mathrm{Y}}^2 = \left(\frac{r_{v_2^2} r_a - 1}{r_{\mathrm{Y}}} \right) + \left(r_{v_2^2} \right) \beta_{2,\mathrm{X}}^2, \qquad r_{v_2^2} = \left\langle v_2^2 \right\rangle_{\mathrm{Y}} / \left\langle v_2^2 \right\rangle_{\mathrm{X}}, \tag{6}$$

The ratios r_a and r_{Y} reflect properties of the initial state geometry and are robust against details of final-state effects. This provides a data-driven way to constrain the β_2. Applied to RHIC data, it allows one to derive a constraint on the $\beta_{2,\mathrm{U}}$ and $\beta_{2,\mathrm{Au}}$, as shown in the right panel of Fig. 97. This highlights how, at present, the low-energy nuclear structure model calculation and the flow data from high-energy nuclear collisions are fairly inconsistent. Relations similar to Eq. 5 can also be written down for v_3 and v_4, which can be used to potentially constrain octupole and hexadecapole deformations.

An additional observable showing large sensitivity to the nuclear quadrupole deformation is the Pearson correlation coefficient, $\rho(v_2^2, [p_T])$, between v_2 and the mean transverse momentum, $[p_{\mathrm{T}}]$. This observable probes in particular the full quadrupole structure of the

colliding ions [349], i.e., both β_2 and its triaxiality γ in Eq. 4. This observable has been measured by the STAR collaboration in U+U and Au+Aucollisions (Fig. 3 in Section 1.1.1), which established unambiguously the large and dominating influence of the nuclear quadruple deformation. The large prolate deformation of ^{238}U yields a strong negative contribution to the $v_2 - [p_T]$ correlation, enough to make it change sign. Similar effect have further been observed in the fluctuations of $[p_T]$ (Fig.4 in Section 1.1.1). Hydrodynamic models based on state-of-the-art initial conditions with deformation values from Table 10 struggle to describe quantitatively all these experimental measurements [20,25,26]. This suggests that the radial flow response of the system to the fluctuations induced by the deformation of the colliding ions is poorly captured by the existing models. Collisions of well-deformed ions, and their comparisons with the collisions of more spherical species, provide us with a new way to test the hydrodynamic description.

We propose thus to collide more species to extract their value of β_2, and other deformation parameters γ, β_3 and β_4, from flow measurements, with a twofold purpose: 1) provide a new handle on the initial state and hydrodynamic response of the QGP, 2) perform studies of nuclear structure physics at high energy to complement the information coming from lower energies, and so assess the consistency of nuclear phenomena across energy scales. The ground state of almost all stable nuclei is deformed (see for example the interactive chart in Ref. [351]). RHIC, with its flexibility to collide almost any nuclei from p+p to U+U, is a unique facility to perform such studies in the foreseeable future. The best example to showcase this capability is the run of isobars performed in 2018, where the two systems, Zr+Zr and Ru+Ru, were alternated on a fill-by-fill basis, leading to extremely small systematic uncertainties on the final observables [80] (also Section 1.2). This allows one to detect minute differences in the physics observables such as multiplicity, $[p_T]$ and v_n in the comparison of the two systems. Consequently, even small differences in the values of β_n of the colliding systems can be precisely mapped [352]. For each species, we need roughly 100 million minimum bias and 50 million 0-5% central events. Assuming the standard 50% RHIC+STAR up time and 1.5 KHz DAQ rate, same as Au+Au running, we will be able to collect 130M minbias events and 64M central events in three days of physics running. This is slightly less than the existing U+U dataset taken in 2011, but with comparable statistical precision due to the increased acceptance from the iTPC. Adding two days of setup time, this leads to about five days of total time for each species.

The system scan we propose can be divided into two steps. Given the tight schedule for the next few years, instead of making an explicit proposal on how much running time are needed to fully explore these topics, we discuss what can be achieved if we are given certain number of days.

- **≈10 days:** In the first step, we would like to scan two nuclei in the vicinity of the most studied species at RHIC, ^{197}Au, to improve the modeling of Au+Au collisions, an information which is crucial for the future precision interpretation of high-statistics data expected during the operation of sPHENIX. To achieve this, ideal candidates are ^{208}Pb and ^{196}Hg (^{198}Hg could be a substitute). Having ^{208}Pb at $\sqrt{s_{NN}} = 200$ GeV provides a crucial bridge with the ^{208}Pb at LHC energies: comparison between ^{208}Pb

measurements at RHIC and the LHC will constrain any possible energy dependence of the initial state effects and pre-equilibrium dynamics. Additionally, ^{208}Pb is nearly spherical, so that Pb+Pb collisions at the same energy will allow us to better understand the impact of the moderate deformation of ^{197}Au in Au+Au collisions. The Hg+Hg collisions would then permit us to understand more deeply the nature of the deformation of ^{197}Au, which, being an odd-mass nucleus, hasn't been determined in low-energy experiments. ^{196}Hg is an oblate nucleus with $|\beta_2| \approx 0.1$, and the observable $\rho(v_2^2, [p_T])$ can be used quantify whether ^{197}Au is more or less oblate than ^{196}Hg, an information which will gauge more tightly the initial geometry of Au+Au collisions. Adding Hg+Hg collisions will also provide an independent cross-check on the initial state, for example one can setup three relations like Eq.6 from Pb+Pb, Hg+Hg and Au+Au to triangulate the consistency of the three deformation values.

- **Additional time:** In the second step, our proposal is to use hydrodynamics and flow measurements to perform precision cross-check of low-energy nuclear physics by constraining the evolution of the quadrupole deformation along the chain of stable samarium isotopes. It would be useful in particular to collide three isotopes: ^{144}Sm ($\beta_2 = 0.08$, as spherical as ^{208}Pb), ^{148}Sm ($\beta_2 = 0.14$, triaxial much as ^{129}Xe and ^{197}Au), and ^{154}Sm ($\beta_2 = 0.34$ well-deformed like ^{238}U). The evolution of the quadrupole deformation can be mapped precisely at RHIC, thus offering a valuable test of nuclear structure knowledge. If data on ^{154}Sm+^{154}Sm collisions is available, it would be desirable to also have ^{154}Gd+^{154}Gd ($\beta_2 = 0.31$) collisions. The comparison between the two well-deformed isobaric systems could potentially yield the most precise information about the relative deformation of two ground states. Theoretical studies further suggest that ground states in the region $Z \sim 56/N \sim 88$ [353] (including the samarium isotopes) may display enhanced octupole correlations, i.e., β_3 values. These would manifest in high-energy collisions as enhanced v_3, as well as in the correlators $\rho(v_3^2, [p_T])$. Evidence of static octupole moments at low energies is rather sparse, and heavy ion collisions might be a more sensitive approach. The study of octupole deformation is also fundamentally interesting because nuclei with large β_3 provides a stringent test of the electric-dipole moment (EDM) [354]. The exact choice of species is still under refinement, presently we have a preference for ^{154}Sm and ^{148}Sm, followed by ^{154}Gd and ^{144}Sm.

  Finally, one should note that the STAR DAQ rate for these moderate-sized systems could be significantly larger, possibly reaching 2KHz. This enhanced DAQ rate will compensate partially the smaller number of charged particles expected in these systems compared to larger systems.

BNL Nuclear Physics PAC 2021 Charge and Agenda
March 16, 2021

6 Charge for 2021 NPP PAC

- STAR: Beam Use Requests for Runs 22-25
- sPHENIX: Beam Use Requests for Runs 23-25
- CeC: Beam Use Requests

The Beam Use Requests should be submitted in written form to PAC by May 14, 2021. The BURs should be based on the following number of expected cryo-weeks. First number is minimal expected RHIC run duration and second number is optimal duration:

2022: 18 (20)
2023: 20 (28)
2024: 20 (28)
2025: 20 (28)

References

[1] STAR, J. Adam *et al.*, Phys. Rev. Lett. **126**, 092301 (2021), 2001.02852.

[2] Y. Aoki, G. Endrodi, Z. Fodor, S. D. Katz, and K. K. Szabo, Nature **443**, 675 (2006), hep-lat/0611014.

[3] B. Friman, F. Karsch, K. Redlich, and V. Skokov, Eur. Phys. J. C **71**, 1694 (2011), 1103.3511.

[4] A. Bazavov *et al.*, (2020), 2001.08530.

[5] S. Borsanyi *et al.*, JHEP **10**, 205 (2018), 1805.04445.

[6] Z.-T. Liang and X.-N. Wang, Phys. Rev. Lett. **94**, 102301 (2005), nucl-th/0410079, [Erratum: Phys.Rev.Lett. 96, 039901 (2006)].

[7] S. A. Voloshin, (2004), nucl-th/0410089.

[8] STAR, J. Adam *et al.*, Phys. Rev. C **98**, 014910 (2018), 1805.04400.

[9] Y. Sun and C. M. Ko, Phys. Rev. C **96**, 024906 (2017), 1706.09467.

[10] Y. Xie, D. Wang, and L. P. Csernai, Phys. Rev. C **95**, 031901 (2017), 1703.03770.

[11] Y. B. Ivanov, V. D. Toneev, and A. A. Soldatov, Phys. Rev. C **100**, 014908 (2019), 1903.05455.

[12] O. Vitiuk, L. V. Bravina, and E. E. Zabrodin, Phys. Lett. B **803**, 135298 (2020), 1910.06292.

[13] STAR, B. I. Abelev *et al.*, Phys. Rev. C **76**, 024915 (2007), 0705.1691, [Erratum: Phys.Rev.C 95, 039906 (2017)].

[14] ALICE, S. Acharya *et al.*, Phys. Rev. C **101**, 044611 (2020), 1909.01281.

[15] D.-X. Wei, W.-T. Deng, and X.-G. Huang, Phys. Rev. C **99**, 014905 (2019), 1810.00151.

[16] STAR, L. Adamczyk *et al.*, Phys. Rev. Lett. **115**, 222301 (2015), 1505.07812.

[17] G. Giacalone, B. Schenke, and C. Shen, Phys. Rev. Lett. **125**, 192301 (2020), 2006.15721.

[18] P. Bozek, Phys. Rev. C **93**, 044908 (2016), 1601.04513.

[19] P. Bozek and H. Mehrabpour, Phys. Rev. C **101**, 064902 (2020), 2002.08832.

[20] B. Schenke, C. Shen, and D. Teaney, Phys. Rev. C **102**, 034905 (2020), 2004.00690.

[21] G. Giacalone, F. G. Gardim, J. Noronha-Hostler, and J.-Y. Ollitrault, Phys. Rev. C **103**, 024909 (2021), 2004.01765.

[22] S. H. Lim and J. L. Nagle, (2021), 2103.01348.

[23] P. Bozek and W. Broniowski, Phys. Rev. C **85**, 044910 (2012), 1203.1810.

[24] G. Giacalone, Phys. Rev. Lett. **124**, 202301 (2020), 1910.04673.

[25] G. Giacalone, Phys. Rev. C **102**, 024901 (2020), 2004.14463.

[26] G. Giacalone, F. G. Gardim, J. Noronha-Hostler, and J.-Y. Ollitrault, Phys. Rev. C **103**, 024910 (2021), 2004.09799.

[27] S. Raman, C. W. G. Nestor, Jr, and P. Tikkanen, Atom. Data Nucl. Data Tabl. **78**, 1 (2001).

[28] C. Nepali, G. Fai, and D. Keane, Phys. Rev. C **73**, 034911 (2006).

[29] M. R. Haque, Z.-W. Lin, and B. Mohanty, Phys.Rev. **C85**, 034905 (2012), 1112.2340.

[30] V. Bairathi, M. R. Haque, and B. Mohanty, Phys. Rev. C **91**, 054903 (2015), 1504.04719.

[31] U. W. Heinz and A. Kuhlman, Phys.Rev.Lett. **94**, 132301 (2005), nucl-th/0411054.

[32] A. J. Kuhlman and U. W. Heinz, Phys. Rev. C **72**, 037901 (2005), nucl-th/0506088.

[33] A. Kuhlman, U. W. Heinz, and Y. V. Kovchegov, Phys. Lett. B **638**, 171 (2006), nucl-th/0604038.

[34] D. Molnar and S. A. Voloshin, Phys. Rev. Lett. **91**, 092301 (2003), nucl-th/0302014.

[35] R. J. Fries, B. Muller, C. Nonaka, and S. A. Bass, Phys. Rev. Lett. **90**, 202303 (2003), nucl-th/0301087.

[36] I. Takashi, I. G. Noriyoshi, A. Sinya, and D. Takumi, Prog. Theor. Phys **124**, 591 (2010), 1007.3559v1.

[37] B. Abelev *et al.*, Science **328**, 58 (2010), 1003.2030v1.

[38] J. Adam *et al.*, Phys. Lett. B **790**, 490 (2019), 1808.02511.

[39] L. Adamczyk *et al.*, Nature **527**, 345 (2015), 1507.07158.

[40] S. Acharya *et al.*, Nature **588**, 232 (2020), 2005.11495.

[41] I. Takashi, I. G. Noriyoshi, A. Sinya, and D. Takumi, Nucl. Phys. A **881**, 28 (2012), 1112.5926v2.

[42] M. Kenji, O. Akira, E. Faisal, and H. Tetsuo, Phys. Rev. C **94** (2016), 1605.06765.

[43] R. Jaffe, Phys. Rev. Lett **38**, 617 (1977).

[44] N. Shah, Y. Ma, J. Chen, and S. Zhang, Phys. Lett. B **754**, 6 (2016).

[45] S. Marzani, G. Soyez, and M. Spannowsky*Looking inside jets: an introduction to jet substructure and boosted-object phenomenology* Vol. 958 (Springer, 2019), 1901.10342.

[46] A. J. Larkoski, S. Marzani, G. Soyez, and J. Thaler, JHEP **05**, 146 (2014), 1402.2657.

[47] A. J. Larkoski, S. Marzani, and J. Thaler, Phys. Rev. D **91**, 111501 (2015), 1502.01719.

[48] STAR, J. Adam *et al.*, Phys. Lett. B **811**, 135846 (2020), 2003.02114.

[49] STAR, M. Abdallah *et al.*, (2021), 2103.13286.

[50] Z.-B. Kang, K. Lee, X. Liu, and F. Ringer, Phys. Lett. B **793**, 41 (2019), 1811.06983.

[51] A. Majumder and J. Putschke, Phys. Rev. C **93**, 054909 (2016), 1408.3403.

[52] Z.-B. Kang, K. Lee, and F. Ringer, JHEP **04**, 110 (2018), 1801.00790.

[53] T. Adye, Unfolding algorithms and tests using RooUnfold, in *PHYSTAT 2011*, Geneva, 2011, CERN, 1105.1160.

[54] F. A. Dreyer, L. Necib, G. Soyez, and J. Thaler, JHEP **06**, 093 (2018), 1804.03657.

[55] STAR, J. Adam *et al.*, Phys. Rev. D **101**, 052004 (2020), 1912.08187.

[56] STAR, J. Adam *et al.*, Phys. Rev. D **102**, 092009 (2020), 2007.04732.

[57] STAR, J. Adam *et al.*, (2021), 2101.11793.

[58] STAR, L. Adamczyk *et al.*, Phys. Lett. B **771**, 13 (2017), 1607.07517.

[59] STAR, J. Adam *et al.*, Phys. Lett. B **797**, 134917 (2019), 1905.13669.

[60] PHENIX, A. Adare *et al.*, Phys. Rev. C **87**, 034904 (2013), 1204.0777.

[61] J.-P. Lansberg and H.-S. Shao, Eur. Phys. J. C **77**, 1 (2017), 1610.05382.

[62] Y. Ma and R. Vogt.

[63] E. G. Ferreiro, F. Fleuret, J. P. Lansberg, N. Matagne, and A. Rakotozafindrabe, Few Body Syst. **53**, 27 (2012), 1201.5574.

[64] K. Zhou, N. Xu, Z. Xu, and P. Zhuang, Phys. Rev. C **89**, 054911 (2014).

[65] X. Zhao and R. Rapp, Phys. Rev. C **82**, 064905 (2010).

[66] NA50, M. C. Abreu *et al.*, Phys. Lett. B **477**, 28 (2000).

[67] L. Kluberg, Eur. Phys. J. C **43**, 145 (2005).

[68] ALICE, B. B. Abelev *et al.*, Phys. Lett. B **734**, 314 (2014), 1311.0214.

[69] ALICE, X. Bai, Nucl. Phys. A **1005**, 121769 (2021), 2001.11925.

[70] STAR, J. Adam *et al.*, Phys. Lett. B **808**, 135663 (2020), 2003.12136.

[71] D. Kharzeev and R. D. Pisarski, Phys.Rev. **D61**, 111901 (2000), hep-ph/9906401.

[72] D. Kharzeev, Phys.Lett. **B633**, 260 (2006), hep-ph/0406125.

[73] S. A. Voloshin, Phys. Rev. Lett. **105**, 172301 (2010), 1006.1020.

[74] W.-T. Deng, X.-G. Huang, G.-L. Ma, and G. Wang, Phys. Rev. C **97**, 044901 (2018), 1802.02292.

[75] B. Schenke, C. Shen, and P. Tribedy, Phys. Rev. **C99**, 044908 (2019), 1901.04378.

[76] H.-J. Xu *et al.*, Phys. Rev. Lett. **121**, 022301 (2018), 1710.03086.

[77] J. Hammelmann, A. Soto-Ontoso, M. Alvioli, H. Elfner, and M. Strikman, (2019), 1908.10231.

[78] STAR 2017 BUR https://drupal.star.bnl.gov/STAR/system/files/STAR_BUR_Run1718_v22_0.pdf.

[79] STAR, P. Tribedy, J. Phys. Conf. Ser. **1602**, 1 (2020), 2009.01230.

[80] STAR, J. Adam *et al.*, (2019), 1911.00596.

[81] STAR, J. Zhao, (2020), 2002.09410.

[82] CMS, A. M. Sirunyan *et al.*, Phys. Rev. **C97**, 044912 (2018), 1708.01602.

[83] H.-j. Xu *et al.*, Chin. Phys. **C42**, 084103 (2018), 1710.07265.

[84] S. A. Voloshin, Phys. Rev. **C98**, 054911 (2018), 1805.05300.

[85] J. Zhao, H. Li, and F. Wang, Eur. Phys. J. C **79**, 168 (2019), 1705.05410.

[86] STAR, J. Adam *et al.*, (2020), arXiv:2006.05035.

[87] STAR, P. Tribedy, Nucl. Phys. A **967**, 740 (2017), 1704.03845.

[88] STAR, J. Adam *et al.*, (2020), arXiv:2006.04251.

[89] STAR, Y. Lin, Nucl. Phys. A **1005**, 121828 (2021), 2002.11446.

[90] N. Magdy, S. Shi, J. Liao, N. Ajitanand, and R. A. Lacey, Phys. Rev. C **97**, 061901 (2018), 1710.01717.

[91] A. H. Tang, Chin. Phys. C **44**, 054101 (2020), 1903.04622.

[92] S. A. Voloshin, Phys. Rev. **C70**, 057901 (2004), hep-ph/0406311.

[93] N. N. Ajitanand, R. A. Lacey, A. Taranenko, and J. M. Alexander, Phys. Rev. **C83**, 011901 (2011), 1009.5624.

[94] S. Choudhury *et al.*, (2021), 2105.06044.

[95] S. Shi, Y. Jiang, E. Lilleskov, and J. Liao, Annals Phys. **394**, 50 (2018), 1711.02496.

[96] Y. Jiang, S. Shi, Y. Yin, and J. Liao, Chin. Phys. C **42**, 011001 (2018), 1611.04586.

[97] S. Shi, H. Zhang, D. Hou, and J. Liao, Phys. Rev. Lett. **125**, 242301 (2020), 1910.14010.

[98] H. Song, S. A. Bass, U. Heinz, T. Hirano, and C. Shen, Phys. Rev. Lett. **106**, 192301 (2011), 1011.2783, [Erratum: Phys.Rev.Lett. 109, 139904 (2012)].

[99] M. Bleicher *et al.*, J. Phys. G **25**, 1859 (1999), hep-ph/9909407.

[100] S. A. Bass *et al.*, Prog. Part. Nucl. Phys. **41**, 255 (1998), nucl-th/9803035, [Prog. Part. Nucl. Phys.41,225(1998)].

[101] W.-T. Deng, X.-G. Huang, G.-L. Ma, and G. Wang, Phys. Rev. C **94**, 041901 (2016), 1607.04697.

[102] L. Finch and S. Murray, Phys. Rev. C **96**, 044911 (2017), 1801.06476.

[103] J. Adams *et al.*, Nucl. Instrum. Meth. A **968**, 163970 (2020), 1912.05243.

[104] STAR, M. Abdallah *et al.*, (2021), 2103.05571.

[105] STAR, L. Adamczyk *et al.*, Phys. Rev. D **95**, 071103 (2017).

[106] D. de Florian, R. Sassot, M. Stratmann, and W. Vogelsang, Phys. Rev. Lett. **113**, 012001 (2014), 1404.4293.

[107] NNPDF, E. R. Nocera, R. D. Ball, S. Forte, G. Ridolfi, and J. Rojo, Nucl. Phys. **B887**, 276 (2014), 1406.5539.

[108] STAR, J. Adam *et al.*, Phys. Rev. D. **98**, 032011 (2018).

[109] STAR, J. Kwasizur, Longitudinal Double-Spin Asymmetries for Dijet Production at Intermediate Pseudorapidity in Polarized Proton-Proton Collisions at $\sqrt{s} = 510$ GeV, in *APS Division of Nuclear Physics Meeting*, 2020.

[110] STAR, Y. Xu, Longitudinal and Transverse Spin Transfer of Λ and $\overline{\Lambda}$ Hyperons in Polarized p+p Collisions at $\sqrt{s} = 200$ GeV at RHIC-STAR, in *XXVIII International Workshop on Deep-Inelastic Scattering and Related Subjects, Stony Brook University*, 2021, https://indico.bnl.gov/event/9726/contributions/46261/.

[111] J. Adam *et al.*, Phys. Rev. D **98**, 112009 (2018).

[112] STAR, B. Pokhrel, Transverse Spin Dependent Azimuthal Correlations of Charged hadrons in Collisions at $\sqrt{s} = 200$ GeV, in *XXVIII International Workshop on Deep-Inelastic Scattering and Related Subjects*, 2021.

[113] STAR, B. Pokhrel, Transverse Spin Dependent Azimuthal Correlations of Charged hadrons(s) in $p \uparrow p$ Collisions at $\sqrt{s} = 200$ GeV, in *XXVIII International Workshop on Deep-Inelastic Scattering and Related Subjects, Stony Brook University*, 2021, https://indico.bnl.gov/event/9726/contributions/46262/.

[114] STAR, J. Adam *et al.*, Phys. Rev. D **103**, 072005 (2021), 2012.07146.

[115] STAR, J. Adam *et al.*, Phys. Rev. D **103**, 092009 (2021), 2012.11428.

[116] U. D'Alesio, F. Murgia, and C. Pisano, Phys. Lett. B **773**, 300 (2017), 1707.00914.

[117] Z.-B. Kang, X. Liu, F. Ringer, and H. Xing, JHEP **11**, 068 (2017), 1705.08443.

[118] Z.-B. Kang, A. Prokudin, F. Ringer, and F. Yuan, Phys. Lett. B **774**, 635 (2017), 1707.00913.

[119] U. D'Alesio, F. Murgia, and C. Pisano, Phys. Rev. D **83**, 034021 (2011), 1011.2692.

[120] Q. Xu, Z. Liang, and E. Sichtermann, Phys. Rev. D **73**, 077503 (2006), 0511061.

[121] STAR, J. Adam *et al.*, Phys. Rev. D **98**, 091103(R) (2018), 1808.08000.

[122] Jefferson Lab Angular Momentum, J. Cammarota *et al.*, Phys. Rev. D **102**, 054002 (2020).

[123] STAR, J. Adam *et al.*, Phys. Rev. D **103**, 012001 (2021), 2011.04708.

[124] NuSea, R. S. Towell *et al.*, Phys. Rev. **D64**, 052002 (2001), hep-ex/0103030.

[125] SeaQuest, J. Dove *et al.*, Nature **590**, 561 (2021), 2103.04024.

[126] STAR, J. Nam, Measurements of W and Z/γ^* cross sections and their ratios in pp collisions at STAR, in *XXVIII International Workshop on Deep-Inelastic Scattering and Related Subjects, Stony Brook University*, 2021, https://indico.bnl.gov/event/9726/contributions/46577/.

[127] STAR, D. Kalinkin, Measurement of Mid-rapidity Inclusive Jet Cross Section in pp Collisions at $\sqrt{s} = 200$ GeV, in *APS Division of Nuclear Physics Meeting*, 2020.

[128] STAR, D. Kalinkin, Measurement of Mid-rapidity Inclusive Jet Cross Section in *pp* Collisions at $\sqrt{s} = 200$ GeV, in *XXVIII International Workshop on Deep-Inelastic Scattering and Related Subjects*, 2021.

[129] STAR, X. Chu, Di-hadron correlations in p+p, p+Au and p+Al collisions at STAR, in *2020 Fall Meeting of the APS Division of Nuclear Physics, online*, 2020, https://meetings.aps.org/Meeting/DNP20/APS_epitome.

[130] J. L. Albacete, G. Giacalone, C. Marquet, and M. Matas, Phys. Rev. D **99**, 014002 (2019), 1805.05711.

[131] CMS, V. Khachatryan *et al.*, JHEP **09**, 091 (2010), 1009.4122.

[132] CMS, S. Chatrchyan *et al.*, Phys. Lett. B **718**, 795 (2013), 1210.5482.

[133] ALICE, B. Abelev *et al.*, Phys. Lett. B **719**, 29 (2013), 1212.2001.

[134] ATLAS, G. Aad *et al.*, Phys. Rev. Lett. **110**, 182302 (2013), 1212.5198.

[135] PHENIX, A. Adare *et al.*, Phys. Rev. Lett. **115**, 142301 (2015), 1507.06273.

[136] PHENIX, A. Adare *et al.*, Phys. Rev. Lett. **114**, 192301 (2015), 1404.7461.

[137] STAR, L. Adamczyk *et al.*, Phys. Lett. B **747**, 265 (2015), 1502.07652.

[138] PHENIX, C. Aidala *et al.*, Phys. Rev. C **95**, 034910 (2017), 1609.02894.

[139] PHENIX, C. Aidala *et al.*, Nature Phys. **15**, 214 (2019), 1805.02973.

[140] J. L. Nagle *et al.*, Phys. Rev. Lett. **113**, 112301 (2014), 1312.4565.

[141] STAR, R. A. Lacey, Nucl. Phys. A **1005**, 122041 (2021), 2002.11889.

[142] J.-w. Qiu and G. F. Sterman, Phys. Rev. D **59**, 014004 (1999), hep-ph/9806356.

[143] K. Kanazawa, Y. Koike, A. Metz, and D. Pitonyak, Phys. Rev. D **89**, 111501 (2014).

[144] L. Gamberg, Z.-B. Kang, and A. Prokudin, Phys. Rev. Lett. **110**, 232301 (2013).

[145] L. Bland *et al.*, Physics Letters B **750**, 660 (2015).

[146] STAR, H. Liu, Measurement of transverse single-spin asymmetries for dijet production in polarized p+p collisions at $\sqrt{s} = 200$ GeV at STAR, in *Nuclear Physics Seminar, Brookhaven National Laboratory*, 2020, https://indico.bnl.gov/event/8633/.

[147] M. Boglione *et al.*, Phys. Lett. B **815**, 136135 (2021), 2101.03955.

[148] STAR, B. Abelev *et al.*, Phys. Rev. Lett. **99**, 142003 (2007), 0705.4629.

[149] M. Bury, A. Prokudin, and A. Vladimirov, Phys. Rev. Lett. **126**, 112002 (2021), 2012.05135.

[150] STAR, L. Adamczyk *et al.*, Phys. Rev. Lett. **116**, 132301 (2016), 1511.06003.

[151] J. P. Ralston and D. E. Soper, Nuclear Physics B **152**, 109 (1979).

[152] R. Jaffe and X.-D. Ji, Nucl. Phys. B **375**, 527 (1992).

[153] P. Mulders and R. Tangerman, Nucl. Phys. B **461**, 197 (1996), hep-ph/9510301, [Erratum: Nucl.Phys.B 484, 538–540 (1997)].

[154] D. Sivers, Nuovo Cim. C **035N2**, 171 (2012), 1109.2521.

[155] C. Alexandrou *et al.*, Phys. Rev. D **98**, 091503 (2018).

[156] R. Jaffe and X.-D. Ji, Phys. Rev. Lett. **67**, 552 (1991).

[157] J. C. Collins, S. F. Heppelmann, and G. A. Ladinsky, Nucl. Phys. B **420**, 565 (1994), hep-ph/9305309.

[158] L. Adamczyk *et al.*, Phys. Lett. B **780**, 332–339 (2018).

[159] M. Radici and A. Bacchetta, Phys. Rev. Lett. **120**, 192001 (2018), 1802.05212.

[160] J. Collins and J.-W. Qiu, Phys. Rev. D **75**, 114014 (2007).

[161] T. C. Rogers and P. J. Mulders, Phys. Rev. D **81**, 094006 (2010).

[162] X. Liu, F. Ringer, W. Vogelsang, and F. Yuan, Factorization and its breaking in dijet single transverse spin asymmetries in *pp* collisions, 2020, 2008.03666.

[163] Z.-B. Kang, K. Lee, D. Y. Shao, and J. Terry, The sivers asymmetry in hadronic dijet production, 2020, 2008.05470.

[164] F. Yuan, Phys. Rev. Lett. **100**, 032003 (2008).

[165] F. Yuan, Phys. Rev. D **77**, 074019 (2008).

[166] STAR, L. Adamczyk *et al.*, Phys. Rev. D **97**, 032004 (2018), 1708.07080.

[167] M. Anselmino *et al.*, Phys. Rev. D **73**, 014020 (2006), hep-ph/0509035.

[168] M. Anselmino *et al.*, Phys. Rev. D **75**, 054032 (2007).

[169] J. Soffer, Phys. Rev. Lett. **74**, 1292 (1995).

[170] U. D'Alesio, F. Murgia, and C. Pisano, Phys, Lett. B **773**, 300–306 (2017).

[171] CJ, S. Park, CJ15 global PDF analysis with new electroweak data, in *XXVIII International Workshop on Deep-Inelastic Scattering and Related Subjects, Stony Brook University*, 2021, https://indico.bnl.gov/event/9726/contributions/46569/.

[172] H1, ZEUS, F. Aaron *et al.*, Eur. Phys. J. C **72**, 2175 (2012), 1207.4864.

[173] CMS, V. Khachatryan *et al.*, Phys. Rev. D **92**, 012003 (2015), 1503.08689.

[174] S. L. Bueltmann *et al.*, Phys. Lett. B **579**, 245 (2004), nucl-ex/0305012.

[175] S. Bultmann *et al.*, Phys. Lett. B **632**, 167 (2006), nucl-ex/0507030.

[176] pp2pp, S. Bultmann *et al.*, Phys. Lett. B **647**, 98 (2007), nucl-ex/0610022.

[177] STAR, L. Adamczyk *et al.*, Phys. Lett. B **719**, 62 (2013), 1206.1928.

[178] T. Sjöstrand *et al.*, Comput. Phys. Commun. **191**, 159 (2015), 1410.3012.

[179] I. Helenius, Recent pythia 8 developments: Hard diffraction, colour reconnection and $\gamma\gamma$ collisions, in *7th International Workshop on Multiple Partonic Interactions at the LHC*, 2015, http://indico.ictp.it/event/a14280/session/266/contribution/1042/.

[180] STAR, C. Dilks, PoS **DIS2016**, 212 (2016), 1805.08875.

[181] M. A. Lisa *et al.*, (2021), 2101.10872.

[182] A. Airapetian *et al.*, Phys. Lett. B **693**, 11–16 (2010).

[183] C. Adolph *et al.*, Phys. Lett. B **744**, 250–259 (2015).

[184] D. Müller, D. Robaschik, B. Geyer, F.-M. Dittes, and J. Hoˇ rejši, Fortsch. Phys. **42**, 101 (1994), hep-ph/9812448.

[185] X.-D. Ji, Phys. Rev. Lett. **78**, 610 (1997), hep-ph/9603249.

[186] A. Radyushkin, Phys. Lett. B **380**, 417 (1996), hep-ph/9604317.

[187] M. Burkardt, Phys. Rev. D **62**, 071503 (2000), hep-ph/0005108, [Erratum: Phys.Rev.D 66, 119903 (2002)].

[188] S. Klein and J. Nystrand, Photoproduction of J / psi and Upsilon in pp and anti-p p collisions, in *5th Workshop on Small x and Diffractive Physics*, 2003, hep-ph/0310223.

[189] S. R. Klein, J. Nystrand, J. Seger, Y. Gorbunov, and J. Butterworth, Comput. Phys. Commun. **212**, 258 (2017), 1607.03838.

[190] J. Lansberg, L. Massacrier, L. Szymanowski, and J. Wagner, Phys. Lett. B **793**, 33 (2019), 1812.04553.

[191] HERMES, A. Airapetian *et al.*, Phys. Lett. B **577**, 37 (2003), hep-ex/0307023.

[192] HERMES, A. Airapetian *et al.*, Nucl. Phys. B **780**, 1 (2007), 0704.3270.

[193] HERMES, A. Airapetian *et al.*, Phys. Lett. B **684**, 114 (2010), 0906.2478.

[194] W. Brooks and H. Hakobyan, Nucl. Phys. A **830**, 361C (2009), 0907.4606.

[195] NuSea, M. Vasilev *et al.*, Phys. Rev. Lett. **83**, 2304 (1999), hep-ex/9906010.

[196] H. Paukkunen, The LHC p+Pb run from the nuclear PDF perspective, in *XXII International Workshop on Deep-Inelastic Scattering and Related Subjects*, 2014, https://indico.cern.ch/event/258017/contributions/1588381.

[197] D. de Florian, R. Sassot, P. Zurita, and M. Stratmann, Phys. Rev. D **85**, 074028 (2012), 1112.6324.

[198] PHENIX, S. Adler *et al.*, Phys. Rev. Lett. **98**, 172302 (2007), nucl-ex/0610036.

[199] K. Eskola, H. Paukkunen, and C. Salgado, Nucl. Phys. A **855**, 150 (2011), 1011.6534.

[200] R. Sassot, M. Stratmann, and P. Zurita, Phys. Rev. D **81**, 054001 (2010), 0912.1311.

[201] K. J. Eskola, P. Paakkinen, H. Paukkunen, and C. A. Salgado, Eur. Phys. J. C **77**, 163 (2017), 1612.05741.

[202] N. Armesto, H. Paukkunen, J. M. Penín, C. A. Salgado, and P. Zurita, Eur. Phys. J. C **76**, 218 (2016), 1512.01528.

[203] H. Paukkunen and P. Zurita, JHEP **12**, 100 (2014), 1402.6623.

[204] E. Aschenauer *et al.*, (2014), 1409.1633.

[205] H. Paukkunen, K. J. Eskola, and C. Salgado, Nucl. Phys. A **931**, 331 (2014), 1408.4563.

[206] K. J. Eskola, H. Paukkunen, and C. A. Salgado, JHEP **10**, 213 (2013), 1308.6733.

[207] L. Gribov, E. Levin, and M. Ryskin, Phys. Rept. **100**, 1 (1983).

[208] E. Iancu and R. Venugopalan, The Color glass condensate and high-energy scattering in QCD, in *In *Hwa, R.C. (ed.) et al.: Quark gluon plasma* 249-3363*, 2003, hep-ph/0303204.

[209] H. Weigert, Prog. Part. Nucl. Phys. **55**, 461 (2005), hep-ph/0501087.

[210] J. Jalilian-Marian and Y. V. Kovchegov, Prog. Part. Nucl. Phys. **56**, 104 (2006), hep-ph/0505052.

[211] F. Gelis, E. Iancu, J. Jalilian-Marian, and R. Venugopalan, Ann. Rev. Nucl. Part. Sci. **60**, 463 (2010), 1002.0333.

[212] G. Giuliani, H. Zheng, and A. Bonasera, Prog. Part. Nucl. Phys. **76**, 116 (2014), 1311.1811.

[213] Y. V. Kovchegov and E. Levin *Quantum chromodynamics at high energy* Vol. 33 (Cambridge University Press, 2012).

[214] A. H. Mueller and J.-w. Qiu, Nucl. Phys. B **268**, 427 (1986).

[215] L. McLerran and R. Venugopalan, Phys. Rev. D **49**, 2233 (1994).

[216] L. McLerran and R. Venugopalan, Phys. Rev. D **49**, 3352 (1994).

[217] L. McLerran and R. Venugopalan, Phys. Rev. D **50**, 2225 (1994).

[218] Y. V. Kovchegov, Phys. Rev. D **54**, 5463 (1996).

[219] Y. V. Kovchegov, Phys. Rev. D **55**, 5445 (1997).

[220] J. Jalilian-Marian, A. Kovner, L. McLerran, and H. Weigert, Phys. Rev. D **55**, 5414 (1997).

[221] A. H. Mueller, Nucl. Phys. **B415**, 373 (1994).

[222] A. H. Mueller and B. Patel, Nucl. Phys. B **425**, 471 (1994), hep-ph/9403256.

[223] I. Balitsky, Nucl. Phys. **B463**, 99 (1996), hep-ph/9509348.

[224] I. Balitsky, Phys. Rev. D **60**, 014020 (1999), hep-ph/9812311.

[225] Y. V. Kovchegov, Phys. Rev. **D60**, 034008 (1999), hep-ph/9901281.

[226] Y. V. Kovchegov, Phys. Rev. D **61**, 074018 (2000), hep-ph/9905214.

[227] J. Jalilian-Marian, A. Kovner, and H. Weigert, Phys. Rev. D **59**, 014015 (1998), hep-ph/9709432.

[228] J. Jalilian-Marian, A. Kovner, A. Leonidov, and H. Weigert, Phys. Rev. D **59**, 014014 (1998), hep-ph/9706377.

[229] E. Iancu, A. Leonidov, and L. D. McLerran, Phys. Lett. B **510**, 133 (2001), hep-ph/0102009.

[230] E. Iancu, A. Leonidov, and L. D. McLerran, Nucl. Phys. **A692**, 583 (2001), hep-ph/0011241.

[231] A. Accardi *et al.*, Eur. Phys. J. A **52**, 268 (2016), 1212.1701.

[232] Y. V. Kovchegov and M. D. Sievert, Nucl. Phys. B **903**, 164 (2016), 1505.01176.

[233] CMS, S. Chatrchyan *et al.*, Eur. Phys. J. C **74**, 2951 (2014), 1401.4433.

[234] STAR, E. Braidot, Nucl. Phys. A **854**, 168 (2011), 1008.3989.

[235] PHENIX, A. Adare *et al.*, Phys. Rev. Lett. **107**, 172301 (2011), 1105.5112.

[236] C. Marquet, Nucl. Phys. A **796**, 41 (2007), 0708.0231.

[237] J. L. Albacete and C. Marquet, Phys. Rev. Lett. **105**, 162301 (2010), 1005.4065.

[238] Z.-B. Kang, I. Vitev, and H. Xing, Phys. Rev. D **85**, 054024 (2012), 1112.6021.

[239] M. Strikman and W. Vogelsang, Phys. Rev. D **83**, 034029 (2011), 1009.6123.

[240] J. Jalilian-Marian and A. H. Rezaeian, Phys. Rev. D **86**, 034016 (2012), 1204.1319.

[241] J. L. Albacete and C. Marquet, Nucl. Phys. A **854**, 154 (2011), 1009.3215.

[242] K. J. Eskola, H. Paukkunen, and C. A. Salgado, JHEP **07**, 102 (2008), 0802.0139.

[243] A. H. Rezaeian, Phys. Rev. D **86**, 094016 (2012), 1209.0478.

[244] T. Sjostrand, S. Mrenna, and P. Z. Skands, Comput. Phys. Commun. **178**, 852 (2008), 0710.3820.

[245] Di-jet production from pythia8.189 is scaled down due to its overestimation of inclusive π_0 yields compared to those reported by BRAHMS in phys. rev. lett. 98 (2007) 252001 and STAR in phys. rev. lett. 97 (2006) 152302.

[246] T. Kaufmann, A. Mukherjee, and W. Vogelsang, Phys. Rev. D **92**, 054015 (2015), 1506.01415, [Erratum: Phys.Rev.D 101, 079901 (2020)].

[247] D. de Florian, R. Sassot, M. Epele, R. J. Hernández-Pinto, and M. Stratmann, Phys. Rev. D **91**, 014035 (2015), 1410.6027.

[248] A. Khouaja *et al.*, Nucl. Phys. A **780**, 1 (2006).

[249] D. de Florian and R. Sassot, Phys. Rev. D **69**, 074028 (2004), hep-ph/0311227.

[250] D. de Florian, R. Sassot, and M. Stratmann, Phys. Rev. D **75**, 114010 (2007), hep-ph/0703242.

[251] D. de Florian, R. Sassot, and M. Stratmann, Phys. Rev. D **76**, 074033 (2007), 0707.1506.

[252] J. L. Nagle and W. A. Zajc, Ann. Rev. Nucl. Part. Sci. **68**, 211 (2018), 1801.03477.

[253] H. Helmholtz, The London, Edinburgh, and Dublin Philosophical Magazine and Journal of Science **33**, 485 (1867), https://doi.org/10.1080/14786446708639824.

[254] C. Shen *et al.*, In preparation.

[255] B. Schenke, S. Jeon, and C. Gale, Phys. Rev. **C82**, 014903 (2010), 1004.1408.

[256] STAR, L. Adamczyk *et al.*, Nature **548**, 62 (2017), 1701.06657.

[257] I. Upsal, *Global Polarization of the $\Lambda/\overline{\Lambda}$ system in the STAR BES*, Ph.D. thesis, The Ohio State University, 2018.

[258] Y. B. Ivanov and A. Soldatov, Phys. Rev. C **95**, 054915 (2017), 1701.01319.

[259] Y. B. Ivanov and A. Soldatov, Phys. Rev. C **97**, 044915 (2018), 1803.01525.

[260] Y. B. Ivanov, V. Toneev, and A. Soldatov, Phys. Atom. Nucl. **83**, 179 (2020), 1910.01332.

[261] Y. B. Ivanov, V. Toneev, and A. Soldatov, J. Phys. Conf. Ser. **1435**, 012012 (2020).

[262] B. Fu, K. Xu, X.-G. Huang, and H. Song, (2020), 2011.03740.

[263] M. Baznat, K. Gudima, A. Sorin, and O. Teryaev, Phys. Rev. C **88**, 061901 (2013), 1301.7003.

[264] O. Teryaev and R. Usubov, Phys. Rev. C **92**, 014906 (2015).

[265] M. I. Baznat, K. K. Gudima, A. S. Sorin, and O. Teryaev, Phys. Rev. C **93**, 031902 (2016), 1507.04652.

[266] W.-T. Deng and X.-G. Huang, Phys. Rev. C **93**, 064907 (2016), 1603.06117.

[267] X.-L. Xia, H. Li, Z.-B. Tang, and Q. Wang, Phys. Rev. C **98**, 024905 (2018), 1803.00867.

[268] A. Zinchenko, A. Sorin, O. Teryaev, and M. Baznat, J. Phys. Conf. Ser. **1435**, 012030 (2020).

[269] G. Bunce *et al.*, Phys. Rev. Lett. **36**, 1113 (1976).

[270] COSY-TOF, F. Hauenstein *et al.*, Eur. Phys. J. A **52**, 337 (2016), 1607.06305.

[271] F. Abe *et al.*, Phys. Rev. D **34**, 1950 (1986).

[272] B. Lundberg *et al.*, Phys. Rev. D **40**, 3557 (1989).

[273] HERA-B, I. Abt *et al.*, Phys. Lett. B **638**, 415 (2006), hep-ex/0603047.

[274] HADES, G. Agakishiev *et al.*, Eur. Phys. J. A **50**, 81 (2014), 1404.3014.

[275] A. Aprahamian *et al.*, Reaching for the horizon: The 2015 long range plan for nuclear science, 2015, The 2015 Long Range Plan for Nuclear Science "Reaching for the Horizon" http://science.energy.gov/~/media/np/nsac/pdf/2015LRP/2015_LRPNS_091815.pdf.

[276] RHIC luminosity projection https://www.rhichome.bnl.gov//RHIC/Runs/RhicProjections.pdf.

[277] SN0619 : A Proposal for STAR Inner TPC Sector Upgrade (iTPC) https://drupal.star.bnl.gov/STAR/starnotes/public/sn0619.

[278] STAR, CBM eTOF Group, The CBM Collaboration eTOF Group, (2016), 1609.05102.

[279] The STAR Forward Calorimeter System and Forward Tracking System beyond BES-II https://drupal.star.bnl.gov/STAR/files/Proposal.ForwardUpgrade.Nov_.2018.Review.pdf.

[280] JETSCAPE, D. Everett *et al.*, Phys. Rev. C **103**, 054904 (2021), 2011.01430.

[281] J. E. Bernhard, J. S. Moreland, S. A. Bass, J. Liu, and U. Heinz, Phys. Rev. C **94**, 024907 (2016), 1605.03954.

[282] G. Nijs, W. van der Schee, U. Gürsoy, and R. Snellings, (2020), 2010.15130.

[283] G. Denicol, A. Monnai, and B. Schenke, Phys. Rev. Lett. **116**, 212301 (2016), 1512.01538.

[284] H. Niemi, G. S. Denicol, P. Huovinen, E. Molnar, and D. H. Rischke, Phys. Rev. **C86**, 014909 (2012), 1203.2452.

[285] B. Schenke and S. Schlichting, Phys. Rev. **C94**, 044907 (2016), 1605.07158.

[286] W. Li, Nucl. Phys. A **967**, 59 (2017), 1704.03576.

[287] P. Bozek, W. Broniowski, and J. Moreira, Phys. Rev. **C83**, 034911 (2011), 1011.3354.

[288] J. Jia and P. Huo, Phys. Rev. **C90**, 034915 (2014), 1403.6077.

[289] L.-G. Pang, H. Petersen, G.-Y. Qin, V. Roy, and X.-N. Wang, Eur. Phys. J. **A52**, 97 (2016), 1511.04131.

[290] CMS, V. Khachatryan *et al.*, Phys. Rev. C **92**, 034911 (2015), 1503.01692.

[291] ATLAS, M. Aaboud *et al.*, Eur. Phys. J. C **78**, 142 (2018), 1709.02301.

[292] STAR Collaboration, L. Adamczyk *et al.*, Manuscript under preparation (2016).

[293] A. Behera, M. Nie, and J. Jia, Phys. Rev. Res. **2**, 023362 (2020), 2003.04340.

[294] C. Shen and B. Schenke, Phys. Rev. **C97**, 024907 (2018), 1710.00881.

[295] BeAGLE: a Tool to Refine Detector Requirements for eA Collisions EIC R&D; Project eRD17 E. Aschenauer, M. Baker, W. Chang, J. Lee, Z. Tu et al. https://wiki.bnl.gov/eic/index.php/BeAGLE.

[296] Z. Tu *et al.*, Phys. Lett. B **811**, 135877 (2020), 2005.14706.

[297] Y. Shi, L. Wang, S.-Y. Wei, B.-W. Xiao, and L. Zheng, Phys. Rev. D **103**, 054017 (2021), 2008.03569.

[298] ATLAS, G. Aad *et al.*, (2021), 2101.10771.

[299] STAR, J. Adam *et al.*, Phys. Rev. Lett. **126**, 162301 (2021), 2012.13601.

[300] STAR, B. Abelev *et al.*, Phys. Rev. C **76**, 064904 (2007), 0706.0472.

[301] Z.-T. Liang, J. Song, I. Upsal, Q. Wang, and Z.-B. Xu, (2019), 1912.10223.

[302] Y. Xie, D. Wang, and L. P. Csernai, Eur. Phys. J. C **80**, 39 (2020), 1907.00773.

[303] X.-L. Sheng, L. Oliva, and Q. Wang, Phys. Rev. D **101**, 096005 (2020), 1910.13684.

[304] X.-L. Sheng, Q. Wang, and X.-N. Wang, (2020), 2007.05106.

[305] A. Bazavov *et al.*, Phys. Rev. D **95**, 054504 (2017), 1701.04325.

[306] S. Cao, G.-Y. Qin, and S. A. Bass, Phys. Rev. C **92**, 024907 (2015).

[307] JETSCAPE, A. Kumar *et al.*, Nucl. Phys. A **1005**, 122009 (2021), 2002.07124.

[308] Y. Mehtar-Tani and K. Tywoniuk, Phys. Rev. D **98**, 051501 (2018), 1707.07361.

[309] Y. Mehtar-Tani and K. Tywoniuk, Nucl. Phys. A **979**, 165 (2018), 1706.06047.

[310] B. G. Zakharov, Eur. Phys. J. C **81**, 57 (2021), 2003.10182.

[311] L. Chen, G.-Y. Qin, S.-Y. Wei, B.-W. Xiao, and H.-Z. Zhang, Phys. Lett. B **773**, 672 (2017), 1607.01932.

[312] A. H. Mueller, B. Wu, B.-W. Xiao, and F. Yuan, Phys. Lett. B **763**, 208 (2016), 1604.04250.

[313] S. K. Das *et al.*, Phys. Lett. B **768**, 260 (2017), 1608.02231.

[314] S. Chatterjee and P. Bożek, Phys. Rev. Lett. **120**, 192301 (2018), 1712.01189.

[315] STAR, J. Adam *et al.*, (2020), 2006.00582.

[316] STAR, N. R. Sahoo, Measurement of γ+jet and π^0+jet in central Au+Au collisions at $\sqrt{s_{\rm NN}} = 200$ GeV with the STAR experiment, 2020, 2008.08789.

[317] F. D'Eramo, K. Rajagopal, and Y. Yin, JHEP **01**, 172 (2019), 1808.03250.

[318] ALICE, J. Norman, Jet acoplanarity via hadron+jet measurements in Pb-Pb collisions at $\sqrt{s_{\rm NN}} = 5.02$ TeV with ALICE, in *10th International Conference on Hard and Electromagnetic Probes of High-Energy Nuclear Collisions: Hard Probes 2020* , 2020, 2009.08261.

[319] ALICE, J. Adam *et al.*, JHEP **09**, 170 (2015), 1506.03984.

[320] STAR, L. Adamczyk *et al.*, Phys. Rev. C **96**, 024905 (2017), 1702.01108.

[321] B. Chen, M. Hu, H. Zhang, and J. Zhao, Phys. Lett. B **802**, 135271 (2020), 1910.08275.

[322] X. Guo, S. Shi, N. Xu, Z. Xu, and P. Zhuang, Phys. Lett. B **751**, 215 (2015), 1502.04407.

[323] B. Chen, X. Du, and R. Rapp, Nucl. Part. Phys. Proc. **289-290**, 475 (2017), 1612.02089.

[324] ALICE, J. Adam *et al.*, JHEP **05**, 179 (2016), 1506.08804.

[325] ATLAS, M. Aaboud *et al.*, Eur. Phys. J. C **78**, 762 (2018), 1805.04077.

[326] CMS, A. M. Sirunyan *et al.*, Phys. Rev. Lett. **118**, 162301 (2017), 1611.01438.

[327] STAR, F. Seck, Nucl. Phys. A **1005**, 122005 (2021).

[328] STAR, L. Adamczyk *et al.*, Phys. Rev. Lett. **113**, 022301 (2014), 1312.7397, [Addendum: Phys.Rev.Lett. 113, 049903 (2014)].

[329] STAR Collaboration, J. Adam *et al.*, Phys. Rev. Lett. **121**, 132301 (2018).

[330] ATLAS Collaboration, M. Aaboud *et al.*, Phys. Rev. Lett. **121**, 212301 (2018).

[331] H. Xing, C. Zhang, J. Zhou, and Y.-J. Zhou, The $\cos 2\phi$ azimuthal asymmetry in ρ^0 meson production in ultraperipheral heavy ion collisions, 2020, 2006.06206.

[332] STAR, J. the STAR Collaboration, Adam *et al.*, Phys. Rev. Lett. **123**, 132302 (2019), 1904.11658.

[333] W. Zha *et al.*, Phys. Rev. C **97**, 044910 (2018).

[334] M. B. G. Ducati and S. Martins, Phys. Rev. D **97**, 116013 (2018).

[335] W. Shi, W. Zha, and B. Chen, Phys. Lett. B **777**, 399 (2018), 1710.00332.

[336] V. Smakhtin *et al.*, Nucl. Instrum. Meth. **A598**, 196 (2009).

[337] A. Abusleme *et al.*, Nucl. Instrum. Meth. **A817**, 85 (2016), 1509.06329.

[338] Iakovidis, George, EPJ Web Conf. **174**, 07001 (2018).

[339] ALICE Collaboration, Phys. Lett. B **784**, 82 (2018), 1805.01832.

[340] CMS, A. M. Sirunyan *et al.*, Phys. Rev. C **100**, 044902 (2019), 1901.07997.

[341] ATLAS Collaboration, (2019), 1911.04812.

[342] Q. Y. Shou *et al.*, Phys. Lett. B **749**, 215 (2015), 1409.8375.

[343] G. Giacalone, J. Noronha-Hostler, M. Luzum, and J.-Y. Ollitrault, Phys. Rev. C **97**, 034904 (2018), 1711.08499.

[344] G. Giacalone, Phys. Rev. C **99**, 024910 (2019), 1811.03959.

[345] S. E. Agbemava, A. V. Afanasjev, and P. Ring, Phys. Rev. C **93**, 044304 (2016), 1603.03414.

[346] P. Möller, A. J. Sierk, T. Ichikawa, and H. Sagawa, Atom. Data Nucl. Data Tabl. **109-110**, 1 (2016), 1508.06294.

[347] L. M. Robledo and G. F. Bertsch, Phys. Rev. C **84**, 054302 (2011), 1107.3581.

[348] S. Hilaire and M. Girod, Eur. Phys. J. A **33**, 237 (2007).

[349] J. Jia, S. Huang, and C. Zhang, (2021), 2105.05713.

[350] G. Giacalone, J. Jia, and C. Zhang, (2021), 2105.01638.

[351] Chart of Nuclear Quadrupole Deformations, https://www.nndc.bnl.gov/nudat2/.

[352] G. Giacalone, J. Jia, and V. Somà, (2021), 2102.08158.

[353] P. A. Butler, J. Phys. G **43**, 073002 (2016).

[354] C. J. Lister and J. Butterworth, Nature **497**, 190 (2013).